UNIVERSIDAD COMPLUTENSE DE MADRID

FACULTAD DE CIENCIAS FÍSICAS

Departamento de Física Teórica I

TESIS DOCTORAL

Spin glasses, the quantum annealing, colloidal glasses and crystals: exploring complex free-energy landscapes

Vidrios de espín, computación cuántica adiabática, vidrios y cristales coloidales : explorando paisajes complejos de energía libre

MEMORIA PARA OPTAR AL GRADO DE DOCTOR

PRESENTADA POR

Beatriz Seoane Bartolomé

Directores

Luis Antonio Fernández Pérez
Víctor Martín Mayor

Madrid, 2013

Spin glasses, the quantum annealing, colloidal glasses and crystals: exploring complex free-energy landscapes

Vidrios de espín, computación cuántica adiabática, vidrios y cristales coloidales: explorando paisajes complejos de energía libre

Memoria de tesis doctoral presentada por
Beatriz Seoane Bartolomé

Directores
Luis Antonio Fernández Pérez
Víctor Martín Mayor

Universidad Complutense de Madrid
Facultad de Ciencias Físicas
Departamento de Física Teórica I
MMXII

A mis padres.

CHAPTER I

Agradecimientos

Con estas líneas pongo punto y final a esta tesis doctoral. Pero no puedo darla por terminada sin antes agradecer el apoyo recibido durante estos cuatros años a toda la gente sin la jamás tendría este texto en mis manos.

En primer lugar, mi más sentido agradecimiento para mis dos directores de tesis, Luis Antonio Fernández y Víctor Martín. Sin su constante dedicación y esfuerzo no sé si habría llegado hasta el final. Desde que comenzamos a trabajar juntos allá por el 2007, siempre he sentido que el éxito de mi trabajo ha sido una de sus prioridades. Nunca olvidaré las horas que han pasado conmigo revisando código, haciendo papeleo o esmerándose en que todo estuviera listo para la fecha señalada, aún a costa de perder muchas horas de su vida. Tengo total convicción de que siempre han hecho todo lo que estaba en su mano para que pudiera tener la mejor carrera investigadora posible. Por todo ello, no puedo decir otra cosa que gracias. Dentro de mi grupo de investigación, también me gustaría agradecer a David Yllanes, mi antiguo compañero de doctorado, toda la ayuda prestada. Me gustaría hacer una especial mención al apoyo de estos últimos meses, ya que sin su ayuda técnica la escritura de la tesis habría sido bastante más complicada.

Durante estos años he sido miembro del Departamento de Física Teórica I de la Universidad Complutense de Madrid, donde siempre me he sentido particularmente a gusto e integrada. Dentro del departamento, siento un especial agradecimiento a su director Antonio Muñoz por todas las horas que hemos compartido. También me gustaría mencionar a su inolvidable secretaria, Chon, a quien debo multitud de favores, y a David, el informático, por su imprescindible ayuda técnica. También quiero agradecer a Víctor Martín, Ramón Álvarez, Diego Porras y Antonio Muñoz la oportunidad de introducirme en la docencia como profesora ayudante de las asignaturas de Fenómenos Colectivos, Física para biólogos, Mecánica Cuántica y Física Cuántica.

También quiero aprovechar para agradecer a la JANUS collaboration el esfuerzo y trabajo conjunto. Además, me gustaría agradecer su predisposición a dejarme reutilizar las configuraciones de [ÁB10a, ÁB10b] para el estudio de caos en tem-

peratura. Dentro de la colaboración, me gustaría dar las gracias a Juan Jesús Ruíz, por el curso intensivo de vidrios de espín que se molestó en preparar hace unos años para los jóvenes miembros de la colaboración. Tampoco quiero olvidar a Sergio Pérez o a Enzo Marinari por su enorme ayuda durante mi período en Roma. Y por supuesto, no puedo dejar de mencionar a Giorgio Parisi, con quien comparto varios trabajos y del que he aprendido muchísimo.

Por otro lado, quiero agradecer al Instituto de Biocomputación y Física de los Sistemas Complejos (BIFI) de la Universidad de Zaragoza, institución de la que soy miembro, la gran cantidad de recursos computacionales puestos a mi disposición durante estos años. El mismo agradecimiento se lo tengo que mandar a la red Española de Supercomputación por haberme permitido utilizar el ordenador *Mare Nostrum*.

En especial, quiero agradecer a Paolo Verrocchio todo su cariño y esfuerzo. Comenzamos a trabajar juntos casi al final de mi licenciatura y desde entonces hemos compartido varios trabajos y estancias. Me da mucha pena pensar en las dificultades que han surgido en los últimos tiempos, y que no vaya a poder estar presente el día que presente mi tesis. Quiero aprovechar estas páginas para mandarle un fuerte abrazo y mucho apoyo. También se merece una especial mención Hidetoshi Nishimori, quién me aceptó sin conocerme unos meses en su facultad en Tokio y me hizo sentir como en casa, de quién he aprendido mucho y a quién debo gran parte de la ilusión por continuar ahora con este gran proyecto de la investigación.

No puedo olvidar tampoco mis inicios en investigación con Miguel Ángel Rodríguez durante la licenciatura, ya que a él le debo mi determinación a comenzar el doctorado. De la misma forma tengo mucho que agradecer a Jacobo Ruiz de Elvira, porque fue con él con quién comencé mi sueño de dedicarme a la física y de continuar después con la investigación, y sin él, no sé muy bien dónde estaría ahora, pero estoy segura de que no sería aquí.

Quiero dedicar los párrafos finales de estos agradecimientos a la parte más personal, a toda la gente que ha estado a mi lado durante estos años a las buenas y a las malas. No considero que el doctorado haya sido una etapa fácil de mi vida, ha estado tan llena de ilusión como de desencanto. Lo que sí que puedo decir es que pese a todo, han sido probablemente los años más felices de mi vida, algo que lo debo a mucha gente. Los nueve años y medio que he vivido en esta facultad no habrían sido lo mismo sin la existencia de Hypatia, del Club Deportivo o del equipo de fútbol femenino de físicas, sin ellos la facultad habría sido un lugar mucho más triste. Tampoco habría sido lo mismo sin todos mis compañeros de doctorado: Jenifer, Ricardo, Jacobo, Giovanni, Guillermo, Édgar, Joserra, Jose, Alejandro, Lourdes, Álvaro, Jose Alberto, Davide, Nikos, Markus, Alexandre, Óscar, Diego, etc. Entre ellos, les debo una especial mención a mis compañeros del DomiLab: Santos, Juantxo, David... y sobretodo a Domingo, Vivy y Marco, porque a ellos les debo los mejores momentos de esta tesis, y porque nuestra relación va mucho más allá de meros compañeros de despacho. Acabo esta etapa con la seguridad de que no encontraré nunca mejores compañeros de viaje.

Siguiendo con los agradecimientos, no puedo olvidar a mis dos incondicionales: José Ramón Vázquez y Javier Andrade, porque no sólo habéis compartido conmigo incontables horas de trabajo y ocio, sino que también habéis aguantado todas mis penas, quejas y dudas, y porque sin vosotros dos, nada habría sido lo mismo. También me gustaría agradecer a Jesús Díaz su compañía durante las largas horas de escritura de esta tesis, así como su interés a la hora de leer y comentar críticamente este texto. Y bueno, antes hablaba de los años más felices de mi vida, y ésto se lo debo sin duda a mis amigos, siempre dispuestos a sonreír ante cualquier mal, o a celebrar todo lo incelebrable. Sé que me dejo a muchos importantes, pero quiero mandar un fuerte abrazo a Izarra, Javi Campos, Amalia, Rubio, Jorge, Alvarito, Marta, Carla, Diego, Punky, Berto, Pitufa, Itxi, Jerbo, Iria, Lon, Champi, Agus, Hugo, Illo, Elena, Eze y Óscar. Tampoco quiero olvidar mandar un cariñoso agradecimiento al grupo Scout Kimball 110, ya que, durante estos últimos años, ha aportado a mi vida una parte solidaria, alegre y completamente diferente a todo lo demás.

Y dejo para el final a los más importantes. El agradecimiento más grande es para mi familia. Entre ellos, a mi hermano, uno de los mejores amigos que tengo y tendré. Y por supuesto, a mis padres. Sin su exigencia desde pequeña, sin su cariño, sin su ayuda, y sin su incondicional apoyo a cualquier empresa, no estaría donde estoy ni sería la persona la que soy. A ellos va dedicada esta tesis.

Durante esta tesis he estado financiada primero por una beca del BIFI, luego por una beca de la Caixa, que me dio la oportunidad de cursar el máster en Física Fundamental, y finalmente, por una beca FPU del Ministerio de Educación, Cultura y Deporte. Por otro lado he recibido apoyo de los proyectos FIS2009-12648-C03 del MICINN y de los Grupos UCM - Banco Santander.

Beatriz Seoane Bartolomé
Universidad Complutense, Madrid, noviembre de 2012

Contents

CHAPTER II

General introduction

Traditionally, the step-forwards in physics are obtained with the "divide and conquer" strategy. In other words, one normally splits up the system in small parts and tries to infer the behavior of the whole by understanding the parts. But what if the system is that interacting or that complex that there is no way to understand the overall problem by the knowledge of the individuals? What if the whole is a lot more than the summation of the parts or something completely different? Many systems in nature can only be studied from a collective point of view, this is the case of a variety of systems such as, for instance, earthquakes, neural networks, protein folding, turbulence, glasses...

This research field has suffered a major boost in the last decades with the upcoming and development of computers. Indeed, computers have allowed scientists to simulate large systems under complicate interactions or with induced disorder, and to study their emerging properties. Furthermore, thanks to the computing improvements, now it is possible to collect and analyze unprecedentedly large amounts of data coming from both from experiments or simulations. Because of that, complex systems have become a whole field by itself, but an interdisciplinary field shared by physicists, biologists, mathematicians, etc.

The most successful theory to approach the equilibrium state of a system composed of a large amount of particles is the statistical mechanics. In this theory, it is assumed that, even though each of one components of the system describes a chaotic behavior, the resulting macroscopic equilibrium state is extremely simple if the system is big enough. Somehow the individual chaotic behavior cancels out when the equilibrium is achieved. But what happens if the system evolves as slowly as the relevant state in nature is out of equilibrium? Then, the traditional notions of thermodynamics do not hold and new surprising phenomena emerge. The traditional control parameters, such as the temperature or the pressure do not longer describe the system by themselves. In fact, one needs to track not only the time elapsed in experiments but also the age of the system in these complex phases. Then, the evolution of the system depends on their whole history, which

results in a very striking behavior: event an inert material chunk (such as a spin glass) ages, rejuvenizes or has memory. Besides, these systems react drastically to slight changes in the external conditions, which is known as chaos (see Chapter 5 in this thesis).

Up to this point, this kind of materials are very discouraging. However not everything is bad news. In fact, when one studies the collective properties of various of these complex systems, one realizes that they exhibit somehow a kind of new universal behavior. Indeed, the same prescriptions seem to work for completely different systems, no matter the properties of the individuals that compose them.

One example of these complex materials are everyday glasses. Macroscopically they behave as solids, but microscopically, they look very much like a fluid. Actually, they present no long range order, but the particles are so packed that the flow is impeded. In fact, glasses are often obtained by cooling fluids very quickly. Normally these fluids would become crystalline if they were freezed slowly enough. Even nowadays, after thousand of years manipulating glasses, the nature of the glassy phase is not understood. In fact, to determine whether the glass transition is a real phase transition or not, is one of the most important open questions in solid-state physics. The glassy phase is characterized by a extremely high viscosity. When the temperature is lowered down the viscosity grows dramatically with the temperature, and then, the particles have no room to move, which results in diverging characteristic flow times. In fact, the system evolves so slowly near the transition point (defined purely dynamically, as the temperature at which the viscosity reaches 10^{13} poises) that one must consider it to be always out of equilibrium.

However, this extremely slow evolution of the dynamic variables associated with disorder is not peculiar to the particle positions in structural glasses. In fact, there are some magnetic allows (known as spin glasses, see Part I in this dissertation) that present a similar frozen phase in their magnetic moments. Indeed, the spin glass phase has a vanishing total magnetization (in absence of magnetic field) but at variance with the paramagnetic phase, each spin in the lattice is frozen in time but in seemingly random spatial pattern. This spin glass phase and the ordinary glass phase share many not understood phenomena, even though their nature is completely different. Indeed, in spin glasses the interaction between particles is magnetic, and particle diffusion does not play any role.

Spin glasses, at least up to now, are useless materials. However, they still carry the fundamental origin of the glass phase. It is hoped that the theoretical treatment will be simpler in spin glasses. Indeed, among other simplifications, particles can be placed in lattice nodes (since no diffusion is involved), which encourages notably the analytical and numerical computations. For this reason, even though structural glasses would be more interesting for practical applications, spin glasses are nowadays the usual benchmark to investigate complex behavior, and most of our intuition about glasses comes precisely from spin glass studies.

This thesis is centered on the numerical study of complex systems. As discussed above, although their fauna is broad, the inner mechanism causing their striking effects, as well as the tools we use to study all of them, are very well

interchangeable from one system to the other. For this reason, in this thesis we worked both with spin glasses (Part I of this dissertation) and colloidal systems (Part II) as two faces of the same coin. When concerning equilibrium in a computer simulation of these kind of systems, the problem is definitely time (or computer resources). As mentioned above, nearby the glass transition, the inner system' dynamics gets stuck in these kind of materials. Indeed, from an experimental point of view, they are permanently out of equilibrium. This freezing in the evolution is also observed in the simulations, which is translated in a divergence on the exponential autocorrelation times that makes equilibrium unreachable in human times for relatively small systems. From the point of view of experiments, the relevant state is out of equilibrium. However, from the theoretical point of view, the limited theories available for these materials correspond to the equilibrium state. This is were the computer simulations come to play. With simulations, we are able to investigate non-perturbately the equilibrium phase on a system, but also can explore its nonequilibrium behaviour (which is relevant to analyze experiments).

In addition to the slow behavior associated to glasses, the numerical study of any phase transition is always hard. Indeed, any phase transition introduces a divergence in the simulation times with the number of particles N (the physical mechanism is related to the growth of one phase into the other). This limits strongly the system sizes that can be equilibrated in a simulation. The problems we are considering here combine both kind of problems, an extremely slow dynamics induced by disorder, and the presence of phase transitions, which makes these problems intrinsically hard in the computer science language (see Chapter 9). For this reason, the research on optimized algorithms or the construction of dedicated supercomputers for these problems is also mandatory in the field. Indeed, although the final research goal is physics, computer and algorithms are important. In fact, no progress is possible we are not able to approach the equilibrium state or to simulate systems big enough to display the desired phenomena.

Roughly a half of this thesis is devoted to fast computation strategies and new algorithms. This emphasis is less strong in Part I devoted to spin glasses, where the Monte Carlo algorithms used are rather standard and the progress relies on either the implementation of multi-spin coding (see Appendix B) or thanks to the JANUS supercomputer. In Part II we deal with colloidal polydisperse systems, systems that combine both a structural glass transition and a first order solidification transition in a narrow region in the space of parameters. First order transitions come together with an divergence (exponential in the number of particles N) of computational times within the normal approaches. For this reason, our main goal has been to beat this divergence. Continuing in the strategy of searching new optimized algorithms to approach glasses, I moved to quantum mechanics (see Part III) during the last months of my Ph.D. In particular, I started to work with the new and promising quantum annealing (also known as adiabatic computation) algorithms.

Most of the results collected in this thesis have appeared in international journals and were presented in international conferences. We take the chance to summarize here all of them. We start with Part I, the part devoted to spin glasses. The

general introduction in Chapter 3 relays heavily on Refs. [ÁB10a, ÁB10b] (by the Janus collaboration to which I belong). However, no original results are presented in Chapter 3. Chapter 4 is mainly based on [Fer10a]. I had the chance to expound this work in an oral presentation in the most important conference in the field, the *STATPHYS 24, the XXIV International Conference on Statistical Physics* that took place in Cairns (Australia) in July 2010. In addition, I also presented a talk about it in the *CompPhys09, 10th International NTZ-Workshop on New Developments in Computational Physics* in Leipzig (Germany) in November 2009. Chapter 5 is based on [Fer12a] (currently under review). Part II concerns to colloidal systems. Chapter 7 is based on [Fer10b]. I presented talks about this work both in *the XII International Workshop on Complex Systems* in Andalo (Italy) in March 2010 and *the International Workshop on Complex Energy Landscapes* in Zaragoza (Spain) in June 2010. On the other hand, Chapter 8 is based on [Fer12b, MM11]. I gave a talk about this work in a satellite meeting to STATPHYS 24, *Monte Carlo Algorithms in Statistical Physics* in Melbourne (Australia) in July 2010, and in a poster session in *Viscous Liquids III* in Rome (Italy) in March 2011. Finally, Chapter 9 is based on [Seo12]. I presented a poster on this subject in the conference *Quantum Information meets Statistical Mechanics* in Innsbruck (Austria) in September 2012.

It is also important to acknowledge that this work has been supported by MECCD (Spain) through the FPU program, and by MICINN (Spain) through research contracts No. FIS2009-12648-C03.

Part I

Spin Glasses

CHAPTER III

General description of spin glasses

It was late in the 1960s when the first unusual effects on spin glasses were detected in experiments. These effects appeared in the now known as canonical spin glasses; the traditional and simple magnetic alloys composed by the mixture of noble-metals and transition metals (such as AuFe or CuMn). Indeed, by that time, researchers were wondering what would happen after introducing magnetic impurities into a non-magnetic matrix. In such a mixture, the magnetic moments coming from the impurities would be dissolved on a sea of conducting electrons, and the direct question was: does the magnetism remain?

The experiments were shocking. The remanent magnetization roughly disappeared at low temperatures, but at the same time the susceptibility presented a broad maximum. Besides, the magnetization and its hysteresis were completely different to what expected for a ferromagnetic phase. Rather they were more similar to the result for a mixture of mutually interacting ferromagnetic and antiferromagnetic domains. On the other hand, experiments pointed out some kind of magnetic random order at low temperature, different from everything known up to that moment.

The name *spin glass* did not appear until 1970s, and it was coined when linking the problem of localization in disordered systems with the magnetic alloy problem.

It was not until around 1975 when theorists became interested in the problem, and when the spin glass boom really started. Since then, a lot of simplified models and theories have been presented, leading to a great progress in the understanding of these "weird" materials. But not only, this knowledge supposed also a breakthrough in the field of disordered systems and statistical mechanics. Nowadays, results or techniques obtained in spin glasses are applied to many different fields, from biology to computer science. However, even after 50 years of intensive spin glass study, many of their most striking properties remain to be explained, and the debate about its equilibrium low temperature phase still remains open.

In this chapter, I will discuss what a spin glass is and will try to outline some outstanding results, including experimental and theoretical work. With this aim,

I will summarize the most important experiments in spin glasses and discuss the most popular simplified theoretical models as well as the main competing theories for the equilibrium spin glass phase. I will end the chapter by an introduction to the numerical techniques in spin glasses, defining the observables that will be used in the following chapters. Finally, I will discuss one of the main progresses recently achieved by means of numerical simulations, the time-length dictionary that finds a quantitative relation between the worlds of equilibrium (where theory is developed) and the nonequilibrium (the one relevant to experiments).

I would like to stress that the results summarized in this introductory chapter are not original. They are based on the general spin glass literature, mainly on [Myd93, You97, Méz87, Vin96]. The review of numerical simulations, I also include some recent results taken from [ÁB10a, ÁB10b].

3.1

What is a spin glass?

The spin glass (SG) is a new state of magnetism, completely different from the traditional ordered ferromagnetic and anti-ferromagnetic phases, but still with a co-operative and collective nature in the low temperature phase. This phase is characterized by the following properties. Below some critical temperature, T_c, the spins are frozen in time. That means that, below T_c, the local magnetization at each site of the lattice $\boldsymbol{x}$ is $\langle s_{\boldsymbol{x}} \rangle_t \neq 0$, being $\langle \cdots \rangle_t$ the average over the experimental time. However, though frozen, the orientation of the spins seems to be completely random, leading to a vanishing total magnetization when summing up over all the system,

$$\boldsymbol{M} = \frac{1}{N} \sum_{\boldsymbol{x}} \langle S_{\boldsymbol{x}} \rangle_t = 0. \tag{3.1}$$

The condition is even stronger. Indeed, there is no long range order of any kind, i.e.

$$\boldsymbol{M}_{\boldsymbol{k}} = \frac{1}{N} \sum_{\boldsymbol{x}} \mathrm{e}^{-\mathrm{i}\boldsymbol{k}\cdot\boldsymbol{x}} \langle S_{\boldsymbol{x}} \rangle_t = 0, \qquad \forall \boldsymbol{k}. \tag{3.2}$$

This last expression includes both the ferromagnetic, $\boldsymbol{k} = (0,0,0)$ and antiferromagnetic, $\boldsymbol{k} = (\pi,\pi,\pi)$, order parameters.[1]

It is interesting to point out the difference between this *frozen* disordered phase, and a normal disordered phase, like a paramagnetic phase. In this latter, there is also a total absence of long range order but spins fluctuate randomly due to thermal excitations, leading to a vanishing local magnetization when one averages over a long time.

[1] Indeed, when the interaction is ferromagnetic, all the spins tend to align in the same direction, whereas in the antiferromagnetic case, nearby spins point to alternate opposite directions to minimize the energy.

Note that this new magnetic phase resembles a normal glass very much. Indeed, in these materials, the particle positions are apparently random but do not evolve with time (structural glasses are characterized by a extreme slow flow). In fact, as mentioned above, the term *spin glass* comes precisely from this similarity between the frozen random orientation of spins and the frozen location of particles in ordinary glasses.

Nowadays we know that the existence of a glassy phase in spin glasses occurs as a consequence of a combination of three basic ingredients: randomness, mixed interactions and frustration. Let us explain briefly each term. The disorder or randomness in the interactions is introduced in spin glasses by randomizing either the distance between the magnetic moments, namely *site randomness*, or the nearest neighbors interaction in a regular lattice, known as *bond randomness*. In addition, these interactions must be, not only random in strength, but also of mixed ferromagnetic and antiferromagnetic nature (for a pair of spins the interaction can be either ferromagnetic, which favors a parallel orientation of both, or antiferromagnetic, which results in an antiparallel layout). The combination of randomness and competing interactions causes *frustration*.

The idea of frustration is exemplified in Figure 3.1. Let us consider four spins each lying on the four vertices of a plaquette. Each spin is connected with only two neighbors and the nature of the interaction is represented through the signs in the edges. When the coupling between two spins is positive (ferromagnetic), the spins minimize their energy by aligning parallelly. On the contrary, if the interaction is negative (antiferromagnetic), they "want" to align anti-parallelly. In Figure 3.1-left, there is no frustration, all the spins can minimize their energy at the same time. On the other hand, in a frustrated plaquette, such as the one shown in Figure 3.1-right, this is not possible. Indeed, let us follow the following procedure. One chooses randomly an orientation for the spin-1 placed in the upper right corner. The election is, for instance, spin up (↑). Now, since the interaction is ferromagnetic, its nearest left neighbor (spin-2) will align parallelly with spin-1, that is, also up (↑). Afterwards, we consider the spin in the left bottom corner (spin-3). The interaction with spin-2 is antiferromagnetic, so it will orientate down (↓) in order to satisfy the coupling. Finally, let us consider the spin in the bottom right corner, where the question mark is. The decision problem appears when spin-4 has to decide its orientation: if considers the coupling with spin-3, it should be down (↓) (parallel to spin-3), but if considers the interaction with spin-1 should point up (↑) (parallel to spin-1). Then, spin-4 cannot satisfy simultaneously both couplings. This absence of a "everybody happy" configuration, is precisely what the term frustration refers to.

The presence of frustration draws a rugged free-energy valley, with many minima and large barriers. Each of these minima corresponds to a frozen state where the system hardly evolves due to the constant competition between the interactions. This "confused" ground state is the origin of the interesting and unique properties of SG. However, frustration is not the only necessary condition for a SG; it must be combined with the randomness and the competition between inter-

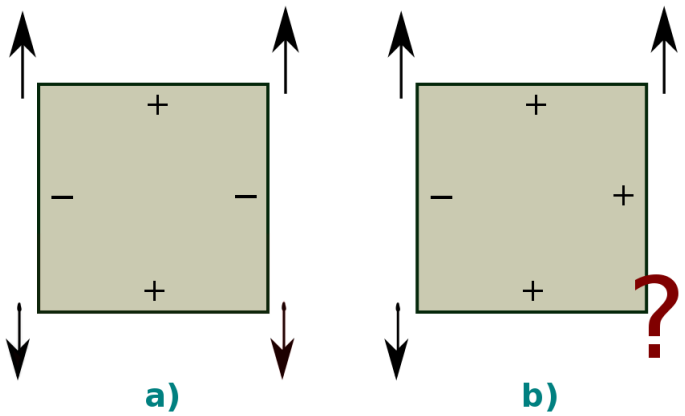

FIGURE 3.1: Examples of **(a)** unfrustrated and **(b)** frustrated plaquettes.

actions discussed above. In fact, the antiferromagnetic, regular triangular lattice is a fully frustrated system, but has no co-operative freezing. In fact, frustration is a direct consequence of the disorder and mixed interactions, but while a necessary condition to induce a spin glass phase, it is not a sufficient one.

3.2 Real spin glasses

Now the question is which kind of materials develop a SG phase. As discussed in the introduction, the first SG were found accidentally in binary allows. In these materials, the magnetic impurities (bearing magnetic moments or localized spins) occupy random sites in a non-magnetic host metal. The concentration of these magnetic impurities, x, can be controlled during the manufacture. The archetypal specimens of the metallic (site random) spin glass are $Cu_{1-x}Mn_x$ or $Au_{1-x}Fe_x$. These noble-metal alloys are known as canonical spin glasses. Indeed, the dissolution of the magnetic solute in the non-magnetic solvent occurs completely randomly, with no particular atomic or chemical short-range order. Then, the system can be treated statistically and modeled using Gaussian probabilities. However, more complicated alloys can be manufactured as well. For instance, it is possible to have SG which are both insulating and conducting. In these materials, one of the non-magnetic sub-lattices is substituted by a magnetic one. As an example we can cite a semiconductor, such as $Eu_xSr_{1-x}S$ or a metal $La_{1-x}Gd_xAl_2$.

Another way of creating site disorder, is to start with an intermetallic com-

pound, e.g. $GdAl_2$ and to destroy its crystalline form by making it amorphous. This can be done with many different techniques such as splat-cooling, quench-condensation or sputtering.

However, as discussed, the randomness in the interactions is not only created through a random distribution of sites, it can be also synthesized in a regular lattice by randomizing the sign of the couplings. In fact, $Rb_2Cu_{1-x}Co_xF_4$ and $Fe_{1-x}Mn_xTiO_3$ can be modeled up to very good approximation on a perfect lattice with only $\pm J$ couplings (see, for instance Eq. (3.3)).

3.2.1 Magnetic interactions

As usual, the magnetic interactions are written in terms of a exchange potential. Let us consider two spins placed at $\boldsymbol{x}$ and $\boldsymbol{y}$, then, the interaction between them two is given by a spin Hamiltonian

$$\mathcal{H}_{xy} = -J_{xy}\, \boldsymbol{S}_x \cdot \boldsymbol{S}_y, \tag{3.3}$$

where the J_{xy} are the *couplings*. As discussed above, a necessary condition for spin glass behavior is that the couplings J_{xy} can take both positive and negative values. This condition is fulfilled by different kinds of interactions as reviewed in [Myd93].

We will only discuss here the classical solution found in the magnetic alloys where the conduction electrons create an indirect exchange interaction known as the Ruderman-Kittel-Kasuya-Yosida (RKKY) interaction [Rud54, Kas56, Yos57], whose Hamiltonian is $\mathcal{H}_{x,y} = J(|\boldsymbol{x} - \boldsymbol{y}|)\, \boldsymbol{S}_x \cdot \boldsymbol{S}_y$. In these materials, the sea of conducting electrons with oscillating spins induce an oscillating interaction between the impurities magnetic moments located at $\boldsymbol{x}$ and $\boldsymbol{y}$ that depends on their separation $r = |\boldsymbol{x} - \boldsymbol{y}|$. For large separations within the impurities, the coupling strength is given by

$$J(r) \simeq J_0 \frac{\cos(2k_{\mathrm{F}} r + \phi)}{(k_{\mathrm{F}} r)^3}, \tag{3.4}$$

where k_{F} is the Fermi momentum of the metal and the phase ϕ accounts for the charge difference between the impurity and the host.

The coupling $J(r)$ is thus an oscillating function of the distance between spins. Now, these distances are determined by the position of the impurities, which are random. Then, the interaction between spins oscillates randomly from positive to negative interactions, as needed to produce a spin glass.

3.3 Experimental spin glasses

As discussed in Section 3.1, the spin glass phase is characterized by a frozen random configuration of spins that hardly evolves with time. In fact, as in other glassy systems, one of its main features is that the relaxation times become exceedingly

long at low temperatures. For this reason, at least to discuss the experimental work, SG must be considered to be always out of equilibrium.

3.3.1 Aging

One of the most studied consequences the nonequilibrium nature of spin glasses is the *aging* [Vin96, Ber03b]. Let us discuss how aging shows up in the simplest experimental protocol, the *direct quench*. The system is cooled down very fast below the critical temperature T_c in presence of a magnetic field, and it is let to equilibrate from $t = 0$ (the time of the quench) for a *waiting time*, t_w. At $t = t_w$ the field is suddenly switched off. The relaxation of the "Thermo-remanent magnetization" (TRM), M, is measured at a later time $t + t_w$, see Figure 3.2–top. It can be decomposed as

$$M(t + t_w) = M_{ST}(t) + M_{AG}(t + t_w, t_w), \quad M_{ST}(t) \equiv \lim_{t_w \to \infty} M(t + t_w, t_w), \tag{3.5}$$

then, there is a fast stationary contribution $M_{ST}(t)$ independent from t_w, and an aging part, which, to good approximation, is a function of the quotient t/t_w, see Figure 3.2–bottom, at least for $10^{-3} < t/t_w < 10$ and t_w in the range 50s—10^4s [Rod03]. This suggests that the effective relaxation time of the system is of the order of its age. This effect is known as *Full Aging*. Nowadays, there is some controversy about the validity of this natural time value. In fact, it has been proposed to use t/t_w^μ with $\mu \lesssim 1$ [Dup05]. At any rate, the moral is that the only relevant time scale in spin glasses seems to be t_w, that is, the age of the system in the SG phase.

Similar consequences are observed when looking to the response to the system to an oscillating field. Indeed, let us consider we cool the system from $T \gg T_c$ to the working temperature $T < T_c$ at $t_w = 0$. Then, we apply a very small oscillating field, and measure the a.c. susceptibility χ at certain frequency ω. What is observed is that the amplitude of χ decreases with t_w (the age of the system as a SG). In other words, the response of the system to the perturbation depends on its thermal history. In fact, χ is both a function of ω and t_w. To a good approximation it can be written as

$$\chi(\omega, t_w) = \chi_{ST}(\omega) + \chi_{AG}(\omega t_w). \tag{3.6}$$

Again, there is a stationary part χ_{ST}, independent of t_w, and an aging one χ_{AG} that scales roughly on the scaling variable ωt_w. Note that M and χ are essentially the Fourier transform one from the other in the linear response theory, so the full aging t/t_w found in M translates to ωt_w in the frequency space.

Let us consider another aging experiment, but now concerning more complicate protocols. This is the case of the response of spin glasses to temperature cycles with or without the influence of a small constant magnetic field H. We investigate the behavior of the dc susceptibility, χ_{dc},[2] under two different cooling procedures. In

[2] As a matter of fact, experimentalists refers to χ_{dc} as $\chi_{DC} = M/H$.

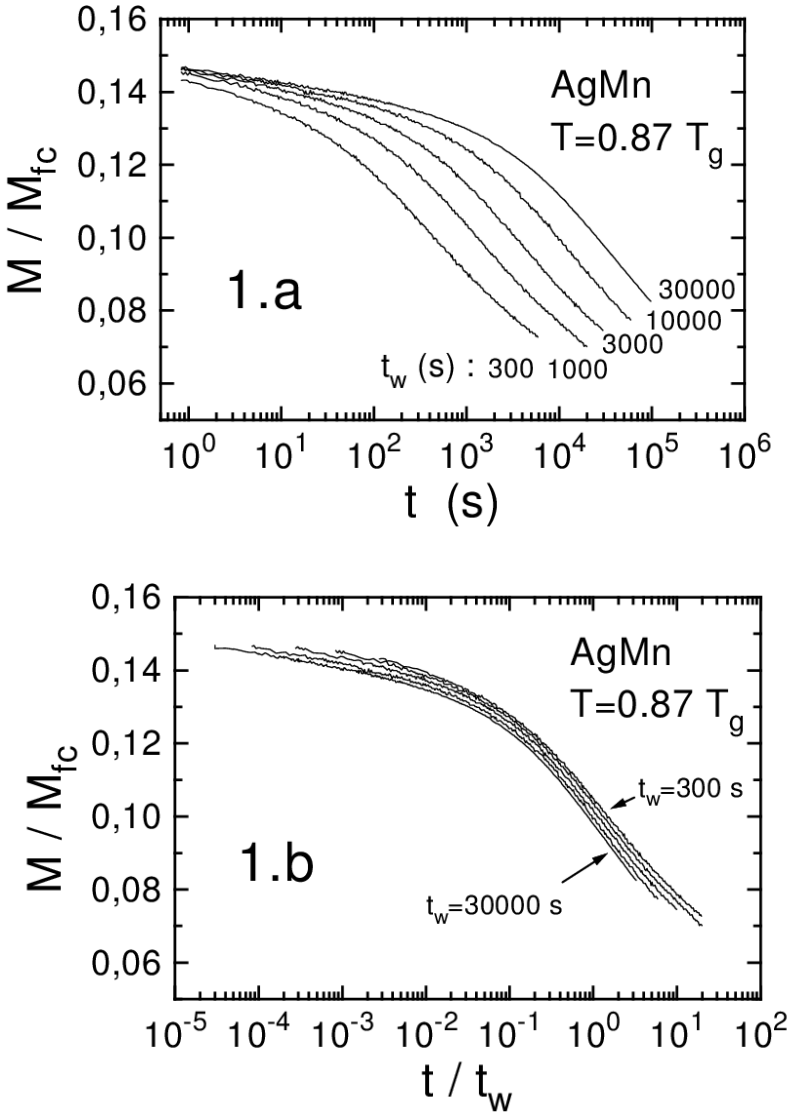

FIGURE 3.2: **(Top)** Thermo-remanent magnetization M normalized by the field-cooled value M_{fc}, vs. time t. **(Bottom)** Same curve but presented as function of t/t_{w}, the full aging scaling. Figures taken from [Vin96].

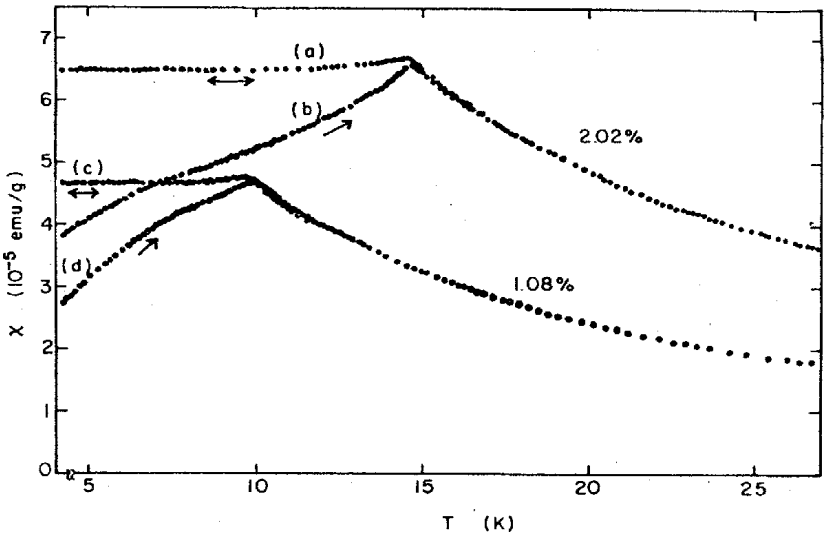

FIGURE 3.3: Comparison of the field-cooled [(a), (c)] and zero-field-cooled [(b), (d)] susceptibilities for two samples of *Cu*Mn with different concentration of impurities. Figure from [Nag73], as quoted in [Myd93].

both protocols, we start on the paramagnetic phase $T_0 \gg T_c$ and end in the spin glass phase at a working temperature $T_1 < T_c$. In the first protocol, named field cooling (FC), the field H is applied constantly during all the cooling process. On the second case, on the zero field cooling (ZFC), the field is only switched on once reached T_1. Figure 3.3 shows the temperature dependency of χ_{dc} for CuMn (1 and 2 at. %) with a field of 6 gauss. Let us discuss the two different behaviors. First, when one performs the field-cooling [curves (a) and (c)], χ_{dc}^{FC} increases as the temperature decreases in the paramagnetic phase up to a point from which it remains constant with temperature, that is, in the spin glass phase region. Now, if one considers the inverse heating cycle, the curve in χ_{dc}^{FC} is roughly reversible. On the other hand, in the ZFC procedure, one cools the sample up to $T_1 < T_c$ with no field. Once at T_1, the field is switched on, and the susceptibility $\chi_{dc}^{ZFC}(t)$ evolves with time. It starts from the initial value zero and grows with time. In the infinite time limit (not achieved in experiments), this susceptibility would reach the FC curve, i.e. $\chi_{dc}^{ZFC}(t \to \infty) \approx \chi_{dc}^{FC}$. Now we let the sample relax some time at fixed temperature until it reaches the curves (b) and (d) in Figure 3.3. If we then increase the temperature keeping also fixed the field, the susceptibility starts to grow until it reaches the FC curve at T_c. From that point, the FC and ZFC curves overlap. Finally, if we restart to cool the system again, the curves that are reproduced are again (a) and (c), that is, the FC curves. That means that the process is not reversible and curves (b) and (d) can only be obtained during the heating of a sample cooled by ZFC, in the direction marked by the flags in Figure 3.3.

3.3.2 Fluctuation-Dissipation Relations

Another consequence from the nonequilibrium nature of SG is the violation of the Fluctuation-Dissipation Theorem (FDT).

In equilibrium, the response $R_O(t+t_w,t_w)$ to an external field h conjugate to any observable O is related to the two-time autocorrelation function $C_O(t+t_w,t_w) \equiv \langle O(t+t_w)O(t_w)\rangle$ by means of the FDT [Bou97],

$$R_O(t+t_w,t_w) \equiv \left.\frac{\delta\langle O(t+t_w)O(t_w)\rangle}{\delta h(t_w)}\right|_{h=0} = R_{O,EQ}(t) = -\frac{1}{T}\frac{\partial C_{O,EQ}(t)}{\partial t}. \quad (3.7)$$

If we introduce the integrated response $\chi(t+t_w,t_w) = \int_{t_w}^{t_w+t} R(t+t_w,t')dt'$, which in equilibrium is nothing but the magnetic susceptibility, the FDT reads

$$\chi(t+t_w,t_w) = \chi_{O,EQ}(t) = \frac{C_{O,EQ}(0) - C_{O,EQ}(t)}{T}. \quad (3.8)$$

One can check the validity of this relation by making a parametric plot of $\chi(t+t_w,t_w)$ vs. $C_O(t+t_w,t_w)$ as shown in Figure 3.4. The linear relation (3.8) is only fulfilled for a system in equilibrium, which means that one should only recover the straight line of slope $-1/T$ (dashed straight line in Figure 3.4) if $t_w \gg t_{EQ}$, where t_{EQ} is the equilibration time.

The FDT is normally violated in nonequilibrium systems. In general, the FDT violation can be parameterized by introducing a violation factor $X(t,t')$ in (3.8), defined as

$$R_O(t,t') \equiv -\frac{X_O(t,t')}{T}\frac{\partial C_O(t,t')}{\partial t'}. \quad (3.9)$$

In analytic studies in spin glasses, it is shown that for large times, this X_O depends on t and t' always through the value of the correlation function, i.e. $X_O(t,t') = X[C_O(t,t')]$. Then, since the different theoretical models for spin glasses predict different behaviors of $C_O(t,t')$, the different theories (see Section 3.5) predict different violation factors that can be compared with experiments.

.

3.3.3 Memory and rejuvenation effects

Among the surprising experiments concerning SG, the experiments of memory and rejuvenation are probably the most striking ones. Besides, these two phenomena are purely a glassy feature, not just a nonequilibrium one. Notice that the concept of aging also applies to the coarsening dynamics in a ferromagnet [Bra94], while no memory or rejuvenation effect has been found in these systems.

We consider the experiment studied in [Jon98] shown in Figure 3.5. In it, the imaginary part of the a.c. susceptibility χ'' is measured as a function of the temperature, under the influence of a low frequency $\omega/2\pi = 0.04$ Hz magnetic field. We consider the two following experiments:

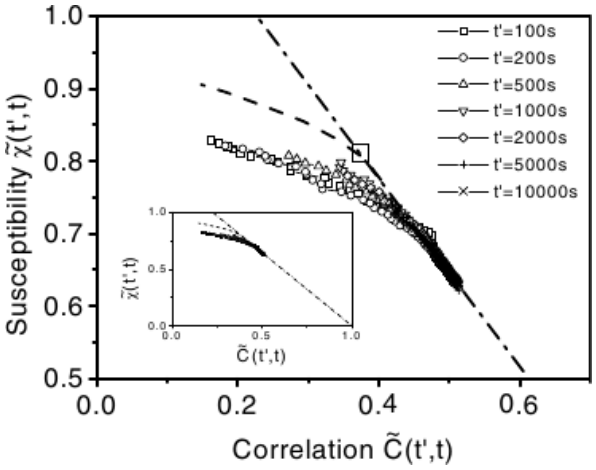

FIGURE 3.4: Experimental realization of the violation of the fluctuation-dissipation theorem (linear relation (3.8) in dotted-dashed line) in a spin glass (from [Hér02], see text for discussion). In the figure, t' corresponds to our t_w and t stands for our $t + t_w$.

1. One starts at a temperature in the paramagnetic phase, that is well above T_c, and cools the system at a constant slow rate of 0.1 K/min (small as compared to the $\omega/2\pi = 0.04$ Hz frequency to ensure one stays in the $t \ll t_w$ regime). The $\chi''(T)$ initially increases while $T > T_c$, then describes a cusp at the transition temperature $T_c \approx 15$ K and finally decreases monotonically in the SG phase. If afterwards the reverse cycle is repeated but now heating the system, the resulting $\chi''(T)$ describes roughly the cooling curve. In other words, the process is essentially reversible. This experiment is represented in Figure 3.5 by a thick black line.

2. This time (curve with empty diamonds), we consider the same cooling procedure, but this time we make a stop of few hours when the sample reaches an intermediate temperature $T_1 = 12\text{K}(< T_c)$ (within the SG phase). The system relaxes (ages at T_1), which produces a dip in the χ'' curve. However, if one restarts the cooling again at the same original cooling rate, the susceptibility quickly returns to the reference curve obtained with experiment 1, as if the cooling had never stopped. This astonishing effect is known as *rejuvenation*. Now, as before, one heats the system again at constant rate until the highest temperature, but this time without making any stop on the path (curve with black diamonds). Even though no stop is made at T_1, the susceptibility remembers the dip and reproduces the curve in empty diamonds. This phenomenon is called *memory*.

The theoretical description for spin glasses will be discussed later on. Although, let us anticipate that there are two possible scenarios to rationalize these experiments:

- The first one is to relate them to the so-called *temperature chaos* predicted for spin glasses [Bra87]. The Chapter 5 is fully devoted to this effect. In this

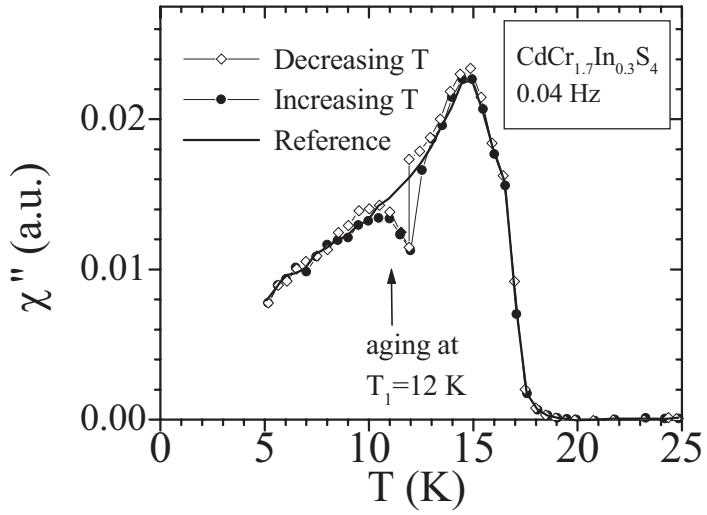

FIGURE 3.5: Memory and rejuvenation in an experimental spin-glass (Figure taken from [Jon98]). Reference line corresponds to experiment 1, while diamonds and circles correspond to the cooling and heating part of experiment 2 respectively.

approach, the frozen spin pattern strongly varies with the temperature. In this picture, the aging at T_1 would not be affected by the aging at $T_2 < T_1$, since the spin pattern at T_1 would look completely random for the eyes of the system at T_2. Rejuvenation is very natural on this scheme, but memory is unexplained. We will come back to this discussion in Chapter 5.

- On the other hand, there is a much simpler approach that assumes length scale separation at different temperatures and fast modes [Ber02a, Ber03a]. Indeed, in all theories, as we shall see, the aging in the spin glass phase is explained as a process where coherence domains grow with time. In Chapter 4, we will study numerically this coherence length. This growth is expected to be slower the lower is the temperature. Then, if one assumes that this speed varies sharply with temperature, handwaving, one can explain handwavingly both the rejuvenation and the memory effects at least in very simple protocols. In order to illustrate this idea, let us consider the cycling experiment $E \to A \to B \to A$, where $T_E \gg T_c$ (E in the paramagnetic phase), and $T_B < T_A < T_c$ (A and B in the SG phase). Now, starting from E, the system is quickly quenched to T_A and is let to age for a time $0 < t < t_A$. Then, the coherence length grows with t, and at every time it will be $\ell(t, T_A)$. That means that, at t, the system will be equilibrated up to length scales $\ell < \ell(t_A, T_A)$, but will continue out of equilibrium for larger scales, evolving still from the state at T_E. If now the system is again cooled to $T_B < T_A$ at t_A (but $T_A - T_B$ large), all length scales are out of equilibrium again (assuming sensibility of the equilibrium phase to external conditions, but not necessarily such a strong sensibility as in the temperature chaos). Then, the rejuvenation is due to the re-equilibration of the small length scales below the new coherence

length $\ell(t, T_B)$ that starts to grow for $t_A < t < t_B$. Now, if the growing speed is a lot slower than at T_A, and $t_B - t_A \approx t_A$ as normally happens in experiments, at $\ell(t_B - t_A, T_B) \ll \ell(t_A, T_A)$. Then, if now the system in heated again to T_A, the intermediate lengths $\ell(t_B - t_A, T_B) < \ell < \ell(t_A, T_A)$ will be already equilibrated for T_A from the previous aging, they *remember* the previous ordering. That would be the explanation to memory.

We should stress, however, that the numerical methods of [Bero2a] can be applied as well to disordered ferromagnets. In fact, one finds as well "memory" and "rejuvenation" [Jimo5], although they do not appear on experimental ferromagnets. One must thus question whether the "memory" and "rejuvenation" on [Bero2a] is related to the experimental effects.

3.4

Spin glass models

All the description up to know was purely experimental. For a theoretical approach a simple model to work with is needed. In nature there are many different kinds of magnetic interactions that lead to the qualitatively similar SG behavior. The only obvious common features have been mentioned: randomness, mixed interactions and frustration. With this idea in mind, the goal for theoretical physicists is to find a model simple enough that it allows analytical treatment but yet complex enough to display the surprising effects observed in experiments.

3.4.1 Edwards-Anderson model

Concerning theoretical physics of SG, on 1975 "all hell broke loose" with the proposal of Edwards and Anderson of a very simple model [Edw75]. In it, the spins $\boldsymbol{s}_i$ ($i = 1, \ldots, N$) lie on a regular, translationally invariant lattice, and the couplings J_{ij} are random. The Hamiltonian is given by

$$\mathcal{H} = -\sum_{i,j} J_{ij} \boldsymbol{s}_i \boldsymbol{s}_j, \tag{3.10}$$

where the $\boldsymbol{s}_i$ are unitary vectors of three components (in Heisenberg spin glasses), two components (XY spin glasses) or with only one component (Ising spin glasses). In principle, the interactions J_{ij} are random variables with a distribution that depends on the distance between the spins $|\boldsymbol{R}_i - \boldsymbol{R}_j|$. However, among all the possible options, the most popular election is the one where the interactions occur only between nearest neighbors. Actually, this model is the one often known as the Edwards-Anderson (EA) model. The Hamiltonian is now

$$\mathcal{H} = -\sum_{\langle i,j \rangle} J_{ij} \boldsymbol{s}_i \boldsymbol{s}_j, \tag{3.11}$$

where $\langle i, j \rangle$ indicates a nearest neighbors summation. The J_{ij} are generally extracted from a probability distribution such that $\overline{J_{ij}} = 0$. The most popular elections are Gaussian and bimodal ($\pm J$) couplings. Actually, the shape of the distribution seems not to be very important.

Edwards and Anderson also came up with a proposal of order parameter for the spin glass phase. Concerning all what discussed in the previous section, this parameter cannot be long-ranged since the spin glass phase has no long-range order, and must depend on the temperature if one assumes temperature chaos. Their proposal was

$$q_{\mathrm{EA}} = \lim_{t\to\infty} \frac{1}{N} \sum_i \langle s_i(0) s_i(t) \rangle_t \,, \tag{3.12}$$

namely the overlap between the spin configurations at two different distant times (in equilibrium). We discussed before that time average of the local magnetization is non-zero in the spin glass frozen phase. In particular, $q = 1$ at $T = 0$ (no evolution at all) and since the transition is second order, we should expect $q \to 0$ when $T \to T_{\mathrm{c}}$ as in a paramagnetic phase. As usual, Eq. (3.12) can be simplified

$$q_{\mathrm{EA}} = \frac{1}{N} \sum_i \langle s_i \rangle^2 \,. \tag{3.13}$$

We will come back to this parameter in Section 3.6.1.

3.4.2 Quenched averages and replicas

Before introducing analytical derivations, it is interesting to discuss how to deal with disorder averages.

In the disordered magnetic systems we are considering here, as in the EA model just defined, the Hamiltonian $H_J(\{s_i\})$ depends on two kinds of variables: the spins, $\{s_i\}$, and the couplings $J \equiv \{J_{ij}\}$. Now, one notes that the diffusion time for impurities (think of Mn atoms on $\mathrm{Cu}_{1-x}\mathrm{Mn}_x$) is huge as compared with the timescale for *spin-flip* (picoseconds). This suggests to work in the *quenched approximation*: spins cannot have any kind of influence over the material impurities. Then, the set of coupling constants in a particular realization of J, namely *sample*, will be considered random variables distributed according to certain probability distribution $P(\{J\})$ known in theoretical models. The free energy density within each sample is then also a random variable, and is given by

$$f_J = -\frac{1}{\beta N} \log Z_J, \tag{3.14}$$

where

$$Z_J = \sum_{\{s\}} \mathrm{e}^{-\beta H_J(\{s\})}, \tag{3.15}$$

is the partition function for this sample.

However, ordinary statistical mechanics tells us how to compute the free energy for a given set of J's. But what if we do not know which is the actual set of J's because they are random? how do we compute f_J? Indeed, the only thing we know about these J's is their probability distribution function. Fortunately, if one considers the $N \to \infty$ limit, thermodynamical magnitudes such as the energy density must take the same value in all the samples (this property is known as self-averaging). That means that the randomness in the samples leads to fluctuations of order $1/N$

$$\overline{f_J^2} - \left(\overline{f_J}\right)^2 = \mathcal{O}\left(\frac{1}{N}\right), \tag{3.16}$$

where $\overline{(\dots)}$ refers to average over samples J's, i.e.

$$\overline{f} \equiv \overline{f_J} = \sum_J P(J) f_J. \tag{3.17}$$

According to this last statement, for finite system sizes, the best way of inferring the thermodynamic limit is to average over all the samples. Indeed, fluctuations will be reduced by $1/N_s$, being N_s the number of samples. That means that from now on we will be interested in the averaged magnitudes. As usual in statistical mechanics, the central magnitude is the free energy $\overline{f}$ defined in (3.17).

This magnitude can be computed easily using the so-called *replica method*. Technically, it is computed as an analytical continuation of the disorder average of the partition function of n uncoupled replicas of the system. Before using this trick, it is useful to introduce some definitions,

$$Z_n \equiv \sum_J P(\{J\}) \left(Z_J\right)^n = \overline{\left(Z_J\right)^n}, \qquad\qquad f_n \equiv -\frac{1}{n\beta N} \log Z_n. \tag{3.18}$$

Now, using the relation $A^n \approx 1 + n \log A$ valid for $n \approx 0$ and the usual $\sum_J P(\{J\}) = 1$, we get

$$\log \overline{\left(Z_J\right)^n} \approx \log\left(1 + n\, \overline{\log Z_J}\right) \approx n\, \overline{\log Z_J}, \tag{3.19}$$

for $n \approx 0$. Then, it is clear that the desired averaged free energy is

$$\overline{f} = \lim_{n \to 0} f_n. \tag{3.20}$$

Here comes the so-called replica trick. If one considers n to be an integer, $\left(Z_J\right)^n$ can be easily computed by means of n uncoupled replicas of the same system (evolving under the same set of J's),

$$\left(Z_J\right)^n = \sum_{\left\{s_i^{(1)}\right\}} \sum_{\left\{s_i^{(2)}\right\}} \cdots \sum_{\left\{s_i^{(n)}\right\}} \mathrm{e}^{-\beta \sum_{a=1}^n H_J\left(\left\{s_i^{(a)}\right\}\right)}, \tag{3.21}$$

where the spins $s_i^{(a)}$ carry two indices: the upper is the replica index, running from 1 to n, and the lower labels the site of the spin, running from 1 to N.

We now use this approach to obtain the famous solution to the Sherrington Kirkpatrick model, the mean field version of the EA model already discussed.

3.4.3 The mean-field spin glass: the Sherrington Kirkpatrick model

At variance with ferromagnets, the mean field (MF) approximation in spin glasses is highly non trivial. We will discuss in this section the mean field solution to the EA spin-glass. As we shall see, although MF allows an exact analytical description, the emergent picture is by no means, simpler. In fact, it is not even clear if it is simpler than the unperturbed problem.

In this section we present a sketch of the derivation of the mean-field solution for the EA spin glass. For a full derivation see, e.g. [Doto1, Méz87]. We will just concentrate on the necessary information to understand its predictions for the spin-glass phase.

The most important MF model in spin glasses is the Sherrington-Kirkpatrick (SK) model [She75], which is both the first and the most studied model. However, more realistic mean field models have been proposed in the last decades, we will discuss some of them in Section 4.2, as well as define a new MF model, called the Hypercube model.

The SK model is the fully connected version of the EA model [She75]. In it, all the spins interact with all the other spins in the system, and the strength of these interactions is random, with no relation with the distance between them. In this sense, this is quite an unnatural model since no distance or, at least, notion of neighborhood exists. In addition, spins are considered to be Ising variables, that is, only two orientations are possible. The Hamiltonian is thus defined as

$$\mathcal{H} = -\sum_{i<k} J_{ik} s_i s_k, \tag{3.22}$$

where the couplings are Gaussian distributed with mean $\overline{J_{ik}} = 0$ and variance $\overline{J_{ik}^2} = \frac{1}{N}$, that is,

$$P(J_{ik}) = \prod_{i<j} \sqrt{\frac{N}{2\pi}} \mathrm{e}^{-\frac{N}{2} J_{ik}^2}. \tag{3.23}$$

With this election, the total energy (3.22) is proportional to N.

Now we apply the replica approach discussed in Section 3.4.2. Our first step is to compute the Z_n introduced in (3.18) using the Hamiltonian (3.22)

$$Z_n = \overline{(Z_J)^n} = \sum_J P(\{J\}) \sum_{\{s\}} \mathrm{e}^{\beta \sum_{a=1}^n \sum_{i<k} J_{ik}\, s_i^{(a)} s_k^{(a)}}, \tag{3.24}$$

where $\sum_{\{s\}}$ denotes the sum over all the possible spin configuration in all the n replicas. We introduce the probability distribution function (pdf) for the couplings, defined in (3.23) and use it to remove the J's dependency. The result is

$$Z_n = \sum_{\{s\}} \mathrm{e}^{\frac{\beta^2}{2N} \sum_{i<k} \left(\sum_{a=1}^n s_i^{(a)} s_k^{(a)} \right)^2} = \sum_{\{s\}} \mathrm{e}^{\frac{\beta^2 N n}{4} + \frac{\beta^2 N}{2} \sum_{1 \le a,b \le n} \left(\sum_{i=1} s_i^{(a)} s_i^{(b)} \right)^2}. \tag{3.25}$$

Finally, one can linearize the sum over the sites using the so-called replica matrix Q_{ab},

$$Z_n = \left(\prod_{a<b}^{n} \int \mathrm{d}Q_{ab}\right) \sum_{\{s\}} \exp\left[\frac{\beta^2 N n}{4} - \frac{\beta^2 N}{2} \sum_{1\leq a,b\leq n} Q_{ab}^2 + \beta^2 \sum_{1\leq a,b\leq n} \sum_i Q_{ab} s_i^{(a)} s_i^{(b)}\right], \tag{3.26}$$

where Q is a $n \times n$ symmetric matrix, with zeros on the diagonal. This last expression can be simplified so that

$$Z_n = \left(\prod_{a<b}^{n} \int \mathrm{d}Q_{ab}\right) \mathrm{e}^{-NA(\{Q\})}, \tag{3.27}$$

$$A(\{Q\}) = -\frac{\beta^2 n}{4} + \frac{\beta^2}{2} \sum_{1\leq a,b\leq n} Q_{ab}^2 - \frac{1}{N} \log \sum_{\{s\}} \exp\left[-\beta H(\{Q,s\})\right], \tag{3.28}$$

$$H(\{Q,s\}) = -\beta \sum_{1\leq a,b\leq n} \sum_i Q_{ab} s_i^{(a)} s_i^{(b)}. \tag{3.29}$$

Then, we can use the saddle-point approximation to compute Z_n for the large N limit, i.e. $Z_n = \min\left[A(\{Q\})\right]$. Therefore, the task is to find the solution to the $n(n-1)/2$ equations $\partial A/\partial Q_{ab} = 0$. It turns out that the solution is given by

$$Q_{ab} = \frac{1}{N} \sum_i \left\langle s_i^a s_i^b \right\rangle_Q, \qquad a \neq b, \tag{3.30}$$

where the average $\langle\cdot\rangle_Q$ is taking using the Hamiltonian $H(\{Q,s\})$ defined in (3.26).

The function $A(\{Q\})$ is symmetric with respect to the exchange of rows or columns: all the replicas are equivalent. The only replica symmetric solution is then

$$Q_{ab} = (1-\delta_{ab})q. \tag{3.31}$$

However, although this solution reproduces the right phase diagram, it leads to a negative value of the entropy at low temperatures and the $q = 0$ solution turns to be a maximum in the free energy for $T > T_c$, which makes no sense. Besides, the $q = 0$ solution below T_c seems to be more stable than the spin glass solution $q \neq 0$ [Alm78]. Furthermore, it leads to a negative susceptibility which contradicts the experiments and basic thermodynamic notions.

Some deeper analysis concluded that the conditions $\partial A/\partial Q_{ab} = 0$ did not imply that $A(\{Q\})$ is a minimum function of Q for all values of n. Indeed, the number of equations, the $n(n-1)/2$ becomes negative when $0 < n < 1$ and for the replica trick one needs precisely to take the $n \to 0$ limit.

The solution to this problem was proposed by Parisi some years later [Par79, Par80], and implies breaking the replica symmetry, i.e the solution is not longer (3.31) (see Fig. 3.6). The starting point is this symmetrical matrix (3.32). Now, one step of Replica Symmetry Breaking (RSB) consists on dividing the matrix into

constant blocks $[(n/m_1) \times (n/m_1)]$ of size $m_1 \times m_1$ and set each diagonal block as a sub-matrix whose off-diagonal elements are all q_1 and the remaining terms stay how they were, i.e with the value q_0, as done in (3.33). A second RSB is taking in the same way, but now introducing a new overlap q_2, see (3.34). This process is continued indefinitely.

Note that with this description, the equivalence between replicas is still conserved. In fact, all the rows or columns have the same components, although the order of appearance of the q_i is different.

The pdf is given by

$$p(q) = \frac{1}{n(n-1)} \sum_{a \neq b} \delta(Q_{ab} - q) \tag{3.35}$$

$$= \frac{n}{n(n-1)} \big[(n - m_1)\delta(q - q_0) + (m_1 - m_2)\delta(q - q_1) \tag{3.36}$$

$$+ (m_2 - m_3)\delta(q - q_2) + \ldots \big], \tag{3.37}$$

and taking the $n \to 0$ limit one gets

$$p(q) = m_1\delta(q - q_0) + (m_2 - m_1)\delta(q - q_1) + (m_3 - m_2)\delta(q - q_2) + \ldots. \tag{3.38}$$

Note that, although by construction $n \geq m_1 \geq m_2 \cdots \geq 1$, when taking the $n \to 0$ limit, it turns around and $0 \leq m_1 \leq m_2 \leq \cdots \leq 1$.

Then, in the limit of infinite RSB steps,

$$m_k/m_{k+1} \to 1 - \mathrm{d}x/x, \qquad \text{and} \qquad q_k \to q(x) \tag{3.39}$$

with $x \in [0, 1]$, i.e. can take whatever value within this interval. Thus, the spin glass order parameter is not a number, but a function. In other words, we have now an infinite number of order parameters. This solution suggests that the SK has infinite number of "frozen spin patterns", whose overlap q' can take all values in $q(0) \leq q' \leq q(1)$.

All the description here was quite naive, specially concerning an integer number of replicas that, at certain point, is analytically continued to zero. However, although later in time, it has been rigorously shown that the RSB scheme produces the correct free energy for the Sherrington-Kirkpatrick model [Talo6].

In addition, the RSB approach leads to an ultrametric distribution of states [Ram86]. Indeed, the order parameter matrix Q_{ab} can be represented by a tree with emanating branches. In order to illustrate this idea, let us consider the 8×8 matrix presented in Figure 3.6 of a system of $n = 8$ replicas. We can represent this matrix on a tree as the one shown in Figure 3.7—left. At the root (no RSB step), all the elements have the same overlap q_0. After one RSB step with $m_1 = 4$ all elements are divided into two branches $\{1, 2, 3, 4\}$ and $\{5, 6, 7, 8\}$, each with overlap q_1. The process continues with many sub-divisions until $q = 1$. Then, the overlap between two given replicas α and β in Figure 3.7—left, $q_{\alpha\beta}$ is given by the level at which the branches coming from each replica join. In the case of the Figure, $q_{\alpha\beta} = q_1$. This

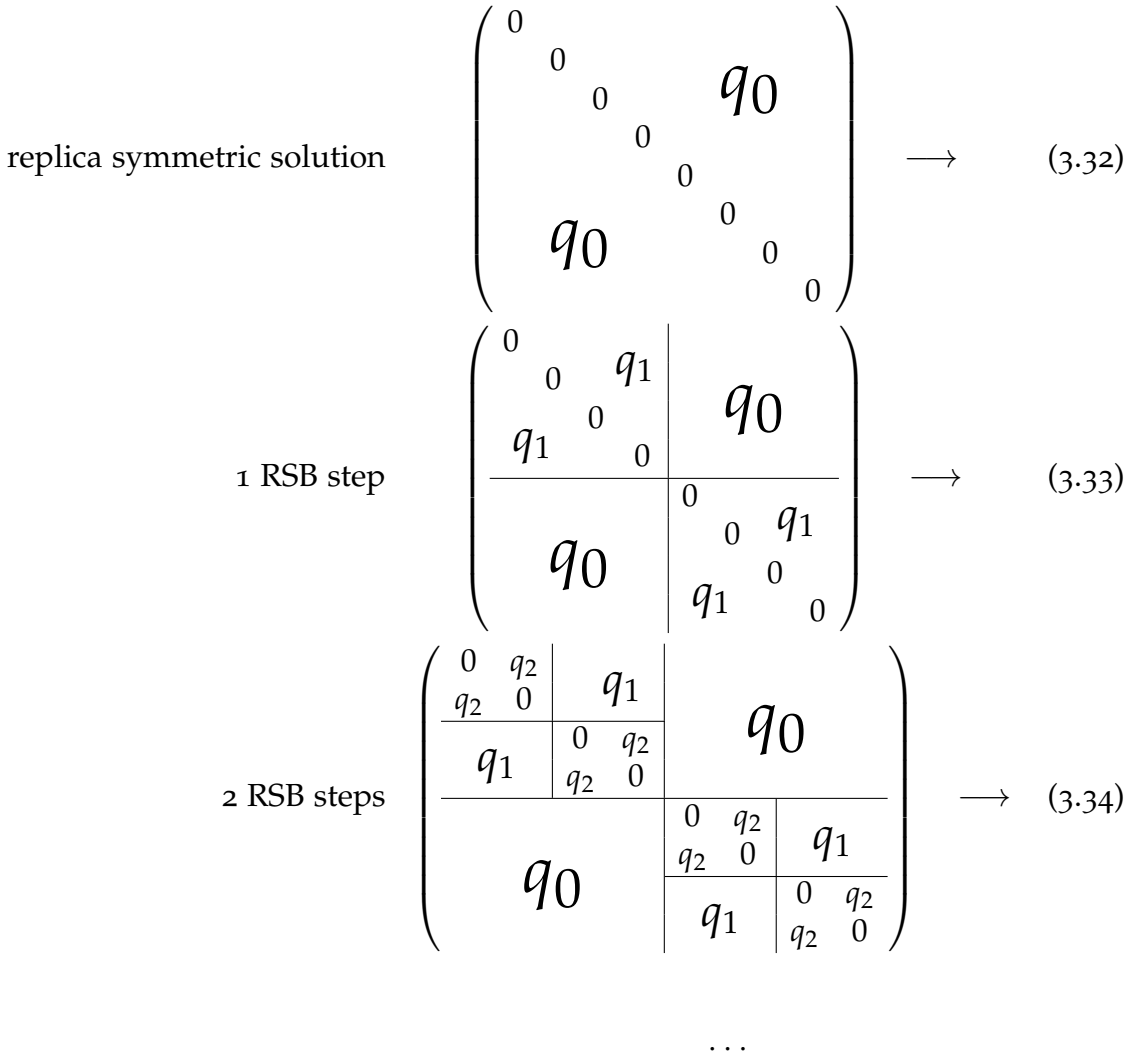

FIGURE 3.6: Sketch of the replica symmetry steps for a problem of $n = 8$ replicas (see main text for discussion).

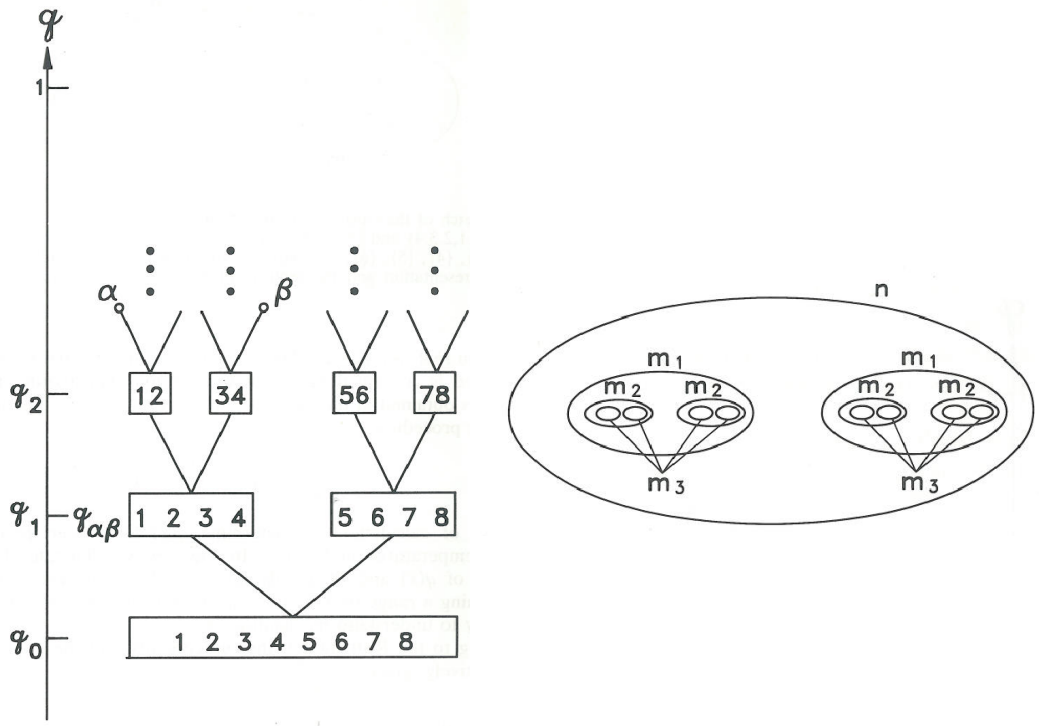

FIGURE 3.7: Sketch of the ultrametric space for $n = 8$ replicas. The trace between α and β one must go back to the point where their branches join, for instance $q_{\alpha\beta} = q_1$. The overlaps of the overlaps within the same row are the same.

leads to a hierarchical distribution of clusters. As in any tree graph, the overlaps fulfill the ultrametric inequality

$$q_{\alpha\beta} \geq \min\{q_{\alpha\gamma}, q_{\beta\gamma}\}. \tag{3.40}$$

This equality implies that the space of states can be divided into clusters of a given overlap, and each of them subdivided in other subclusters and so on, see 3.7—right for the previous example. Note that there is no overlap between clusters of similar order, each point lies on one single cluster. An space with an organization like the one described here is called ultrametric.

One of the most important features of the RSB solution is that the $p(q)$ is non-trivial, as discussed above. In addition, another important feature of the RSB solution of the SK model, is that the spin glass phase is not destroyed in the presence of a magnetic field. Besides, when computing the susceptibility, it reproduces the constant behavior $\chi(T)$ in the field cooling (FC) experiments discussed in Section 3.3.

3.5

Theoretical scenarios: the Droplets and the RSB pictures

There are mainly two competing theories for explaining the equilibrium SG phase: the *droplets* [Fis86, Fis87, Hus87, Fis88a] and the RSB one [Maroo]. In addition, numerical simulations suggested an intermediate picture between these two. This theory is known as the TNT [Krzoo, Paloo] (we will leave its discussion for Section 3.6.3).

On one hand, the *droplets* picture is based on the Migdal-Kadanoff renormalization, exact for $D = 1$ EA model. According to the *droplets* picture, the SG phase would be ferromagnetic-like, with a complicated spin texture due to the disorder, but essentially with only two equilibrium states related by spin-flip symmetry. The dynamics is thus explained in terms of low lying excitations of compact domains (droplets) of coherently flipped spins about these states. Since the couplings are disordered, the boundaries of these domains wander so that they can take advantage of the unsatisfied bonds and avoid the stronger satisfied ones. This effect results in a non convex droplet structure. Indeed, droplets are expected to be fractal of dimension $D - 1 \leq D_s < D$, thus, not space filling. In addition, this theory assumes that the lowest energy excitations of spatial extent ℓ typically cost a free energy

$$F_\ell \sim \gamma(T)\ell^\theta, \tag{3.41}$$

where $\gamma(T)$ is called the *stiffness modulus* and θ the *stiffness coefficient*, which fulfills

$$0 < \theta < (D-1)/2. \tag{3.42}$$

Hence, in the thermodynamic limit, an excitation involving a finite fraction of the total spins, i.e. $\ell = O(L)$, would cost an infinite free energy. Then, this approach only expects excitations of size $\ell \ll L$. As a consequence of this model, the spatial correlations decay with θ,

$$C(r_{ij}) = \overline{\langle s_i s_j \rangle^2} - \overline{\langle s_i \rangle^2 \langle s_j \rangle^2} \sim \frac{1}{r_{ij}^\theta}, \tag{3.43}$$

which makes the pdf for the overlap trivial, i.e. $P(q) = \delta(q^2 - q_{\mathrm{EA}}^2)$, as mentioned before.

On the other hand, the RSB is based on the mean-field solution sketched in Section 3.4.3. There is a growing consensus that the RSB is valid for the EA model for dimensions $D > D_u = 6$, with D_u being the upper critical dimension. In this theory, the $D = 3$ EA spin-glass is drawn as a perturbative extension from the exact solution obtained above for the SK model. The emerging picture is very similar to the one presented in the previous section: the equilibrium SG phase is composed by an infinite number of degenerate states organized through an ultrametric structure. Indeed, as in the SK solution, the pdf for the order parameter $P(q)$ is not trivial, and all values for the overlap between $[-q_{\mathrm{EA}}, +q_{\mathrm{EA}}]$ are possible even in the infinite

volume limit. The RSB theory expects non-compact domains whose surface is space filling, that is, the fractal dimension D_s is equal to the space dimension D. In addition, as in the SK model, there can be excitations that involve flipping an $O(L)$ number of spins with a finite energy cost (the MF prediction is $\theta_{\mathrm{MF}} = 0$). In addition, in this scenario, the spin glass survives under the influence of a magnetic field.

For both theories, *Aging* is a explained as a process where coherent domains of low temperature phase grow with time. The characteristic length scale for these domains is $\xi(t_w)$, the coherence length. The two theories disagree in their predictions for these domains properties:

- For the droplets theory, these domains are compact objects: the surface-volume ratio vanishes in the high $\xi(t_w)$ limit [Fis88b]. The SG order parameter is non zero inside of each domain.

- The RSB theory expects space filling domains with a surface-volume ratio constant for large $\xi(t_w)$. The SG order parameter vanishes inside those domains.

It is interesting to point out that even though the droplet picture is simpler compared to the RSB, it still accounts for the complex physics of experimental spin glasses. A curious example of the diverse explanations of the same effects appears on the evolution of the spin freezing pattern with temperature and the apparition of temperature chaos, see Chapter 5 (let us note that temperature chaos has not been directly measured in experiments, but it is predicted by both theories). In the droplet theory, the compact domains can suddenly flip due to an infinitesimal change of the temperature, because of a delicate balance between the free energy (3.41) and the entropy of the system. We will discuss this approach in detail in Section 5.1. On the contrary, the RSB explains it with a hierarchical structure of the ground states as function of the temperature, as shown in Figure 3.8. In it, during the aging at certain temperature T, the system samples the infinitely many metastable states at a given level of the hierarchical tree. The aging is later restarted upon lowering the temperature following the subdivisions in possible states in the free energy of each valley. The system must find the equilibrium state but always inside the branch already chosen. Within this approach, the rejuvenation and memory effects discussed in Section 3.3.3 are directly explained. Once we lower the temperature, the aging is reactivated with the subdivision, leading to the rejuvenation effect. But if the temperature is increased again, the system returns to the initial valley. In the same sense, temperature chaos is expected in such a picture, the distribution of valleys in free-energy changes completely from one temperature to the other.

As mentioned before, even after 40 years of intense study, there is not still consensus about which is the nature of the equilibrium phase. One of the main difficulties to test experimentally these different scenarios is precisely the fact that the real spin glasses are always out of equilibrium. Then, one needs to find a way

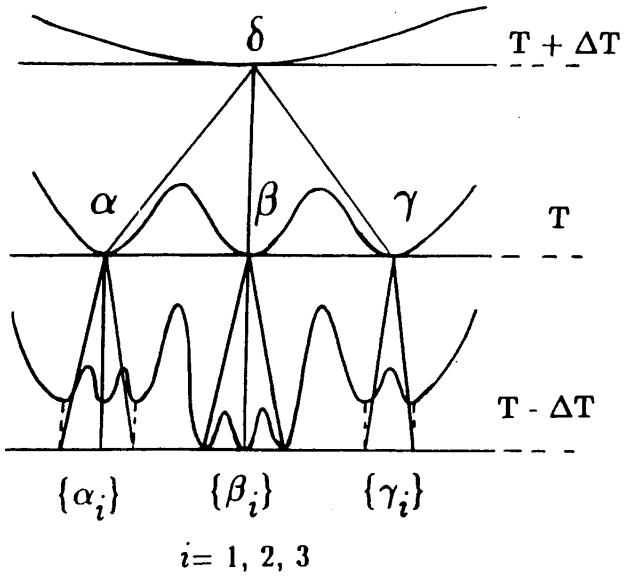

FIGURE 3.8: Sketch of the hierarchical structure of metastable states as a function of temperature. Figure taken from [Vin96].

of tracking the influence of the equilibrium configuration in the nonequilibrium evolution of the system. An example of this idea is found in the violation of the fluctuation-dissipation theorem (FDT) discussed in Section 3.3.2. Indeed, as discussed above, the violations of the FDT can be quantified by means of the violation factor $X(t, t')$ introduced in (3.9). In equilibrium, $t, t_w \to \infty$ and $C(t, t_w) \to q$, then, the susceptibility

$$\chi(t + t_w, t_w) = \int_0^t R(t + t_w, t' + t_w) dt' \to -\frac{1}{T} \int_{q_{min}}^{q} dq' \, P(q'). \tag{3.44}$$

That means that the violation of the FDT depends on the equilibrium pdf for the overlap $P(q)$. Since this pdf is radically different in the two scenarios, the prediction for $x(q) \equiv \int_{q_{min}}^{q} dq' \, P(q')$ changes from one theory to the other. This factor can be measured in a experiment if comparing with the linear behavior with the $1/T$ expected for the FDT, as was shown in Figure 3.4. As long as in the droplet theory the overlap distribution is trivial, one would expect a constant behavior below q_{EA}, while in the RSB theory, this function should decrease with q as shown in the dashed lines in Figure 3.4.

3.6

Spin glasses in numerical simulations

The two theoretical scenarios for the equilibrium phase discussed above are both exact in two different oversimplified models for spin glasses. Namely, in those models where the mean field approximation (in the case of RSB) or the Migdal-Kadanoff renormalization (in the case of droplets) are exact. However, their validity for describing real spin glasses or, at least for more realistic theoretical models, such as the $D = 3$ EA model, is not clear.

That is precisely where computer simulations are essential: they can fill the gap between experiments and theory (obtained in oversimplified models). Indeed, numerical simulations allow us to explore the SG phase in more realistic theoretical models which, because of their complexity, cannot be solved analytically. Furthermore, simulations allow both equilibrium and non equilibrium studies, which enable to compare results either with theory or with experiments.

Basically without exceptions, numerical work in $D = 3$ is best described by the RSB theory (see [Mar00] for a review, refs. [Con06, Con07, Con09, ÁB10a] for recent work and refs. [Krz00, Pal00, Jör08] for some somewhat dissenting views). However, the system sizes that can be thermalized in reasonable times in a simulation are so small that one should question whether the observed effects are really coming from the nature of the SG phase or are just finite size effects [Moo98, Bok00]. The same situation is observed in nonequilibrium, where the simulation times are often too far away from experimental scales to account for the interesting phenomena. In other words, the computer capacity is currently the real bottleneck in spin glass studies.

However, the situation has improved notably in the last years, with the large-scale simulations performed on Janus [Bel06, Bel08a], a special-purpose computer designed for the simulation of SG. Indeed, the Janus computer outperforms the conventional computing architectures by several orders of magnitude, both in times and in lengths scales. Considering nonequilibrium simulations [Bel08b], it was able to follow the nonequilibrium dynamics up to times $\sim 0.1s$, which improves by three orders of magnitude a conventional computer. This time must be compared with the experimental window that goes from seconds to hours. Simulations still cannot reproduce experiments, but Janus is almost there. On the other hand, with the Janus computer it is possible to thermalise lattices of size $L = 32$ down to temperatures $T \approx 0.64 T_c$. This is not only a world record, but provides as well the best glimpse on the low temperature SG phase ever. We will use these unprecedentently large configurations, thermalized up to very low temperature for our study of temperature chaos in Chapter 5. The existence of these configurations will be crucial for the conclusions achieved.

Leaving aside the computer capacity improvements, the finite time/size problems can be useful. Indeed, the comparison between dynamics and statics has created a bridge between these two separate worlds. A dictionary between finite-time nonequilibrium and finite-size equilibrium simulations has been established, allowing us to directly relate non equilibrium experiments (which also take place

in finite times as compared with the relaxation times in glasses) with theory, which is almost exclusively concerned with equilibrium. Before introducing this equivalence, it is convenient to present the observables usually measured in computer simulations. These magnitudes will be used in the following chapters as well.

3.6.1 Observables

The starting point is the Edwards-Anderson model, discussed in Section 3.4. For the following, we will consider only Ising spins, which means that our spin variables, s_i, can only take two opposite values ± 1. The Hamiltonian is then,

$$\mathcal{H} = -\sum_{\langle i,j \rangle} J_{ij} s_i s_j, \tag{3.45}$$

where $\sum_{\langle i,j \rangle}$ refers to the summation over the nearest neighbors.

As in the ferromagnetic case, the Hamiltonian (3.45) has a global symmetry $\mathbb{Z}_2$ ($s_i \to -s_i$ for all i), which is spontaneously broken in the low temperature phase. Not as obvious is the gauge symmetry induced by the disorder average over couplings (see Section 3.4.2). In fact, we choose a random sign for each position, $\varepsilon_i = \pm 1$, the energy (3.45) remains invariant under the transformation

$$s_i \to \varepsilon_i s_i\,, \quad J_{ik} \to \varepsilon_i \varepsilon_k J_{ik}\,. \tag{3.46}$$

Now, since the transformed couplings $\varepsilon_i \varepsilon_k J_{ik}$ are just as probable as the original ones, the quenched mean value of $\overline{O(\{s_i\})}$ is identical to that of its gauge average $\sum_{\{\epsilon_j = \pm 1\}} \overline{O(\{\epsilon_j s_i\})}/2^N$, which typically is an uninteresting constant value. Then, we need to define observables that are invariant under the gauge transformation (3.46). The Hamiltonian (3.45) provides, of course, a first example. For the rest of magnitudes, we first form gauge invariant fields. This can be done by considering two systems at equal time, that evolve independently with the same set of couplings couplings, $\{s_i^{(1)}, s_i^{(2)}\}$ (this is nothing but the replicas introduced as a trick in Section 3.4.2) or, alternatively, from a single system considered at two different times:

$$\begin{aligned} q_i(t_{\rm w}) &= s_i^{(1)}(t_{\rm w}) s_i^{(2)}(t_{\rm w})\,, \\ c_i(t, t_{\rm w}) &= s_i^{(1)}(t + t_{\rm w}) s_i^{(1)}(t_{\rm w})\,. \end{aligned} \tag{3.47}$$

Indeed, as discussed in Section 3.3, relaxation depends on two times. One considers pairs of times $t_{\rm w}$ and $t + t_{\rm w}$, with $t, t_{\rm w} > 0$, after a sudden quench from a fully disordered state to the working temperature T.

We discuss first the time-dependent observables to end up with the equilibrium observables.

3.6.1.1 One-time-quantities.

The order parameter

$$q(t_{\rm w}) = \frac{1}{N} \sum_i q_i(t_{\rm w})\,, \tag{3.48}$$

vanishes in the nonequilibrium regime (so the system is much bigger than the coherence length, $\xi(t_w)$). We define the SG susceptibility as

$$\chi_{SG}(t_w) = N\overline{q^2(t_w)}\,. \tag{3.49}$$

The long t_w limit of $\chi_{SG}(t_w)$ is proportional to the non-linear magnetic susceptibility, but only in the paramagnetic phase. In the SG phase, for an infinite system, χ_{SG} grows with t_w without bound (in fact, as a power of $\xi(t_w)$).

The Binder parameter provides us with information about the fluctuations

$$B(t_w) = \frac{\overline{q^4(t_w)}}{\overline{q^2(t_w)}^2}\,. \tag{3.50}$$

In the Gaussian regime $B = 3$. In a ferromagnetic phase, $B = 1$. In the SG phase, the long time limit and the infinite size limit do not commute. If one takes first the thermodynamic limit, one stays forever in the $q = 0$ sector of the nonequilibrium dynamics. In this regime $B = 3$ since the fluctuations are Gaussian. On the other hand, if one takes before the limit of long t_w, thermal equilibrium is reached. B grows with the temperature from $B = 1$ at $T = 0$. The equilibrium paramagnetic phase is in Gaussian regime.

3.6.1.2 Two-time-quantities

The correlation spin function tells us about the memory kept by the system at time $t + t_w$, about the configuration at t_w:

$$C(t, t_w) = \frac{1}{N}\overline{\sum_i c_i(t, t_w)}\,. \tag{3.51}$$

As discussed in Section 3.3.2, the SG susceptibility and the time correlation function are related through the fluctuation-dissipation theorem (3.8), $\chi(\omega = 2\pi/t, t_w) \propto [1 - C(t, t_w)]/T$, which is only valid in equilibrium (then, in the SG phase this is true only for $t \ll t_w$ [Bou97]).

On the other hand, when t_w is fixed, $C(t, t_w)$ is just the thermo-remanent magnetization presented in (3.5) and Figure 3.2. Indeed, using the gauge transformation (3.46), it is possible to rewrite an ordered configuration (by an external magnetic field, for instance), as the spin configuration found at time t_w after a random start.

The link correlation function (z being the connectivity of the system)

$$C_{link}(t, t_w) = \frac{1}{zN}\overline{\sum_{\langle ik\rangle} c_i(t, t_w)c_k(t, t_w)}\,, \tag{3.52}$$

carries the information of the density of the interfaces between coherent domains at t_w, that at $t + t_w$ have flipped. Indeed, the sum $\sum_{\langle ik\rangle}$ runs only over the connected spins.

3.6.1.3 Spatial correlation functions

In all the scenarios considered above for the SG phase, the dynamics are characterized by the growth of coherent domains. For this reason, we introduce separately the spatial correlation functions.

For the sake of simplicity, for these definitions, we will label the spins in the lattice by their spatial coordinates $\boldsymbol{x}$, instead of just the index i as done before. Then, the spatial correlation function is

$$c_4(\boldsymbol{r}, t_{\rm w}) = \frac{1}{N}\overline{\sum_{\boldsymbol{x}} q_{\boldsymbol{x}}(t_{\rm w}) q_{\boldsymbol{x}+\boldsymbol{r}}(t_{\rm w})}\,. \tag{3.53}$$

The large distance decay defines a coherence length $\xi(t_{\rm w})$ through the scaling of the form

$$c_4(r, t_{\rm w}) \to \frac{1}{r^a} f\left(\frac{r}{\xi(t_{\rm w})}\right). \tag{3.54}$$

The function f is a damping function. It must be there, if anything else fails, because of causality. It is normally assumed an exponential decay.

Note that this $c_4(r, t_{\rm w})$ is related to the SG susceptibility [defined in (3.49)] by means of the relation

$$\chi_{\rm SG}(t_{\rm w}) = \int {\rm d}^D \boldsymbol{r}\; c_4(r, t_{\rm w}). \tag{3.55}$$

We define one additional spatial correlation function that takes aging explicitely into account. For this reason, we introduce the *non-equilibrium spatial correlation function*,

$$c_{2+2}(\boldsymbol{r}; t, t_{\rm w}) = \frac{1}{V}\sum_{\boldsymbol{x}} \overline{\langle s_{\boldsymbol{x}}(t_{\rm w}) s_{\boldsymbol{x}}(t+t_{\rm w}) s_{\boldsymbol{x}+\boldsymbol{r}}(t_{\rm w}) s_{\boldsymbol{x}+\boldsymbol{r}}(t+t_{\rm w})\rangle}. \tag{3.56}$$

3.6.1.4 Equilibrium Observables

Equilibrium quantities are a straight-forward generalization of the nonequilibrium ones. In this case the explicit dependence with time is not longer necessary and magnitudes are averaged over the time history. We will use now two kinds of averages, the disorder average $\overline{(\cdots)}$ already introduced, and the time average, represented by $\langle\cdots\rangle$.

The Edwards-Anderson order parameter, the *spin overlap*, already defined in (3.13), is

$$q = \frac{1}{N}\sum_i q_i\,, \tag{3.57}$$

with q_i, the overlap field,

$$q_i = s_i^{(1)} s_i^{(2)}\,. \tag{3.58}$$

In particular, it yields the (non-connected) spin-glass susceptibility

$$\chi_{\rm NC}(T) = N\overline{\langle q^2\rangle}\,, \tag{3.59}$$

that diverges at T_c with the critical exponent γ. For all $T < T_c$, one expects $\chi_{\mathrm{NC}} = \mathcal{O}(N)$. We shall also consider the Binder ratio

$$B(T) = \frac{\overline{\langle q^4 \rangle}}{\overline{\langle q^2 \rangle}^2}, \tag{3.60}$$

Which as its nonequilibrium counterpart, takes $\lim_{L\to\infty} B = 3$ for all $T > T_c$. Its behavior in the low temperature phase is controversial. For a *disguised ferromagnet* picture one expects B to approach 1 in the limit of large lattices. On the other hand, for an RSB system one expects $1 < B < 3$ in the SG phase ($T < T_c$).

The link overlap is

$$Q_{\mathrm{link}} = \frac{1}{zN} \overline{\left\langle \sum_{\langle ik \rangle} q_i q_k \right\rangle}. \tag{3.61}$$

We will devote the next section to discuss the implications of this observable.

Finally, we introduce the overlap spatial correlation function in equilibrium

$$c_4(\boldsymbol{r}) = \frac{1}{V} \sum_{\boldsymbol{x}} \overline{\langle q_{\boldsymbol{x}}\, q_{\boldsymbol{x}+\boldsymbol{r}} \rangle}. \tag{3.62}$$

3.6.2 On the link overlap and the overlap equivalence

We devote this section to the link overlap Q_{link} (3.61) [or its nonequilibrium counterpart $C_{\mathrm{link}}(t, t_{\mathrm{w}})$ (3.52)] and its relation with the spin overlap q (3.57) [or $C(t, t_{\mathrm{w}})$ (3.51) in nonequilibrium]. From a mathematical point of view, the square of the overlap represents the covariance of the Hamiltonian in the SK model, while the link overlap is the covariance of the Hamiltonian in the EA model. For this reason, it has been suggested that the Q_{link} should be the fundamental quantity to describe the SG phase below the upper critical dimension [Cono3, Cono5, Cono6].

When summing over all the spins in the system, a priori, these two overlaps should lead to different global order parameters. Indeed, Q_{link} refers to the correlation between the links, and q between the spins. However, in the SK model (defined in Section 3.4.3) they are essentially the same quantity. In fact, it is trivial to check that $Q_{\mathrm{link}} = q^2$ [and $C_{\mathrm{link}}(t, t_{\mathrm{w}}) = [C(t, t_{\mathrm{w}})]^2$]. On the other hand, when one considers only nearest neighbors interactions, like in the EA model, these two magnitudes have different behaviors under spin inversion: q undergoes changes of volume sizes after spin flips, while Q_{link} suffers only surface changes. Indeed, after a domain flip, Q_{link} is only affected by the links that cross its domain's surface.

According to the previous discussion, in the droplet theory (where the domains' surface-to-volume ratio vanishes in the large-L limit), Q_{link} should become constant, no relation with q^2 should be observed. On the contrary, in the RSB theory (were the domains are space-filling) these two magnitudes would be completely correlated, as in the SK model. In other words, in the RSB theory, the link overlap distribution is also non trivial.

In fact, this relation between the overlaps is known as *overlap equivalence* [Paroo]. This property states that all the mutual information about two equilibrium configurations is encoded in the mutual overlap, and thus, no other definition of overlap (such as the Q_{link}) can increase the knowledge of the system. This overlap equivalence is equivalent to ultrametricity, but a lot simpler to check. Its validity in MF is straight-forward but there is still a broad discussion about its validity in the $D = 3$ EA model. Indeed, according to the previous discussion, the overlap equivalence is not fulfilled in the droplets theory.

3.6.3 The TNT picture

The above discussion about the geometry of the excitations and its relation with the behavior of the overlap and the link overlap, led to an intense study of the properties of these two magnitudes in realistic EA models. Simulations leading to a somehow mixed scenario between the droplets and the RSB predictions [Krzoo, Paloo]. The emerging picture was named trivial-non-trivial (TNT), accounting for a trivial distribution of Q_{link} and a non trivial distribution of q. Let us explain this last statement.

The new model would behave like the droplets theory for finite length scales and like RSB for system sizes excitations. In that sense, there would be two transient stiffness coefficients θ, as introduced in (3.41). One, θ_{l}, valid for local excitations $\ell \ll L$, whose free energy would scale like droplets' $F(\ell) \propto \ell^{\theta_{\text{l}}}$. And another, $\theta_{\text{g}} \approx 0$ (like MF), for the global excitations $\ell = O(L)$. This allowed large excitations lead to a probability distribution of the overlap composed by many valleys, like in RSB. Then, a non-trivial distribution for q. However, concerning the geometry of these excitations, they should be like the droplets, since locally this scenario behaves like them. Then, one would expect a vanishing surface-volume ration and thus, a trivial distribution for the link overlap. According to this scheme, as in the droplets, no overlap equivalence should be found.

3.6.4 Statics-dynamics relation: the time-length dictionary

As discussed many times in this section, the theory of spin glasses accounts for an equilibrium phase, which for experimental samples is unreachable in a laboratory. However, it is assumed that this equilibrium phase still conditions the nonequilibrium behavior.

However, one should make this above statement quantitative. We recently established a quantitative relation between the statics and the dynamics correlation functions [Belo8b, ÁB10a]. The proposal is that the equilibrium correlation functions computed in finite systems reproduce the nonequilibrium counterparts in the thermodynamic limit but for finite times. The idea besides this statement is that a system with finite coherence length $\xi(t_{\text{w}})$ can be regarded as a collection of finite systems with $L \sim \xi(t_{\text{w}})$ in equilibrium. If this relation holds, it is possible to stablish a time-length dictionary $t_{\text{w}} \leftrightarrow L$.

The goal is to relate the equilibrium correlation function $c_4(\boldsymbol{r})$ in (3.62) with the two-times spatial correlation function $c_{2+2}(\boldsymbol{r}, t, t_{\mathrm{w}})$ in (3.56). Now, the explicit dependency on t_{w} is removed using $L \sim \xi(t_{\mathrm{w}})$ and the dependency on t, is taken from the two-times correlation function $C(t, t_{\mathrm{w}})$ defined in (3.51). Indeed, as aging states, there is one-to-one relation between t and $C(t, t_{\mathrm{w}})$ for fixed t_{w}. Furthermore, in order to relate $c_4(\boldsymbol{r})$ and $c_{2+2}(\boldsymbol{r}, C(t, t_{\mathrm{w}}), t_{\mathrm{w}})$ one needs to consider the equilibrium correlation function conditioned to a fixed value of q (as an analogy to the dependency on $C(t, t_{\mathrm{w}})$ in the nonequilibrium counterpart). Summing up, the sought relation is taken between

$$c_{2+2}(\boldsymbol{r}, C(t, t_{\mathrm{w}}), t_{\mathrm{w}}) \leftrightarrow c_4(\boldsymbol{r}|q). \tag{3.63}$$

For the q-conditioned $c_4(\boldsymbol{r}|q)$, the natural election would be using the pdf for the overlap

$$p_1(q) = \overline{\left\langle \delta\left(q - \frac{1}{N}\sum_{\boldsymbol{x}} q_{\boldsymbol{x}}\right)\right\rangle}, \tag{3.64}$$

however, for finite systems this is a non smooth function composed by a sum of $N+1$ Dirac deltas. As a solution, we considered a smoother version of it, the convolution of $p_1(q)$ with a Gaussian of width $1/\sqrt{N}$

$$p(q = c) = \int_{-\infty}^{\infty} q'\ p_1(q')\mathscr{G}_N(c - q') = \overline{\left\langle \mathscr{G}_N\left(c - \frac{1}{N}\sum_{\boldsymbol{x}} q_{\boldsymbol{x}}\right)\right\rangle}, \tag{3.65}$$

$$\mathscr{G}_N(x) = \sqrt{\frac{N}{2\pi}}\mathrm{e}^{-Nx^2/2}. \tag{3.66}$$

Using this $p(q)$, they defined a new conditional expectation value for fixed q as

$$\mathrm{E}(O|q = c) = \frac{\overline{\left\langle O\mathscr{G}_N\left(c - \frac{1}{N}\sum_{\boldsymbol{x}} q_{\boldsymbol{x}}\right)\right\rangle}}{\overline{\left\langle \mathscr{G}_N\left(c - \frac{1}{N}\sum_{\boldsymbol{x}} q_{\boldsymbol{x}}\right)\right\rangle}}. \tag{3.67}$$

Using this definition, the standard expectation values can be easily computed from these $\mathrm{E}(O|q)$, by means of

$$\overline{\langle O\rangle} = \int_{-\infty}^{\infty} q\ p(q)\mathrm{E}(O|q). \tag{3.68}$$

Finally, the fixed-q correlation function we were looking for is obtained as

$$c_4(\boldsymbol{r}|q) = \mathrm{E}\left(\frac{1}{N}\sum_{\boldsymbol{x}} q_{\boldsymbol{x}} q_{\boldsymbol{x}+\boldsymbol{r}}\middle| q\right). \tag{3.69}$$

In the first attempt to stablish this time-length dictionary [Belo8b], the non-equilibrium curve $c'_{2+2}(r = 1, t, t_{\mathrm{w}})$ as a function of $[C(t, t_{\mathrm{w}})]^2$ was compared to

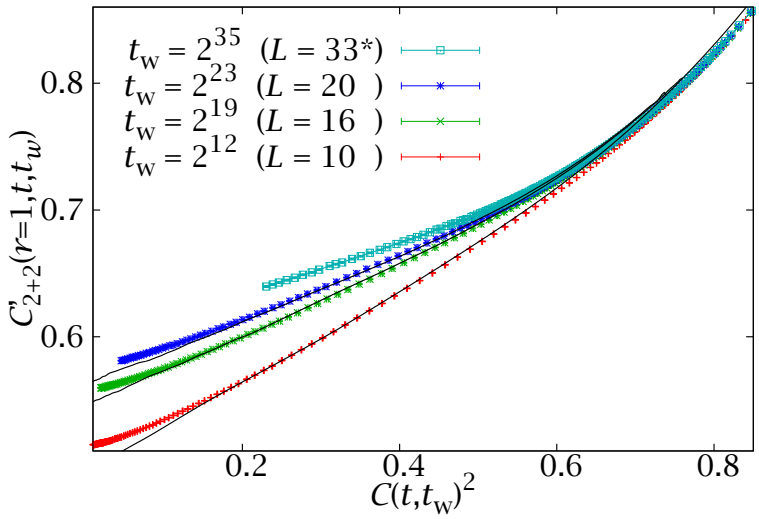

FIGURE 3.9: Comparison of the nonequilibrium curve $C'_{2+2}(r = 1, C^2, t_w)$ vs. C^2 for for several waiting times at $T = 0.7$ (in points), with the equilibrium $C_4(r = 1|q)$ vs. q^2 (in continuous lines). Figure taken from [Belo8b].

the equilibrium $c_4(r = 1|q)$ versus q^2. Both curves could be superposed almost perfectly (see Figure 3.9) if we take as time-length dictionary

$$L(t_w) \approx 3.7\xi(t_w). \tag{3.70}$$

In a second attempt in [ÁB10a] unprecedently large sizes could be thermalized thanks to JANUS computer, reaching $L = 32$ (see [Yll11] for details), leading to more precise results. The equivalent curves are displayed in Figure 3.10 for other values of $r(> 1)$. According to the time-length dictionary, the $L = 32$ equilibrium simulations can be corresponded with non equilibrium simulations with $t_w \approx 2^{31}$, while the $L = 24$ correspond to $t_w \approx 2^{26}$.

The equivalence has some striking consequences. The longest times t_w studied in these numerical works [Belo8b, ÁB10a, ÁB10b], are, thanks to Janus computer, very near to the experimental times. Indeed, these works reached 2^{32} MCS which corresponds roughly to 0.1 seconds. This are not that short times in comparison with the experiments, and still, they correspond to equilibrium simulations for rather small systems. This leads to the direct question of how important is the thermodynamical limit in equilibrium for the experiments. In fact, we considered a typical experiment, which takes place in 1 hour, and extrapolated the correspondent length for equilibrium. The result was that the relevant length scale for nonequilibrium experiments [ÁB10b] was $L \sim 100$, which is definitely very far away from the thermodynamic limit. This relation brings closer the simulations to the experimental behavior. Indeed, the state-of-the-art in the equilibrium studies is around $L = 32$, then, not that far as one would expect.

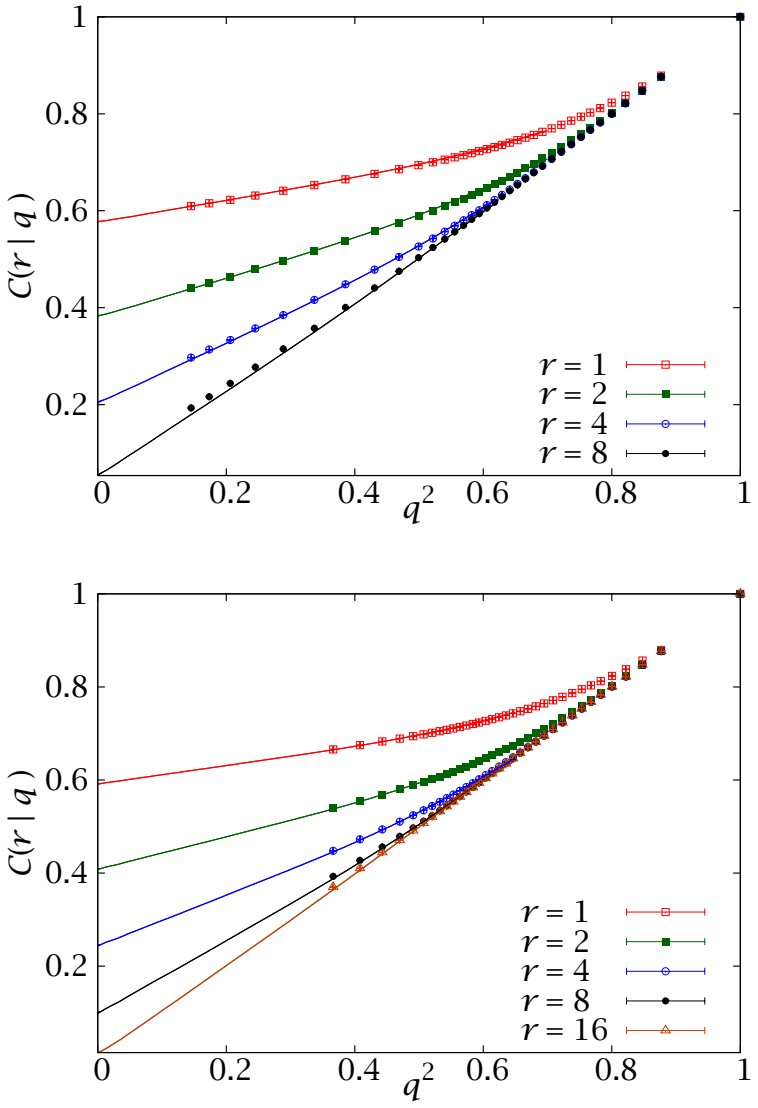

FIGURE 3.10: Comparison of our non-equilibrium correlation functions $C'_{2+2}(r, C^2, t_w)$ (points) and equilibrium $C_4(r|q)$ (lines) at $T = 0.7$. In the top panel we compare $L = 24$ with $t_w = 2^{26}$ and on the bottom one we consider $L = 32$ and $t_w = 2^{31}$. Figure taken from [ÁB10a].

CHAPTER IV

The hypercube model

4.1 Introduction

As discussed in Chapter 3, our understanding of the spin glass phase comes, to a considerable degree, from analythical results obtained under mean field (MF) approximations. As discussed then, the mean field solution to the EA model (the Sherrington-Kirkpatrick (SK) model, see Section 3.4.3) still accounts for most of the complex physics found spin glasses, and draws a picture of an intricate structure for the SG phase characterized by an infinite number of equilibrium states following an ultrametric organization. Even though the SK model allows analythical calculations, there are many phenomena which are not yet understood not even in MF.

In fact, the understanding of the nonequilibrium behavior is not yet well understood not even in the SK model. And, as was widely supported all over the Chapter 3, the nonequilibrium is the only relevant regime for a real spin glass. However, the analythical treatment for the simplest experiments of aging is difficult, not to say anything about explaining more complicate temperature protocols such as the one necessary for the memory and rejuvenation experiments discussed in Section 3.3.3. Furthermore, not only the nonequilibrium is not fully understood, some equilibrium effects such as the temperature chaos (see Chapter 5) are still under investigation [Par10].

For this reason, even at MF level, non perturbative tools, such as Monte Carlo (MC) calculations, are still necessary. Indeed, simulations in MF models, understanding MF model as a model where the MF approximation becomes exact in the thermodynamical limit, can be most useful considering that our large theoretical understanding of these models provides us with much extra information when approaching other unknown phenomena.

We introduced our first MF model in Section 3.4.3 when talking about the

Sherrington-Kirkpatrick model SK, which was the simplest possible MF model for the Edwards-Anderson Hamiltonian (3.11). As explained then, in the SK model all spins are connected, which simplifies a lot the analytical calculations, but makes simulations unaffordable (energy calculations for the MC tests are $\mathcal{O}(N^2)$). Besides, it lacks either from a finite coordination number or a notion of neighborhood, which spaces it out from more realistic models where the spins hardly interact beyond nearest neighbors. For these two reasons, a whole family of solvable MF models with finite connectivity has been proposed in the last years, [Par06, Méz01]. Among all the MF models, those formulated on graphs have become very popular. First, because they allow an analytical approach based on the statistical mechanics' iterative methods typical for tree-like structures, and second, because they are deeply connected with the random optimization problems in computer science (see Section 9.1), which turn out to have finite connectivity too.

We discuss here some popular tree-like lattices with finite connectivity z for the connections between spins before introducing our own new model. We start with the so-called *Cayley tree*. In this graph, starting from site $i = 0$, one chooses randomly a first shell of z neighbors. Afterwards, each of these spins in the first shell is connected again with $z - 1$ new neighbors for the second shell and so on, until there are no more new spins to connect. Thus this graph is a true tree, in the sense that nearest neighbors are only connected by their common link, there is no overlap between new neighbors. However, in such construction, there is finite number of spins lying on the boundary, which makes the system very inhomogeneous. Indeed, these boundary spins origin properties that are far from the usual finite dimensional problems. To avoid this problem, the *Bethe lattice* is normally considered. In it, only the first L' shells of the Cayley graph are considered. This approach works well as long as the graph completely forgets the information from the boundaries, which is not the case, in general, for spin glasses, where boundaries still impose some degree of frustration. For this reason, spin glasses are often defined on other kind of Bethe lattice structures. Now, let us consider a *random graph with fluctuating connectivity* known as *Erdos-Renyi graph*. In it, each link between the pair (i, j) is active with probability z/N. Then, each spin is connected in average with z spins. As a subgroup of this last set, one can define the *fixed connectivity random graphs* containing only those graphs where each spin interacts with exactly z neighbors. We will come back these two models in further detail later on.

Then, we want to define a spin glass on a graph. As we did when presenting the SK model, the starting point is the EA model discussed in Section 3.4.1 for Ising spins, i.e. $s_i(\pm 1)$. With the sake of clarity, at variance with the discussion when describing the EA model, we encode the nearest neighbor summation by introducing a connectivity matrix, $n_{ik} = n_{ki} = 1, 0$ ($n_{ik} = 1$ as long as spins i and k interact). In addition, we must consider the coupling constants, $J_{ik} = J_{ki}$ too carrying the information of the ferromagetic or antiferromagnetic character of the interaction (we will consider $J_{ik} = 1$ for the ferromagnet and $J_{ik} = \pm 1$ for the SG, which defines our energy scale). In other words, we consider now two quenched variables (see Section 3.4.2), the conectivity matrix $\{n\}$ and the couplings $\{J\}$. Using these two

kinds of variables, the interaction energy is now

$$\mathcal{H} = -\sum_{i<k} J_{ik} n_{ik} s_i s_k \,. \tag{4.1}$$

Now we consider the Erdos-Renyi graph described above. As defined, this graph is drawn by connecting each possible couple of spins, (i,k), (among the $N(N-1)/2$ possible ones) with probability $z/(N-1)$. In terms of the variables described just above, activating a link means setting $n_{ik} = 1$. According to this probability, the number of neighbors of spin i or coordination number n_i, follows a Bernoulli distribution function

$$p(n_i) = \left(\begin{array}{c} N-1 \\ n_i \end{array} \right) \left(\frac{z}{N-1} \right)_i^n \left(1 - \frac{z}{N-1} \right)^{N-1-n_i}, \tag{4.2}$$

which tends to a Poisson distribution function with average z (the connectivity) in the large-N limit,

$$p(n_i) = \frac{z^{n_i}}{n_i!} e^{-z}. \tag{4.3}$$

We will consider $z = 6$ to mimic a three dimensional system. This kind of graphs are locally cycle-less: the mean shortest length among all the closed loops that passes through a given point is $\mathcal{O}(\log N)$, i.e. the system is still locally tree-like. In order to support his statement, let us compute the the amount of all possible closed graphs of length l,[1] that pass through a given point of the graph, multiplied by the probability of all the links involved are active,[2]

$$\frac{(N-1)(N-2)\cdots(N-l+1)}{2l} \left(\frac{z}{N-1} \right)^l = \frac{(N-1)!}{2l(N-l)!} \left(\frac{z}{N-1} \right)^l, \tag{4.4}$$

taking the $N \to \infty$ limit, and using the Stirling relation $n! \approx \sqrt{2\pi n}(n/\mathrm{e})^n$ for large n, we get

$$\frac{z}{2l} \left(\frac{z}{e} \right)^{l-1} \frac{1}{N-1}. \tag{4.5}$$

Then, the only surviving loops are those whose length is $\mathcal{O}(\log N)$. In other words, there are no local loops a the Erdos-Renyi graph. We will see that this condition is enough for the Bethe approximation to hold.

This spin glass in an Erdos-Renyi graph has a finite connectivity as we needed for a numerical study, but we still want to step forward and to find a model that also allows us to define a notion of distance. Indeed, as discussed, the origin of

[1] Defining distance between nodes as the minimum number of links that must be crossed for going from one node to the other.

[2] Once one spin of the loop is chosen, the amount of eligible spins decreases by one, and so on. Indeed, we talk about a loop of size l, but there are only $l-1$ links can be freely elected. In addition, in order to not count the same loop more than once, we must divide by $2l$, which takes into account all the possible starting spins within the same loop.

the SG phase is an association of the spins in coherent domains, and the different theories precisely differ in the properties of these domains. For this reason, we want a MF model that lets us to explore as well the growth of a coherence length $\xi(t_w)$.

In this chapter, we will present a new MF model for SG: the spin glass on a D-dimensional hypercube with *fixed* connectivity [Mar95]. In such a model, as we will discuss later, the Bethe approximation becomes exact in the thermodynamic limit (which coincides with the large D limit for this model). As a consequence, the statics is of Bethe-lattice type and can be computed. A nice feature of this new model, is that it has a natural definition of distance, which allows us to study the spatial correlations within MF approximation. In other words: this MF model is more similar to a real $D = 3$ system than any of those considered previously. Indeed, it let us to compute space correlation functions.

4.2 The hypercube model

A simple alternative consists on formulating the spin model on a D-dimensional unit hypercube, see Figure 4.1. Thus, the spins are located in each of the hypercube vertices $\boldsymbol{x}$ (then, $N = 2^D$) and the bonds lie on the edges, $\boldsymbol{x}, \hat{\boldsymbol{\mu}}$, where $\hat{\boldsymbol{\mu}}$ labels the D possible unit vectors in the $D-$dimensional space. We consider periodic boundary conditions, and then, each spin can be connected with, at most, $D = \log_2 N$ spins. The interaction energy (4.1) is now written as

$$\mathcal{H} = -\frac{1}{2}\sum_{\boldsymbol{x},\hat{\boldsymbol{\mu}}} J_{\boldsymbol{x},\hat{\boldsymbol{\mu}}} n_{\boldsymbol{x},\hat{\boldsymbol{\mu}}} s_{\boldsymbol{x}} s_{\boldsymbol{x}+\hat{\boldsymbol{\mu}}}\,, \tag{4.6}$$

where $n_{\boldsymbol{x},\hat{\boldsymbol{\mu}}} = 1$ if spins $s_{\boldsymbol{x}}$ and $s_{\boldsymbol{x}+\hat{\boldsymbol{\mu}}}$ interacts, and $n_{\boldsymbol{x},\hat{\boldsymbol{\mu}}} = 0$ if not. In the sections below, we will discuss how to distribute these connectivity variables.

Note that, at variance with other infinite-dimensional graphs, this hypercube model has at least two natural notions of distance: Euclidean metrics and the postman metrics. In the postman metrics, the distance between two points, $\boldsymbol{x}$ and $\boldsymbol{y}$, is given by the minimum number of edges, either occupied or not, that must be covered when joining $\boldsymbol{x}$ and $\boldsymbol{y}$. The two distances are essentially equivalent, since the Euclidean distance between two sites in the hypercube is merely the square root of the postman distance.

In the following we shall use the postman metrics, which has some amusing consequences. For instance, our correlation-length will be the *square* of the Euclidean one, thus yielding a critical exponent $\nu = 1$, doubling the expected $\nu_{\rm MF} = 1/2$. Of course, if we use the Euclidean metric we recover the usual exponent $\nu = 1/2$.

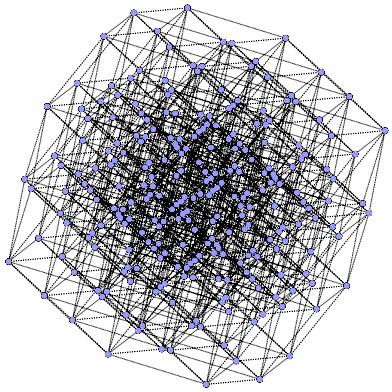

FIGURE 4.1: Projection of a $D = 8$ hypercube. Spins are placed in the nodes, represented by blue circles, and links are the edges.

4.2.1 Random connectivity model

By analogy with the Poissonian graph, we consider that a link is active (i.e. $n_{ik} = 1$) over each edge with probability z/D. We call this model *random connectivity hypercube*. This model is also a Poisson graph. Indeed, in the thermodynamic limit ($D \to \infty$) the probability distribution function for the coordination number n_i of the ith spin is locally Poissonian, i.e.

$$p(n_i) = \frac{z^{n_i}}{n_i!} e^{-z}. \tag{4.7}$$

with average the coordination number z. We show in Figure 4.2 an example of this graph for $D = 8$.

Again, this graph is also locally cycle-less. In a hypercube with only nearest neighbor interactions, for drawing a loop, one must move only along orthogonal directions. Besides, if one wants to close a loop, each orthogonal direction can be either covered an even number of times or not covered at all. Then, when drawing a loop of l links, only half of them can be freely chosen, the remaining half steps are forced to cover previous directions. Then, if the length of the loop is $l = 2r$, and it contains movements along n different orthogonal directions ($n \leq r$, directions can be repeated), the number of possible loops multiplied by the probability that all the links are active, is

$$f(n)\ D(D-1)\cdots(D-n+1)\left(\frac{z}{D}\right)^{2r}, \tag{4.8}$$

where $f(n)$ is a function only of n. Clearly, the less suppressed contribution in D corresponds to $n = r$, i.e. when each direction in the loop is covered only twice. We

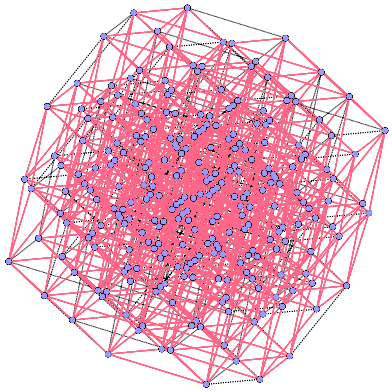

FIGURE 4.2: Random connectivity hypercube with $z = 6$ for a $D = 8$ hypercube. Active links, i.e. $n_{x,\hat{\mu}} = 1$ are represented in pink.

may count the number of loops of length $l = 2r$ that imply r different orthogonal directions in space:[3]

$$\frac{D!}{(D-r)!}\frac{(r-1)(r-1)!}{2r}\left(\frac{z}{D}\right)^{2r}. \tag{4.9}$$

Then, for $D \to \infty$, the number of loops of length $l = 2r$ is

$$\frac{(r-1)(r-1)!}{2r}e^{-r}\frac{z^{2r}}{D^r}, \tag{4.10}$$

then, the density of closed loops of length l decays, at least, with D^{-2} (i.e. with the squared logarithm of N, as it also happens in the Erdos-Renyi graph). But there can be still closed loops in the graph, those of length $\mathcal{O}(D)$. Nevertheless, the absence of closed loops of finite length is sufficient for the Bethe approximation to be exact in the thermodynamic limit, as we discuss in Appendix A.1.

However, it turns out that the random connectivity hypercube suffers a major disadvantage. The inverse of the critical temperature in a ferromagnet (see Appendix A.1 for details of the calculation) or in a SG [Tho86] can be computed within the Bethe approximation:

$$K_c^{\mathrm{FM}} = \operatorname{atanh}\frac{1}{\langle n\rangle_1 - 1}\ ,\ K_c^{\mathrm{SG}} = \operatorname{atanh}\frac{1}{\sqrt{\langle n\rangle_1 - 1}}. \tag{4.11}$$

[3]Again, once a direction has been taken, there are only $D-1$ available directions for the following step, and so on. As before, we can cover the same loop beginning in any of its nodes, then we have to divide the final expression by a factor l. However, in contrast to the Poisson graphs discussed in the previous section, in an elementary hypercube, a loop can be covered only in one orientation due to its periodical boundary conditions (both orientations are equivalent).

In this expression $\langle n \rangle_1$ is a conditional expectation value for n, the coordination number of a given site in the graph. This conditional expectation value is computed knowing for sure that our site is connected to another *specific* site (this is different from the average number of neighbors of a site that has at least one neighbor!). A simple calculation (see Appendix A.1) shows that $\langle n \rangle_1 = 1 + z - \frac{z}{D}$ in the random connectivity model. Since $D = \log_2 N$, we must expect huge finite size corrections ($\mathcal{O}(1/\log N)$) at the critical point. Note that this problem is far less dramatic for a Erdos-Renyi graph where $\langle n \rangle_1 = 1 + z - \frac{z}{N-1}$.

The cure seems rather obvious: place the occupied links in the hypercube in such a way that $n = z$ (here, $z = 6$). Unfortunately, drawing these graphs poses a non trivial problem in Computer Science. Our solution to this problem is discussed in the next subsection.

4.2.2 The fixed connectivity hypercube

We have not found any systematic way of activating links in the hypercube that respects the fixed connectivity condition. Thus, we have adopted an operational approach: the distribution of bonds is obtained by means of a dynamic MC. We must define a MC procedure that generates a set of graphs that remains invariant under all symmetry transformations of the hypercube group. We include a detailed description of the program used to implement this MC in a computer in Appendix B.

Specifically, we start with an initial condition in which all bonds along the directions 1 to 6 are activated (of course, this procedure makes sense only for $D \geq 6$). Clearly enough, the initial condition verifies the constraint $n = 6$. We shall modify the bond distribution by means of movements that do not change n. We perform what we called a "plaquette" transformation (a plaquette is the shortest possible loop in the hypercube, of length 4).

We randomly pick, with uniform probability, one hypercube plaquette. In case this plaquette contains only two parallel active links ($n_{ik} = 1$), these two links are deactivated at the same time that the other two are activated. On the opposite case, nothing is done.[4] This transformation is illustrated in Figure 4.3. This guarantees that the set of generated graphs is isotropic.

In order to this procedure to be useful, the dynamic MC correlations times must be short. In Figure 4.4, we show the MC evolution of the system isotropy. We make kN plaquette transformations, and we control the density of occupied bonds in two directions: the first direction (initially occupied in every vertex) and the seventh direction (initially unoccupied). As we see, for two different system sizes,

[4]This movement keeps each vertex connectivity unaltered. Besides, a transformation and its opposite are equally probable. As a consequence the Detailed Balance Condition is satisfied with respect to the uniform measure on the ensemble of fixed connectivity graphs. An standard theorem [Ami05] ensures that the equilibrium state of this Markov chain is the uniform measure over the subset of fixed connectivity hypercubes reachable from the initial condition by means of plaquette transformations

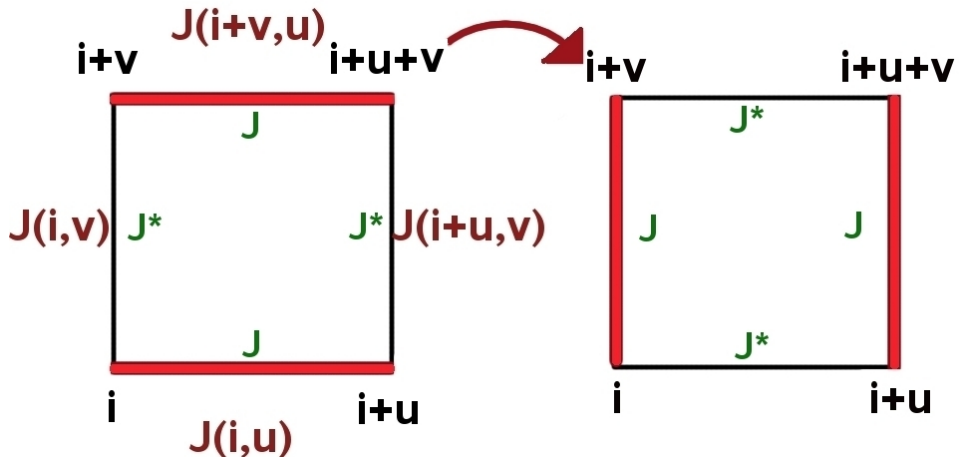

FIGURE 4.3: Plaquette transformation.

we get short isotropization exponential times (for $D = 22$ we get $\tau_{\text{exp}} \approx 7.4N$).[5] For this reason, we assume that taking $k = 100$ is long enough to ensure that the configurations obtained are completely independent from the initial condition.

At this point, a question arises about the completeness of set of graphs we can generate by means of this procedure. Can we achieve all the possible graphs of fixed connectivity in the hypercube? or on the contrary, we only create graphs within a fixed subgroup. Nevertheless, as we will show below, most of the sample dispersion is induced by the coupling matrix $\{J_{ik}\}$. One could argue that there the generated set of graphs is incomplete for a simple reason: the plaquette transformation cannot break loops. Indeed, when we interchange neighboring links we can only either join two different loops or split up a loop into two loops as shown in Figure 4.5. Due to the hypercube boundary conditions, in the initial configuration all sites belonged to closed loops. This situation cannot be changed by plaquette transformations. However, this objection does not resist a close inspection. In fact, a non-closed lattice path formed by occupied links should have an ending point with an *odd* coordination number, which violates the constraint $n = z$ for any even z. Thus, all lattice paths compatible with our fixed connectivity constraint, do form closed loops. This argument, as well as the numerical checks reported below, make us confident that the set of generated graphs is general enough for our purposes. Actually, we conjecture that our algorithm generates *all* possible fixed connectivity graphs with z even.

One may worry as well about the applicability of the Bethe approximation to the fixed connectivity model, since all loops are closed. Actually, the crucial point to apply the Bethe approximation is that the probability of having a closed path of any *fixed* length should vanish in the large D limit. It is easy to prove for the random connectivity model . In the fixed connectivity case, one may argue as

[5] Note that the article [Fer10a] we presented $\tau_{\text{exp}} \approx 4.2N$. However, a refined analysis using two exponentials instead of just one for the fit, leaded to this more accurate new result.

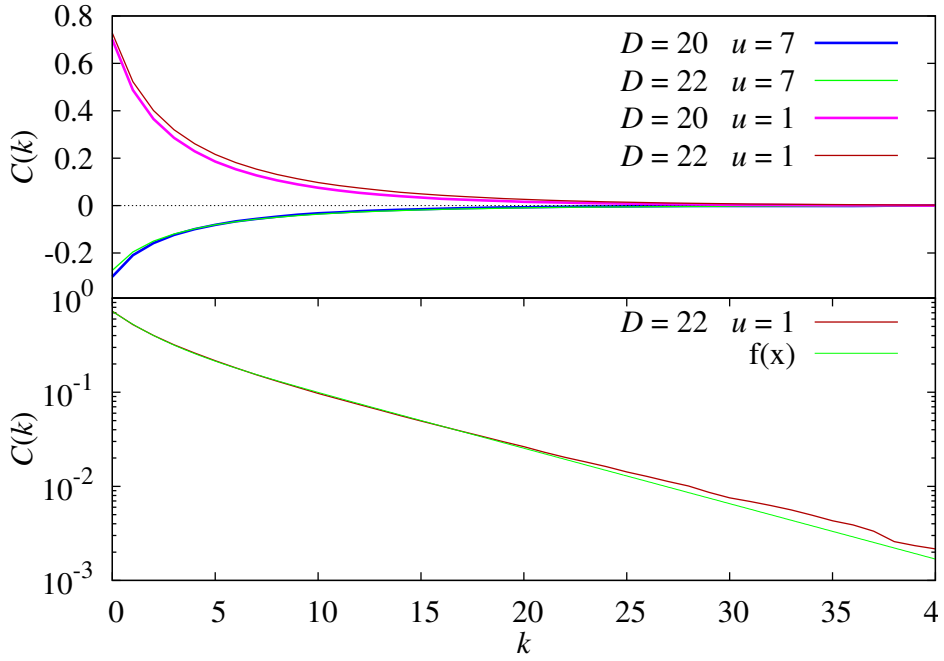

FIGURE 4.4: Generation algorithm of fixed connectivity graphs: (top) for two system sizes ($D=20,22$) and two spatial directions ($u=1,7$), we represent the density of occupied edges as function of the MC time. As MC time goes on, the system recover the lost isotropy induced by the initial condition. (Bottom) Fit of the upper data for $D=22$ and $u=1$ to a double exponential $Ae^{-x/B}+Ce^{-x/D}$ obtaining $B\approx 7.37N$ and $D\approx 1.76N$.

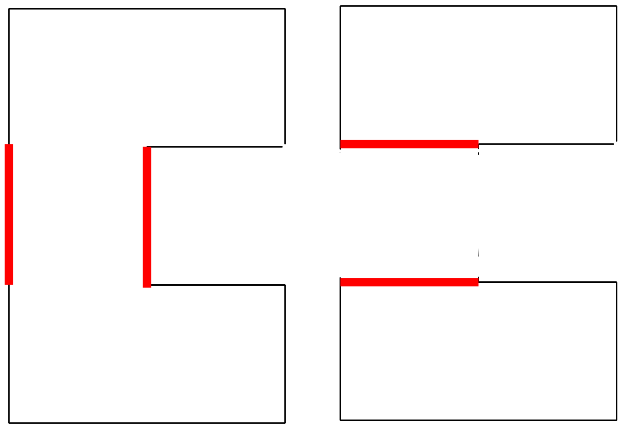

FIGURE 4.5: Illustration of the effect of a plaquette transformation on a loop of active links, as discussed in the main text, it can never open a loop. Here we present a proyection in two dimensions of a small loop of active links (in lines) in the hypercube, before and after applying a plaquette transformation represented by thick red lines.

follows. Let us imagine a walk over the closed path. On the very first step, the probability that the chosen link is present is z/D, whereas in the following step the probability of finding the link is $(z-1)/(D-1)$ in the limit of large D (since one of the z links available at the present site was already used to get there). This estimate implicitly assumes that the occupancy of different links is statistically independent. The independency approximately holds for large D and becomes exact in the $D \to \infty$ limit, where occupied links form a diluted set. At this point, the estimate of the number of paths of any given fixed length in the large D limit is analogous to the one perfomed for the random-connectivity case but changing the probability of active link. In other words, one finds that, in the fixed connectivity case, the number of closed loops of a given length per site also decays at least as $\mathcal{O}(1/D^2)$.

In addition to the above considerations, we can compute numerically the probability of having graphs of a given length in our set of generated graphs for a finite dimension D. The idea is to obtain the length of the second shortest path that joins two connected nearest neighbors $i_1,\ i_2$ in the hypercube, and this we can by iterating the connectivity matrix. In fact, we consider a truncated connectivity matrix, $\tilde{n}$, that coincides with the true one, n, but for the link $i_1 - i_2$, which is deactivated: $\tilde{n}_{i_1,i_2} = \tilde{n}_{i_2,i_1} = 0$. We take a starting vector $\boldsymbol{v}^{(0)}$ with all its components set to zero but the component i_1 which is set to one. We iteratively multiply the vector by the truncated connectivity matrix, i.e. $\boldsymbol{v}^{(t)} = \tilde{n}\boldsymbol{v}^{(t-1)}$, until the i_2-th component is nonzero. The sought length is just the minimum value of t that fulfills the stopping condition.

In Figure 4.6, we compare the probabilities for the length of such paths in the random (top) and fixed (bottom) connectivity models, for different system sizes obtained by averaging over 10^4 set of graphs. In both cases, we note that the maximum of the probability shifts to larger length as D grows. We note as well that, for fixed connectivity, no tree-like graph arises.[6]

4.2.3 Ising model in the hypercube

As a first check of the model, we study numerically the Ising model on these two kinds of hypercube graphs. We will see that the random-connectivity model suffers from very strong finite size effects that makes it essentially useless for computer simulations. However, we will show that this problem is origined precisely in the randomness on the connectivity, and then, the cure is as simple as to fix the connectivity.

The Ising model is simpler than the spin glass. The interaction now is always ferromagnetic, i.e. $J_{x,\hat{\mu}} = 1$, and thus the randomness is only introduced through the connectivity matrix $n_{x,\hat{\mu}}$. Besides, as explained in Appendix A.1, one can obtain many analytical results for this model, always under the Bethe approximation. For this reason, the Ising model is here a perfect benchmark to study the performance of these newly introduced random graphs, as measured by the magnitude of finite

[6] We say that a graph is a tree-graph if, once the link between two neighboring spins is removed, there is no way of joining them following any other path.

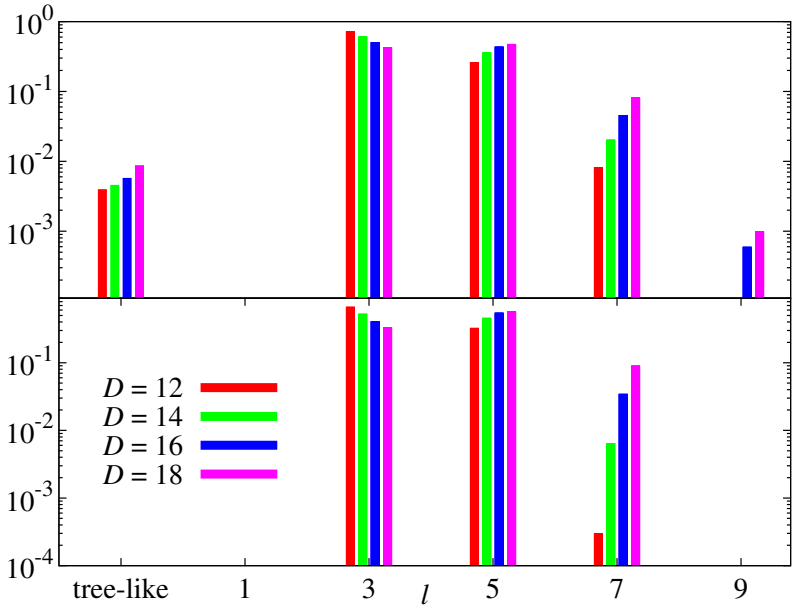

FIGURE 4.6: Probability distribution function of the length of the *second shortest* path joining nearest-neighbors in hypercubes of random-connectivity (**top**) or fixed-connectivity (**bottom**). For both pannels, the average connectivity is $z = 6$ and several system dimensions have been considered. Lines have been slightly displaced in order to help the visualization. Mind that the vertical axis is shown in logarithmic scale.

size effects.

4.2.3.1 Simulation details

For this study, we run simulations using parallel tempering [Huk96] for the temperature updates, and the spin updates (at constant temperature) is done with the cluster algorithm [Ami05]. Thermalising a ferromagnet is easy, however we use parallel tempering to correlate the measurements at different temperatures within the same sample. This correlation helps us to reduce the error when averaging over disorder.

We diplay in Tables 4.1 and 4.2 the relevant simulation parameters for the study in the random-connectivity and the fixed connectivity graphs respectively. We include the number of temperatures N_T simulated in parallel for each dimension, the number of samples N_{samples}, and the time expended for each sample N_t. Time lengths are written in terms of an elementary Monte Carlo step, defined here as the combination of one cluster update and one single tempering update.

D	N_T	$1/T_{\min}$	$1/T_{\max}$	N_{samples}	N_t^{sim}	N_t^{term}
6	6	0.135	0.275	1000	1000	1000
8	7	0.151	0.247	1000	1000	1000
10	6	0.171	0.211	1000	1000	1000
12	10	0.172	0.208	1000	1000	1000
14	10	0.171	0.189	1000	1000	1000
16	12	0.175	0.185	1000	1000	1000
18	19	0.1735	0.1825	665	1000	1000

TABLE 4.1: Technical data for the simulation of the Ising model in random-connectivity graphs.

D	N_T	$1/T_{\min}$	$1/T_{\max}$	N_{samples}	N_t^{sim}	N_t^{term}
6	6	0.135	0.275	1000	1000	1000
7	4	0.151	0.247	1000	1000	1000
8	7	0.151	0.247	1000	1000	1000
9	7	0.1545	0.247	1000	1000	1000
10	6	0.19	0.24	1000	1000	1000
11	6	0.19	0.22	1000	1000	1000
12	11	0.19	0.235	1000	1000	1000
13	9	0.184	0.2175	1000	1000	1000
14	14	0.185	0.2175	1000	1000	1000
15	8	0.195	0.21	1000	1000	1000
16	19	0.185	0.215	1000	1000	1000
17	8	0.1996	0.2057	1000	1000	1000
18	17	0.2	0.21	1000	1000	1000

TABLE 4.2: Technical data for the simulation of the Ising model in fixed-connectivity graphs.

4.2.3.2 Determination of the critical point

The final aim of this section, is to reproduce numerically the critical point obtained in Appendix A.1 with the Bethe approximation for the two kinds of graphs: the random connectivity,

$$K_c(D) = \tanh^{-1}\left(\frac{D}{z\,(D-1)}\right). \tag{4.12}$$

and the fixed connectivity graph

$$K_c = \tanh^{-1}\left(\frac{1}{z-1}\right). \tag{4.13}$$

One must recall that these two expressions are only exact in the $D \to \infty$ limit, where the Bethe approximation becomes exact. The presence of short loops, as the ones presented in Figure 4.6 should introduce corrections of $\mathcal{O}(D^{-2})$ for finite dimensions, i.e. logarithmic corrections in N. As mentioned before, we expect the random connectivity model to display as huge D-corrections, to become completely useless for numerical purposes. Indeed, not only suffers from finite-loops corrections, but the Bethe approximation itself leads to a $D-$dependent expression for K_c (4.12).

With this purpose, we compute the Binder cumulant. We already introduced this quotient in (3.60) for a spin glass. Now, since the order parameter in a ferromaget is the magnetization

$$\mathcal{M} = \sum_i s_i, \tag{4.14}$$

instead of the overlap, we define the Binder parameter as the dimensionless quotient

$$B = \frac{\langle \mathcal{M}^4 \rangle}{\langle \mathcal{M}^2 \rangle^2}. \tag{4.15}$$

As discussed then, the expectation value for the Binder parameter is 3 in the disordered paramagnetic phase. At variance with the spin glass, the expectation value for the ferromagnetic phase is estricly 1. We can use the cross over between these two limiting behaviors to obtain numerically $K_c(D)$.

We show in Figure 4.7 the dependence of the Binder cumulant with the temperature for different system sizes. As predicted, it drops from 3 to 1 when K increases (K is proportional to the inverse temperature) but the point at which the fall occurs displaces a lot with the system size, which makes difficult to obtain K_c^∞ by means of crossings between curves, as it is normally done using a finite size scaling approach [Ami05]. Instead, as an alternative, we compute the average of two values of K where $B(K, D)$ takes prescribed values. We refer to this estimate as K_c^{mp}. This $K_c^{\text{mp}}(D)$ tends to the desired K_c^∞ when $D \to \infty$. We present the results obtained for the midpoint defined as

$$K_c^{\text{mp.}}(D) = \frac{B^{-1}(1.2) + B^{-1}(2.4)}{2}, \tag{4.16}$$

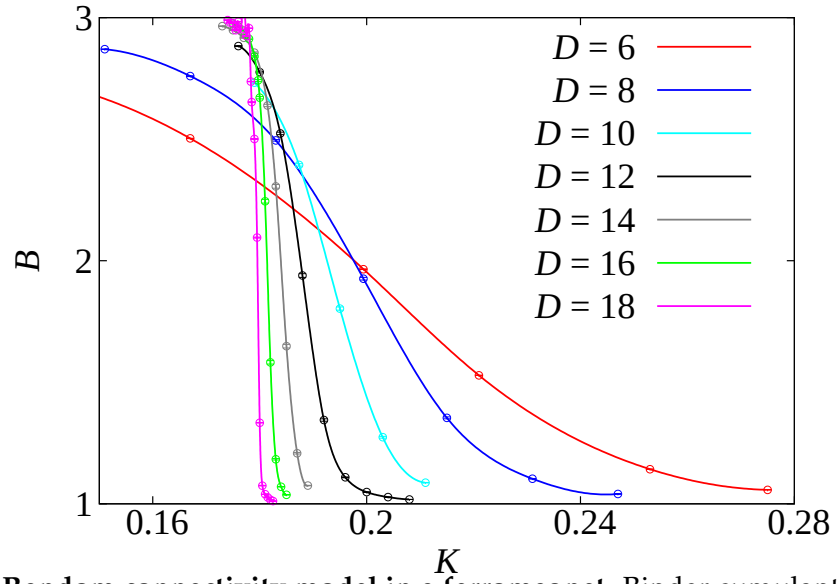

FIGURE 4.7: **Random connectivity model in a ferromagnet**. Binder cumulant as function of K for different D. The lines are interpolated from the simulation points using cubic spline.

D	K_c^{Bethe}	K_c^{mp}
6	0.20273	0.216(2)
8	0.19283	0.207(5)
10	0.18735	0.195(2)
12	0.18386	0.1889(15)
14	0.18145	0.1846(8)
16	0.17969	0.1818(4)
18	0.17834	0.17967(3)

TABLE 4.3: **Random connectivity model in a ferromagnet**. Comparison of the analytical estimates of $K_c(D)$, eq. (4.12), with the numerical estimate $K_c^{\text{mp}}(D)$, eq. (4.16).

in Table 4.3 together with the analytical expectation values obtained by means of the Bethe approximation (4.12). As we previously discussed, one should not expect to have compatible values for finite values of D, since both calculations are plagued by finite size corrections, they should only be equal in the $D \to \infty$ limit. Indeed, the higher D, the better mutually agreement is.

In order to study more quantitatively this convergence, we fit the $K_c^{\text{mp}}(D)$ values to

$$K_c(D) = K_c^{\infty} + \frac{a_1}{D} + \frac{a_2}{D^2} + \frac{a_3}{D^3}, \tag{4.17}$$

keeping K_c^{∞} fixed. We summarize the results in Table 4.4. The conclusion of this fit, though expected, is devastating. The large coefficients a_1 and a_2 show how important the finite size corrections are.

Clearly, the random connectivity hypercube is a disaster even for the Ising

$D_{\min}$	χ^2/dof	a_1	a_2	a_3
6	0.53/4	0.073(13)	2.9(3)	-9.8(15)
8	0.0313/3	0.117(7)	1.6(2)	-0.7(13)
8	0.0342/4	0.1208(15)	1.53(3)	0

TABLE 4.4: **Random connectivity model in a ferromagnet**. Results of the fits of $K_c^{\text{mp}}(D)$ to $K_c^{\text{mp}}(D) = K_c^\infty + \frac{a_1}{D} + \frac{a_2}{D^2} + \frac{a_3}{D^3}$. K_c^∞ was fixed to the exact value $K_c^\infty = 0.16824\ldots$. We include in the fit all data with $D \geq D_{\min}$. In the last row, $a_3 = 0$ has been taken.

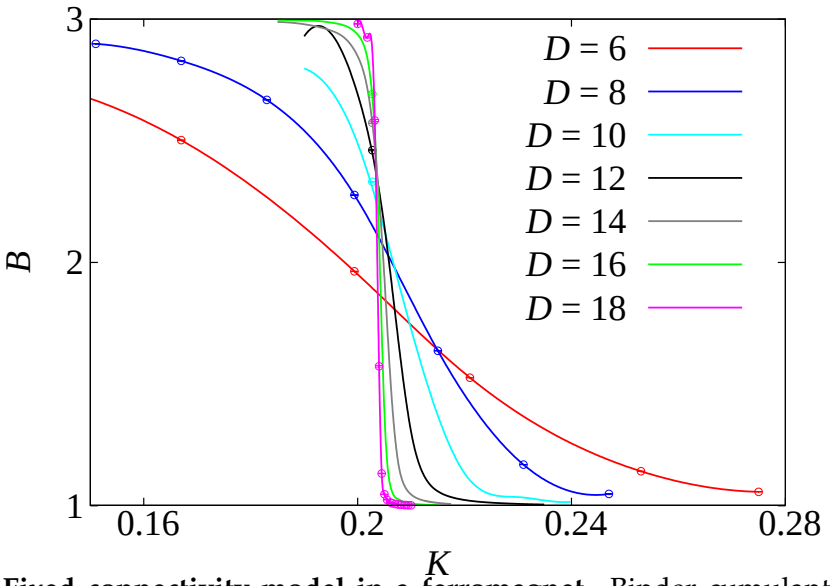

FIGURE 4.8: **Fixed connectivity model in a ferromagnet**. Binder cumulant as a function of K for different dimensions. The lines are interpolated from the simulation points using cubic spline.

model, so we will not consider it to study the SG, where randomness makes a lot more difficult to control finite size effects.

On the contrary, if we perform exactly the same study but on the fixed connectivity graph, we obtain more promising results. Indeed, we plot in Figure 4.8 the Binder cumulant as a function of K. The finite sizes effects are reduced drastically.

In this case, we may easily compute the crossings between two consecutive curves in B, and thus obtain the the crossing estimator $K_c^{D,D+1}$. We expect a scaling ($K_c^\infty = 0.20273\ldots$)

$$K_c(D) = K_c^\infty + \frac{c_2}{D^2} + \frac{c_3}{D^3} + \cdots . \tag{4.18}$$

Indeed, as discussed previously, the contribution of closed loops (plaquettes or larger) are of order $1/D^2$. Hence, the linear term in $1/D$ found for the random connectivity model arises exclusively from the Bethe equation (4.12). These expectations are confirmed by our numerical data shown in Figure 4.9. Note that while the random connectivity model did not reach the asymptotic $1/D$ regime even for

$D_{\min}$	χ^2/dof	c_2	c_3
12	6.41/4	0.07(2)	1.3(3)
13	0.92/3	0.114(14)	0.66(20)
14	0.40/2	0.136(18)	0.3(3)

TABLE 4.5: **Fixed connectivity model in a ferromagnet**. Results of the fits of $K_c^{D,D+1}$ to $K_c^\infty + \frac{c_2}{D^2} + \frac{c_3}{D^3}$. K_c^∞ is fixed to the exact value $K_c^\infty = 0.20273\ldots$. We include in the fit all data with $D \geq D_{\min}$.

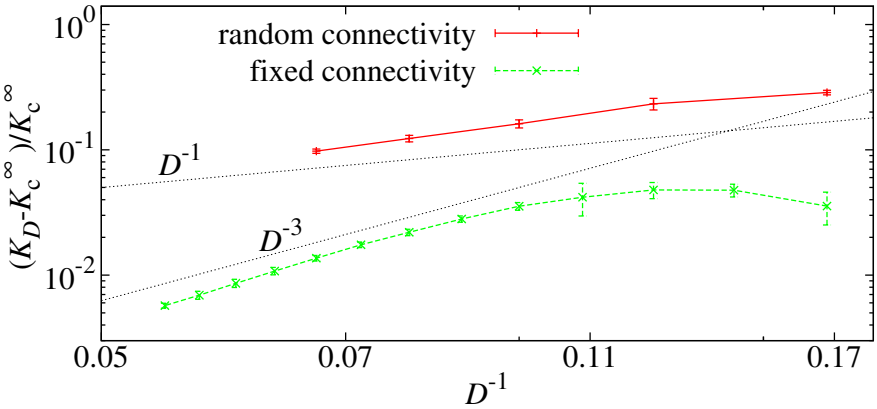

FIGURE 4.9: Comparison of the finite volume effects at the critical point in K_c^D for the ferromagnetic Ising model, both in the random **(red circles)** and fixed **(green circles)** connectivity hypercubes. As a guide to the eye, we have included two different scalings with D.

$D = 18$, for fixed z the asymptotic $1/D^2$ regime is reached, although strong $1/D^3$ corrections are visible for $D < 14$. This qualitative picture on scale corrections is confirmed by a χ^2 test in Table 4.5.

A summary of our efforts is shown in Figure 4.9, where we plot the dependency of the critical point with D for the ferromagnetic Ising model for the two kinds of graphs. As anticipated several times already, the random connectivity model suffers very important finite volume corrections which make it essentially useless for numerical studies. The problem is solved using fixed connectivity hypercubes instead, where the finite volume effects are only caused by the residual presence of short closed loops. From now on, we will only consider this second kind of graphs.

4·3

Spin glass in the fixed connectivity hypercube

After this last short preliminary study in the Ising model, we can be confident about the introduced graphs (and its generation algorithm). Indeed, numerical

results were compatible with the expected analytical determinations of the critical point at $D \to \infty$. Furthermore, now we know that we should only consider fixed-connectivity hypercubes if we want to reduce the finite size effect as much as possible. Thus, we are ready to move to our final interest, the numerical study of a spin glass on these graphs.

In particular, we will consider a diluted spin glass where couplings can take only two possible values $J_{x,\hat{\mu}} = \pm 1$, randomly chosen with probability $1/2$ each. Since we only consider a fixed connectivity graph, each spin is connected with exactly 6 neighbors (among the D possible nearest neighbors).

The structure of this section will be the following. We will begin in Section 4.3.1 with a description of the used numerical methods and a discussion on the particularities of the spatial correlation functions in the hypercube in Section 4.3.2. Later on in Section 4.3.3, we will study the equilibrium behavior (where we have analythical predictions to compare with), to end up with the final goal of this chapter, the nonequilibrium study in Section 4.3.4

4.3.1 Numerical Methods

All the variables involved in the Hamiltonian (4.6), the spins and the couplings, are binary. They can thus be coded in the bits of a computer word, making this model highly parallelizable. In fact, we implement the so-called *Multi-spin Coding*: we simultaneously codify 64 systems in one single 64 bits computer word. Besides, being the nodes of the lattice distributed on an unit hypercube, also sites can be written in term of bits, see the appendix Section B.1.2 for a detailed definition. For the computational point of view, it is a challenge to write a simulation program that takes fully benefit of the parallelization of bitwise operations. For this reason, we have included a section in the Appendix B where we explain in detail how to do it.

Following this approach, one can simulate 64 samples in practically the same time it would take to simulate just one. However, in order to keep the parallelism, all the samples in the same run share the same connectivity matrix $n_{x,\hat{\mu}}$ (and differ only in the configuration of couplings $J_{x,\hat{\mu}}$). With this common matrix, we find errors which are ~ 7 times smaller than those obtained with one single sample per matrix. This should be compared with the error reduction by a factor 8, expected if 64 truly independent samples were simulated. Our program needs 0.29 ns/*spin-flip* in an Intel i7 at 2.93GHz (in Ref. [Haso8a] they report ~ 1.2 ns/*spin-flip* on an Opteron at 2.0 GHz, for the simulation of the $D = 3$ EA model in the cubic lattice)[7].

In a nonequilibrium dynamical study such as ours, one computes both one-time and two-times quantities, see Sect. 3.6.1. The calculation of two-times quantities implies the storage on disk of intermediate configurations. Disk capacity turned out to be the main limiting factor for the simulation. For this reason, we have worked in parallel with two program versions: one valid for measuring quanti-

[7]Note that we are considering the $z = 6$ case. Then, the core of the Metropolis algorithm is equivalent to the $D = 3$ EA model in a cubic lattice.

ties at one and two times and another restricted to the computation of one-time quantities.

We have computed two-time quantities at temperature $T = 0.7T_c$, on systems with $D = 16, 18, 20$ and 22. The number of simulated samples were 8×64 samples for each system size (hence, for self-averaging quantities (see Section 3.4.2) the statistical quality of our data grow with D).

Besides, since this new model requires intensive testing, we have computed *equilibrium* one-time quantities at $T/T_c = 0.95, 0.97, 0.99, 1, 1.1, 1.2, 1.3$ and 1.4. The system sizes were again $D = 16, 18, 20$ and 22. The number of simulated samples was 128×64 samples per temperature (at T_c we computed 256×64 samples).

4.3.2 Spatial correlation functions in the hypercube

As mentioned in the objectives of this work, the goal of this proyect was to define a MF model that allows to approach the domain growth in spin glasses. Indeed, we discussed in Section 4.2 that the hypercube geometry let us to define a distance based on the minimum number of edges one needs to cross to join two nodes. Then, as in the 3-D EA model, we can use the standard spatial correlation functions defined in Section 3.6.1.3 but using the postman metrics instead of the Euclidean one. However, even being basically the same definitions, the hypercube introduces certain particularities that will be discussed in this section.

The main problem here appears when averaging $c_4(\boldsymbol{r}, t_w)$ defined in (3.53) over all the displacements $\boldsymbol{r} = r$. In the hypercube, at variance with the 3-D EA model, the number of spins separated by r depends strongly on the precise value of r. Indeed, a short calculation tells us that it is given by $N_r = \binom{D}{r}$. As a consecuence, when we consider the average

$$C_4(r, t_w) = \frac{1}{N_r} \sum_{\boldsymbol{r}, |\boldsymbol{r}|=r} c_4(\boldsymbol{r}, t_w)\,, \tag{4.19}$$

see Figure 4.10, $C_4(r, t_w)$ does not present a limiting behavior with D for a given t_w. We can get a clue by looking at $\chi_{SG}(t_w)$ (defined in (3.49)), see Figure 4.11, which does reach a thermodynamic limit. It was discussed in (3.55) that $\chi_{SG}(t_w)$ is nothing but the integral of $C_4(r, t_w)$ with a Jacobian that here is precisely N_r, that is $\binom{D}{r}$. Then, it seems reasonable to define the following spatial correlation function instead:

$$\hat{C}_4(r, t_w) = \sum_{\boldsymbol{r}, |\boldsymbol{r}|=r} c_4(\boldsymbol{r}, t_w)\,. \tag{4.20}$$

We can see that $\hat{C}_4(r, t_w)$ does reach the high-D limit, Figure 4.12, at least for short t_w. Besides, in the paramagnetic phase, it is possible to compute analytically $\hat{C}_4(r, t_w)$, see Appendix A.2, taking first the limit $t_w \to \infty$ and making afterwards $D \to \infty$. The resulting correlation function, which is only valid in the paramagnetic phase, is a simple exponential. Hence, both the equilibrium and the nonequilibrium computations, suggest that one should focus on $\hat{C}_4$ rather than on C_4.

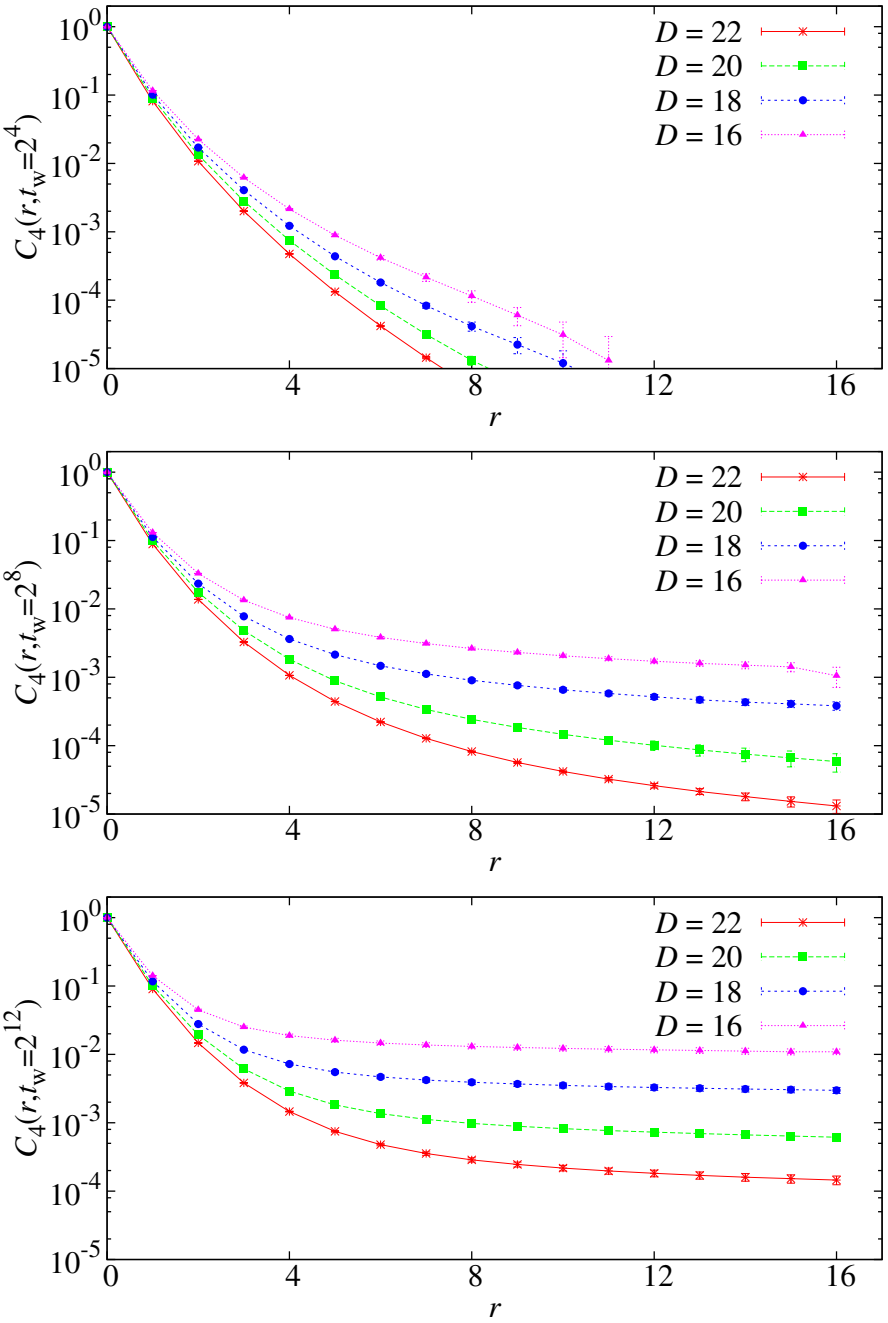

FIGURE 4.10: $C_4(r, t_w)$, (4.19), for (top) $t_w = 2^4$, (center) $t_w = 2^8$ and (bottom) $t_w = 2^{12}$, and different system sizes, $N = 2^D$, at $T = 0.7T_c$.

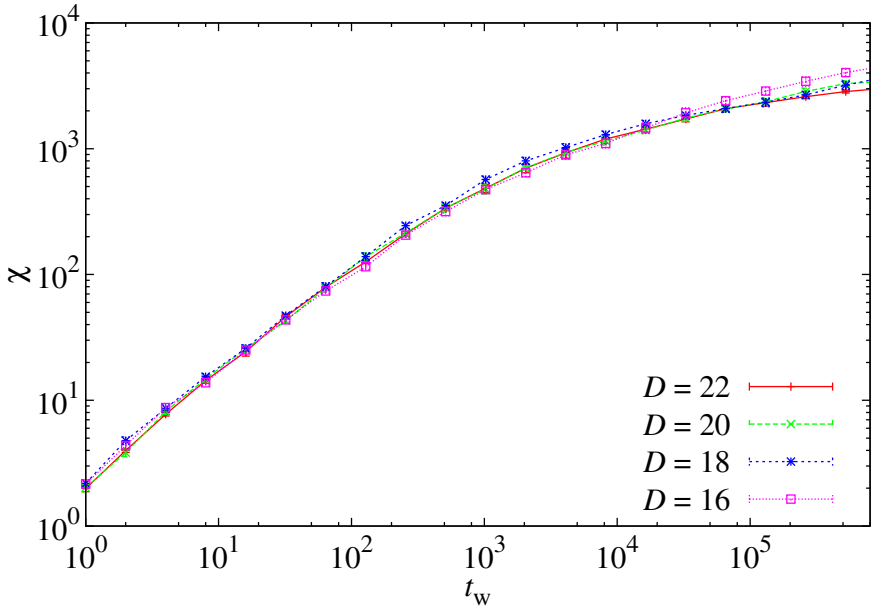

FIGURE 4.11: SG susceptibility a $T = 0.7T_c$ as function of t_w for different system sizes, $N = 2^D$.

We note in Figure 4.12, that in the SG phase, $\hat{C}_4$ is non monotonically decreasing with r, but rather presents a maximum. This maximum moves to bigger r with t_w, then, the system has a characteristic length that increases with time. Thus, we can estimate the coherence length, by means of the integral estimator $\xi_{0,1}(t_w)$:

$$\xi_{0,1}(t_w) = \frac{\int_0^\infty dr\ r\ \hat{C}_4(r, t_w)}{\int_0^\infty dr\ \hat{C}_4(r, t_w)}\,. \tag{4.21}$$

When computing numerically this $\xi_{0,1}(t_w)$, we only summed up to certain cutoff in order to avoid meaningless noise in the determination of $\hat{C}_4(r, t_w)$. Our actual criterium was to sum up contributions while $\hat{C}_4(r, t_w)$ was higher than 3 times its error (obtained with the fluctuations between samples). A major advantage of $\xi_{0,1}$ over more heuristic definitions of the coherence length, is that it is computed from self-averaging quantities (see details in [Belo8a, Belo9], we note that, in this work, we have not tried to estimate the contribution to the integrals by the noise-induced long distance cutoff).

The existence of such a characteristic length is the main advantage of the hypercube model over other MF models.

In addition to this correlation function in the real space, we will also be interested in its behavior in the Fourier space. We define the Fourier transform in the standard way. Our wave vectors are $\boldsymbol{k} = \pi(n_1, n_2, \ldots, n_D)$ with $n_i = 0, 1$. The propagator is

$$G(\boldsymbol{k}, t_w) = \sum_{\boldsymbol{r}} e^{i\boldsymbol{k}\cdot\boldsymbol{r}} c_4(\boldsymbol{r}, t_w). \tag{4.22}$$

In particular, $G(0, t_w) = \sum_{r=0}^{D} \hat{C}_4(r, t_w) = \chi_{SG}(t_w)$.

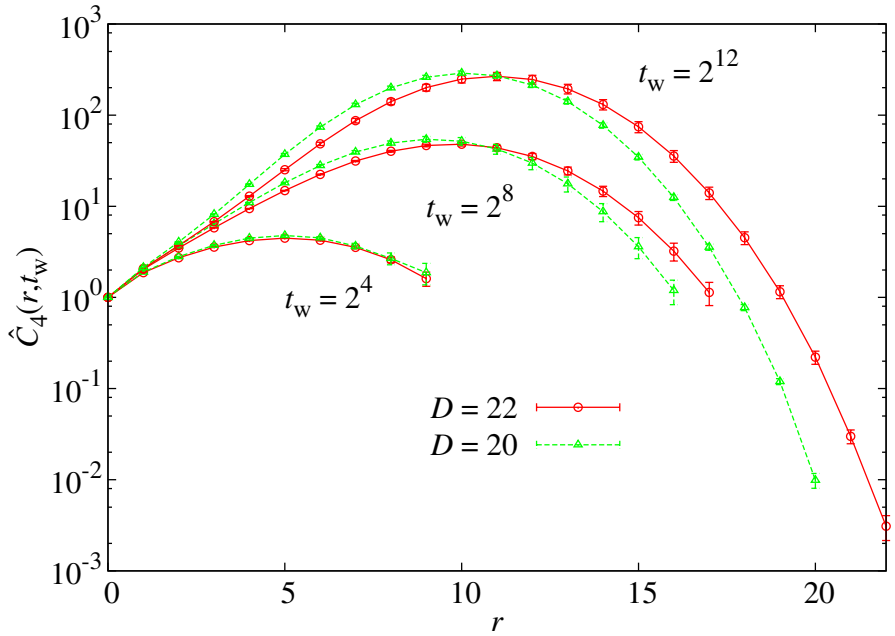

FIGURE 4.12: $\hat{C}_4(r,t_w)$, (4.20), for $D=20$ and 22 for $t_w=2^4$, 2^8 and 2^{12} at $T=0.7T_c$. This has to be compared with the behavior of $C_4(r,t_w)$, Figure 4.10.

Now, because of the disorder average, $c_4(\boldsymbol{r},t_w)$ is only a function of $r=|\boldsymbol{r}|$ (postman metrics). It follows from (4.25) that $G(\boldsymbol{k},t_w)$ actually depends only on $k=|\boldsymbol{k}|$.

The rotational invariance allows us for a major simplification [Paro6][with a slight abuse of notation, we write $c_4(r,t_w)$ rather than $c_4(\boldsymbol{r},t_w)$],

$$G(k,t_w) = \sum_{r=0}^{D} K_r(D,k)\; c_4(r,t_w), \tag{4.23}$$

where $K_r(D,k)$ are the *Krawtchouk polynomials*:

$$K_r(D,k) = \sum_{m=\max(0,r+k-D)}^{\min(k,r)} (-1)^m \binom{k}{m}\binom{D-k}{r-m}. \tag{4.24}$$

It is interesting to point out that neither $K_r(D,k)$ nor $c_4(r,t_w)$ have a thermodynamic limit, while $G(k,t_w)$ does so. In fact, when $k=0$, $K_r(D,0)=\binom{D}{r}$ is diverging. Thus, we can rewrite (4.23) in terms of quantities with a well defined limit, i.e.

$$G(k,t_w) = \sum_{r=0}^{D} \frac{K_r(D,k)}{\binom{D}{r}}\; \hat{C}_4(r,t_w). \tag{4.25}$$

4.3.3 Equilibrium Results

Since the present work is the first study ever made of a EA model on a fixed connectivity hypercube it is necessary to make a few consistency checks. Equilibrium

T	$\chi(T)_{D=\infty}$	$\chi(T)_{D=20}$	$\chi(T)_{D=22}$
$1.4T_c$	2.4497...	2.41(3)	2.44(3)
$1.3T_c$	3.0176...	2.98(4)	2.98(4)
$1.2T_c$	4.1650...	4.08(6)	4.10(7)
$1.1T_c$	7.6344...	7.11(13)	7.43(11)
T_c	∞	26(2)	98(7)

TABLE 4.6: Comparison between the SG susceptibility in large D limit for the paramagnetic phase, (4.26), and numerical results for $D = 20, 22$.

results are most convenient in this respect, since we have analytical computations (valid only for the large D limit) to compare with.

We will briefly study the spatial correlations in the paramagnetic phase. In addition, we will check, by approaching to T_c from the SG phase, that the SG transition does lie on the predicted T_c, (4.11).

4.3.3.1 Paramagnetic Phase

Our very first check will be the comparison between the Monte Carlo estimate of the SG susceptibility defined in (3.59) (at finite D) with the analytical computation for infinite D:

$$\chi(K) = 1 + \frac{z \tanh^2 K}{1 - (z-1)\tanh^2 K}, \tag{4.26}$$

see Appendix A.2. Our results are presented in Table 4.6. We see that finite size effects increase while approaching T_c. For our larger system, $D = 22$, the susceptibility significantly deviates from the asymptotic result only in the range $T_c < T < 1.1T_c$.

After the fast convergence to the large D limit observed in the SG susceptibility, the results for $\hat{C}_4$ are a little bit disappointing. In Figure 4.13 we display $\hat{C}_4(r, D) - \hat{C}_4(r, \infty)$ as a function of r ($\hat{C}_4(r, \infty)$ is obtained using (A.37) in Appendix A.2). We can see that finite size effects become more important once one approaches T_c. Besides, finite D corrections as a function of r oscillate between positive and negative values. This is not surprising: the finite D corrections to the susceptibility are very small, and they are nothing but the integral under these curves. More quantitatively, we see in Table 4.7 that the corrections with D for $r = 1, 2$ are $\mathcal{O}(D^{-1})$. Indeed, the path counting arguments in Appendix A.2 are plagued by corrections of $\mathcal{O}(D^{-1})$.

4.3.3.2 SG phase

In the SG phase, our test has been restricted to a check of (4.11), that predicts a SG phase transition for the high-D limit. With this aim, we compute the Binder cumulant, $B(T)$, defined in (3.60), nearby T_c. For all $T < T_c$, we expect $B(T) < 3$

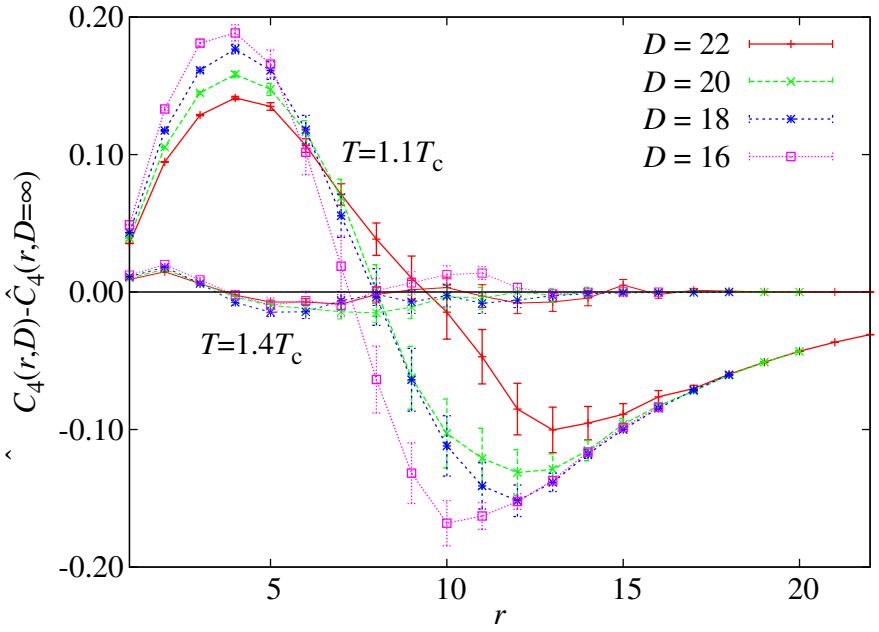

FIGURE 4.13: Difference between the numerical and analytical spacial correlation function for different system sizes at two temperatures $T = 1.1T_c$ and $T = 1.4T_c$.

	$r = 1$		$r = 2$	
D	$T = 1.1T_c$	$T = 1.4T_c$	$T = 1.1T_c$	$T = 1.4T_c$
16	0.783(6)	0.198(5)	2.130(18)	0.320(12)
18	0.779(4)	0.201(3)	2.115(11)	0.327(7)
20	0.784(2)	0.202(2)	2.109(6)	0.332(4)
22	0.7776(12)	0.2006(9)	2.083(4)	0.324(2)

TABLE 4.7: D times the difference between $\hat{C}_4(r)$, for finite D and infinite D (using (A.37) in Appendix A.2), as computed for $r = 1, 2$. The absence of any D evolution evidences finite-D corrections of order $1/D$.

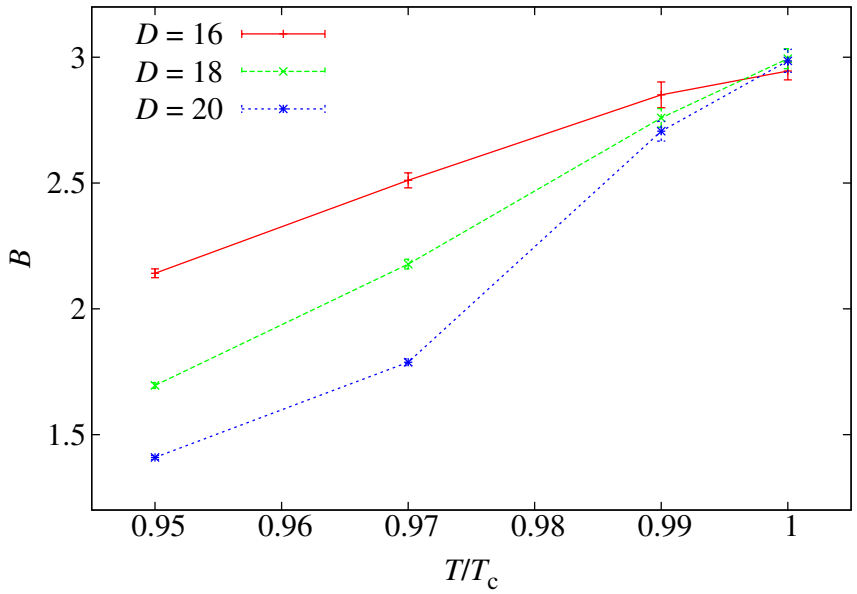

FIGURE 4.14: Equilibrium values of the Binder cumulant, (3.60), for several system sizes, as function of the temperature in units of the exact asymptotic value of T_c, (4.11), in the SG phase.

for large enough D. As we show in Figure 4.14, $B(T)$ decreases with T and shows sizeable finite size effects. In fact, at $T = 0.99T_c$, we need to simulate lattices as large as $D = 20$ to find values below 3. Right at T_c, the Gaussian value $B(T) = 3$ is found for all the simulated sizes.

4.3.4 Nonequilibrium Results

In this section we will address the main features of the nonequilibrium dynamics obtained in our largest system, $D = 22$. The issue of finite D corrections will be postponed to Sect. 4.3.7.

4.3.4.1 The structure of isothermal aging

We widely presented evidences of isothermal aging in experiments in Section 3.3.1. Now we approach it in numerical simulations. The picture of isotermal aging dynamics in MF models of SG behavior was largely drawn in [Cug94] (see also [You97]). The dynamics is ruled by an infinite number of *time-sectors*:

$$C(t, t_w) = \sum_i f_i \left(h_i(t_w)/h_i(t + t_w) \right), \tag{4.27}$$

where $C(t, t_w)$ is the two-time correlation function introduced in (3.51). The scaling functions f_i are positive, monotonically decreasing and normalized, i.e. $1 = \sum_i f_i(1)$. The unspecified functions h_i are such that, in the large t_w limit, $h_i(t_w)/h_i(t + t_w)$ is 1 if $t \ll t_w^{\mu_i}$, while it tends to zero if $t \gg t_w^{\mu_i}$. In other words, the decay of

C between values C_i and C_{i+1} is ruled by the scaling function f_i and takes place in the *time-sector* $t \sim t_{\rm w}^{\mu_i}$.

This picture is radically different to the *Full Aging* often found both in experiments (recall Figure 3.2) and in $3D$ simulations. A full aging dynamics is ruled only by two sectors of time, $\mu_i = 0, 1$. Nevertheless, recent experimental studies [Keno6] show that full aging is no longer fulfilled for $t \gg t_{\rm w}$. Probably more time-sectors must be considered to rationalize these experiments.

However, (4.27) is probably an oversimplification, since the spectrum of exponents μ_i might be continuous. An explicit realization of this idea was found in the critical dynamics of the trap model [Bero2b], where the correlation function behaves for large $t_{\rm w}$ as

$$C(t, t_{\rm w}) = f\left(\alpha(t, t_{\rm w})\right) , \quad \alpha(t, t_{\rm w}) = \log t / \log t_{\rm w} . \tag{4.28}$$

Again, the scaling function f is positive and monotonically decreasing. Clearly enough, in the limit of large $t_{\rm w}$ and for any positive exponent μ, if $t = A t_{\rm w}^{\mu}$, the correlation function takes a value that depends only on μ, no matter the value of the amplitude A.

As expected, $C(t, t_{\rm w})$ is clearly not a function of $t/t_{\rm w}$ in our model, see Figure 4.15. On the contrary, data seem to tend to a constant value when $t_{\rm w} \to \infty$ in any finite range of the variable $t/t_{\rm w}$. This is precisely what one would expect in a time-sectors scheme. On the other hand, if we try (without any supporting argument) the Bertin-Bouchaud scaling, (4.28), see Figure 4.16, the data collapse is surprisingly good. Therefore, the nonequilibrium dynamics in the SG phase seems ruled by a, not only infinite but continuous, spectrum of time-sectors.

We note *en passant* that the scaling (4.28) is ultrametric only if the scaling function reaches a constant value for all $\alpha(t, t_w) > 1$, for details see Appendix C. In fact, dynamic ultrametricity is a geometric property [Cug94] that states that for all triplet of times $t_1 \gg t_2 \gg t_3$, one has in the limit $t_3 \to \infty$:

$$C(t_1 - t_3, t_3) = \min\left\{C(t_1 - t_2, t_2), C(t_2 - t_3, t_3)\right\} . \tag{4.29}$$

Finding dynamical ultrametricity in concrete models has been rather elusive up to now. An outstanding example is the critical trap model [Bero2b], where $f(\alpha > 1) = 0$. It is amusing that the trap model is *not* ultrametric from the point of view of the equilibrium states, as discussed in Section 3.4.3. Thus, the casual connections between static and dynamic ultrametricity are unclear to us. At any rate, since our scaling function in Figure 4.16 does not show any tendency to become constant for $\alpha(t, t_w) > 1$, we do not find compelling evidences for dynamic ultrametricity in this model.

We have also looked directly to the plots of $C(t_1 - t_2, t_2)$ versus $C(t_2 - t_3, t_3)$ (see Appendix C) and we have not found convincing indications for the onset of dynamical ultrametricity. In this respect, it is worth to recall similarly inconclusive numerical investigations of the Sherrington-Kirkpatrick model [Cug94, Bero0]. There are two possible conclusions:

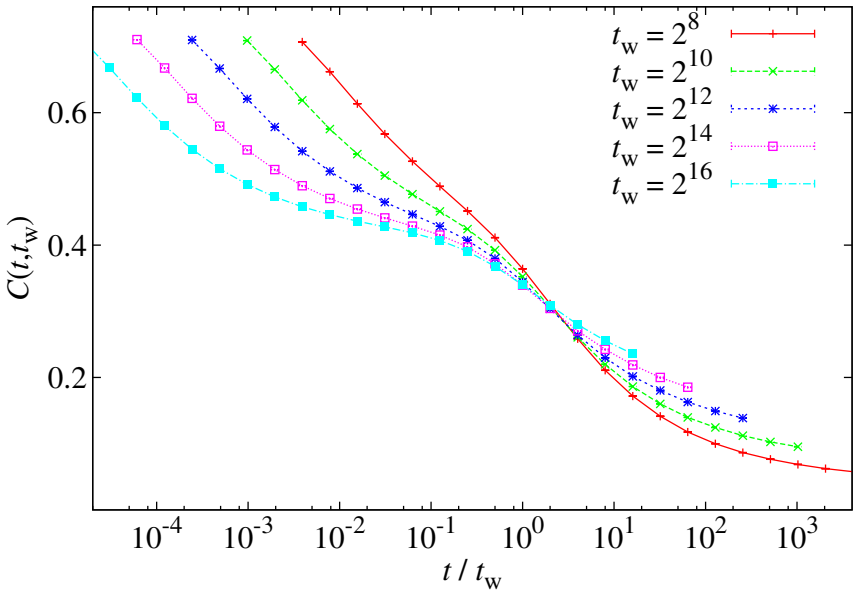

FIGURE 4.15: $C(t, t_w)$ over t/t_w for $D = 22$ and $T = 0.7T_c$.

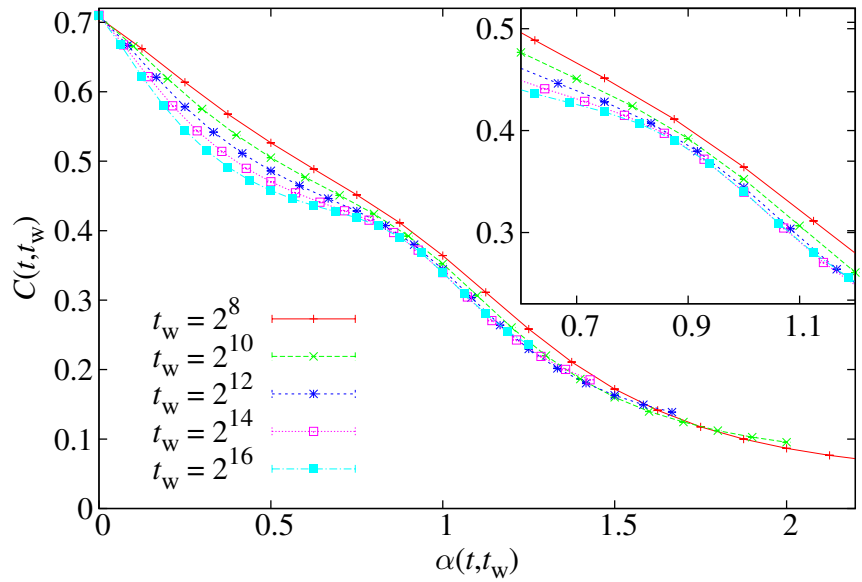

FIGURE 4.16: Same data of Figure 4.15, as a function of $\alpha(t, t_w)$, defined in (4.28). The window is a zoomed image of the central region.

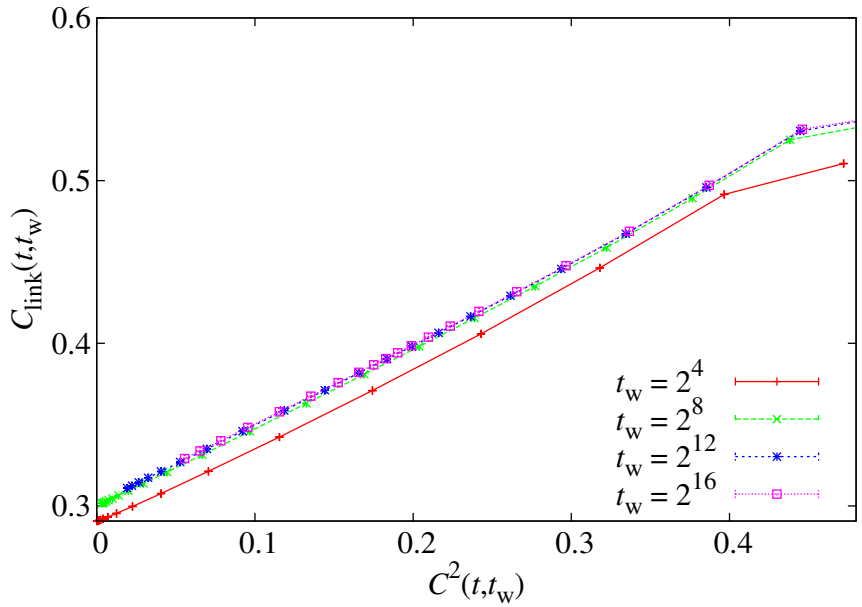

FIGURE 4.17: C_{link} over $C^2(t,t_w)$ for different t_w at $T=0.7T_c$ and for $D=22$.

1. the model does not satisfy dynamical ultrametricity in spite of the fact that it satisfies (according to the standard wisdom) static ultrametricity.

2. Dynamical ultrametricity holds but its onset is terribly slow.

Both conclusions imply that it is rather difficult to use the dynamic experimental data (or any kind of data) to get conclusions on static ultrametricity.

4.3.5 Aging in C_{link}

Just as in the 3D case [Belo8a], the aging dynamics in SG in the hypercube is a domain-growth process, see Figure 4.23. For any such process, the question of the ratio surface-volume arises. When this ratio vanishes in the limit of large domain size, as it is the case for any RSB dynamics (recall the discussion on the replica equivalence in Section 3.6.2), one expects a linear relation between $C_{\text{link}}(t,t_w)$ (defined in (3.52)) and $C^2(t,t_w)$. This is precisely what we find in Figure 4.17.

It is interesting to point out, that the linear relation found for $D = 22$ is the same one in the rest of system sizes, see Figure 4.22.

4.3.6 Thermoremanent magnetization

The experimental work indicates that for $T < 0.9T_c$, the thermoremanent magnetization follows a power law with an exponent proportional to T_c/T [Gra87]. The data obtained in JANUS for a three dimensional SG (see Figure 4.18 and [Belo9]) agree with this statement. However, the data obtained in the hypercube model does not follow such power law, neither can them be rescaled with $T \log t$.

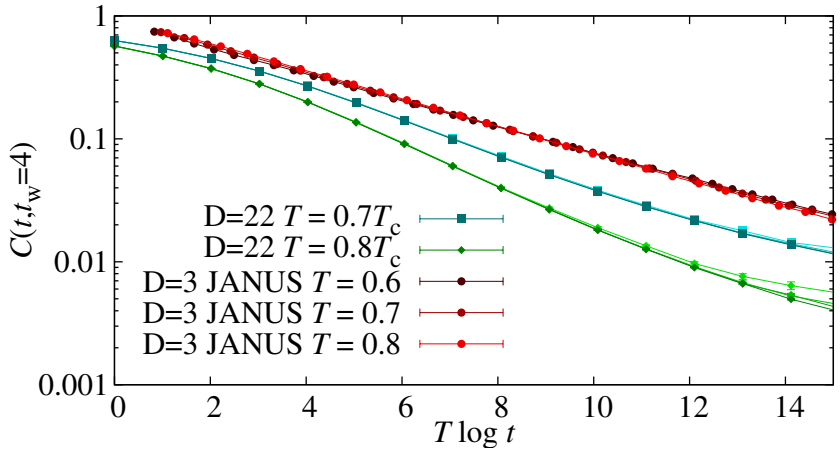

FIGURE 4.18: Thermoremanent magnetization over $T \log t$. The JANUS data (in red circles), follow a power law with an exponent $\propto 1/T$. Our results for $D = 22$ are shown in dark tonalities (lighter colors: $D < 22$).

This lack of an algebraic decay is surprising on the view of the exact results of Ref. [Par97]. Indeed, it was analytically shown there that, at T_c, the thermoremanent magnetization of the SK model decays as $t^{-5/4}$. Universality strongly suggests that the same scaling should hold for our model. Although it seems not to be the case, at the first glance, Figure 4.19—top, a closer inspection confirms our expectation. Indeed, when plotted as a function of $t^{-5/4}$, see inset in Figure 4.19—top, the thermoremanent magnetization curve has a finite non-vanishing slope at the origin. As we show in bottom panel of Figure 4.19, finite size effects do not contradict this claim. In summary, the magnetization decay for the hypercube suffers from quite strong finite time effects, but asymptotically it scales with the proper exponent, at least at T_c.

4.3.7 Nonequilibrium Correlation Functions and Finite Size Effects

The importance of finite size effects in nonequilibrium dynamics has been emphasized recently [Belo8a, Belo9]. In our case, we have encountered important size effects, both in $C(t, t_w)$, Figure 4.20, and in $\xi(t_w)$, Figure 4.23–top.

We compare in Figure 4.21 the finite D effects in $C(t, t_w)$ for two different MF models with fixed connectivity: the hypercube and a previously studied model (the random graph with connectivity $z = 6$, where each spin can interact with any other spin with uniform probability [Leuo8]). Clearly enough, the effects are much weaker in the hypercube model.

It is interesting to point out that, although the finite size effects seems to be important in $C(t, t_w)$, they are largely absorbed when one eliminates the variable t in favor of $C^2(t, t_w)$, see Figure 4.22. Hence, one of our main findings (the linear

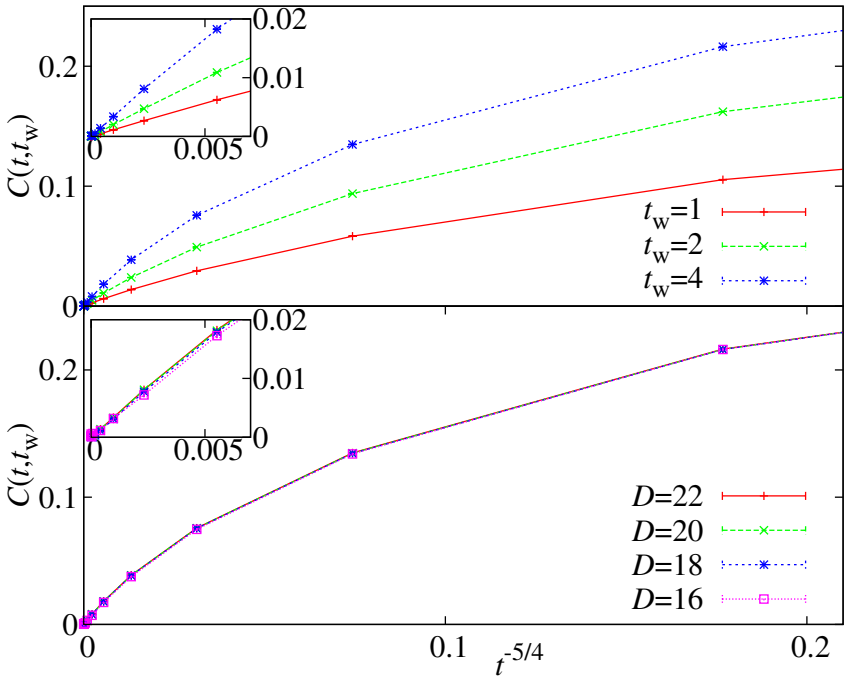

FIGURE 4.19: Thermoremanent magnetization at T_c vs. $t^{-5/4}$, for **(up)** different t_w and $D = 22$, and **(down)** different system sizes for $t_w = 4$. The two insets are close-ups of the origin.

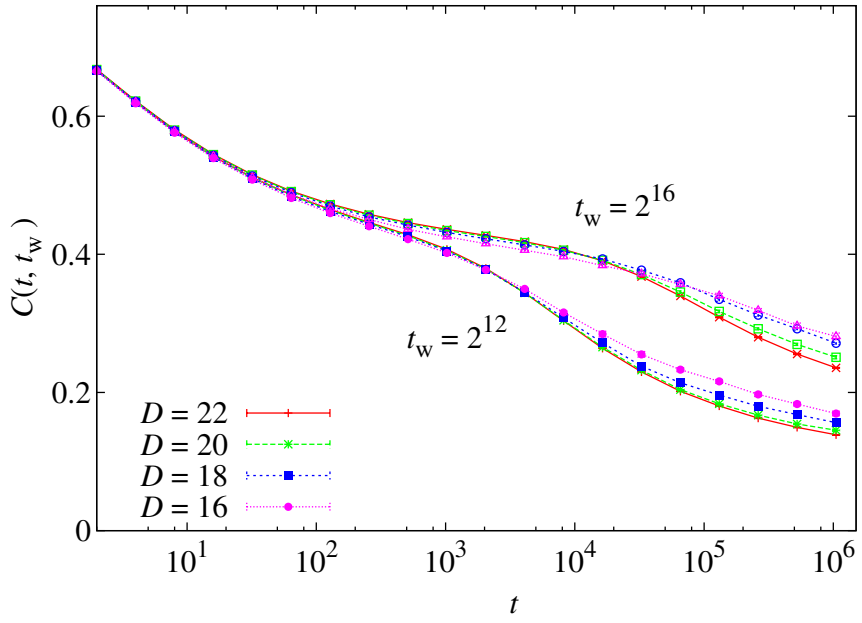

FIGURE 4.20: Finite size effects in $C(t, t_w)$ at $T = 0.7T_c$.

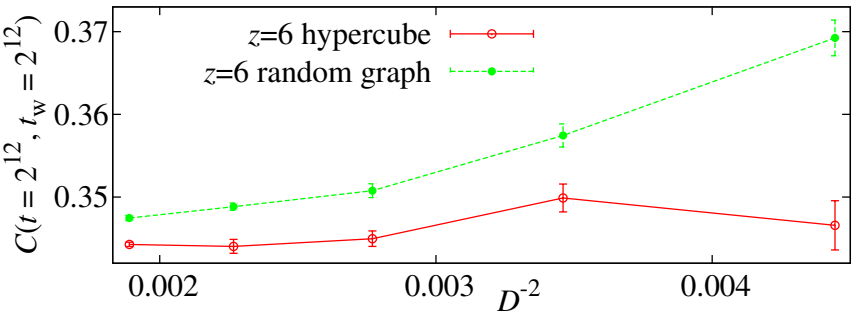

FIGURE 4.21: $C(t, t_w)$ at $T = 0.7T_c$ for $t = t_w = 2^{12}$ vs. $1/D^2$. We compare results obtained with two $z = 6$ models: one with hypercubic topology **(red open circles)** and another in a totally random graph **(green full circles)**.

behavior of C_{link} as function of C^2) seems not endangered by finite size effects.

A very clear finite size effect is in the coherence length, $\xi(t_w)$. By definition, it cannot grow beyond D. Furthermore, what we find is that it hardly grows beyond $D/2$, Figure 4.23–top. Nevertheless, at short times, we can identify a D-independent region, where it grows roughly as $\log t_w$. Hence, one is tempted to conclude that $\xi_{D=\infty}(t_w) \propto \log t_w$. At this point, finite size scaling suggests that both ξ_D/D and $\log t_w/D$ are dimensionless scaling variables. This is confirmed in Figure 4.23–bottom, where a spectacular data collapse occurs. This is further confirmed by the Fourier transform $G(k)$, defined in (4.25). Now, since k can range from 0 to D, it is clearly a dimensionless quantity (a dimensionful momentum would be $p = k/D$). It follows that $G(k)/G(0)$ is a dimensionless quantity that may depend only on a dimensionless variable, such as $\log t_w/D$. Our data support this expectation, see Figure 4.24.

As for the k dependence of $G(k)$, we expect a $1/p^4$ behavior in the range of $1/\xi(t_w) \ll p \ll 1$ [Dom93, Dom98, Dom06]. Indeed, when comparing nonequilibrium with equilibrium spatial correlation functions, it should be kept in mind that the nonequilibrium ones correspond to the equilibrium $q = 0$ sector [Belo8a, ÁB10a] (since we take the large D limit at fixed t_w).

Now, it is very important to recall that p^4 in Euclidean metrics translates into p^2 in the postman metrics. We have also seen that the dimensionful p (postman metrics) corresponds to k/D. Thus, since in our range of t_w, $\xi(t_w) \sim \log t_w$, the product $G(k)\left(p^2 + 1/\log^2 t_w\right)$ should be roughly constant as D grows. As we show in Figure 4.25, the scaling is better for p of order 1 ($k \sim D$), although it seems to improve for smaller p as D grows. As far as we know, this is the first observation of the p^4 propagator in a numerical work.

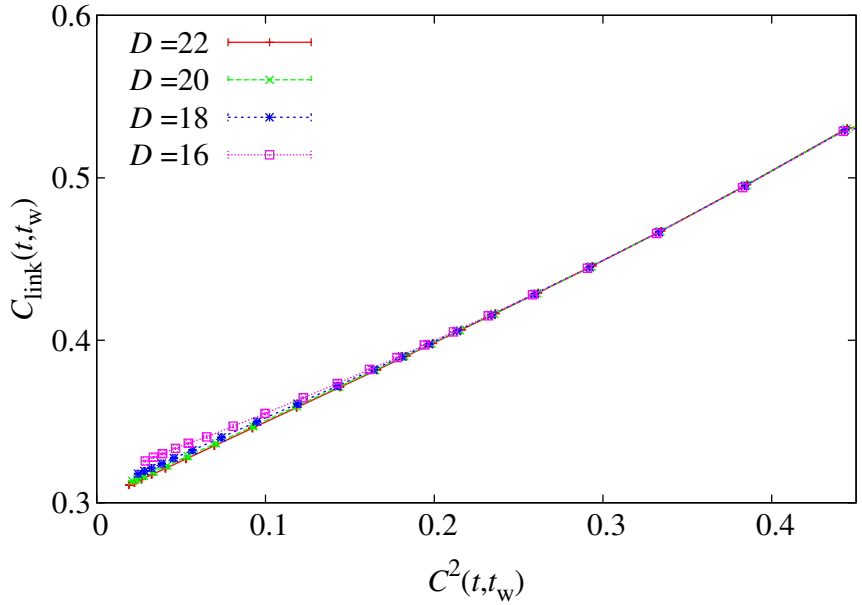

FIGURE 4.22: $C_{\rm link}$ over $C^2(t,t_{\rm w})$ at $T=0.7T_{\rm c}$ for $t_{\rm w}=2^{12}$ and for different system sizes.

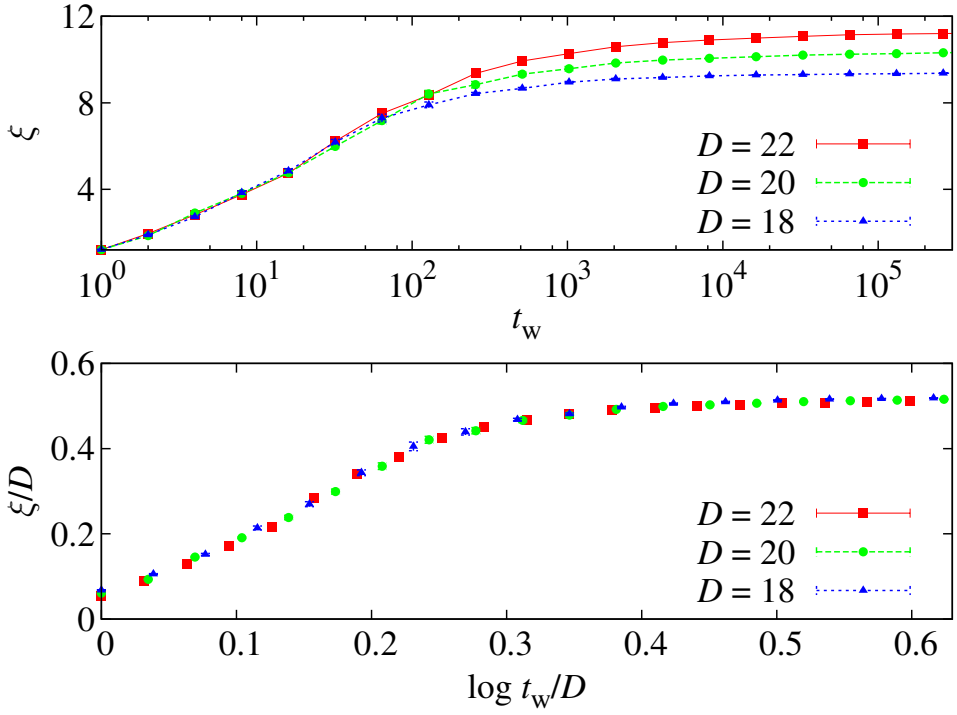

FIGURE 4.23: **(Top)** Coherence length ξ in the SG phase at $T=0.7T_{\rm c}$ vs. $t_{\rm w}$ for different system sizes. **(Bottom)** same data of the top panel rescaled by D as a function of $\log t_{\rm w}/D$.

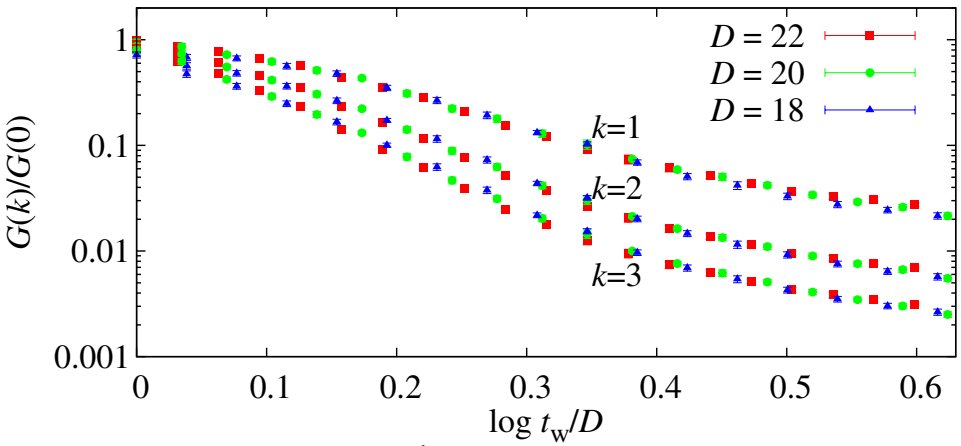

FIGURE 4.24: Fourier transform $G(k)$ of $\hat{C}_4(r)$ in units of $G(0)$ as a function of $\log t_w/D$ for several values of D and k at $T = 0.7T_c$. For each value of k, a different scaling function is found.

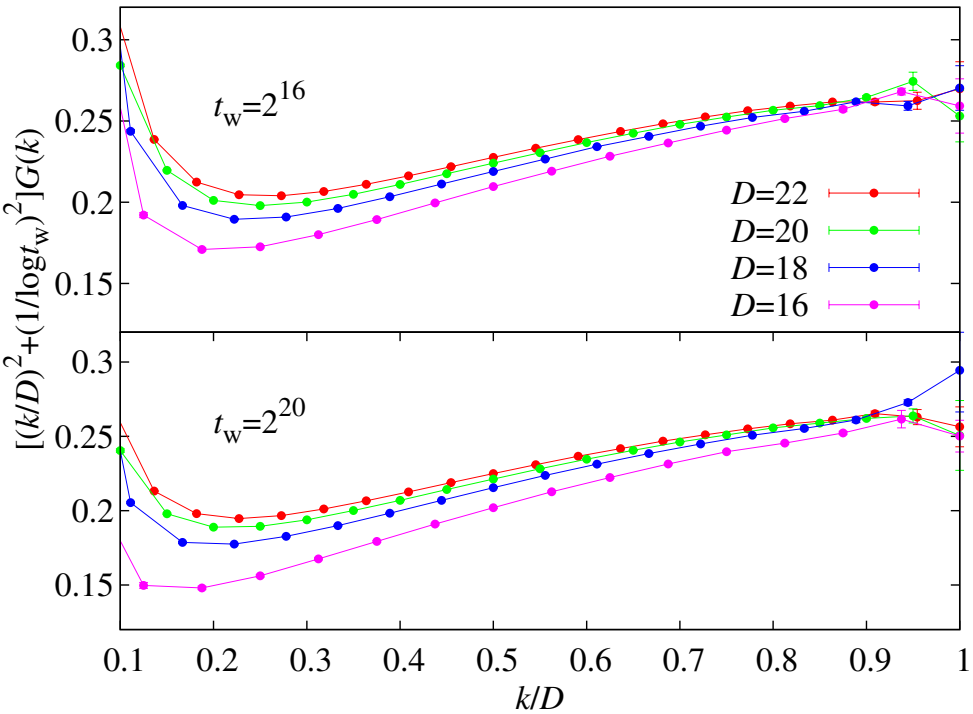

FIGURE 4.25: Fourier transform $G(k)$, (4.25), in units of the propagator $[(p^2 + 1/\xi^2(t_w))^{-1}]$ [Dom93, Dom98, Domo6] as a function of p, where the dimensionful momentum is $p = k/D$ and $\xi(t_w) \sim \log t_w$. Recall that we are using postman metrics, hence, p^2 translates to p^4 in the Euclidean metrics. We show results for two waiting times: $t_w = 2^{16}$ **(top)** and $t_w = 2^{20}$ **(bottom)**.

CHAPTER V

Temperature Chaos

5.1 Introduction

Spin glasses (SG) display an anomalously large response to external perturbations. This phenomena is known as *chaos*. Some of these instabilities are well established. This is the case of the chaos induced in the system by a magnetic field [Par84] or by small perturbations in the bond configurations, known as disorder chaos. However, the temperature counterpart (the fragility of the equilibrium state of a SG when the the temperature is slightly changed) remains to be understood. This effect is named *temperature chaos* and will be the scope of this chapter.

In the last years, temperature chaos has attracted a lot of attention because of its suspected relation with the impressive memory and rejuvenation experiments (see Sect. 3.3.3) which are still far from being understood. In fact, chaos is one of the simplest explanations for rejuvenation. Indeed, if the equilibrium states at two different temperatures, T_1 and T_2 ($T_2 < T_1$), were completely uncorrelated, the susceptibility would not be affected by the isothermal aging at the previous temperature T_1. Memory is still compatible with temperature chaos because of the length scale separation discussed in Sect. 3.3.3, the ghost domains in droplets scenario [Yoso3, Jönо4] or a hierarchical organization of states with T, as discussed in Section 3.5.

The property of temperature chaos was predicted a lot time ago [Bra87], but unfortunately, it remains still nowadays an elusive phenomenon. The analytical work on temperature chaos is based on two different approaches:

- First, by means of scaling arguments and real renormalization analysis [Bra87, Fis88b, Ban87]. The scaling approach appears in the droplet theory framework (see Sect. 3.5). As discussed below, this theory assumes that the lowest-energy excitations of the system are compact domains of coherently flipped

spins, the so-called droplets. Because of its relevance in the field, we will spend some few lines in describing how chaos is described phenomenologically using this droplet picture. However, we will not follow this approach in our work, we will explain why later.

By definition, the temperature chaos appears if the spin polarizations at two temperatures T_1 and T_2 are decorrelated beyond certain characteristic length, $\xi_C(T_1, T_2)$, namely the *chaotic length*. One can estimate this length using thermodynamic arguments and the scaling picture. Indeed, two states will be uncorrelated if from temperature T_1 to T_2 a droplet of size higher than this $\xi_C(T_1, T_2)$ has flipped. This happens if the free-energy inverts the sign between these two temperatures. We use thermodynamic arguments to compute this free energy. Let us consider two states at T_1 that differ one from the other by a large droplet of size ξ. Then, using (3.41), the two free energies differ by $\Delta F(T_1) \approx \gamma(T_1)\xi^\theta$. Now, we slightly change the temperature to T_2, so that $|T_2 - T_1| \ll T_1$. The total change of free-energy will be

$$\Delta F(T_2) \approx \gamma(T_1)\xi^\theta \pm |T_2 - T_1|\sigma(T_1)\xi^{D_s/2}, \tag{5.1}$$

with $\sigma(T_1)$ the *entropy stiffness* and D_s the fractal dimension of the droplet's surface. Here, with the sake of clarity, we considered only very small variations in temperature in order to neglect the changes with the temperature in γ and σ (these effects can be considered without too much change in the final expression, as done in [Kato7]).

According to (5.1), if $\theta \leq D_s/2$, as happens in the droplet theory, the free energy $\Delta F(T_2)$ can have opposite sign than $\Delta F(T_1)$ because of the entropic term. This will occur for scales greater than

$$\xi_C(T_1, T_2) \propto \left[\frac{\gamma(T_1)}{\sigma(T_1)|T_2 - T_1|}\right]^{1/\zeta}, \tag{5.2}$$

with $\zeta = D_s/2 - \theta$ being the *chaotic exponent*. Summarizing, when the temperatures are changed, even for very small variations, the equilibrium configurations are expected to differ in scales higher than this $\xi_C(T_1, T_2)$.

There is a lot of numerical work available both in MF [Bilo0, Bilo2] or in more realistic EA models [NN97, NN98, Aspo2, Rizo3, Krzo4, Saso5, Kato7], and almost invariably, numerical data were analyzed using a scaling picture.

- Second, using large deviation functionals and perturbation theory in MF models [Bilo2, Rizo3, Par10]. In MF analytical calculations, temperature chaos is described in terms of a large-deviation functional (the free-energy of a system constrained to have similar spin configurations at two different temperatures in the SG phase, $T_1, T_2 < T_c$). Later on, this functional is obtained by means of a perturbative approach. The existence of this large-deviation functional implies a large fluctuation in the possible overlaps, which anticipates a dramatic sample-to-sample variability.

A full analytical study of temperature chaos has been achieved recently [Riz03, Par10] in mean field models, expected to be accurate in spatial dimensions above $D=6$. Surprisingly, it has been shown that the most studied MF model, the SK model (see Section 3.4.3) suffers anomalously weak temperature chaos effects, which explains why it has been that slippery to find it in computer simulations (even more than in more realistic models) [Bil00, Bil02]. Indeed, all the lower power terms in the perturbative expansion of the large-deviation functional pathologically vanish in the particular case of the SK model. In fact, the temperature chaos has been studied in diverse Bethe lattices models reaching the conclusion that chaos is stronger the more heterogeneous the model is.

Despite of the intensive numerical work on this topic in the last 15 years [Bil02, NN97, NN98, Krz04, Sas05, Kat07] the numerical confirmation for the scaling picture is rather weak. All the evidences presented are based on an indirect phenomenological renormalization approach. Indeed, authors find nice scalings of the data which allow them to infer the chaos exponent ζ (for instance in EA models, $\zeta \approx 1.07$ in $D=3$ [Kat07] and $\zeta \approx 1.12$ in $D=4$ [Sas05]) which seems to be compatible with the accepted values for D_s and θ in each model. However, this method presents a major caveat: scaling holds also for $T_1, T_2 > T_c$, that is, deep in the paramagnetic phase (see [NN97, NN98, Kat07] and Figure 5.18–bottom) where no chaos should be found.

Moreover, apart from this phenomenological renormalization, no numerical work has succeeded in presenting clear evidences of chaotic behavior, that is, in the sense of decorrelation between spin configurations at different temperatures. This failure has been attributed to a very large $\xi_C(T_1, T_2)$, comparable or larger than the simulated system sizes [Asp02]. Summing up, this approach states that chaos should be there but we are in the border of detecting it. Because of that, the overall emerging picture is that of a gradual and extremely weak phenomenon. However, if this $\xi_C(T_1, T_2)$ were as large as suggested ($\xi_C \approx 20$ for $T_1 = 0.7$ and $T_2 = 0.4$ [Asp02]), the effect of temperature chaos should also be very weak in experiments which handle with coherent clusters of roughly $\sim 10^5$ spins [Ber04] (i.e. $\xi \sim 40$ lattice spacings). On the other hand, rejuvenation is observed both in experiments [Jon98] and simulations [Jim05], which means that either there is no connection between temperature chaos and rejuvenation (as some authors suggest [Ber02a, Ber03a] and Section 3.3.3), or there is something wrong in this picture and the chaos pops up at much shorter length scales. Our analysis suggests this second scenario. In fact, in this chapter we shall extend the MF picture and the large deviation functional approach to the $D=3$ EA model.

However, even if the temperature chaos is an *equilibrium* property, experimental SG are out of equilibrium as was widely shown all over Chapter 3. As discussed in Section 3.6.4, this gap between theory and experiment has been recently filled for isothermal aging. The static-dynamics dictionary relates equilibrium properties of *finite-size* systems, with macroscopic aging samples at *finite-times*. Unfortunately, the dictionary presented in Section 3.6.4 works only for the simplest experimental

protocol, in which you cool the SG as fast as possible to the working temperature, then keep T constant. Instead, memory and rejuvenation effects are exposed only by temperature-varying protocols. Static-dynamics dictionaries are yet to be built for these richer protocols. Experimental attempts to establish them were very crude [Jön02, Jön04, Ber04]. Indeed, a crucial ingredient was missing: the characterization of equilibrium temperature-chaos and of its system-size dependence. Here, we achieve this task, thus paving the way for extensions of the isothermal time-length dictionary to temperature-varying experiments.

5.2

Simulation set-up

In this work, we revisit numerically the temperature chaos problem in the $D = 3$ Edwards-Anderson model studied in [Kat07] but using significantly higher systems ($L_{\max} = 32$ here vs. 10 in [Kat07]) thermalized up to unprecedentedly low temperatures. For this purpose, we reanalyze JANUS' equilibrium spin configurations already used for previous equilibrium studies [ÁB10a, ÁB10b].

Our Ising spins $s_{\boldsymbol{x}} = \pm 1$ are placed in the $V = L^D$ nodes $\boldsymbol{x}$ of a cubic lattice of linear size L, with periodic boundary conditions. The interaction is restricted to lattice nearest neighbors. The coupling constants $J_{\boldsymbol{x},\boldsymbol{y}} = \pm 1$ are chosen with 50% probability. This model undergoes a SG transition at $T_c = 1.109(10)$ [Has08b]. We study 4000 realizations of disorder, named *samples*, for $L = 8$, 12, 16 and 24 (1000 samples for $L = 32$). The minimal temperature in the Parallel Tempering simulation increased with L (for $L = 32$ it was $T_{\min} = 0.7026$). Simulation details are summarized in Table 5.1.

L	$T_{\min}$	$T_{\max}$	$\mathcal{N}_T$	$\mathcal{N}_{\text{mes}}$	$\mathcal{N}_{\text{HB}}^{\min}$	$\mathcal{N}_{\text{HB}}^{\max}$	$\mathcal{N}_{\text{HB}}^{\text{med}}$	$\mathcal{N}_{\text{s}}$	System
8	0.245	1.575	8	10^3	1.0×10^6	6.48×10^8	2.30×10^6	4000	PC
12	0.414	1.575	12	5×10^3	1.0×10^7	1.53×10^{10}	3.13×10^7	4000	PC
16	0.479	1.575	16	10^5	4.0×10^8	2.79×10^{11}	9.71×10^8	4000	Janus
24	0.625	1.600	28	10^5	1.0×10^9	1.81×10^{12}	4.02×10^9	4000	Janus
32	0.703	1.549	34	2×10^5	4.0×10^9	7.68×10^{11}	1.90×10^{10}	1000	Janus

TABLE 5.1: Parameters of our spin-glass parallel tempering simulations. In all cases we have simulated four independent real replicas per sample. The $\mathcal{N}_T$ temperatures are uniformly distributed between $T_{\min}$ and $T_{\max}$ (except for the runs of the first row, which have all the temperatures of the second one plus $T = 0.150$ and $T = 0.340$). In this table $\mathcal{N}_{\text{mes}}$ is the number of Monte Carlo Steps between measurements (one MCS consists of 10 heat-bath updates and 1 parallel-tempering update). The table shows the minimum, maximum and medium simulation times ($\mathcal{N}_{\text{HB}}$) for each lattice, in heat-bath steps (the length of each simulation depends on the sample, for thermalization protocol see [Yll11]). Lattice sizes $L = 8, 12$ were simulated on conventional PCs, while sizes $L = 16, 24, 32$ were simulated on JANUS. Whenever we have two runs with different $T_{\min}$ for the same L the sets of simulated samples are the same for both. The total spin updates for all lattice sizes sum 1.1×10^{20}.

5.3

Selecting the right observables to change the paradigm

As discussed above, the temperature chaos has been an elusive phenomenon up to now. In this work, we argue that the reason for its apparently small consequences was in the observables and the statistical methods used in previous studies. In this section, we will support that a change of paradigm is necessary: chaos must be treated as a *rare event driven* phenomenon. Since this approach is quite novel, we will spend some lines discussing which magnitudes are better to detect the temperature chaos, and to define the concept of *chaotic event*.

In analogy with the rest of SG studies, the natural parameter to approach the temperature chaos is the two temperatures overlap:

$$q_{T_1,T_2} = \frac{1}{V}\sum_{\boldsymbol{x}} s_{\boldsymbol{x}}^{T_1} s_{\boldsymbol{x}}^{T_2}\,, \tag{5.3}$$

i.e. the traditional spin overlap (see Eq. (3.57)) but mixing configurations at two different temperatures. As it also happens at one single temperature, the overlap (5.3) is the one preferred magnitude for mean-field analytical computations [Riz03, Par10]. As an extension, numerical approaches to temperature chaos in MF (only available in the SK model) also investigated this overlap [Bil00, Bil02], obtaining an extremely low chaotic signal. For some time, this signal was so low that this fact was used to support the non existence of this temperature chaos phenomenon. Nowadays we now that, among the mean field models, the SK model is pathological, in the sense that chaos is anomalously weak on it [Par10] and all terms in

perturbation theory below the ninth order vanish in this precise model [Riz03].

Here we want to detect chaos in the $D = 3$ EA model. As a first attempt, we try to look directly to the spin overlap. According to the chaos hypothesis, the overlap between equilibrium states at two different temperatures should be always zero. That means that the pdf $P(q_{\rm C})$ should be a delta function centered on $q_{\rm C} = 0$. Of course, this the large L-limit, for a finite system one would expect a growing peak with L around $q_{\rm C} = 0$ in the pdf. However, as we discuss below, the chaotic signal through this magnitude is still too weak in our computation, and more sophisticate quantities are needed.

The two-temperatures overlap is a stochastic variable, with two sources of randomness: the thermal fluctuations, and the choice of the nearest-neighbors couplings. In practice, for each sample, we have at our disposal four independent sets of thermalized configurations (each independent set corresponds to a single parallel-tempering Markov chain) [ÁB10a]. Consider Monte Carlo times t_A and t_B, from the Parallel-Tempering chains A and B.[1] In a fully explicit way, the two-temperatures overlap is computed as

$$q_{T_1,T_2}(t_A, t_B; J) = \frac{1}{V} \sum_{\boldsymbol{x}} s_{\boldsymbol{x}}^{T_1}(t_A) s_{\boldsymbol{x}}^{T_2}(t_B)\,. \tag{5.4}$$

Computing such a large amount of overlaps in a feasible time was not an easy task,[2] multispin coding techniques were necessary. We include an explanation about these techniques in Appendix B.2.

In Figure 5.1–top, we show its accumulated pdf, namely the probability of finding a value of $q_{T_1,T_2}(t_A, t_B; J)$ no larger than ε. In the chaos scenario, one would expect a step function in $\varepsilon = 0$. Clearly, we are far away from this limit, but the evolution with L seems to approach it. However, these curves must be compared with the curves at one single temperature, i.e. $T_1 = T_2$, see Figure 5.2–top, which do not suffer from chaos. We can see that the situation is very much the same, these one-temperature curves displays a strong size-dependency too.

In order to absorb the spurious non-chaotic finite-size effects, we employ the lattice-size dependent Edwards-Anderson parameter, $q_{EA}(L, T)$, defined in (3.13), obtained with the same set of data in [ÁB10a]. In fact, if we rather compute the pdf for the following modified parameter,

$$\hat{q}_{T_1,T_2} = \frac{q_{T_1,T_2}}{\sqrt{q_{\rm EA}(L, T_1)\; q_{\rm EA}(L, T_2)}}, \tag{5.5}$$

see Figure 5.1–bottom, we realize that the chaos signal is basically non-existent for $L \leq 16$, and extremely weak for $L = 24, 32$. On the other hand, if we consider

[1] For each chain, we pick a subset of N_t configurations, evenly spaced in Monte Carlo time (for $L = 32$, $N_t = 100$).

[2] For a single sample, we compute $6N_t^2$ such overlaps (there are six ways of choosing a pair $A \neq B$ out of four parallel-tempering chains). These thermal fluctuations will be integrated out for further studies, but here, instead, we want to explore what happens when the thermal fluctuations *are* considered. In addition, there are $N_T^2/2$ possible couples of temperatures, being N_T the number of temperatures simulated.

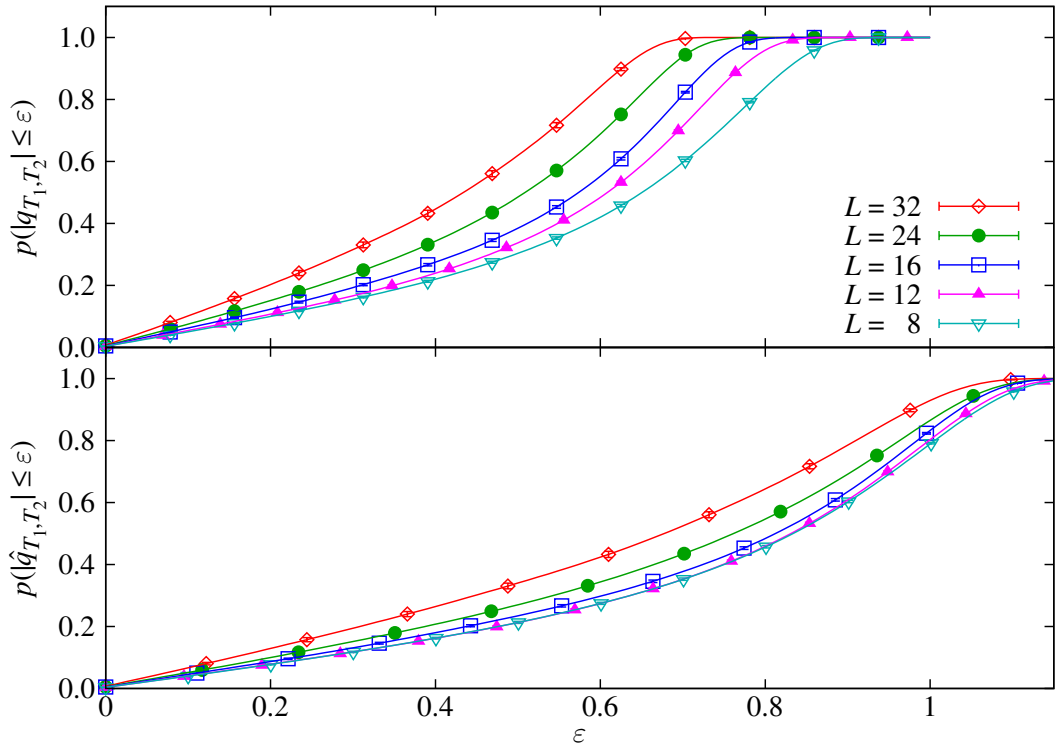

FIGURE 5.1: **(Top)** Probability distribution function for the overlap defined in (5.4), $p(|q_{T_1=0.7026,T_2=0.90318}| \leq \varepsilon)$. **(Bottom)** Same as top panel, but subtracting system-size effects with the parameter $\hat{q}_{T_1,T_2}$, defined in (5.5). Error bars (smaller than the symbol size) are displayed.

the analogous curve for $T_1 = T_2$, see Figure 5.2–bottom, the curves collapse as one would expect. Clearly enough, other effects with no relation with chaos (such as the global spin reversal $\mathbb{Z}_2$ symmetry and the non-triviality of the $P(q, T_1, T_2 = T_1)$, at least on small lattices), are responsible for most of the probability at low q_{T_1,T_2}.

With this idea idea in mind, now integrating out times and replicas, we use a popular slight-modification to the $\hat{q}_{T_1,T_2}$ parameter discussed before, known as the *chaotic parameter* [NN97]

$$X^J_{T_1,T_2} = \frac{\left\langle q^2_{T_1,T_2} \right\rangle_J}{\sqrt{\left\langle q^2_{T_1,T_1} \right\rangle_J \left\langle q^2_{T_2,T_2} \right\rangle_J}}. \tag{5.6}$$

Here, $\langle \cdot \rangle_J$ refers to thermal-averages within the same sample. By definition, $0 \leq X^J_{T_1,T_2} \leq 1$. In fact, $X^J_{T_1,T_2}$ is similar to a correlation parameter (if $X^J_{T_1,T_2} = 1$ two typical spin-configurations at T_1 and T_2 are indistinguishable in a particular sample, while $X^J_{T_1,T_2} = 0$ indicates completely different configurations, then, extreme chaos). This parameter absorbs many of the spurious effects found in the two-temperatures

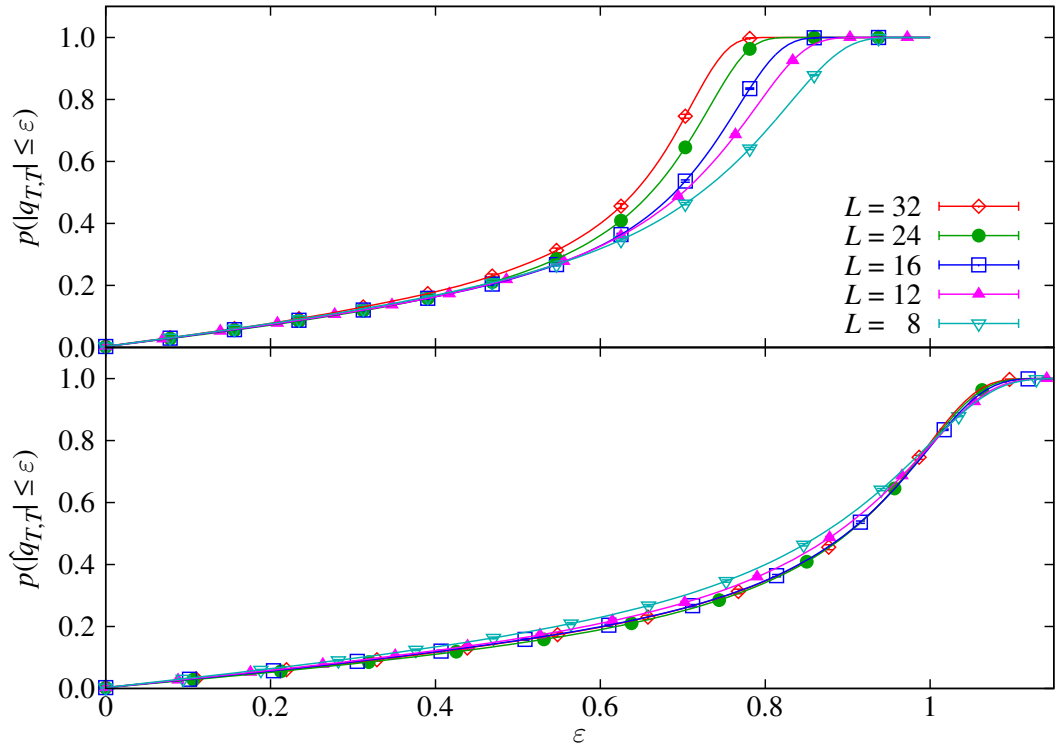

FIGURE 5.2: **(Top)** Probability distribution function for the overlap at the same temperature, $T_1 = T_2 = 0.7026$, $p(|q_{T_1=0.7026,T_2=0.7026}| \leq \varepsilon)$. **(Bottom)** Same as top panel, but subtracting system-size effects with the parameter $\hat{q}_{T_1,T_2}$, defined in (5.5). Error bars (smaller than the symbol size) are displayed.

overlap, but still, this $X^J_{T_1,T_2}$ was used in numerical works before [NN97, NN98, Kato7], and the standard analysis (wrongly) concluded that chaos was very weak. That means that this parameter (5.6) is not enough by itself, and we need something more.

We look for some intuition. We seek it in the Monte Carlo dynamics, specifically in the temperature flow of the Parallel Tempering (PT) [Huk96, Mar98]. Indeed, if the equilibrium configuration for two neighboring temperatures are too different (temperature chaos), a bottleneck in the temperature random-walk should appear. This is precisely what we find in the simulations, as it is illustrated in Figure 5.3 for one of our configurations. The simulation temperature flow can be characterized using the exponential autocorrelations times, as we already did in [ÁB10a] to establish a thermalization protocol. Besides, the performance of PT deteriorated dramatically when the system size grows from $L = 8$ to $L = 32$. In fact, it was precisely this strong stagnation of the PT dynamics in certain samples, what made us fell that a strong form of temperature chaos was waiting to be unveiled. This idea of identifying equilibrium properties using the dynamics is not new, it was used in the glassy context before [Sch07, Fer06a].

The temperature-flow dynamics is characterized by its exponential autocorre-

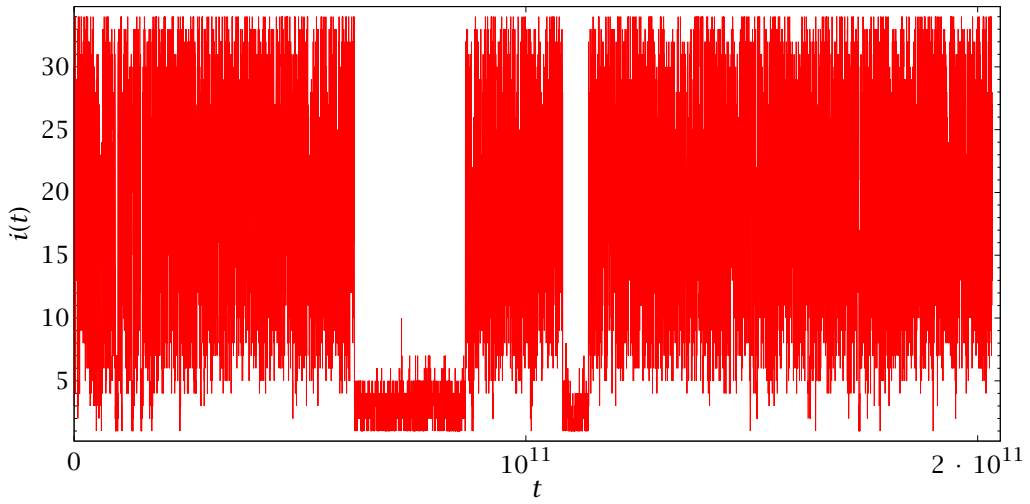

FIGURE 5.3: Temperatures random walk of a single configuration of one of the spin glass samples. The temperature index $i(t)$ is plotted as a function of the time in units of heat bath updates. The critical temperature corresponds to $i_c = 17$ (in the middle range). Clearly there is a well defined blockage in the dynamics' ergodicity around $i \sim 5$, our bet is that its origin is precisely the temperature chaos.

lation time, τ_{exp} [Sok97, ÁB10a]. Our standpoint is that the quantity that better correlates with $\log \tau_{\text{exp}}$ will also be the most informative about chaos. The reason for seeking correlations with $\log \tau_{\text{exp}}$ instead of just τ_{exp} is precisely the large sample to sample variability. Indeed, given the disparity of times, one must take $\log \tau_{\text{exp}}$ in order to ensure that familiar concepts from Gaussian statistics, such as the correlation parameter, make sense.

As a first step, we study the correlation of the probability of finding small overlaps (5.3), $p(|q^J_{T_1=0.7026,T_2=T_c}| < 0.1)$, with $\log \tau_{\text{exp}}$ for each sample in Figure 5.4. Indeed, chaotic samples should have very small overlaps, but as discussed above, the histogram for q_{T_1,T_2} around 0, is affected by other non chaotic effects (that do not hamper thermalization), and thus the correlation with times is poor. The situation is very much improved if we consider the correlation of the chaotic parameter $X^J_{T_1,T_2}$ with $\log \tau_{\text{exp}}$ instead. We show in Figure 5.5 this magnitude computed for $T_1 = T_{\text{min}}$ (our lowest temperature for $L = 32$), and $T_2 = T_c$, the critical temperature, versus $\log \tau_{\text{exp}}$. The correlation is higher, but still we can find a better magnitude. In fact, our optimum is the integral of $X^J_{T_1,T_2}$ with temperature, i.e.

$$I = \int_{T_1}^{T_{\text{max}}} X^J_{T_1,T_2} \, \mathrm{d}T_2 \tag{5.7}$$

, see Figure 5.6. This integral will be small in the case that $X^J_{T_1,T_2}$ suffers a sharp drop at low T_2, and as seen, the samples with small I correspond with those where the temperature flow is likely to get stuck. This correlation calls for the notion of *chaotic event*, rather than an analysis based on sample-averages.

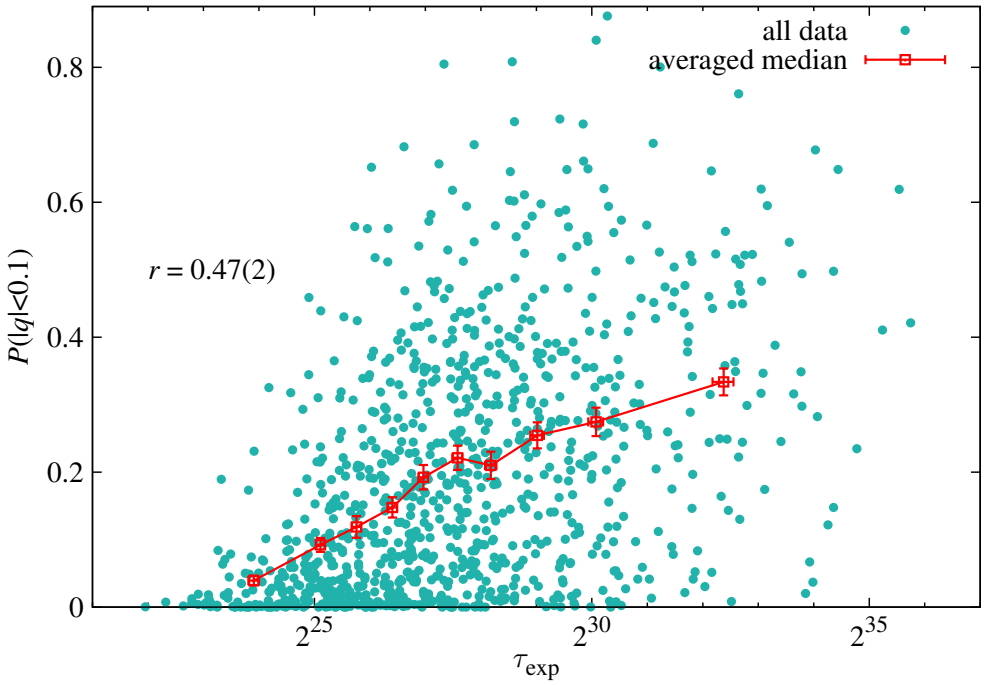

FIGURE 5.4: Seeking clues about temperature chaos on the parallel tempering autocorrelation time τ_{exp} [ÁB10a]. We show the scatter plot $p(|q^J_{T_1=0.7026,T_2=T_c|} < 0.1)$ [$q^J_{T_1,T_2}$ in (5.3)] versus $\log \tau_{\text{exp}}$. The correlation parameter r is displayed. To compute the red lines, we ordered the samples by increasing $\log \tau_{\text{exp}}$ and made groups of 100 consecutive samples. Within each group, medians were computed (errors from bootstrap).

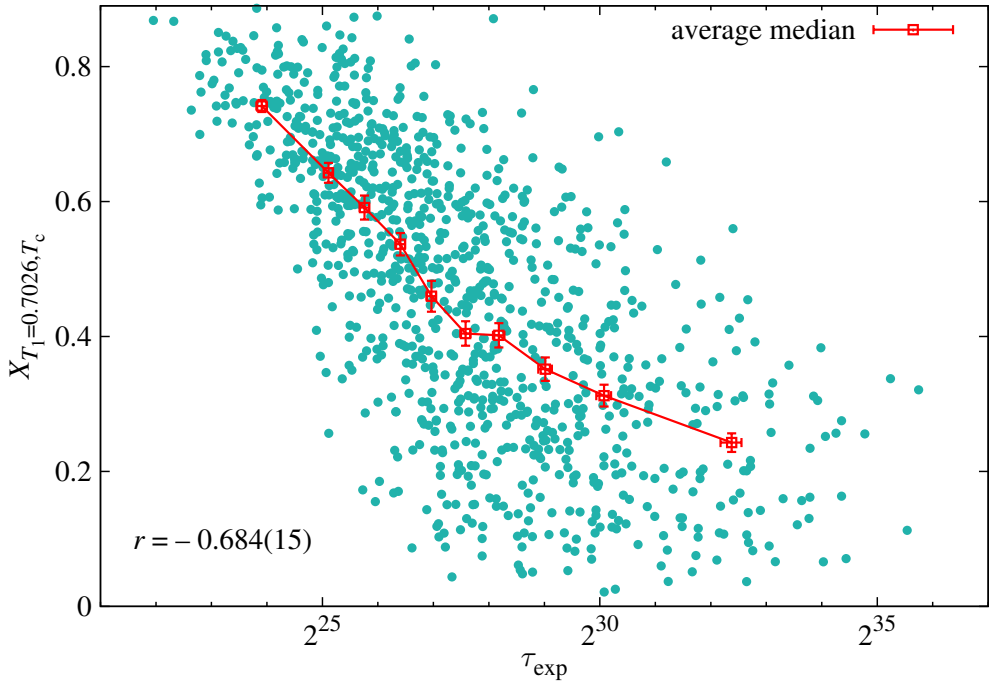

FIGURE 5.5: Scatter plot of $X_{T_1=T_{\rm min},T_2=T_c}$ vs. the logarithm of the exponential autocorrelation time, $\tau_{\rm exp}$. Data for $L = 32$. The correlation parameter r is displayed. The line is obtained in the same way than in Figure 5.4.

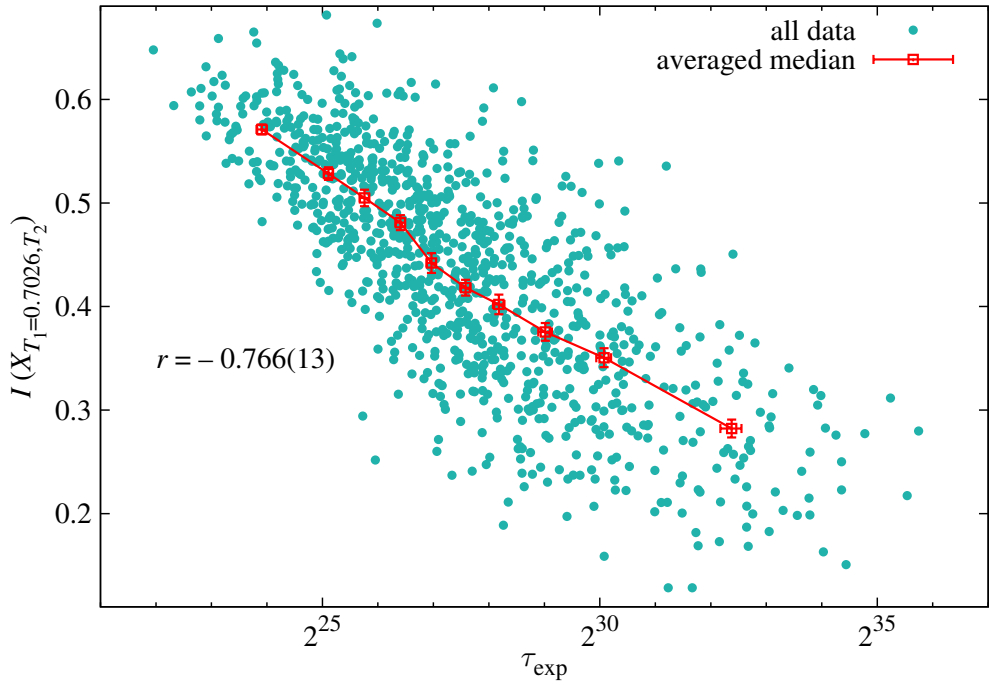

FIGURE 5.6: Scatter plot of $I = \int_{T_1}^{T_{\rm max}} X^J_{T_1,T_2}\, {\rm d}T_2$ versus $\tau_{\rm exp}$, [$X^J_{T_1,T_2}$ in (5.6), $T_1 = T_{\rm min} = 0.7026$, $T_{\rm max} = 1.549$, data for $L = 32$]. The line is obtained in the same way than in Figure 5.4.

Figure 5.7 describes this change of paradigm. The top panel shows the standard average over the samples of $X^J_{T_1,T_2}$, as a function of T_2. In agreement with previous work [NN97, NN98, Kato7], our simulated sizes are painfully away from the large-L limit, where the average of $X^J_{T_1,T_2}$ should vanish if $T_2 \neq T_1$. Instead, our curves are smooth and cross T_c without qualitative changes. This smoothness is a clear indicator that chaos is not being detected. Indeed, temperature chaos is a inner property of the spin glass phase, it cannot be found in the paramagnetic phase. Yet, the behavior of individual samples is quite different, see Figure 5.7—center. For some samples, $X^J_{T_1,T_2}$ falls abruptly at well defined temperatures T_2. This we name *chaotic event*. The temperature at which these events occur is random (many samples do not suffer any). In fact, as L grows, the sample dispersion of $X^J_{T_1,T_2}$ in the SG phase, see Figure 5.7–bottom, approaches $1/\sqrt{12}$ (which is the dispersion of a random variable uniformly distributed between 0 and 1), whereas it tends to zero if $T_2 > T_c$. This is quite a remarkable achievement: it is the first time that a quantitative different behavior is observed between the SG phase (with chaos) and the paramagnetic phase (without chaos). We conclude that a statistical analysis based on sample averages (as shown in Figure 5.7—top) throws away crucial information about temperature chaos.

Now, even though the temperature at which one of these sudden drops takes place is random distributed within the SG phase, it has strong effects in the Parallel Tempering' performance (as suggests Figure 5.6). Indeed, the deeper in the SG phase, the more stagnant the temperature flow is. In order to compute the correlation of this temperature with the exponential autocorrelation time, we need to define a method to compute this temperature. Our choice is the following: for each sample, we consider the dependency of $X^J_{T_1,T_2}$ on T_2, keeping fixed T_1 (as shown in Figure 5.7—center). We compute its derivative with T_2, i.e. $\mathrm{d}X^J_{T_1,T_2}/\mathrm{d}T_2$, and obtain the temperature at which it reaches its maximum value. This temperature will be our *chaos temperature*, $T^J_{\mathrm{chaos}}(T_1)$. This definition counts drops for all the samples, even in those whose $X^J_{T_1,T_2}$ displays a soft behavior without any chaotic effect. However, if this were the case, these temperatures would, in majority, lay nearby T_c or on the paramagnetic phase. Now we study the correlation of this $T^J_{\mathrm{chaos}}(T_1)$ with $\log \tau_{\mathrm{exp}}$, see Figure 5.8. The conclusion of this figure is clear, the deeper in the SG phase the drop takes place, the longer the thermalization time.

In summary, our statement is that chaos was not clearly observed in numerical simulations up to now because the portion of samples that suffered chaotic events was still too limited in the simulated system sizes. Then, chaos seemed to be very week because it was very rare. Indeed, we have seen that, when appearing, it is a strong phenomenon. Of course, in order to chaos to be relevant in the large-L limit this portion of chaotic samples must grow with L. We devote the next section to this discussion.

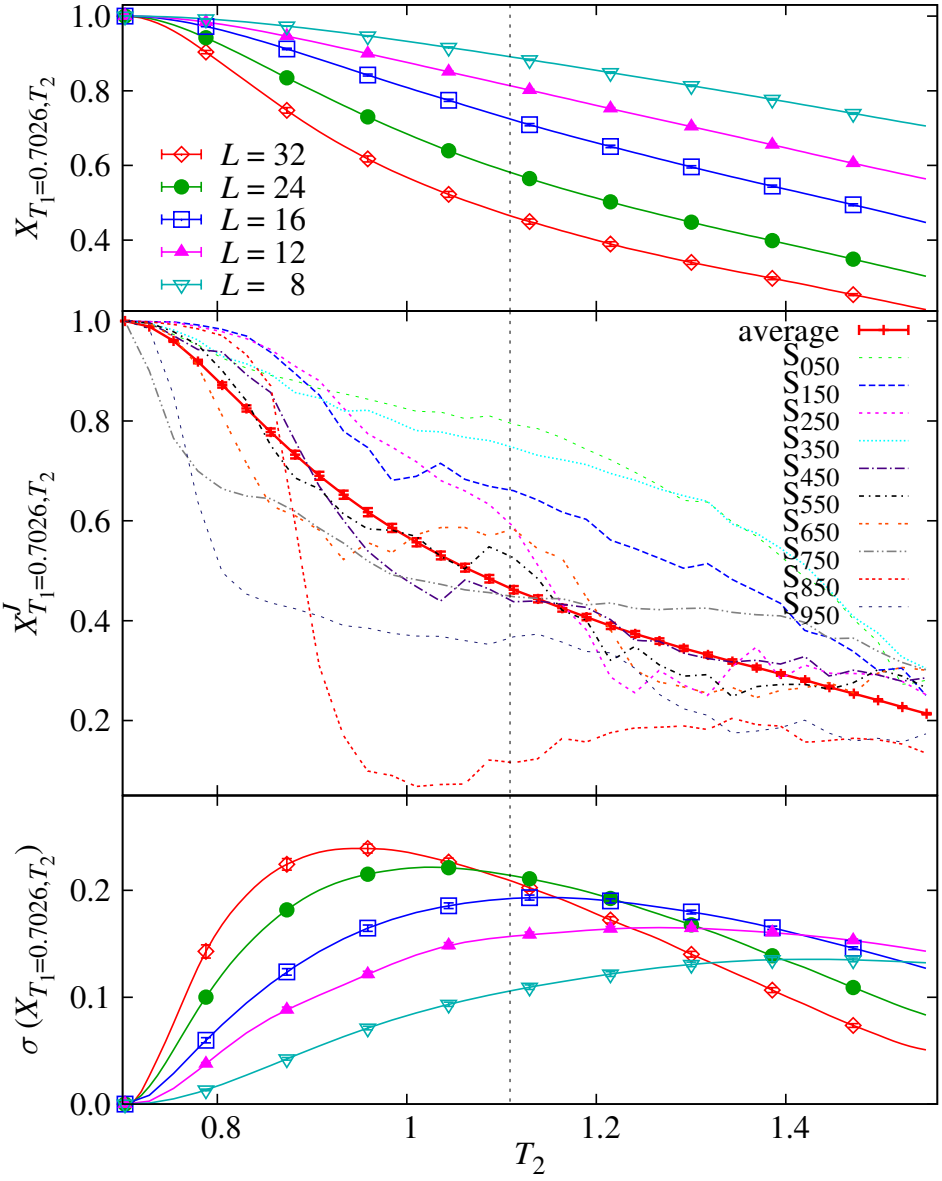

FIGURE 5.7: Different views on $X^J_{T_1,T_2}$, (5.6), as function of T_2 ($T_1 = 0.7026$, the vertical line is $T_2 = T_c$).**(Top)** For all our system sizes, sample-average of $X^J_{T_1,T_2}$. **(Center)** For $L = 32$, we show $X^J_{T_1,T_2}$ for ten samples evenly spaced on a list of growing τ_{exp}, recall Fig 5.4. **(Bottom)** For all our system sizes, we show the dispersion (i.e. square root of variance over the samples) of $X^J_{T_1,T_2}$.

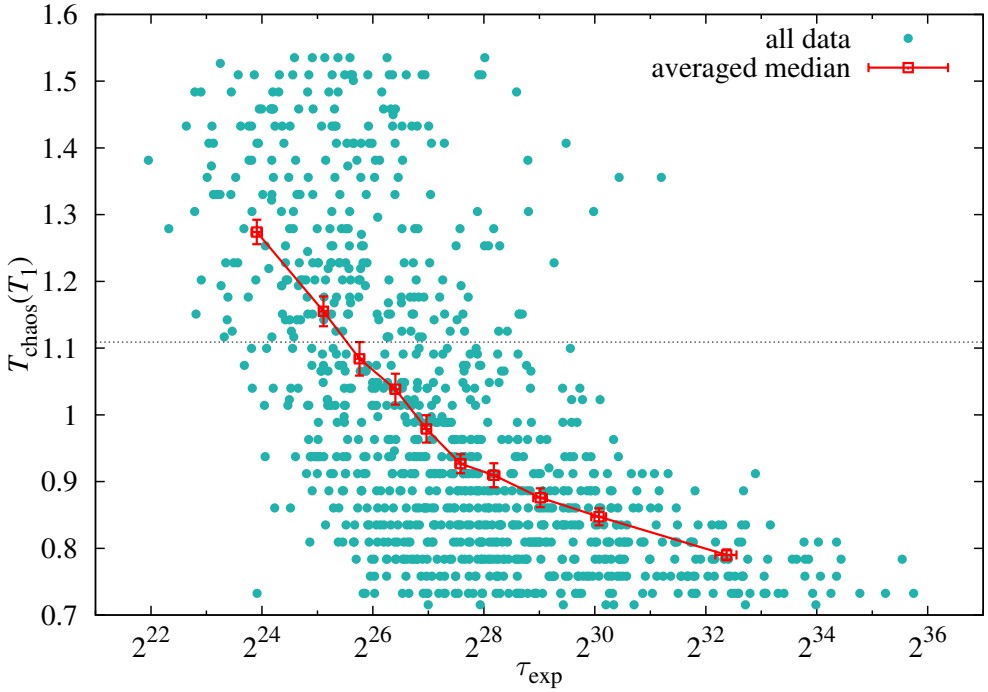

FIGURE 5.8: Chaos temperature, $T^J_{\rm chaos}$, defined in the text versus the logarithm of the exponential autocorrelation time $\tau_{\rm exp}$. Data for $L = 32$. The red line is obtained in the same way than in Figure 5.4. Horizontal dashed line corresponds to $T_c = 1.109$ [Haso8b].

5·4

Large-deviation approach

In this section, we will check that the fraction of samples that suffer a chaotic event for any pair of temperatures T_1, T_2 ($T_1 < T_2 < T_c$) indeed increases with L. With this aim, we compute the cumulative distribution function for the chaotic parameter $X^J_{T_1,T_2}$ (i.e. the probability that $X^J_{T_1,T_2} \leq \varepsilon$), for several system sizes. Results are summarized in Figure 5.9 for $T_1 = 0.7026$ and Figure 5.10 for $T_1 = 0.625$ (this last one is only available for $L \leq 24$, see Table 5.1). According to these results, the portion of samples whose chaotic parameter is smaller than a given value seems to increase very fact with the system size no matter the couple of temperatures considered.

This fact suggests the introduction of a large-deviation potential, $\Omega^L_{T_1,T_2}(\varepsilon)$, as the one introduced in MF computations [Riz03, Par10]:[3]

$$\text{Probability}[X^J_{T_1,T_2} > \varepsilon] = \mathrm{e}^{-L^D \Omega^L_{T_1,T_2}(\varepsilon)}, \tag{5.8}$$

note that here we are considering the complementary probability to the one discussed before. The notion of a large-deviation potential is useful only if $\Omega^L_{T_1,T_2}(\varepsilon)$

[3]The large-deviation potential is normally associated to the probability density, instead of the accumulative probability. Nevertheless both statements are equivalent in the large-L limit. From a numerical point of view, computing the accumulative probability is easier than the probability.

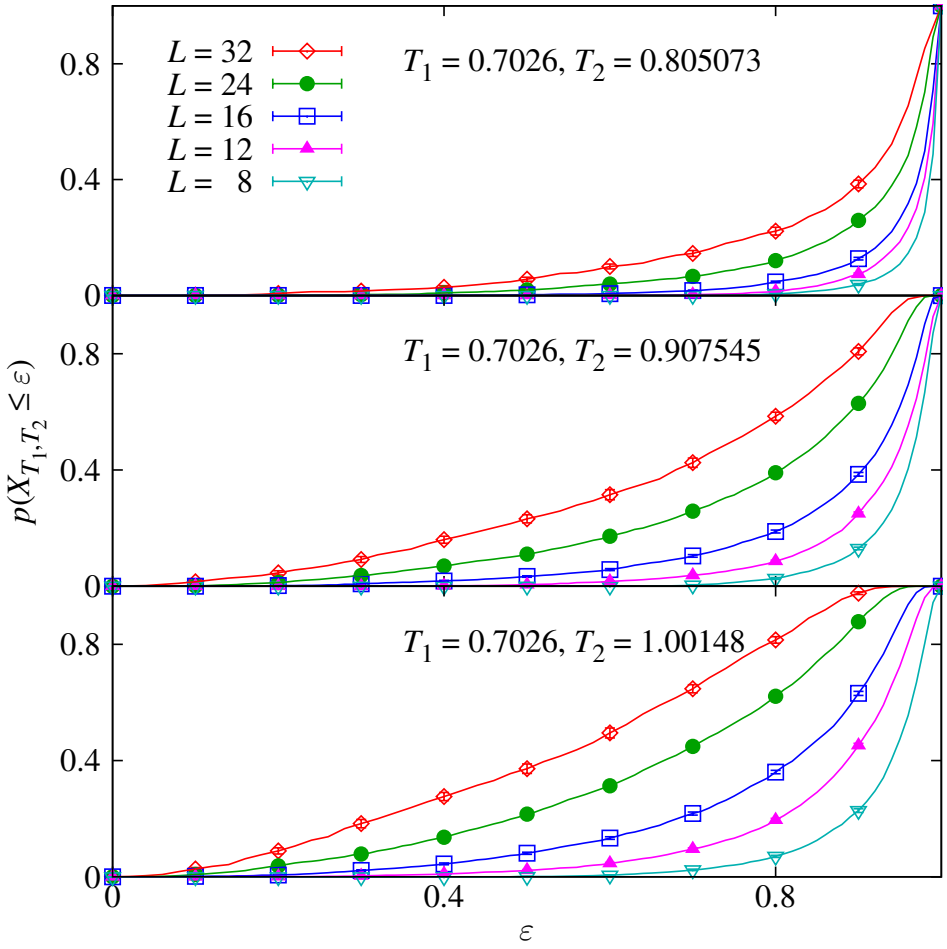

FIGURE 5.9: Probability distribution function for $X^I_{T_1,T_2}$ for $T_1 = 0.7026$ and **(top)** $T_2 = 0.805703$, **(center)** $T_2 = 0.907545$ and **(bottom)** $T_2 = 1.00148$.

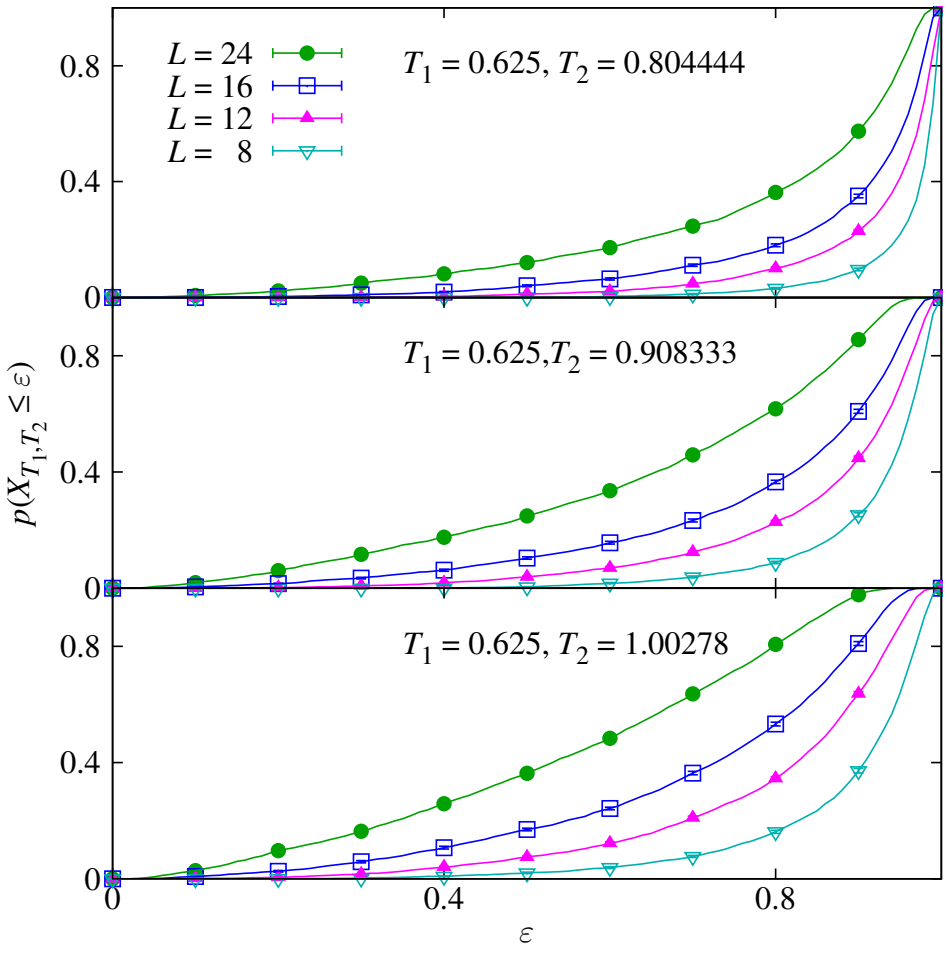

FIGURE 5.10: Probability distribution function for $X^I_{T_1,T_2}$ for $T_1 = 0.625$ and **(top)** $T_2 = 0.80444$, **(center)** $T_2 = 0.908333$ and **(bottom)** $T_2 = 1.00278$.

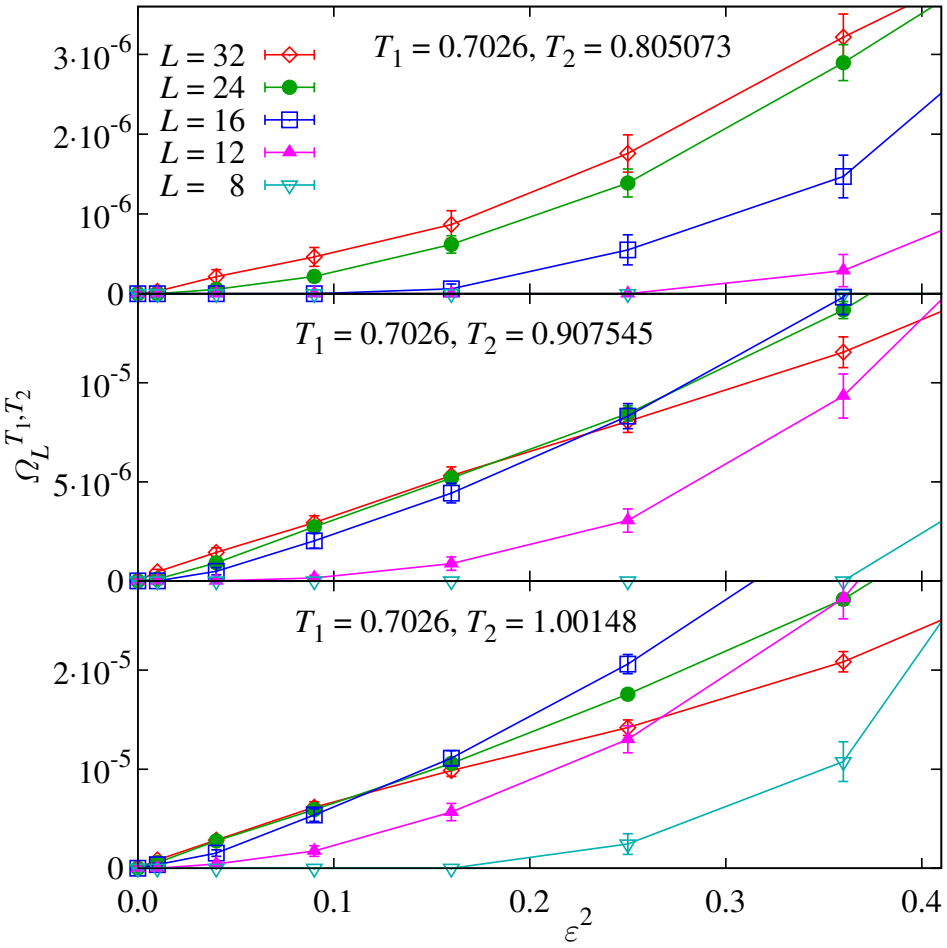

FIGURE 5.11: Large deviation potential for $T_1 = 0.7026$ and **(top)** $T_2 = 0.805703$, **(center)** $T_2 = 0.907545$ and **(bottom)** $T_2 = 1.00148$.

becomes L-independent for moderate system sizes. In a chaotic scenario, this probability should vanish in the thermodynamic limit for $\varepsilon > 0$. In terms of the large deviation potential, $\Omega_{T_1,T_2}(\varepsilon)$ must remain positive for large L and all $\varepsilon > 0$.

We plot $\Omega_{T_1,T_2}(\varepsilon)$ in Figs. 5.11 and 5.12 for $T_1 = 0.7026$ and 0.625 respectively. As expected for chaos, $\Omega_{T_1,T_2}(\varepsilon)$ is nonnegative and increases with ε, but suffers from very strong finite size effects. However, $\Omega_{T_1,T_2}(\varepsilon)$ does reach the large-L limit for the largest systems, at least for small ε. Besides, the lower T_1 is (that is, the deeper in the SG phase), the faster the convergence is achieved. Actually, the large-L limit is reached for $L = 24$ for $T_1 = 0.7026$ and for $L = 16$ for $T_1 = 0.625$. It is important to point out that this study only makes sense for low ε. Indeed, for a finite amount of samples N_S, there is always a $X^{\max}_{T_1,T_2} \leq 1$ above which the potential diverges, i.e. $\Omega_{T_1,T_2}(\varepsilon > X^{\max}) = \infty$, and then no fit makes sense.

Both Figs. 5.11 and 5.12 suggest a linear behavior of $\Omega^L_{T_1,T_2}$ on ε^2, at least for the large-L limit. Besides, chaos seems to weaken the closer T_2 is to T_1. These two

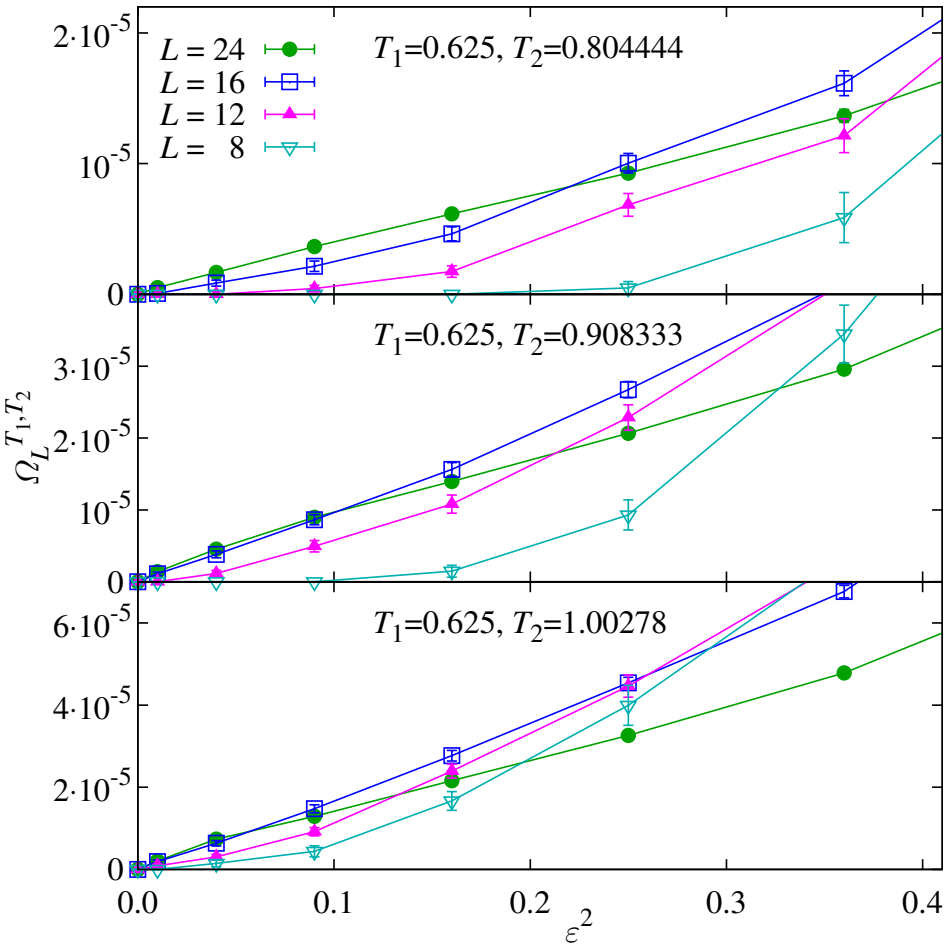

FIGURE 5.12: Large deviation potential for $T_1 = 0.625$ and **(top)** $T_2 = 0.80444$, **(center)** $T_2 = 0.908333$ and **(bottom)** $T_2 = 1.00278$.

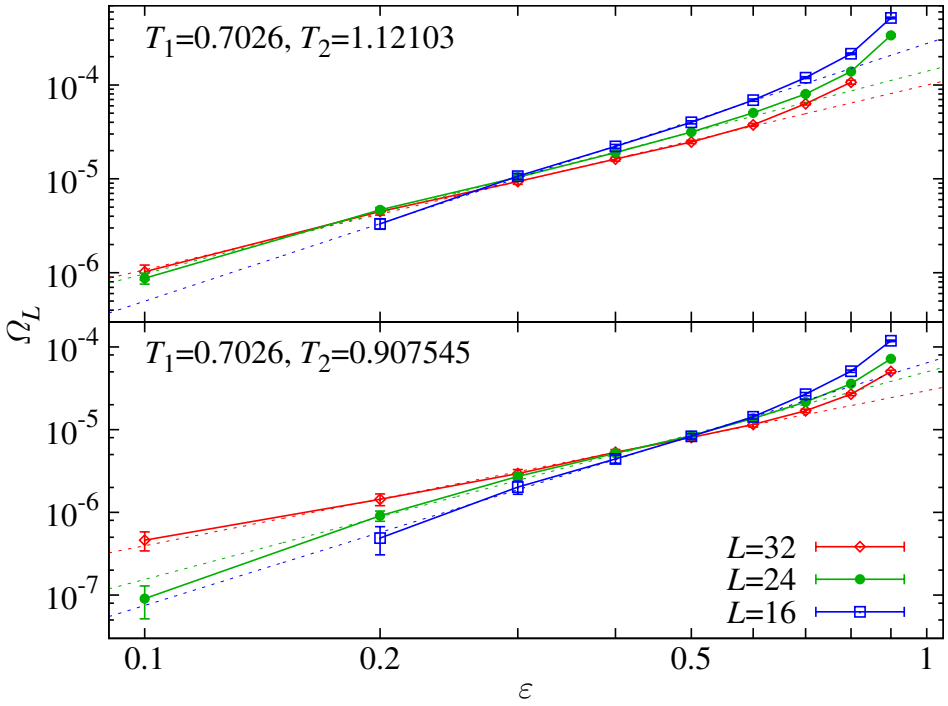

FIGURE 5.13: Computation of exponent β, in (5.9). $\Omega_L(\varepsilon)$ is fitted to $a\,\varepsilon^\beta$ for $L = 32$, 24, and 16 and for two different values of T_2. The fitted exponents are $\beta^{L=32} = 1.94(4)$, $\beta^{L=24} = 2.16(5)$, and $\beta^{L=16} = 2.74(5)$ for $T_2 = 1.12103$, while $\beta^{L=32} = 1.88(4)$, $\beta^{L=24} = 2.51(15)$ and $\beta^{L=16} = 2.93(7)$ for $T_2 = 0.907545$.

properties suggest a MF-inspired scaling (see [Par10] and later discussion)

$$\Omega^L_{T_1,T_2}(\varepsilon) \propto |T_2 - T_1|^b \varepsilon^\beta. \tag{5.9}$$

For later discussion, we note that the MF analytical calculations obtain a large deviation potential which is sum of several terms like this one, with different exponents.

To check this scaling, we fit our data for different system sizes to

$$\Omega^L_{T_1,T_2}(\varepsilon) \propto A(|T_1 - T_2|)\varepsilon^\beta. \tag{5.10}$$

As shown in Figures 5.13 and 5.14 for different pairs of temperatures, data agree very well with one single β exponent. Again, the determination for β suffers from finite size effects, though seems to converge to a finite large-L limit clearly $\beta > 1$ (this will have important consequences later). All the data fit very well to scaling (5.9). Indeed, the values of χ^2/dof of the fits are in most cases in the interval [0.25,0.5], but the different points are very statistically correlated, then, the errors in the fitting parameters are probably underestimated.

On the other hand, when one compares the two fits for each value of T_1, though similar, the fitted β seems to depend on T_1 and T_2. We explore this point. With this aim, we plot the exponent β as a function of $T_1 - T_2$ (only for $T_1 = 0.7026$) in Figure

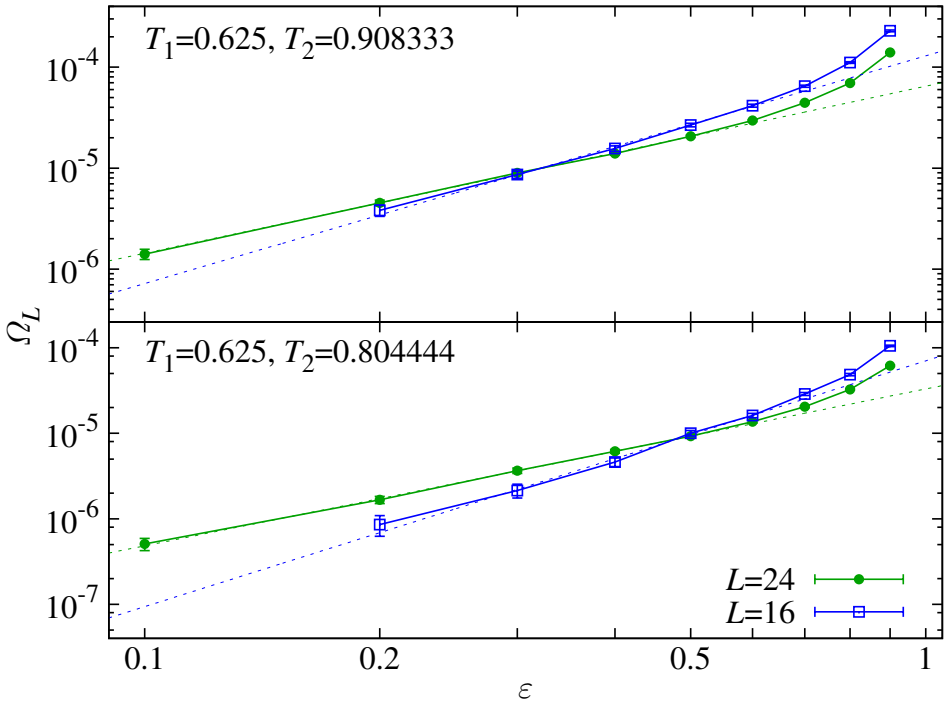

FIGURE 5.14: As in Figure 5.13, for $T_1 = 0.625$. The fitted exponents are $\beta^{L=24} = 1.65(2)$ and $\beta^{L=16} = 2.27(7)$ for $T_2 = 0.908333$, while $\beta^{L=24} = 1.84(2)$ and $\beta^{L=16} = 2.87(13)$ for $T_2 = 0.904444$.

5.15. For $L = 32$ one obtains quite stable values. The situation for $L = 24$ is very different. It monotonically drops from $\beta \approx 3$ at low temperature differences, until it reaches certain temperature, from which, it remains stable. Low temperature differences imply little chaos, which indicates that the scaling (5.9) is only valid when chaos is present.

Once obtained β we can compute the other exponent b in (5.9). According to Figure 5.15 only data for $L = 32$ can be considered as a representative from the large-L behavior in the whole temperature range. For this size, we fix $\beta \sim 2$ and obtain the temperature dependent part of the potential by fitting the data to $A(T_1, T_2)\varepsilon^2$. This temperature dependent factor $A(T_1, T_2)$ is shown in Figure 5.16. Afterwards, b is obtained by fitting this factor to

$$A(T_1, T_2) \propto |T_2 - T_1|^b. \tag{5.11}$$

We distinguish in Figure 5.16 two different regimes. On one hand, for small temperature differences $b \approx 2.8$, while for bigger ones, $b \approx 1.16$. We will come back to this discussion later. We would like to point out, that the election of β to obtain $A(T_1, T_2)$ is not crucial, one obtains compatible results at least for $b \in [1.7, 2]$.

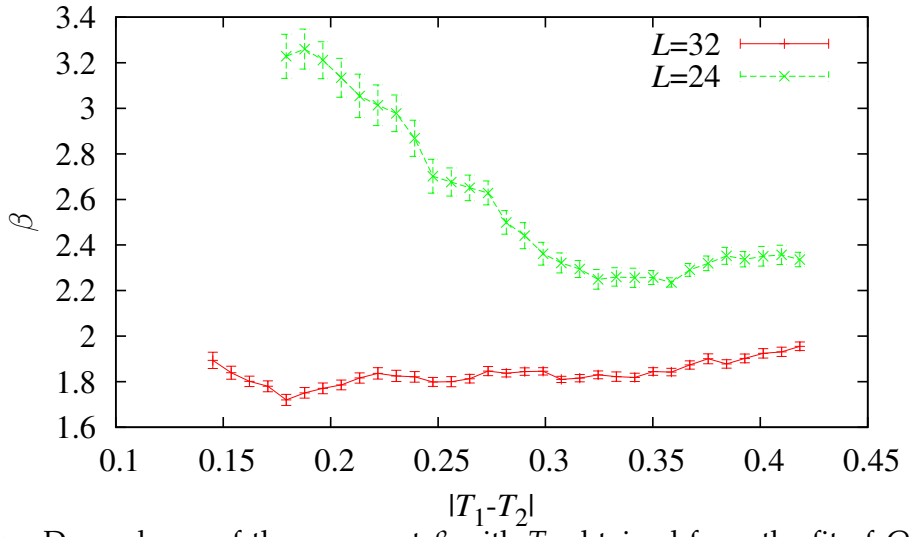

FIGURE 5.15: Dependency of the exponent β with T_2 obtained from the fit of $\Omega^L_{T_1,T_2}(\varepsilon)$ for $T_1 = 0.7026$ and $L = 32$ and 24, to the scaling function (5.9). The exponent for $L = 32$ obtained with the data the interval $\varepsilon \in [0.03, 0.4]$ obtaining a $\chi^2/dof \in [2.95/35, 11.3/35]$. The data for $L = 24$ was fitted in the interval $\varepsilon \in [0.05, 0.25]$. As discussed before, all the data are very correlationed, which means that errors in this figure are probably underestimated.

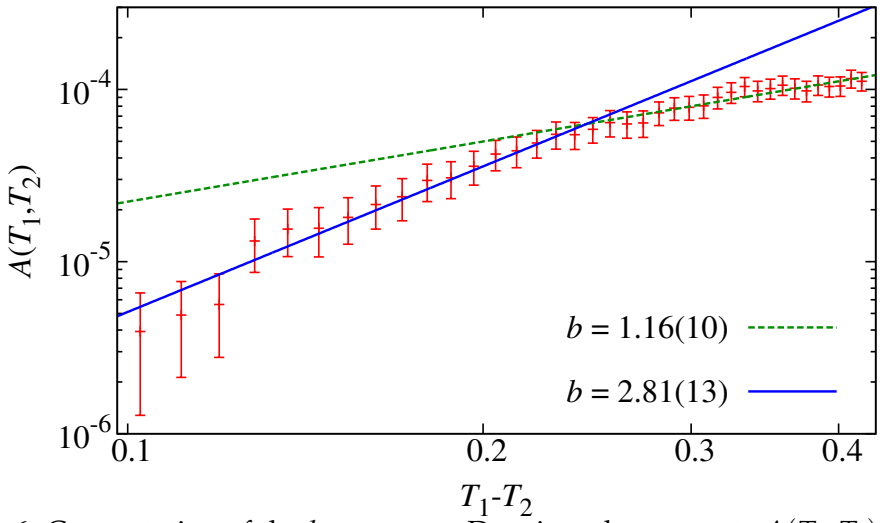

FIGURE 5.16: Computation of the b exponent. Data in red represents $A(T_1, T_2)$, lines in blue and green corresponds to the low and high values of T_2. Fitting data is displayed in the label.

5.5 Spatial correlation functions

As discussed in the introduction, almost all numerical work up to now was based on the scaling picture. In it, it is possible to identify the ζ exponent, associated with the correlation length by collapsing the curves $X_{T_1,T_2}(L)$ (averaged over all the samples in the system). This approached predicted a correlation length as well as its critical exponent which seemed to be recovered in simulations. Some authors argued [Aspo2], that the chaotic correlation lengths would be very large (in the order of the system sizes reached in simulations) to be observed in numerical work.

According to the above discussion, all measures of the correlation length in previous studies were obtained in an indirect way. Considering our discussion in Section 5.3, we argued that the averaged curves studied in previous studies had lost most of the chaos signal, so we did not believe that this phenomenological scaling study could carry information about chaos. To prove that, we compute directly the correlation length, by means of the spatial correlation functions. Indeed, now we defined the concept of chaotic event, we can compute the actual correlation length in a chaotic sample.

With this aim, we shall be considering here two types of spatial correlation functions. The simplest one is

$$C^J_{T_1,T_2}(r) = \frac{1}{3V} \sum_{\boldsymbol{r}=r\boldsymbol{e}_{x,y,z}} \sum_{\boldsymbol{x}} \left\langle s^{T_1}_{\boldsymbol{x}} s^{T_2}_{\boldsymbol{x}} s^{T_1}_{\boldsymbol{x}+\boldsymbol{r}} s^{T_2}_{\boldsymbol{x}+\boldsymbol{r}} \right\rangle_J , \tag{5.12}$$

which is the two temperatures version of the equilibrium spatial correlation function c_4 introduced in (3.62) but averaged over all the $\boldsymbol{r}$ of the form $\boldsymbol{r} = r\boldsymbol{e}_i$, with $i = x,\ y,\ z$.

Alternatively, in analogy with the chaotic parameter $X^J_{T_1,T_2}$, we may consider also a renormalized function:

$$K^J_{T_1,T_2}(r) = C^J_{T_1,T_2}(r) / \sqrt{C^J_{T_1,T_1}(r)\, C^J_{T_2,T_2}(r)}\,. \tag{5.13}$$

Note that computing these correlation functions is even harder (in number of operations' sense) than computing the overlaps. We discuss in Appendix B.2 how to take benefit of multispin coding to obtain these magnitudes.

Considering all the discussion performed before about chaotic events, we cannot average the two correlation functions over all samples if we want to keep track of the chaos phenomena. But we still have disorder and need to average in order to infer something about the thermodynamic limit. Our approach is the following: we compute separately the chaotic or the non chaotic spatial correlation functions by averaging only over the most chaotic samples or over the less chaotic samples. Of course we need a criterion to select which samples belong to each sets. We use the chaotic parameter $X^J_{T_1,T_2}$ for this purpose. Indeed, the lower $X^J_{T_1,T_2}$ the more

chaotic the sample is conversely the higher, the less chaotic. Then, our choice is to consider as chaotic (non chaotic) samples, the 10% of the samples for $L = 32$ with smallest (higher) $X^J_{T_1,T_2}$ and average within each group of samples. This selection (in our systems) is equivalent to the condition $X^J_{T_1,T_2} \leq 0.33$ or $X^J_{T_1,T_2} > 0.93$ for $T_1 = 0.7026$ and $T_2 = 0.90318$. We argued before that in thermodynamic limit all samples would be chaotic, then, only the average over the chaotic-samples is the one really representative of the thermodynamic limit. Actually, if one wanted to get a representative over the convergence to thermodynamic limit, one should average over samples with

$$X^J_{T_1,T_2} \sim 1/L^{D/\beta}|T_2 - T_1|^{-b}, \tag{5.14}$$

with β and b defined in (5.9).

We show in Figure 5.17 $C_{T_1,T_2}(r)$ either averaged over all the samples, or over the set of chaotic or non-chaotic samples. As expected, the behavior is qualitatively different when chaos is present, and the global behavior is more similar to the non-chaotic behavior than to the chaotic one. On the contrary as what scaling theory predicts, curves for the chaotic samples fall down at very short lengths, noticeable shorter than when there is no chaos. According to this, chaos can be detected even at very short distances (which contradicts all previous knowledge about it).

One can make this discussion quantitative by fitting the curves to decaying exponentials as expected for long distances (3.54), i.e.

$$C^J_{T_1,T_2}(r) \sim \exp[-r/\xi_C]/r^a, \tag{5.15}$$

in order to obtain the correlation length.

We found that all the $C_{T_1,T_2}(r)$ are extremely well fitted by a sum of two exponentials,

$$C_{T_1,T_2}(r) \sim \sum_{i=1,2} A_i\left(\mathrm{e}^{-r/\xi_i} + \mathrm{e}^{-(L-r)/\xi_i}\right), \tag{5.16}$$

in the range $2 \leq r \leq L/2$, see Figure 5.17 and Table 5.2 for the fitting details. According to our data, there is no need for a pre-algebraic factor, and thus $c \approx 0$. According to the the χ^2 test, see Table 5.2, the fits are extremely good. However, the resulting values of χ^2/dof are too small (smaller than $1/10$ for all four fits). The reason for that, is that we only use, as usual, the diagonal elements in the covariance matrix to compute χ^2 and the non-diagonal elements are very important here due to the large correlation of our data. Hence, the error estimates in the fitted parameters must be regarded as merely indicative.

As a summary of the the fits, on non-chaotic samples, the correlation length is $\xi_{NC} \approx L/2$ while, for the chaotic ones, $\xi_C \approx 6$ for $L = 32$ (or $\xi_C \approx 4$ for $L = 24$). Given the disparity of scales, it is not obvious how to estimate the *single* chaotic length of Refs. [Fis86, Bra87].

We include also show in Figure 5.17 the average over the $L = 32$ chaotic samples for $K^J_{T_1,T_2}(r)$. The renormalization with respect to $C_{T_1,T_2}(r)$ allows to fit to a single-exponential for $6 \leq r \leq L/2$. However, the renormalization causes a change

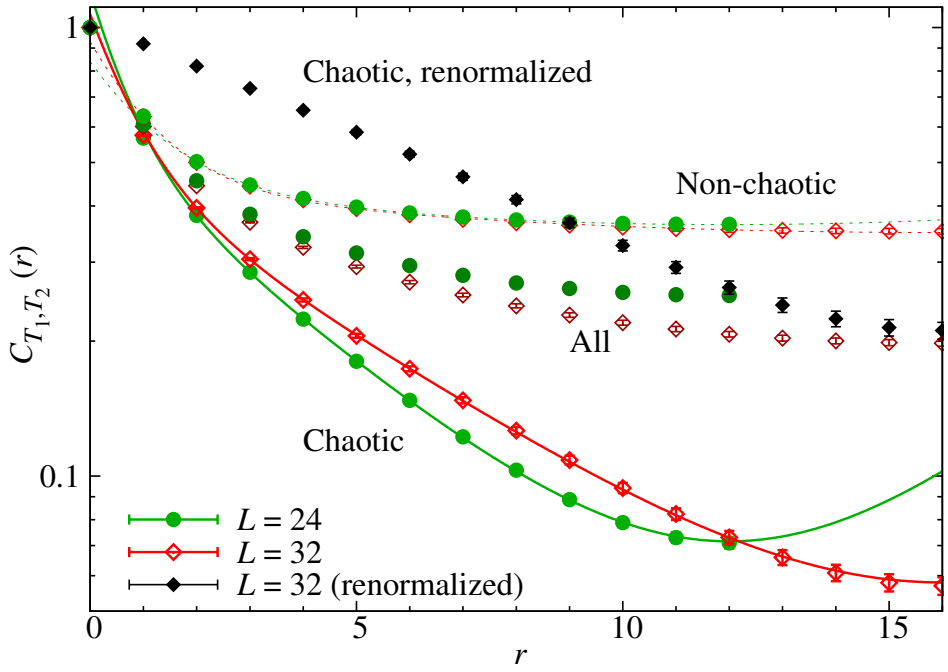

FIGURE 5.17: Spatial correlation function for $T_1 = 0.70260$ and $T_2 = 0.90318$, (5.12), as averaged over different sets of samples: all samples, non-chaotic samples ($X_{T_1,T_2} > 0.93$) and chaotic samples ($X_{T_1,T_2} \leq 0.33$). The filled black diamonds correspond to the average of $K^J_{T_1,T_2}(r)$ (5.13) over the $L = 32$ chaotic samples. Lines are fits to $\sum_{i=1,2} A_i\left(e^{-x/\xi_i} + e^{-(L-x)/\xi_i}\right)$. For each fit, the largest correlation lengths were $\xi^{L=32}_{\text{chaos}} = 5.69(2)$, $\xi^{L=24}_{\text{chaos}} = 4.447(15)$, $\xi^{L=32}_{\text{non-chaos}} = 23.7(7)$, $\xi^{L=24}_{\text{non-chaos}} = 18.9(3)$.

	$L = 32$		$L = 24$	
	Chaotic	Non-chaotic	Chaotic	Non-chaotic
A_1	0.483(3)	0.343(6)	0.531(3)	0.343(4)
A_2	0.59(6)	0.498(6)	0.67(10)	0.401(7)
ξ_1	5.687(22)	23.7(7)	4.447(15)	18.9(3)
ξ_2	0.84(4)	0.343(6)	0.70(5)	1.31(3)
χ^2/dof	1.03/11	3.3/12	0.5/7	0.3/7

TABLE 5.2: Fitting variables obtained by fitting $C_{T_1,T_2}(r)$, (5.12), averaged over the chaotic and not chaotic samples as defined in the text, to the curve $\sum_{i=1,2} A_i\left(e^{-r/\xi_i} + e^{-(L-r)/\xi_i}\right)$. The longest length corresponds to the correlation length.

of curvature in the small r region, that can be fitted for $r \geq 2$ as $(1+r^2)^{0.18/2}$ times a decaying exponential. Anyhow, we also obtain $\xi_C \approx 6$, in qualitative agreement with the estimate from $C_{T_1,T_2}(r)$. According to that, in the case of the spatial correlation function, there is no particular improvement in detecting chaos by using $K^J_{T_1,T_2}(r)$ instead of $C_{T_1,T_2}(r)$. In fact, $K^J_{T_1,T_2}(r)$ makes the fitting more difficult.

It might be quite shocking that the chaotic correlation length, though small in comparison with L, increases with the system size ($\xi_C \approx 6$ for $L = 32$ and $\xi_C \approx 4$ for $L = 24$). Our data seem to suggest a non finite correlation length. This somehow strange result is however what one should expect, as we discuss below.

Indeed, barring normalizations, $\langle q^2_{T_1,T_2}\rangle_J$ is the space integral of the correlation function (5.12), recall (3.55). Then, if one considers an exponential decay with r/ξ_C in (5.15) or (5.16), it follows that

$$\langle q^2_{T_1,T_2}\rangle_J \propto (\xi_C/L)^D. \tag{5.17}$$

Let us assume that, below T_c, both $\langle q^2_{T_1,T_1}\rangle_J$ and $\langle q^2_{T_2,T_2}\rangle_J$ are of order one (the EA parameter depends on L but has a finite large-L limit). Then, also

$$X^J_{T_1,T_2} \sim (\xi_C/L)^D. \tag{5.18}$$

Using this scaling, we are ready to discuss the size dependency of the chaotic length ξ_C. Indeed, let us plug (5.9) with $\beta \approx 1.7$ in (5.8). If the probability in (5.8) is to remain of order one for large L, then

$$X^J_{T_1,T_2} \sim 1/L^{D/\beta}. \tag{5.19}$$

Then, combining (5.18) with (5.19), one obtains

$$X^J_{T_1,T_2} \sim (\xi_C/L)^D, \tag{5.20}$$

which leads to

$$\xi_C \sim L^d, \tag{5.21}$$

with $d = (\beta-1)/\beta \approx 0.4$. In other words, the chaotic correlation length increases with L, but still is very small as compared with the system size. In other words, $\xi_C/L \to 0$ for long L.

Let us come back to the spatial correlation scaling (5.15). Our data suggest that, at least for our system sizes, there is no need of algebraic pre-factor, i.e. $a \approx 0$. However, in numerical work it is not possible to distinguish a very small a from the clean 0 value. Besides, let us discuss briefly the effect in the previous scaling of an hypothetical pre-factor. Then, we consider the case $a \neq 0$. It follows that

$$\langle q^2_{T_1,T_2}\rangle_J \propto \xi_C^{D-a}/L^D, \tag{5.22}$$

which would lead to

$$\xi_C \sim L^{D(\beta-1)/(\beta(D-a))}. \tag{5.23}$$

The above conclusion is shocking: the chaotic-length [Fis86, Bra87] is expected to be infinite for large L. Actually, only $\beta = 1$ in (5.9) would be compatible with a finite ξ_C (recall we obtained $\xi_C \sim L^{(\beta-1)/\beta}$), and our data suggests a β clearly above this value. However, mean-field results [Par10] warns about transient effects. In fact, in mean-field, for small overlap and $|T_1 - T_2|$, the large-deviations potential scales as

$$\tilde{\Omega}^{\text{mean-field}} \propto A q^2_{T_1,T_2} |T_1 - T_2|^3 + B |q_{T_1,T_2}|^3 |T_1 - T_2|^2 , \tag{5.24}$$

(A and B are constants). Either of the two terms can be dominant for some region of q, N and $T_1 - T_2$ (N is the number of spins). We now let N grow at fixed $T_1 - T_2$, and seek q such that $\tilde{\Omega} \sim 1/N$ [i.e. probability of order one, see (5.8)]. We realize that there is a crossover size $N^* \sim |T_1 - T_2|^{-5}$ such that $q^2 \sim N^{-2/3}$ if $N \ll N^*$. On the other hand, if $N \gg N^*$, $q^2 \sim N^{-1}$: the mean-field prediction for (5.9) is $\beta = 1$. That means that in MF it is possible to define a finite correlation length. This might be quite strange if one thinks in SK model 3.4.3, where no notion of distance or at least neighborhood exists. However, in this precise model, as discussed in the introduction, all the coefficients in the perturbation in q below $|q|^9$ ($\beta = 4.5$) vanish [Riz03, Par10]. On the other hand, the Eq. (5.24) was obtained for Bethe lattices discussed in Sect. 4.2, where although distance is not yet well defined, there exists a notion of neighborhood.

5.6

Phenomenological scaling

A question arises at this point: if the chaotic-length is not finite (at least for our system sizes that yield $\beta \approx 1.7$), what is the chaos exponent ζ computed in previous works [Sas05, Kat07]? We argue that this exponent is actually $\zeta = D/b$ [b is the temperature-difference exponent in (5.9)]. According to that, the exponent ζ would be unrelated to the chaotic length.

Indeed, some reflection reveals that phenomenological renormalization [Kat07] can be cast as follows. For the purpose of discussion, we fix the lowest temperature T_1. Then, for each L, we find a $T_2(L)$ such that the probability distribution function for $X^J_{T_1,T_2(L)}$, becomes L-independent, see Figure 5.18–top. The scaling picture is based on the statement that $X_{T_1,T_2} = F\left(\xi_C(T_1,T_2)/L\right)$, with F a universal function and $\xi_C(T_1,T_2)$ following the scaling

$$\xi_C(T_1,T_2) \propto \left[\frac{\gamma(T_1)}{\sigma(T_1)|T_2 - T_1|}\right]^{1/\zeta} . \tag{5.25}$$

Then, once collapsed all the curves, the exponent ζ of Ref. [Kat07] follows from $L \propto |T_1 - T_2(L)|^{1/\zeta}$. In fact, we can fit our data to

$$T_1 - T_2(L) \propto 1/L^{\zeta}, \tag{5.26}$$

obtaining $\zeta = 1.02(3)$ (for $L \leq 32$, $T_1 = 0.7026$ and $T_2(L = 8) = 0.90318$, with $\chi^2/\text{dof} = 3.57/3$) or $\zeta = 1.07(2)$ (for $L \leq 24$, $T_1 = 0.625$ and $T_2(L = 8) = 0.815$, with $\chi^2/\text{dof} = 1.77/2$). These results are compatible to the exponent $\zeta \approx 1.07$ obtained in [Kato7].

On the other hand, if we combine (5.8) and (5.9), we obtain that the phenomenological renormalization amounts to

$$L^D |T_1 - T_2(L)|^b = \text{constant}, \tag{5.27}$$

which is equivalent to $\zeta = D/b$.

We have already computed b, see the fits in Figure 5.16. We discussed then that there seem to be two different regimes. For $|T_1 - T_2(L)| < 0.25$ we got $b = 2.81(13)$, which implies $\zeta = 1.07(5)$, which in excellent agreement with [Kato7] and with the data collapse just discussed shown in Figure 5.18—bottom. We note, however, that this b value only applies for small $|T_1 - T_2(L)| < 0.25$, when the chaotic events are extremely rare for our system sizes. In a nutshell, the phenomenological renormalization applies where chaos is not present. It is thus not surprising that their results hold also in the paramagnetic phase.

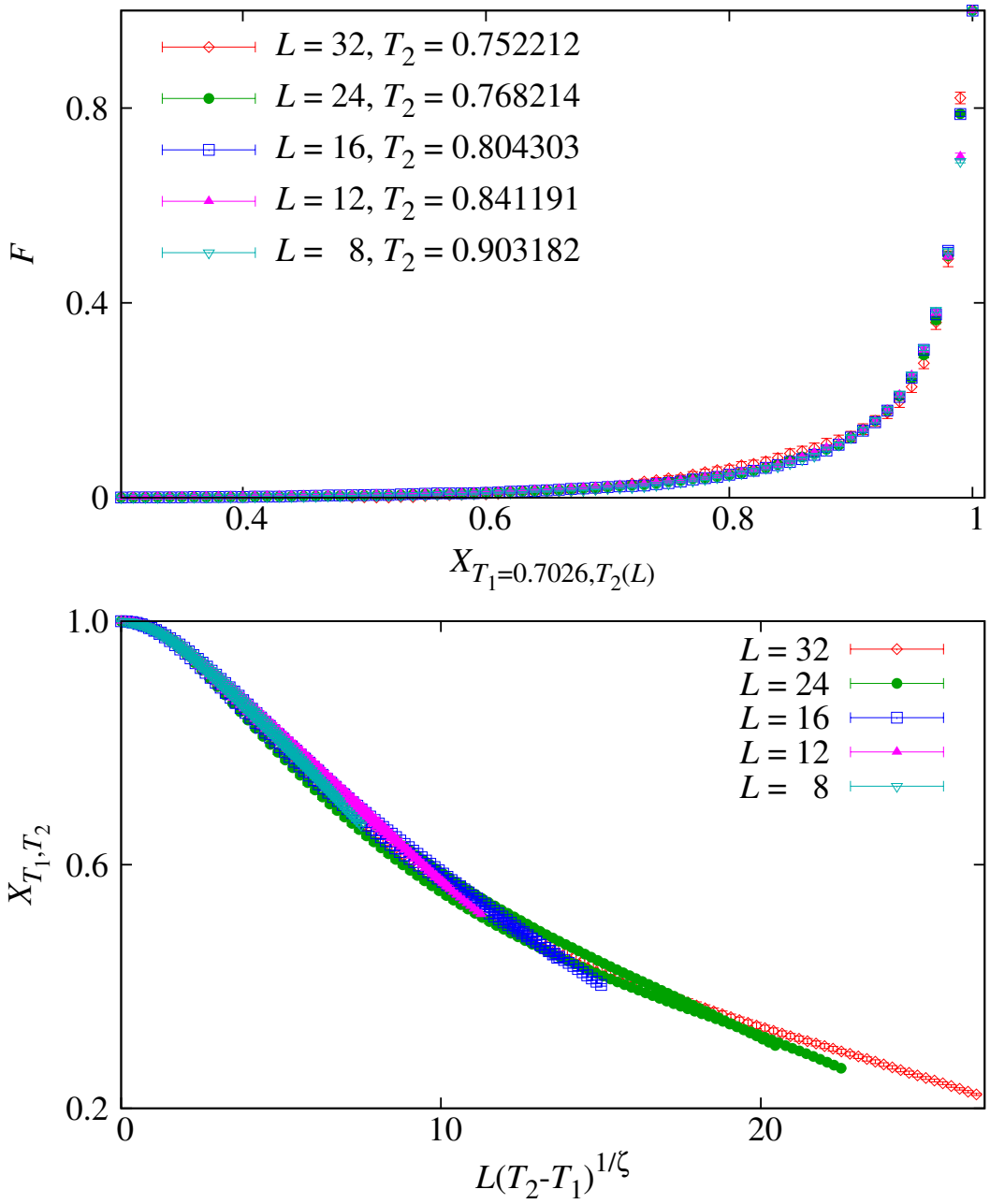

FIGURE 5.18: **(Top)** Phenomenological renormalization: for each L, we seek $T_2(L)$ such that the distribution function $p\left(X^J_{T_1=0.7026,T_2(L)} \leq \varepsilon\right)$ best resembles the $L = 8$ distribution for $T_1 = 0.7026$ and $T_2 = 0.90318$. **(Bottom)** Sample-averaged $X^J_{T_1,T_2}$ vs. $L(T_1 - T_2)^{1/\zeta}$ using $\zeta = 1.06$ (data for $T_1 = 0.7026$ and, when $L \leq 24$, also for $T_2 = 0.625$). The data collapse is found both for $T_2 < T_c$ and for T_2 in the paramagnetic phase.

5.7

Overlap equivalence

The fact that the chaotic samples have a fairly small correlation length suggests to ask whether chaos might be detected even at distance $r = 1$. This quantity is nothing but the link-overlap (3.61) but defined for two temperatures

$$Q^{\text{link},J}_{T_1,T_2} = \frac{1}{zN} \sum_{\langle ik \rangle} q_i^{T_1 T_2, J} q_k^{T_1 T_2, J}\,, \tag{5.28}$$

where the sum runs on the nearest neighbors $\langle ij \rangle$. With this aim, we perform the same study we did for $X_{T_1 T_2}$ in Figure 5.7 but this time for an analogous $X^{\text{link}}_{T_1 T_2}$ defined as

$$X^{\text{link},J}_{T_1,T_2} = \frac{\left\langle Q^{\text{link},J}_{T_1,T_2} \right\rangle}{\sqrt{\left\langle Q^{\text{link},J}_{T_1,T_1} \right\rangle \left\langle Q^{\text{link},J}_{T_2,T_2} \right\rangle}}, \tag{5.29}$$

as shown in Figure 5.19. The results are very much the same that the ones discussed in Section 5.3. In fact, the notion of *chaotic event* makes just as much sense if we study the link overlap. This fact suggests the overlap-equivalence property discussed in Section 3.6.2. As discussed then, the overlap equivalence leads to the notion of ultrametricity, and this time, it is between overlaps at different temperatures, which somehow contradicts oversimplified pictures of temperature chaos as a scale-separation phenomenon [Ber02a] discussed in Section 3.3.3 and suggests an explanation based on a hierarchical structure of states as the one discussed in Section 3.5.

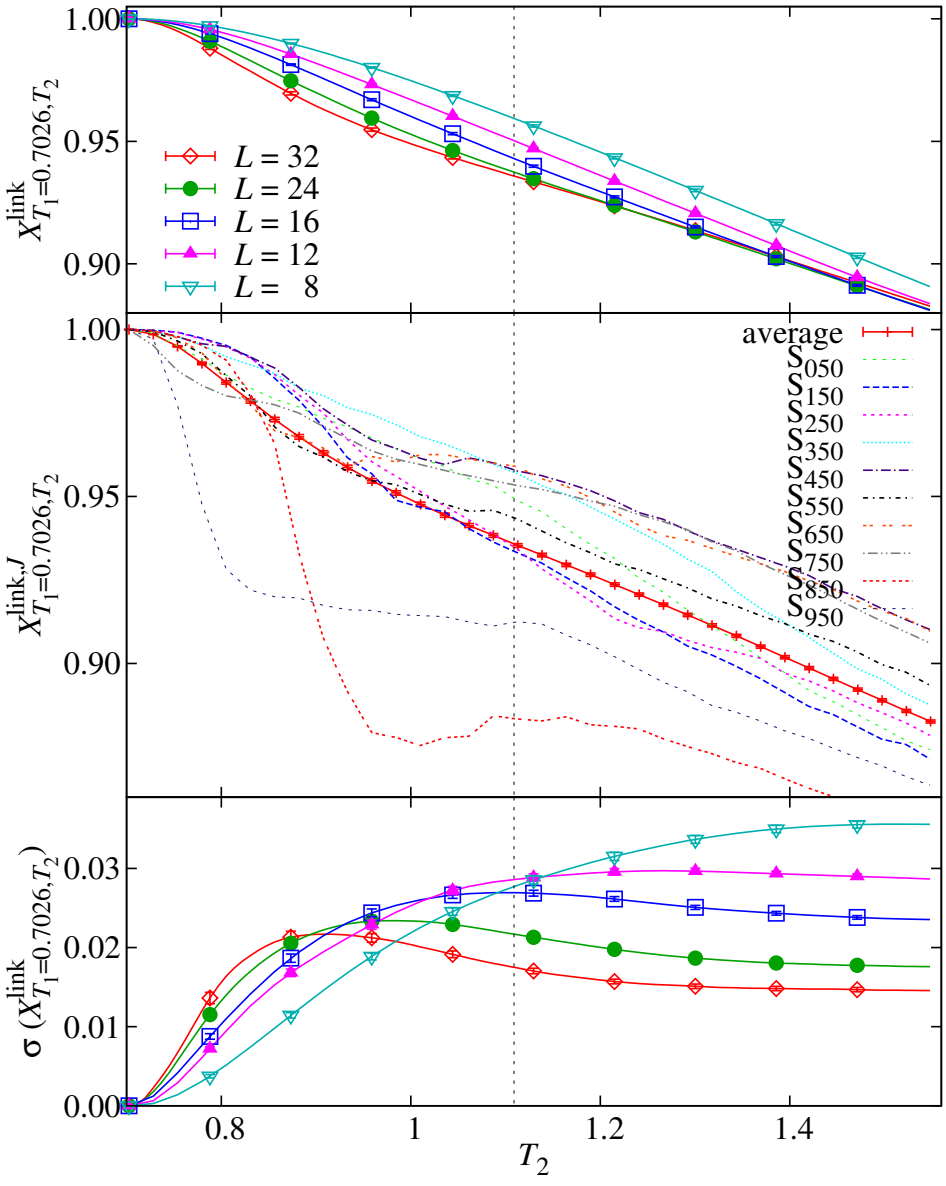

FIGURE 5.19: Analogous of Figure 2 of the main text, but for $X^{\text{link}}_{T_1,T_2}$.

Part II

Colloids

CHAPTER VI

Introduction to colloidal systems

6.1

The problem

We devoted all the Part I of this thesis to the study of the effect of inherently disordered interactions on magnetic systems. As discussed then, the low temperature phase is characterized by a frozen disordered orientation of the spins. At variance with other problems in condense matter, the spatial ordering of the impurities is not an important feature of the spin glass phase (although there is other kind of order, as already discussed). This fact let us to model them as lying on a regular lattice and simplify the theoretical calculations, as well as to speed up the computer simulations. For this last reason, the effect of disorder has been extensively addressed in lattice systems (spin glasses, magnetic materials in random field, etc.) while the situation in off-lattice systems is much less understood. In this Part II, we tackle the same problem but this time in colloidal or liquid systems. In these systems, disordered interactions can be induced by for instance, a random distribution of charges, polymer chain lengths, or particle sizes as we shall consider here.

Let us make some general considerations about disorder in statistical mechanics. There are two well defined limits [Par92]. The first one, the *quenched* disorder, was introduced in the Part I when studying spin glasses. As discussed in Section 3.2, the spin glasses are alloys, normally a core of metal with a few magnetic impurities that carry the spins. These impurities are in random positions after the synthesize process (inducing the random interactions), but interactions make them diffuse although at geological times as compared with the spin evolution characteristic times. For this reason, the *quenched* approximation assumes that the spin configuration has no influence in the distribution of disorder. Then, we always seek the equilibrium configuration of the spins within a given fixed realization of disorder (sample). With this approach we are not considering the much stabler minimum achieved after the equilibration of the impurities (a ferromagnet dot in a

non-magnetic matrix, for instance) since the time at which it would be relevant is far beyond our experimental window. The opposite limit is observed in the fluid phase of the systems considered here. Now the particles (carrying the disorder on their random size) can easily diffuse through the total volume but this diffusion is very influenced by the instantaneous distribution of disorder. Indeed, the particles tend to crowd with those of similar size since the small ones diffuse faster than the big ones. This kind of disorder where there is not clear scale separation between distribution of disorder and the particle motion, is known as *annealed* disorder.

However in colloidal systems, when considering the solid phase, the diffusion is almost suppressed, and the equilibration of disorder occurs at much longer times than local formation of crystal clusters. For instance, a big particle could minimize the free-energy by locating in a conglomerate far away in the system, but if gets trapped in a crystal structure will hardy ever move. This situation is better described by the quenched than the annealed approximation. This problem is not clearly recognized in literature. In fact, among the chemical physics' community, it has become fairly common the use of semi-grand canonical ensembles to approach these kind of systems [Sol10]. These ensembles accelerate the annealing dynamics by changing the disorder. These algorithms are indeed very powerful to study the fluid phase, but when applied to the solid phase, the equilibrium obtained corresponds to the relevant state at much longer time-scales that what can be found in experimental times (when the disorder equilibrates). In fact, these simulations lead to a fractionation scenario (see the discussion below) and phase diagrams that are not observed in experiments [Lid11].

In spite of this conceptual problems, the solid phases are also important. Indeed, most fluids become crystalline solids upon cooling or compression. Then, crystallization is a vast field of research, where a fruitful exchange is achieved between experiments and theory. Consider, for instance, the simplest model of fluid, the hard spheres (HS). The numerical finding of a fluid-solid phase transition [Ald57, Woo57] motivated experiments on colloidal suspensions [Pus86a, Pus89]. Nowadays, an accurate assessment of the equilibrium phases (and phase-boundaries) for colloids is crucial to address novel challenges for statistical mechanics, such as super-solidity (as modeled by quantum HS) or self-assembly (the spontaneous organization of particles into desired arrangements). Moreover, the custom design of particles with non-spherical interaction potentials (Janus particles) opens exciting opportunities [Man03, Glo07], but puts further demands on numerical work [Sci09, Rom11].

It seems reasonable that if the size dispersion δ (i.e. the ratio of the particles' size dispersion with the average, see definition in (7.1)) is very high, it would be difficult to accommodate the particles in a lattice structure and thus the crystal phase should somehow destabilize. Experiments confirm this hypothesis. In fact, crystallization of very viscous colloidal samples with δ larger than 12% does not occur, even after several months spent from the sample preparation [Pus86b]. This leads to several basic questions about the equilibrium phase diagram of polydisperse systems [Bar98, Kof99, Aue01, Fas04, Dul04, Cha05, Fer07b, Bra09, Zac09a, Wil10,

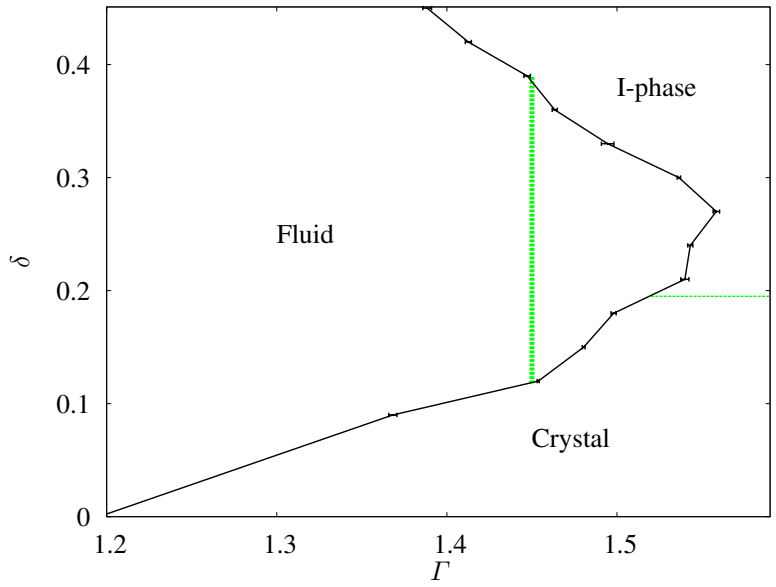

FIGURE 6.1: Phase diagram $\delta - \beta$. The green vertical line corresponds to the dynamical glass transition, while the black one refers to the freezing transition. Figure taken from [Fer07b].

Sol10]. Does enough large polydispersity hinder crystallization? Is the suppression of crystallization a dynamical effect arisen from the low diffusivity of large particles [Eva01], the interplay with the glass transition [Bra09, Zac09a, Fer07b] or anomalously large barriers [Aue01]? Is the glass phase stable rather than only metastable? And, probably at a more fundamental level, is thermodynamic equilibrium relevant at all to describe real polydisperse materials or these are instead inherently off-equilibrium over the experimental time scales? Answering such questions is crucial for condensed matter physics, since polydispersity is found both in artificial (synthetic colloids, polymers) and natural systems, from supercooled liquids on the atomic scale up to biological fluids such as blood.

An attempt to rationalize the experimental findings is the so-called terminal polydispersity scenario where a characteristic value $\delta_t \sim 0.12$ exists above which the homogeneous crystal becomes thermodynamically unstable (see the phase diagram in Figure 6.1). There is not consensus however about what kind of structure should replace such single phase crystal. Density functional analysis [Cha05] predicts the instability of any crystal structure (even partial) above δ_t, thus leaving the amorphous ones (either liquid or solid) as the only possibility. Yet, the moment free-energy approach [Fas04] predicts *fractionation*: phase separation between many crystal phases [though of the same ordering, face centered cubic (FCC) for instance], each one with a much narrower size dispersion than δ. Fractionation is supported by a recent numerical simulation that found that a first-order fluid-solid transition actually occurs at any polydispersity [Fer07b]. However, the found solid phase is quite complex, at least in the high polydispersity region. In fact, for

$\delta > 0.19$ the transition regards only a fraction of the particles and the ordered state is inhomogeneous. Such state has been previously referred to as I-phase [Fer07b] (I stands for inhomogeneous).

In this part of the thesis, the final goal is to study the phase diagram for this high polydispersity region and the properties of this new solid phase using computer simulations. Approaching equilibrium in this kind of systems is very discouraging, the equilibration times become excessively large for numerical purposes even for rather small systems. In fact, the typical numerical equilibrium studies cover only $N \lesssim 500$ particles which must be compared with the $N = 2^{22}$ (Chapter 4) or 32^3 (Chapter 5) spins studied for lattice systems. The difficulties we must face can be summarized in three points:

- First, at variance with lattice systems, such as the spin models studied in the Part I, the MC updates imply a random three dimensional displacement instead of just a spin flip. In addition, particles can diffuse, and then, the nearest neighbors are no longer fixed. This means that computing energies for the Metropolis updates would, in principle, imply $N^2/2$ operations. However, if the interaction is short-ranged, one can reduce the problem to $O(N)$ as we shall discuss below.

- Second, when $\delta > 0$, the system suffers from the dynamic glass transition. This fact results in a divergence of the relaxation times, and thus the equilibration times as well. Simulated typical Brownian dynamics get completely stuck as it happens in experiments, and optimized MC methods (implying not physical moves) must be introduced. In fact, the *swap* algorithm [Gri01a, Fer06b, Fer07a] accelerates the dynamics and makes possible to thermalize large systems below the kinetic glass temperature.

- Third, the freezing transition is first order, and then, suffers from exponential dynamic slowing down (EDSD). Indeed, in the vicinity of the transition two or more phases are metastable at the simulation conditions. Therefore, all these phases should be found in an equilibrium simulation. The system tunnels between these phases by building interfaces of size of order L^2 whose free-energy cost is $\beta\gamma L^2$ (being γ the surface tension).[1] Then, the probability of creating such an interface is $\exp\left[-\beta\gamma L^2\right]$ and thus the natural time scale for the simulation grows exponentially with $N^{2/3}$. This effect could be neutralized if one could constrain the simulation to one single phase. This can be done by choosing properly the order parameters so that there are not multiple metastable states. In other words, if one could avoid jumps between phases (they are informally named as *flip-flops*). This EDSD is, by far, the hardest of the three problems presented in here, and going beyond it has been one of our main purposes of this thesis.

[1] The number of particles is proportional to the overall volume by means of the relation $N = \rho L^3$, where ρ is the density of particles. Hence, if ρ is fixed, $L \sim N^{1/3}$.

Finding computational strategies to speed up the simulations is specially important in off-lattice systems, where the amount of available efficient methods is very reduced as compared to its lattice counterpart. For this reason, a large part of our efforts have been put in proposing new algorithms to study this kind of systems. We will devote more time to algorithm description than in Part I of the thesis, where we used rather standard methods. In particular, it was necessary to move among many statistical ensembles, some of them standard, some of them not: we go from the regular ones (canonical, isobaric and microcanonical) to end up with new ones, original from this thesis: the isocorical and the tethered ensembles as applied to a first order transition. We include a summary of all them in Appendix D.

6.2

Research outline: Beating the exponential dynamic slowing down

This Part of the thesis is based on three papers [Fer10b, MM11, Fer12b], as well as some unpublished failed trials. Our break through in this problem is a story of an underestimated problem, unsuccessful approaches, upcoming new questions and steps back to simpler problems that were finally solved. For this reason, I decided to present this part the thesis, not only as a summary of the physical results we obtained, but also as a description on the research path we followed. In other words, I will structure this part of the thesis in a chronological order.

The starting point was the problem discussed above, the study of the phase diagram in polydisperse systems but paying special attention to the high-polydispersity region, where the standard simulation methods fail to thermalize even for very small systems. The origin of this divergence in equilibration times is precisely the fluid-solid first-order transition and its associated EDSD mentioned above.

If one seeks to mimic the experiments, the appropriate ensemble should be the NpT ensemble (constant pressure). Of course, in equilibrium one expects ensemble equivalence in the large-N limit, but the convergence to it can be significantly different from one statistical ensemble to other. For this reason, our first naive proposal was that, since in nature the NpT situation are preferred, so should they be in numerical simulations. The results clearly contradict this statement, we find strong metastabilities that leads to very long thermalization times. One could anticipate this result easily. Indeed, the fluid and the solid phase have different characteristic volumes, and since the volume fluctuates in this ensemble, both phases can be accommodated at the same pressure.

According the last naive explanation, the direct solution would be to fix the total volume in the system. However, the same problem was studied with NVT simulations in [Fer07b] and the same behavior was observed. Indeed, one can define the pressure using the virial equation, for instance, and also a different pressure

can accommodate the two involved phases in the same volume. At that moment is clear that not all the magnitudes that suffer a discontinuity at the transition are proper *reaction coordinates* (magnitudes that describe univocally the reaction path).

Then, our goal from that point on was to identify an ensemble that forbids metastabilities at all simulation conditions. In fact, if phase-tunneling can be avoided, there are no reasons to expect EDSD. Since this objective has been fulfilled in simulation studies of first order transitions in lattice magnetic systems, we can try to export their solutions. Now, our bet was that the microcanonical ensemble, that was determinant to prove the first-order nature in the disordered Potts model [Fero8a], should also split up the fluid and the solid phase here.

Following this intuition, we implemented the microcanonical Monte Carlo method strategy [Lus98, MM07] to the problem studied in [Fero7b] for $\delta = 0.24$ (large polydispersity, in the region where no crystal is stable). This study is presented in Chapter 7, which is based on Ref. [Fer10b]. Unfortunately, as we shall discuss, the energy turned out not to be a good reaction coordinate in this particular problem. In plain words, we still suffered from EDSD. Even though the main strategy to thermalize had failed, we still could improve over previous work and to thermalize in the solid phase thanks to the combination of this microcanonical MC algorithm with a modified version of the Parallel Tempering (PT) algorithm [Huk96, Mar98].

At that point, the physics of the problem was clearer to us. However, we still could not make a clear breakthrough in the size of the systems that could be thermalized. Indeed, we could equilibrate samples but more with brute force (very long simulations) than thanks to a clever election of the simulation methods. Nevertheless, we were not placed at the same point that we were at the beginning: now we knew that the microcanonical strategy failed because the first-order transition actually corresponded to a phase separation in our problem. We needed an order parameter that controlled the size of the segregated regions of solid phase growing in the fluid.

However, if these metastabilities really arose from a phase separation, this very same problem should come up in any kind of solidification/melting problem, not necessarily related to disorder. In particular, it should arise in the simplest possible problem: the crystallization of monodisperse hard spheres. The HS freezing transition is well established since 1968 [Hoo68], but, to our surprise when reviewing thoroughly the literature, not even at HS level the EDSD problem was controlled. At this stage, we decided to step backward, and to seek a method that truly controls the crystallization in this simple model. This goal is achieved in Chapter 8, which is based on Refs. [MM11, Fer12b].

Once the mechanism is fully understood, we would return to the original and more interesting problem. This last step is beyond this thesis, but we would like to emphasize that the tools developed here will be extremely useful for further studies not only in polydisperse soft spheres, but also for any problem involving a first-order transition.

6.3

Crystalline order parameters

In this section we introduce the standard crystalline order parameters used in the modern crystallization studies. The parameter discussed here was introduced by Steinhardt *et al.* in 1983 [Ste83]. It will be studied in the two following chapters, and for this reason, we decided to place its discussion in a common section. As we shall see, some details in the definition need to be tuned, so we will take up the discussion again in each related chapter. In addition, we want to note that in Chapter 8 we will introduce an extra crystalline order parameter, but we leave its definition to that moment.

The main task of the parameter discussed here is to measure both the local and the extended orientational symmetries. For this reason, these kind of parameters are also called bond-orientational order parameters. The idea underlying its definition is to consider a "bond" joining each couple of "nearest neighbors" (even though they do not necessary interact, as in hard spheres).[2] This "bond" has the direction of the vector that joins the centers of the particles i and j, i.e. $\boldsymbol{r}_j - \boldsymbol{r}_i$. We do not work with perfect lattices in general, then each particle i will have a different number of neighbors, namely $N_b(i)$.

For each particle, we associate a spherical harmonic $Y_{lm}\left(\theta(\hat{\boldsymbol{r}}), \phi(\hat{\boldsymbol{r}})\right)$ to each of its outgoing bonds, where $\hat{\boldsymbol{r}}$ is the unit vector along the bond direction. We are only interested in the bonds' orientation, not in their direction. For this reason, we will only consider even values of the quantum number l. Now, summing up over all the $N_b(i)$ bonds, we obtain each particle contribution,

$$q_{lm}(i) \equiv \sum_{j=1}^{N_b(i)} Y_{lm}(\hat{\boldsymbol{r}}_{ij})\,. \tag{6.1}$$

Using this approach, the bonds that belong to a crystal structure will add up constructively, while the total contribution coming from random ordered neighbors would cancel out. As in the rest of magnitudes, we are interested in the overall structure, so we also average over all the particles in the volume,

$$Q_{lm} \equiv \frac{\sum_{i=1}^{N} q_{lm}(i)}{\sum_{i=1}^{N} N_b(i)}\,. \tag{6.2}$$

Finally, we sum up over all the rotationally invariant combinations to get a rotationally invariant operator,

$$Q_l \equiv \left(\frac{4\pi}{2l+1}\sum_{m=-l}^{l} |Q_{lm}|^2\right)^{1/2}\,. \tag{6.3}$$

[2] In an off-lattice system, the definition of nearest neighbor is, of course, arbitrary. In fact, we will use different definitions for monodisperse and polydisperse particles, but we postpone the discussion to the following chapters.

These Q_l are quasi-order parameters, in the sense that they are $\mathcal{O}(1)$ (independent of N) in a crystalline phase and $\mathcal{O}\left(1/\sqrt{N}\right)$ in a disordered phase. In particular we will be interested in the case where $l = 6$. This Q_6 has well defined values in perfect lattices,[3] in particular, $Q_6 \approx 0.574$ in a FCC and 0.510 in a body centered cubic (BCC). For defective crystals we should expect smaller values ($Q_6 \approx 0.4$ is fairly common).

[3]Defining the nearest neighbors as the particles in the first shell of neighbors.

CHAPTER VII

Polydisperse soft spheres

We devote this section to the problem largely described in Section 6.1 in the previous chapter. We use a microcanonical strategy that will be detailed in the following sections. This Chapter is based on [Fer10b].

7.1 The Model

We take as a paradigm for polydisperse off-lattice systems the polydisperse soft spheres (PSS) model. We consider particles of radius σ_i, with $i = 1, 2, \ldots, N$. The particle size σ_i is drawn from a probability distribution function (pdf) $P(\sigma)$. Size polydispersity is in general characterized by a single parameter, δ, defined as the ratio among the standard deviation and the mean of $P(\sigma)$:

$$\delta = \frac{\sqrt{\langle \sigma^2 \rangle - \langle \sigma \rangle^2}}{\langle \sigma \rangle}. \tag{7.1}$$

At least for small polydispersity, δ seems to be the only feature of $P(\sigma)$ that controls the physical results.

Our particles interact via a continuous pair potential:

$$V(x_{ij}) = \begin{cases} \epsilon \left[f(x_{ij}) - f(x_c) \right] & \text{if } x_{ij} < x_c, \\ 0 & \text{if } x_{ij} > x_c, \end{cases}$$

with,

$$f(x) = \frac{1}{x^{12}} + x, \quad x_{ij} = \frac{|\boldsymbol{r}_i - \boldsymbol{r}_j|}{\sigma_i + \sigma_j}, \quad \text{and } x_c = 12^{\frac{1}{13}}. \tag{7.2}$$

We take ϵ as energy unit. Note that we use the long distance cut-off of Refs. [Fero7a, Yano4a]. The existence of this cut-off allows us to divide the system in boxes so that the energy computation is only $O(N)$. Indeed, Eq. (7.2) tells us that two particles with radius σ_i and σ_j interact as long as $|\boldsymbol{r}_i - \boldsymbol{r}_j| \leq x_c(\sigma_i + \sigma_j)$. This has a straight-forward consequence: no couple of particles would interact for separations $|\boldsymbol{r}_i - \boldsymbol{r}_j| \geq 2x_c\sigma_i^{\max} = r^{\max}$. We can use this fact to divide our total volume in cubic cells of side $a \gtrsim r^{\max}$. Within this division, a given particle would only interact at most with the particles in each its 9 neighboring cells. Then, if one keeps a count on the cell in which each particle is contained, the number of total interactions to compute the total energy becomes $O(N)$ instead of the number of pairs, $N(N-1)/2$.

Although (7.2) generalizes well known models for simple liquids [Han86], its scale-invariant form suggests that it may describe as well colloids, whose size is in the micrometer range. In fact, the interaction in (7.2) is short-ranged as it is appropriate for colloidal systems.

Our length unit, σ_0, is fixed by

$$\sigma_0^3 = \int \mathrm{d}\sigma_i \mathrm{d}\sigma_j P(\sigma_i) P(\sigma_j) (\sigma_i + \sigma_j)^3 \,. \tag{7.3}$$

We simulated N particles in a box with periodic boundary conditions at density $\rho = \sigma_0^{-3}$. Due to the scale invariance of the potential, the thermodynamic parameter that controls the problem is the combination $\Gamma \equiv \rho\, T^{-1/4}$ (T is the temperature).

Here we study the case where the size distribution is flat (constant in the range $[\sigma_{\min}, \sigma_{\max}]$). Sample-to-sample fluctuations, as discussed for spin glasses in Part I, are eliminated by picking the diameters in a deterministic way [Sano1, Fero7b],

$$\sigma_i = \sigma_{\min} + (i-1)\frac{\sigma_{\max} - \sigma_{\min}}{N-1} \,. \tag{7.4}$$

The polydispersity of the system is thus given by

$$\delta = \frac{1}{\sqrt{3}} \frac{(r-1)}{(r+1)}, \text{ with } r = \frac{\sigma_{\max}}{\sigma_{\min}} \,. \tag{7.5}$$

Hence, $\sigma_{\max}/\sigma_{\min} \to \infty$ at $\delta_\infty = 1/\sqrt{3} \approx 0.57735$.

The phase diagram for this model is shown in Figure 7.1. It was obtained in [Fero7b] with simulations in the (N, V, T) ensemble. Let us sketch the main features obtained in this previous work. First, a fluid-solid transition (in black lines in Figure 7.1) is always found for any polydispersity δ. This last fact rules out the final polydispersity scenario. However, even though there is a solid phase thermodynamically stable for each δ, it might be dynamically inaccessible in experimental times due to the presence of the kinetic glass transition (in green). The exact location of the kinetic glass transition can be obtained using the same criterion than in a experiment. That is, simulating Brownian motion dynamics (standard MC steps), and locating it at the point where the relaxation time τ reaches the 10^6 MC steps

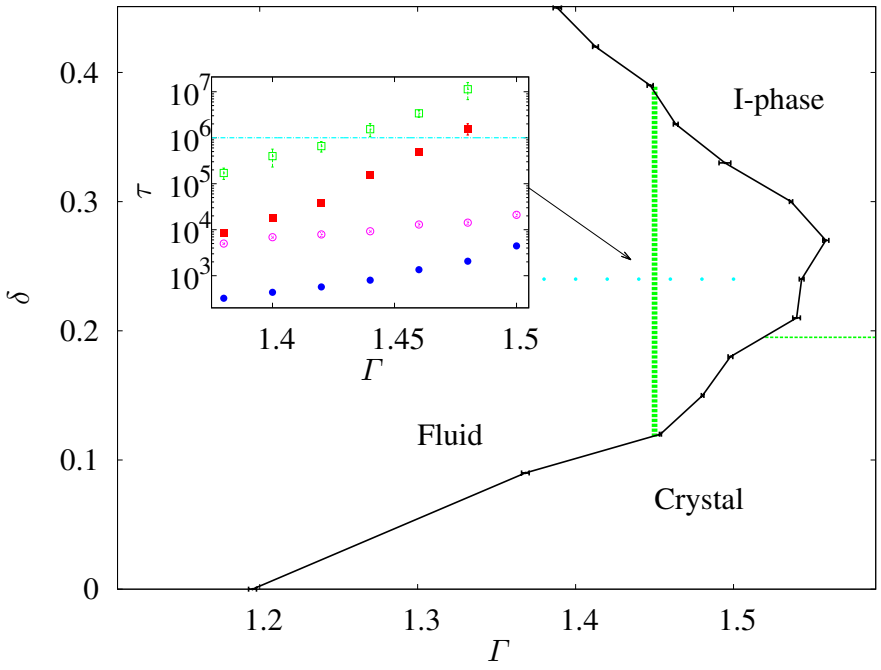

FIGURE 7.1: Phase diagram $\delta - \beta$. The green vertical line corresponds to the dynamical glass transition, while the black one refers to the freezing transition. (Inset) Integrated relaxation time for several observables for standard (squares) and local swap (squares) MC updates. Figure taken from [Fero7b].

(see inset in Figure 7.1). For colloids a standard MC step corresponds roughly to 0.01 seconds of experimental time [Simo4], then, this choice is equivalent to relaxations of $\sim$ 3 hours of physical time. Both for $N = 500$ and 864 particles, we find that $\Gamma_g = 1.455(5)$. With this definition, there is a region in polydispersities $\delta \in [0.12, 0.38]$, where the the dynamic glass transition occurs in the stable rather than in the metastable fluid region. In this work, we focus precisely in this high polydispersity region, in particular, we will fix $\delta = 0.24$.

In previous studies, it was shown that the local swap algorithm (a modified version of the global swap discussed in Section 7.3.1) accelerated by several orders of magnitude (see inset in Figure 7.1) the dynamics below Γ_g. However, the situation above this value is rather more difficult. Indeed, the local swap helps to avoid the cage effect that origins the glass transition. In the case of solidification, the effect of the swap is not enough to counteract the effect of the previously discussed exponential dynamical slowing down associated to the first-order transition. Actually, the thermalization deep into the solid phase was not even attempted in [Fero7b].

7.2

The constant energy ensemble

As we already discussed in Chapter 6, our first proposal to overcome the EDSD was to work in the microcanonical, (N, V, E), ensemble (see Section D.4 for a description of the statistical ensemble). Specifically, we use the Lustig's microcanonical Monte Carlo [Lus98] in the formulation of [MM07].

In this ensemble, the total energy per particle, e, is fixed. Within this description, the microcanonical average of an arbitrary function of the particle positions $\{\boldsymbol{r}\}_i$ and of the energy density e, $O(\{\boldsymbol{r}\}_i; e)$ is obtained using the following expression

$$\langle O \rangle_e \equiv \frac{\int \prod_{i=1}^{N} \mathrm{d}\boldsymbol{r}_i \, O(\{\boldsymbol{r}\}_i; e) \omega_N(\{\boldsymbol{r}\}_i; e)}{\int \prod_{i=1}^{N} \mathrm{d}\boldsymbol{r}_i \, \omega_N(\{\boldsymbol{r}\}_i; e)}, \tag{7.6}$$

where the weight is given by

$$\omega_N(\{\boldsymbol{r}\}_i; e) = (e-u)^{\frac{N}{2}-1} \theta(e-u), \tag{7.7}$$

with $u = U/N$, with U the total potential energy, defined as

$$U(\{\boldsymbol{r}_i\}) = \sum_{i<j} V\left(\frac{|\boldsymbol{r}_i - \boldsymbol{r}_j|}{\sigma_i + \sigma_j}\right), \tag{7.8}$$

where $V(r)$ is the soft-spheres interaction introduced in (7.2).

7.2.1 Observables

7.2.1.1 The inverse temperature

As it is discussed and obtained in Appendix D, the main observable in a microcanonical simulation is the inverse temperature, computed as a microcanonical expectation value at fixed energy e:

$$\beta(e) \equiv \langle \hat{\beta} \rangle_e, \quad \hat{\beta} = \frac{N-2}{2N(e-u)}. \tag{7.9}$$

The function $\beta(e)$ holds the key to connect the microcanonical formalism with the canonical one. Indeed, the *canonical* probability density for e,

$$P_\beta^{(N)}(e) \propto \exp[N(s_N(e) - \beta(e)e)], \tag{7.10}$$

can be recovered from $\beta(e)$:

$$\log P_\beta^{(N)}(e_2) - \log P_\beta^{(N)}(e_1) = N \int_{e_1}^{e_2} \mathrm{d}e \, (\beta(e) - \beta). \tag{7.11}$$

In the *thermodynamically stable region* (i.e. $\mathrm{d}\beta(e)/\mathrm{d}e < 0$), there is a single root of $\beta(e) = \beta$, located at the value of e where $P_\beta^{(N)}(e)$ is maximum. Instead, at phase coexistence there are several solutions for $\beta(e) = \beta$. Their interpretation is explained in Sect. 7.4.1.

7.2.1.2 The particle-density field

Preceding studies [Fer07b] suggested that a very heterogeneous solid phase would replace the crystal for high polydispersities. For this reason, we need to define an observable that tracks this property. With this aim, we compute explicitely the particle density fluctuations. In particular, we do it along three perpendicular directions at the smallest, non-vanishing wavenumber allowed by the periodic boundary conditions, i.e. $\boldsymbol{q} = (2\pi/L, 0, 0)$, $(0, 2\pi/L, 0)$ and $(0, 0, 2\pi/L)$. Then

$$\mathcal{F}(\boldsymbol{q}) = |\hat{\rho}(\boldsymbol{q})|^2 , \tag{7.12}$$

L being the linear dimension of the cubic simulation box and the Fourier field is

$$\hat{\rho}(\boldsymbol{q}) = \frac{1}{N} \sum_{i=1}^{N} e^{\mathrm{i}\boldsymbol{q}\cdot\boldsymbol{r}_i}, \tag{7.13}$$

where $\boldsymbol{r}_i$ is the position of the i-th particle. In Chapter 8 we shall be interested in the spatial distribution of these fluctuations, but here we just want to investigate the overall inhomogeneity. For this reason, we will only consider the averaged value over the three directions

$$\mathcal{F} \equiv= \frac{1}{3}\mathcal{F}(2\pi/L, 0, 0) + \text{permutations}. \tag{7.14}$$

In the homogeneous phases, in a fluid or in a crystal, for instance, $\mathcal{F}$ must vanish as $1/N$. On the contrary, in an inhomogeneous phase, one would expect $\mathcal{F}$ to remain $O(1)$.

7.2.1.3 Crystalline order parameters

We are not only interested in heterogeneity, but also in crystallinity. We want to distinguish whether the new solid is disordered or, on the other hand, there are crystals on it. In addition, we need a tool to distinguish different kinds of crystals in order to investigate fractionization. With this purpose, we generalize the (rotationally invariant) standard crystal order parameter introduced in Section 6.3, by measuring the crystal order only within a given set of particles $\mathcal{I}(x)$ (namely, particles whose index i verifies $|i - xN| < 0.05N$, hence only particles of similar size are considered):

$$Q_l(x) \equiv \left(\frac{4\pi}{2l+1} \sum_{m=-l}^{l} |Q_{lm}(x)|^2 \right)^{1/2}, \tag{7.15}$$

where (Y_{lm} are the spherical harmonics):

$$Q_{lm}(x) \equiv \frac{\sum_{\sigma_i \in \mathcal{I}(x)} q_{lm}(i)}{\sum_{\sigma_i \in \mathcal{I}(x)} N_b(i)}, \; q_{lm}(i) \equiv \sum_{j=1}^{N_b(i)} Y_{lm}(\hat{r}_{ij}). \tag{7.16}$$

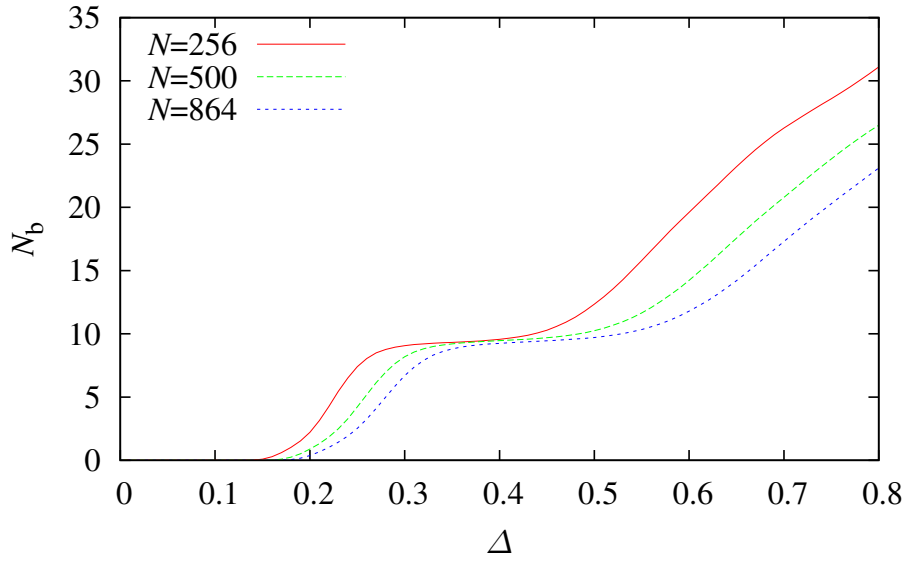

FIGURE 7.2: Averaged number of neighbors $N_b(i)$ over the half of biggest particles ($i \geq N/2$), as a function of Δ.

The index j in the latter sum runs over the $N_b(i)$ neighbors of the particle i and $\hat{r}_{ij}$ is the unit vector linking the position of particles i and j. Particles i and j are said to be neighbors if $||\boldsymbol{r}_i - \boldsymbol{r}_j|| < \Delta$. In order to meaningfully fix the scale Δ, we considered the average number of neighbors as a function of Δ in Figure 7.2 for the half of the biggest particles (which we shall see that are the ordered ones). We find a well defined plateau along which the number of neighbors remains constant. The height of this plateau is remarkably N-independent, although its *width* increases with N (then, the particular choice of Δ becomes less critical as N grows). Our choice was to fix $\Delta = 0.35$ (in units of the maximum cut-off for the potential $2\sigma_{\max} x_c$). This selection guarantees that all the values of N used in our simulations lie on the plateau for all the energies in the solid phase.

7·3 Numerical Algorithms and thermalization tests

In order to study the fluid-solid phase transition we implement a microcanonical MC strategy[MM07, Lus98]. Fixing the total energy density e, while the temperature and the potential energy fluctuate (see (7.9) and (7.8)), we follow the evolution from one phase to the other by studying e in the *energy gap* between the two phases. This strategy turned out to be essential to assess the first-order nature of the phase transition in disordered Potts models [Fer08b]. Being the freezing transition a first order as well, we expected this method to be also promising for this problem.

The peculiarity of the polydisperse models addressed here, as compared with

Potts and similar models, is in that the phase transition actually corresponds to a phase separation. In fact, our low energy state is inhomogeneous [Fero7b]. Thus moving e from large values (fluid) to small ones (partly solid) we gently *accompany* the system during the growth of the spatially segregated regions. Because of that, the internal energy will not be the only reaction coordinate (see below). However, the combination of this algorithm with a modified Parallel Tempering (PT) algorithm [Huk96, Mar98] has allowed us to thermalize in the solid phase.

For the sake of clarity, we divide the remaining part of this Section in three paragraphs: particle movements at fixed energy (Sect. 7.3.1), Parallel Tempering (Sect. 7.3.2), and thermalization checks (Sect. 7.3.3).

7.3.1 Particle movements at fixed energy

The particle moves at fixed energy were, with 50% probability, either standard Metropolis single-particle moves, or *global swap* attempts (modified for a polydisperse system). Let us recall that in a swap move, one attempts to exchange the position of two particles of different sizes [Gri01b].

Both for single-particle and for swap moves we compute the ratio of the microcanonical weights, defined in (7.7), for the new and the old configuration $\omega_N^{\rm old}/\omega_N^{\rm new}$. The new configuration is accepted with Metropolis probability $\min\{1, \omega_N^{\rm old}/\omega_N^{\rm new}\}$.

To fully describe the swap algorithm, we need to discuss how we choose the pair of particles, A and B, whose position we are trying to interchange. Note that one needs to balance two effects in polydisperse systems. The acceptance is larger the closer the two particle sizes are. However, exchanging very different particles produces a more significant effect when trying to equilibrate the system. Our compromise has been the following. We pick particle A with uniform probability over the N possibilities. We pick B with uniform probability among particles such that $|\sigma_B - \sigma_A| < 0.2(\sigma_{\rm max} - \sigma_{\rm min})$. Particle B is accepted with probability 1 if $|\sigma_B - \sigma_A| > 0.1(\sigma_{\rm max} - \sigma_{\rm min})$ or with probability 0.2 in the opposite case. In case of rejection, a new particle B is selected until a suitable candidate is picked.

In contrast to [Fero7b], we used here a modified version of the global swap instead of *local swap*. The difference between both algorithms consists on the way of selecting the two particles whose positions we try to interchange. In the local swap once chosen one particle, the swap update is only tried with a particle in its vicinity. On the contrary, for us, the selection of the two particles does not depend on their separation distance, but on their relative size. In this work we favored this second kind of move. The reason for this choice is that, as we shall see, in the heterogenous solid phase, the particles tend to crowd only with particles of similar size, and then, the local swap has little effect.

We check that on the coexistence-line, the swap moves reduced by three orders of magnitude the tunneling time between the fluid and the solid phase.

7.3.2 The microcanonical parallel tempering

In our Parallel Tempering simulations,[1] several statistically independent copies of the system at different energies are simulated.

Each Monte Carlo time unit consists of two steps:

1. For each copy of the system, we perform $10^5 \times N$ particle move attempts at fixed energy (either single-particle displacements or particle-swap attempts). During this stage, each copy of the system is completely independent from the others.

2. Copies of the system at neighboring energies try to exchange their particle configuration. We first try to sweep the two configurations at the lowest energy, afterwards the second lowest with third lowest, etc. In this way, the particle-configuration at the lowest energy has a chance of getting to the highest energy in a single sweep.

   For the sake of clarity let us name A, B the two systems that are currently attempting to exchange their particle configuration. The exchange is accepted with probability

$$\min\left[1\,,\ \frac{\omega_N(\{\boldsymbol{r}_i^{(A)}\}; e^{(B)})\,\omega_N(\{\boldsymbol{r}_i^{(B)}\}; e^{(A)})}{\omega_N(\{\boldsymbol{r}_i^{(A)}\}; e^{(A)})\,\omega_N(\{\boldsymbol{r}_i^{(B)}\}; e^{(B)})}\right]. \tag{7.17}$$

   The microcanonical weights ω_N are given in (7.7).

Further details on the simulation are summarized in Table 7.2.

Let us finally note that the here used Monte Carlo method is quite similar to that of Refs. [Yano4b, Yano4a]. We briefly mention the main differences. First, particle swap at fixed energy was not used in Refs. [Yano4b, Yano4a]. Second, phase coexistence (and the related Maxwell construction) was not studied. Third, in the formulation of [Yano4b], one has a single copy of the system that performs a random-walk in energy space: it is a sort of simulated annealing simulation [Mar98], rather than our parallel tempering. Besides, the approximation $\beta(e) \approx (N-2)/[2N\langle(e-u)\rangle]$ is used, which coincides with Eq. (7.9) only up to corrections of order $1/N$. The formulation of [Yano4a] is somehow intermediate between simulated annealing and parallel tempering. The energy range of interest is spliced into non-overlapping subranges. Each copy of the system is assigned to an energy subrange, where it performs a simulated annealing. From time to time one uses parallel tempering to exchange the copies of the system attached to neighboring energy subranges.

7.3.3 Thermalization checks

The PT algorithm has proved to be a very powerful tool for minimization problems. Indeed, its update consists on proposing jumps from one valley of the function one

[1] Parallel tempering is also known by Replica exchange MC. In the habitual formulation one tries to interchange replica configurations at different temperatures, from there comes the term "tempering" [Huk96, Mar98]. Here instead of temperatures, we have energy interchange attempts.

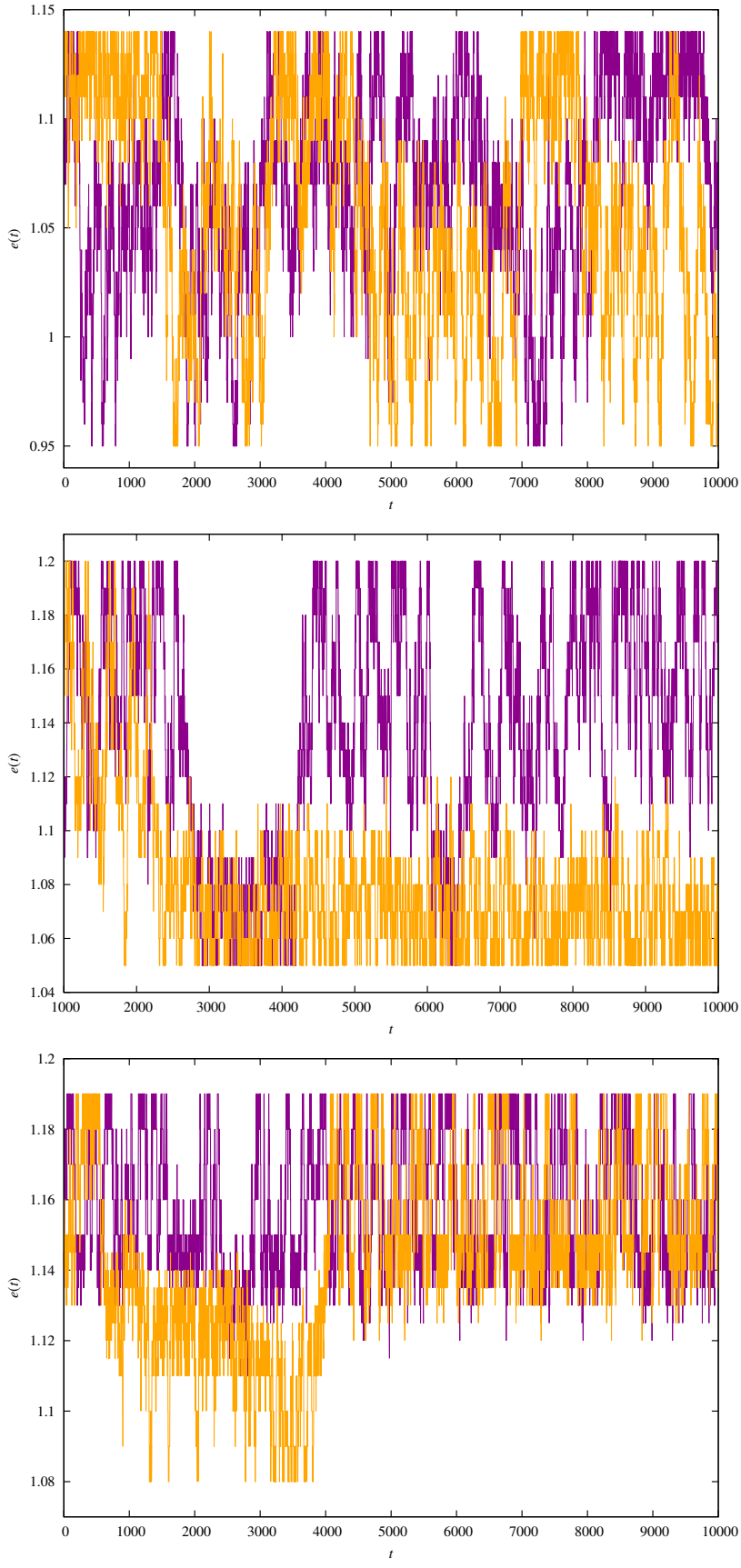

FIGURE 7.3: PT random walks for 2 copies of the system in (top) $N = 256$, (center) $N = 500$ and (bottom) $N = 864$.

N	N_e	$e_{\min}$	$e_{\max}$	L_{sim}
256	20	0.95	1.14	5×32000
500	16	1.05	1.2	2×30000
864	16	1.08	1.19	1×12000

TABLE 7.1: Simulation details. For each number of particles, N, we perform $10^5 N$ MC steps at fixed energy, then try a PT sweep. We also report the total length of our simulations in units of PT sweeps (5×32000 stands for 5 independent runs of 32000 PT sweeps each). The energies chosen for the PT were evenly spaced $e_{i+1} - e_i = 0.01$, in the intervals $[e_{\min}, e_{\max}]$. For $N = 864$ we added to the PT energy list the values $1.115, 1.125, 1.135$ and 1.145 in the fluid-solid energy gap.

wants to minimize to other. However, this flow between relative minima can be frustrated when the barriers between them are very high (as also happens with the simulated annealing discussed in Section 9.1). In such case, the PT random walk for each configuration could get stuck in one region of the state space for a long time (or indefinitely in the case the barriers were infinitely high) thus making the algorithm inefficient. Our minimization problem here is to obtain the equilibrium configuration for each fixed energy e (those with maximum entropy in our ensemble). One can guarantee that the system is thermalized as long as each configuration visits uniformly all the energies, this would mean that we have sampled all the state space. In other words, even when it is not efficient, the PT algorithm gives an easy way to check the thermalization [Fer09a].

We summarize in Table 7.1 the technical data used for our PT simulations. For each system size we consider N_e copies of the system each at a different energy in the intervals $[e_{\min}, e_{\max}]$. As an illustration of the problem, we display in Figure 7.3 these PT random walks in energies for two configurations. Clearly, the probability of tunneling from the fluid phase (high energies) to the solid phase (low energies) and vice-versa becomes more and more difficult the higher N is. Furthermore, the characteristic tunneling times, even for $N = 256$ are significant long as compared with the total simulation length (see Table 7.1). The combination of these two features shows that the PT strategy is failing and the worsening with N suggests phase coexistence between the fluid and the solid at intermediate energies. Indeed, the barriers between both states grow with N shooting up the tunneling times. These non ergodic random walks point out that the microcanonical strategy is not fulfilling our final goal, to avoid jumps between phases and its corresponding exponential dynamic slowing-down.

We can make this last statement quantitative by looking at the probability distribution function of $\mathcal{F}$, defined in (7.12). Our results are shown in Figure 7.4. At values of e close to the transition (see Figure 7.4–top), we identify two coexisting peaks. One of them is located at $\mathcal{F} \sim 1/N$, as expected for an homogenous fluid phase. On the other hand, the position of the large $\mathcal{F}$ maximum becomes N-independent (this is clearer at lower energies, see bottom panel in Figure 7.4), as it should occur for an inhomogeneous solid. As discussed above, such phase coexis-

tence makes us to expect a large growth with N of the autocorrelation times[Lanoo]. Actually, the pdf for $\mathcal{F}$ at low energies (Figure 7.4–bottom) displays a shoulder at large $\mathcal{F}$, which corresponds to even more inhomogeneous solids. Hence, the PT dynamics is ruled by two different processes: tunneling from fluid to solid, and a second tunneling to even more inhomogeneous configurations.

The random-walk in the energy space shown in Figure 7.3 is best described through a PT time autocorrelation function (defined in Eq. (E.1) in Appendix E). One can fit these functions to a double exponential for $N = 256$ and $N = 500$, see Figure 7.5. Mind that the *time* in this correlation functions correspond to the time-unit defined in Sect. 7.3.2. It is not related to any physical time-correlation.

As expected from the above discussion, we identify two different time scales in Table 7.2, one associated to the coexistence of the homogeneous and inhomogeneous phase, τ_{FS}, and a larger time, τ_{SS}, related to the more inhomogeneous configurations. For $N = 864$, we could only identify the τ_{FS} scale. Probably, τ_{SS} is larger than the total time in our simulation. We remark that τ_{FS} for $N = 256$ can be estimated with a 5% accuracy, while only the order of magnitude of τ_{SS} is determined. We have explicitly checked that the effects of these very inhomogeneous configurations on the Maxwell construction is fortunately smaller than our statistical errors.[2] Furthermore, from the point of view of our measured crystalline order parameters (see below), the more inhomogeneous configurations are not distinguishable from the main peak in the pdf.

[2]Indeed, we could compute $\beta(e)$ conditioned to a given value of $\mathcal{F}$. Since the more heterogeneous phase had higher values of $\mathcal{F}$, we could compare the Maxwell construction including all data or only the data corresponding to the first peak and the liquid. We could not find any difference beyond the statistical errors.

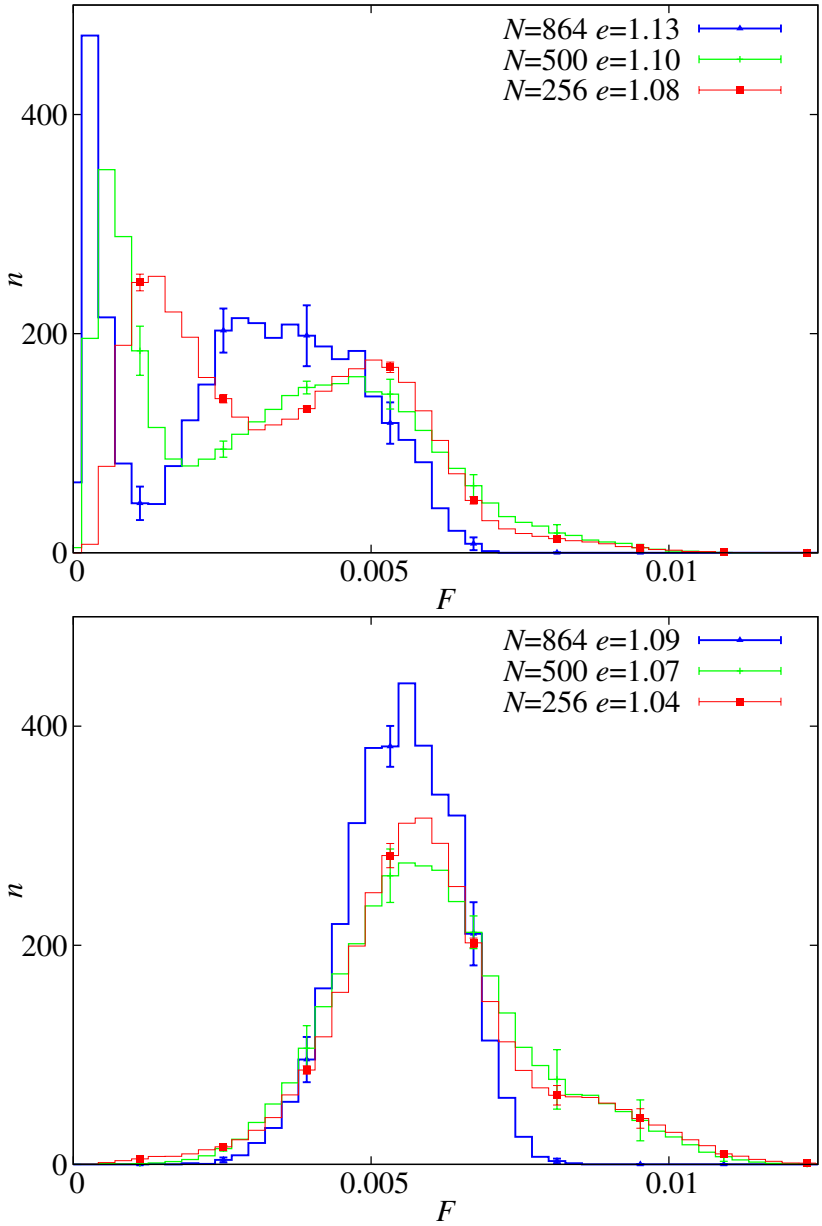

FIGURE 7.4: pdf of $\mathcal{F}$, (7.12) at various representative values of e. Data in the top panel are computed at energy densities in the energy gap between the fluid and the solid phases. The double peak structure reveals phase coexistence (the position of the leftmost peak scales as $1/N$). Data in the bottom panel are computed for e in the solid phase (the e-dependency there is very mild).

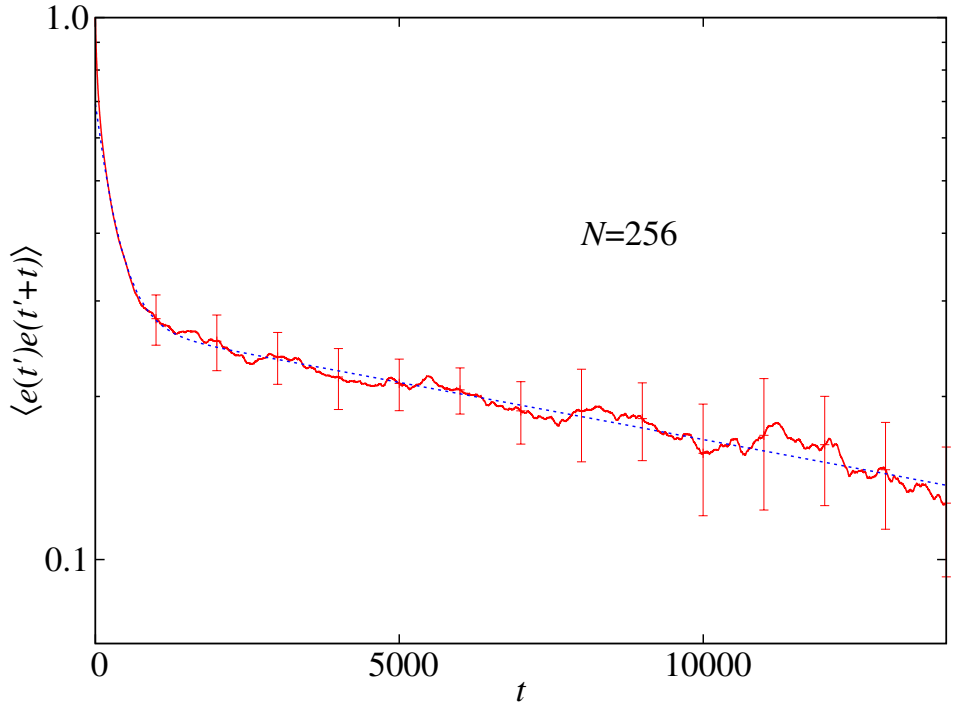

FIGURE 7.5: The (connected) time autocorrelation function for the energy in the PT for $N = 256$ can be fitted (dotted line) as $\langle e(t')\, e(t'+t)\rangle = a_{FS}\mathrm{e}^{-t/\tau_{FS}} + a_{SS}\mathrm{e}^{-t/\tau_{SS}}$. Fitted values are displayed in Table 7.2.

7.4 Numerical Results

7.4.1 The Maxwell construction

As was mentioned in Sec. 7.2.1, in a microcanonical simulation, a quantity of major interest is the (inverse) temperature, $\beta(e)$, see (7.9). Thermodynamic stability requires that $\beta(e)$ be a decreasing function (i.e. positivity of the specific heat). Yet, see main panel in Figure 7.6, this is not the case close to a first-order phase transition. The lack of monotonicity can be used to obtain the critical temperature, surface tension, etc. through the Maxwell construction (see below, and Ref.[MM07] for details). Generally speaking, $\beta(e)$ has two distinct branches, one describing the fluid and the other the solid phase, where the specific heat $C_v \equiv -\beta^2 de/d\beta$ is positive. The two branches connected by a thermodynamically instable line where $C_v < 0$. Although at finite N the system does not undergo a real phase transition, there are various criteria to define an (inverse) critical temperature, β_c^N, where the two different phases coexist with the same thermodynamic weight. Here we utilize the Maxwell construction, which amounts to obtain β_c^N as a solution of:

$$0 = \int_{e_N^S(\beta_c^N)}^{e_N^L(\beta_c^N)} \mathrm{d}e \, \left(\beta(e) - \beta_c^N\right) , \tag{7.18}$$

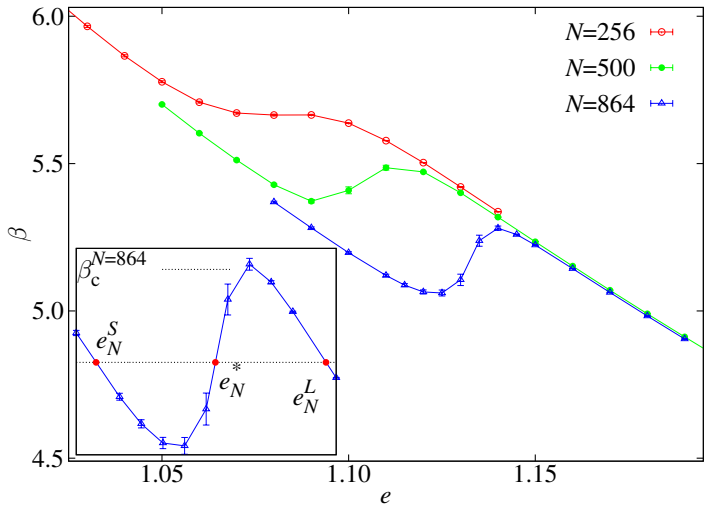

FIGURE 7.6: Finite size effects in the Maxwell construction. (Main panel) The inverse temperature $\beta(e)$ as a function of the energy density e for various sizes of the sample. (Inset) Enlarged plot of $\beta(e)$ for $N = 864$, including $\beta_c^{N=864}$ and the three solutions for $\beta(e) = \beta_c^N$: solid $e_N^S(\beta_c^N)$, midpoint $e_L^*(\beta_c^N)$ and fluid $e_N^L(\beta_c^N)$.

where the energy $e_N^L(\beta_c^N)$ ($e_N^S(\beta_c^N)$) in turn corresponds to the rightmost (leftmost) root of the equation $\beta(e) = \beta_c^N$ (see inset in Figure 7.6). The relation of the β integrals and the canonical probability (7.11) shows that the Maxwell constructions amounts to the famous equal-height rule for the canonical probability-distribution function $P_\beta(e)$.

In Fig. 7.6 we show the function $\beta(e)$ for $N = 256, 500, 864$. At odds with other models displaying a first order transition, as N grows, both the supercooled fluid (fluid branch with $\beta > \beta_c^N$) and the overheated solid (solid branch with $\beta < \beta_c^N$) lines become longer.

As for the values of β_c^N reported in Table 7.2, they decrease with N. Asymptotically, finite N corrections are of order $1/N$ (see [MM07] and references therein). A fit $\beta_c^N = \beta_c^\infty + a_1/N$ fails badly the χ^2 test. In other words, our estimates for β_c^N are accurate enough to resolve sub-leading scaling corrections in $1/N$. Thus, we have used a different approach. Let us assume that scaling corrections take the form of a smooth function in $1/N$, $\beta_c^N = \beta_c^\infty + a_1/N + a_2/N^2 + \ldots$. If we have at our disposal three values of N, we may compute a quadratic estimator (exact, up to corrections of order $1/N^3$):

$$\begin{aligned} \beta_c^{\infty,\mathrm{quad}} &= \beta_c^{N_1} \frac{N_1^2}{(N_1 - N_2)(N_1 - N_3)} + \\ &+ \beta_c^{N_2} \frac{N_2^2}{(N_2 - N_1)(N_2 - N_3)} + \\ &+ \beta_c^{N_3} \frac{N_3^2}{(N_3 - N_1)(N_3 - N_2)} . \end{aligned} \tag{7.19}$$

Computing the *statistical* error in $\beta_c^{\infty,\mathrm{quad}}$ is trivial, since $\beta_c^{N_1}$, $\beta_c^{N_2}$ and $\beta_c^{N_3}$ are sta-

N	β_c	Γ_c	$\gamma^{(N)}\beta_c^N\sigma_0^2$	τ_{FS}	τ_{SS}
256	5.665(3)	1.5428(2)	—	317(15)	∼20000
500	5.432(5)	1.5267(2)	0.0035(2)	∼1000	∼15000
864	5.162(4)	1.5073(2)	0.0088(4)	∼7000	—
∞	4.624(2)	1.4664(15)			

TABLE 7.2: The (inverse) critical temperature (and the associated $\Gamma_c = \rho\beta_c^{1/4}$), as well as the dimensionless surface tension $\gamma\beta_c^N\sigma_0^2$, as computed from Maxwell's construction.

tistically independent random variables. Using the data in Table 7.2 we get

$$\beta_c^{\infty,\text{quad}} = 4.624(20)\,, \quad \Gamma_c^{\infty,\text{quad}} = 1.4664(15)\,. \tag{7.20}$$

However, the quadratic polynomial in $1/N$ that interpolates our values $\beta_c^{N_1}$, $\beta_c^{N_2}$ and $\beta_c^{N_3}$ displays a maximum by $N \approx 256$, and decreases for smaller N. Hence, $\beta_c^{\infty,\text{quad}}$ probably overemphasizes curvature effects. On the other hand, a linear (in $1/N$) extrapolation from $N_1 = 864$ and $N_2 = 500$ yields

$$\beta_c^{\infty,\text{linear}} = 4.791(11)\,, \quad \Gamma_c^{\infty,\text{linear}} = 1.4795(9)\,. \tag{7.21}$$

The correct thermodynamic limit probably lies in between of the two estimators $\Gamma_c^{\infty,\text{quad}}$ and $\Gamma_c^{\infty,\text{linear}}$, above the kinetic glass transition at $\Gamma_g = 1.455(5)$.

Furthermore, $\beta(e)$ also allows us to compute the surface tension. Indeed, the quotient in the canonical probabilities between the fluid root $e_N^{\text{L}}(\beta_c^N)$ and the central point in the spinodal curve $e_L^*(\beta_c^N)$ (were we expect a strip configuration at least for a homogeneous system, see Section 8.7 for a detailed description) will be given precisely by the inverse of the probability of creating the two involved interfaces,

$$P_{\beta_c^N}^{(L)}(e_N^{\text{L}}(\beta_c^N))/P_{\beta_c^N}^{(L)}(e_L^*(\beta_c^N)) = \mathrm{e}^{2\beta_c^N\gamma^{(N)}\sigma_0^2L^2}. \tag{7.22}$$

Then, using (7.11) one gets

$$\beta_c^N\sigma_0^2\gamma^{(N)} = \frac{N}{2L^2}\int_{e_L^*(\beta_c^N)}^{e_N^{\text{L}}(\beta_c^N)} \mathrm{d}e\,\left(\beta(e) - \beta_c^N\right)\,. \tag{7.23}$$

Data is shown in Table 7.2.

7.4.2 Fractionation and crystalline ordering

Finally, we study the solid phase structure. For the discussion it is interesting a visual inspection of a typical $N = 864$ low-energy configuration, see Figure 7.7. In fact, the smallest 400 particles (particle index $i < 400$) and some of the intermediates ($i \in [600, 725]$) show no sign of spatial order (bottom), while particles with $i > 725$ and $i \in [400, 600]$ form crystalline planes. Ordered and disordered particles fill different regions of the sample.

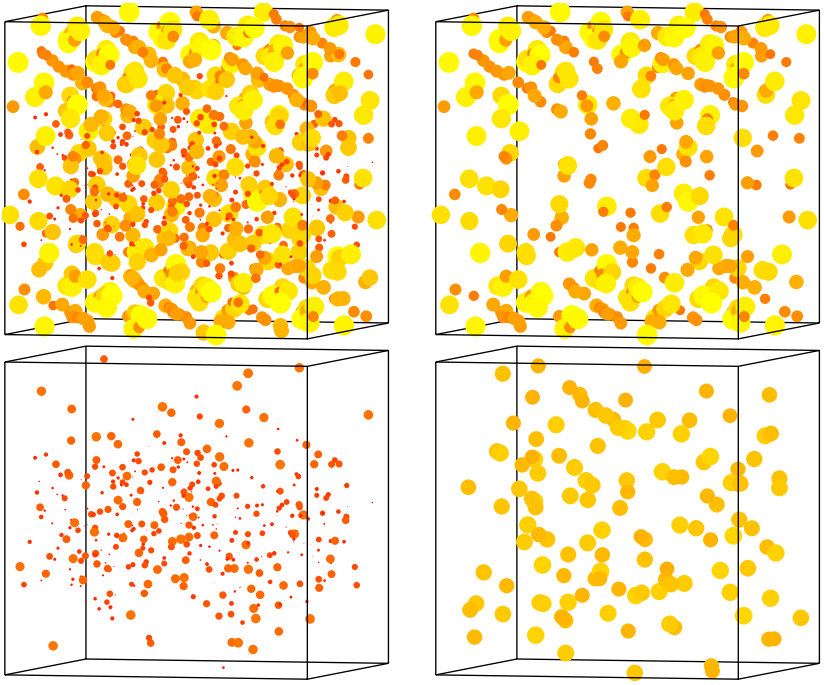

FIGURE 7.7: Snapshot of a typical low energy configuration ($N = 864$, $e = 1.01$). Top-left: whole system. Top-right: particles with index $i > 725$ and $i \in [400, 600]$. Bottom-left: particles $i < 400$. Bottom-right: particles $i \in [600, 725]$. The size of the circles are proportional to the particle sizes.

We can confirm this picture by means of the crystalline parameter $Q_6(x)$ introduced in Section 7.2.1.3. As discussed above, we compute the order within sets of particles of similar size, in fact, between those whose index i satisfies $|i - xN| < 0.05N$. We show this $Q_6(x)$ in Figure 7.8. For $x < 0.45$ the crystalline order parameters decay as $1/\sqrt{N}$ (see Figure in Figure 7.9), while for $x = 0.55$ and $x = 0.95$ we obtain results roughly N independent. Thus, while the latter group of particles form a crystal (Q_6 is somewhat smaller than expected for FCC ordering), the former one remains amorphous. As for polydispersities, in the two-components crystal we estimate that $\delta \sim 0.15$, while in the fluid $\delta \sim 0.24$.

In summary, at low energies the system divides spatially into an amorphous and a crystalline part. Particles distribute themselves according to their size following a complex pattern not described by any fractionation scenario known to us.

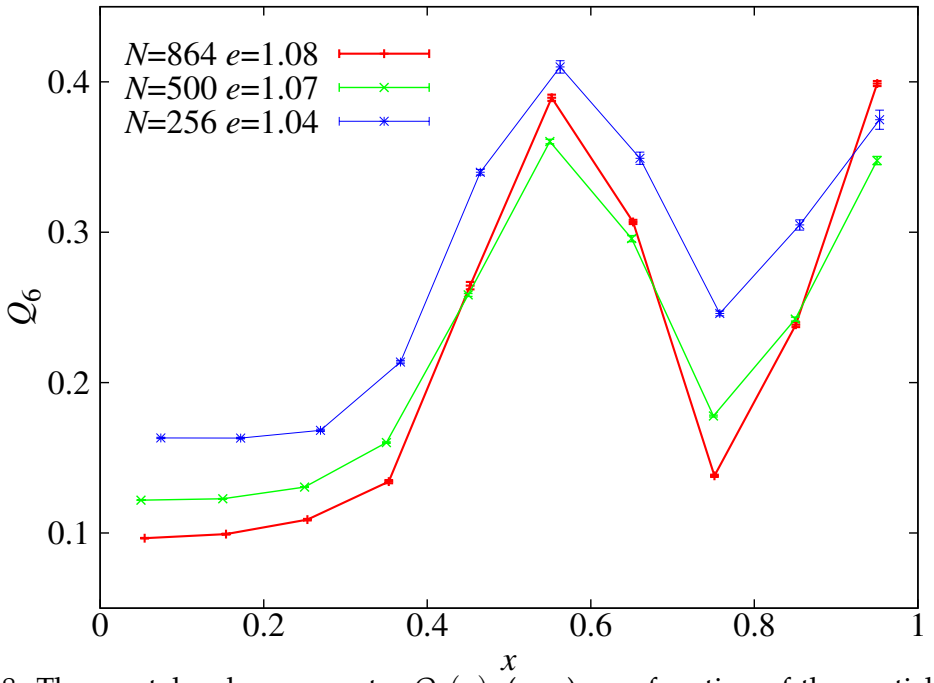

FIGURE 7.8: The crystal order parameter $Q_6(x)$, (7.15) as a function of the particles size x, for different N values.

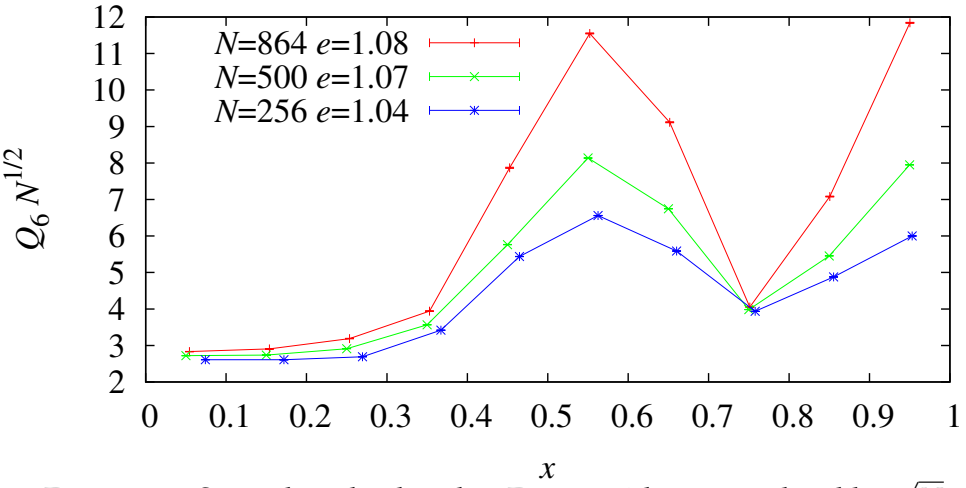

FIGURE 7.9: Same data displayed in Figure 7.8 but normalized by $\sqrt{N}$.

CHAPTER VIII

Hard spheres crystallization

As discussed in Chapter 6, we now step back to the simplest possible case of solidification, with the aim of beating the exponential dynamic slowing down (EDSD) associated with a first order fluid-solid transition. With this aim, we study the hard spheres (HS) crystallization problem with a novel approach based on the tethered ensemble that allows us to obtain unprecedently high-accuracy estimates of the fluid-solid coexistence pressure and the interfacial free energy. This chapter is concerned with the results published in Refs. [Fer12b, MM11].

This chapter is organized as follows. In Section 8.1 we review some of the previous approaches available in the literature concerning the crystallization of hard spheres. The hard spheres model is described in Section 8.2. In Sections 8.3 we try to apply the tethered approach to the problem by constraining the mean value of the bond-order parameter Q_6. In the process, we shall understand why not one but two bond-order parameters are necessary, and devote Section 8.4 to introduce the new one. At this point, we start the discussion of our final approach. The tethered formalism and simulation details are discussed in Section 8.5. In Section 8.6 we explain the fluctuation dissipation approach that allows us to draw a Maxwell construction to obtain the coexistence pressure from it. Finally, we devote Section 8.7 to the geometric transitions observed for the larger system sizes, as well as to the computation of the interfacial free-energy. The details concerning to the thermalization checks are quoted in Appendix E.

8.1 Background on hard spheres crystallization

Up to now, numerical simulations of crystallization phase transitions have been well behind their fluid-fluid counterpart (e.g. vapor-liquid equilibria [All89]). Actually, HS are the preferred benchmark for numerical approaches to crystallization. Yet, the lack of exact solutions enhances the importance of accurate numerical

and/or experimental studies.

However, for preexisting numerical methods, a simulation whose starting configuration is a fluid never reaches the equilibrium crystal. Much as in experiments [Pus89], the simulation gets stuck in a metastable crystal, or a defective crystal (or even a glass [Zac09b]). The proliferation of metastable states defeats optimized Monte Carlo (MC) methods that overcome free-energy barriers in simpler systems [Ber92, Wan01, MM07]. Besides, experimental and numerical determinations of the interfacial free energy are plainly inconsistent (maybe due to a small electrical charge in the colloidal particles [And02]).

Since feasible numerical methods [Veg08] could not form the correct crystalline phase spontaneously, choosing the starting particle configuration became an issue (e.g. crystalline or a carefully crafted mixture of solid and fluid phases). Methods can be classified as *equilibrium* or *nonequilibrium.* In the phase switch MC [Wil00], one tries to achieve fluid-crystal equilibrium (only up to $N = 500$ HS [Err04]). An alternative to compute the coexistence pressure is the separate computation of the fluid and solid free energies, supplemented with the conditions of equal pressure, temperature and chemical potential. For the fluid's free energy, one resorts to thermodynamic integration, while choices are available for the crystal (Wigner-Seitz [Hoo68], Einstein crystal [Fre84, Pol00], Einstein molecule [Veg07]). On the other hand, the nonequilibrium *direct coexistence* method [Lad77, Noy08] handles larger systems [ZT10].

As for the accuracy, in equilibrium computations the coexistence pressure p_{co} was obtained with precisions of $\sim 0.1\%$. Yet, the N values that can be simulated are rather small. An $N \to \infty$ extrapolation is mandatory, which degrades the final accuracy to $\sim 1\%$ [Err04, Wil00, Veg07] (results are summarized in Table 8.2). The situation improves by an order of magnitude for the direct-coexistence method. With the exception of [Err04], the different estimations of p_{co} are compatible, although with widely differing accuracies.

The computation of the interfacial free energy, γ, is more involved, since the issue of spatially heterogeneous mixtures of fluid and solid can no longer be skipped (as done in equilibrium computations of p_{co}). Indeed, recent estimations are precise but mutually incompatible [Dav10, Cac03, Här12], or of lesser accuracy [Mu05].

In this context, it is useful to summarize what has been achieved in this thesis. We introduce a tethered MC [Fer09b, MM11] approach to HS crystallization. The correct crystal appears in our simulation by constraining the value of two order parameters. At variance with preexisting methods, the crystal found is independent from the starting particle configuration. Tethered MC provides a major simplification for the standard umbrella sampling method [Tor74, Tor77, Bar00, Wol95]: chemical-potential differences among fluid and crystal are very precisely computed from a thermodynamic integration. In fact, our method resembles studies of liquid-vapor equilibria [Sch09, Bin11]. We go continuously from the fluid to the crystal by varying a reaction coordinate that labels the intermediate states. Rather than particle density, our reaction coordinate is a blend of bond-orientational crystal order parameters with different symmetries [Ste83, Dui92, AU10]. Very accurate

determinations of the coexistence pressure and the interfacial free energy follow. The number of HS ranges $108 \leq N = 4n^3 \leq 4000$, ($n$ integer), is large enough to undergo surface-driven geometric transitions [Biso2, Bino3, Maco6], which entitles us to safely extrapolate to $N = \infty$.

8.2

The hard spheres model

We consider a collection of N hard spheres, of diameter σ_0. They are contained in a cubic simulation box, with periodic boundary conditions. The system is held at constant pressure p (hence the simulation box may change its volume, but remaining always cubic).

Let us introduce the shorthand $\boldsymbol{R}$ for the set of particle positions, $\{\boldsymbol{r}_i\}_{i=1}^N$. The constraint of no overlapping spheres is expressed with function $H(\boldsymbol{R})$, which vanishes if any pair of spheres overlaps ($H(\boldsymbol{R}) = 1$ otherwise).

The NpT ensemble is discussed in Appendix D.3. For hard-spheres, the Gibbs free-energy density, $g(p, T)$ (which is the chemical potential), and the partition function are given by

$$\Upsilon_{NpT} = \mathrm{e}^{-N\beta g(p,T)} = \frac{p\beta}{N!\Lambda^{3N}} \int_0^\infty \mathrm{d}V \mathrm{e}^{-\beta pV} \int \mathrm{d}\boldsymbol{R}\, H(\boldsymbol{R})\,, \tag{8.1}$$

where Λ is the de Broglie thermal wavelength, while $\beta = 1/(k_\mathrm{B}T)$. The phase diagram for this model is shown in Figure 8.1.

Since the hard spheres cannot overlap, the most stable crystal is given by the structure with the highest possible packing fraction. This condition is fulfilled by the FCC, which is actually the equilibrium crystal of our problem. However, the HCP crystal has exactly the same packing fraction. Because of that, it has been a problem of decades to proof which of both was the correct structure in this problem. This dilemma was solved in the 90's, and not analytically, in fact, it was necessary to apply sophisticate numerical methods [Bol97].

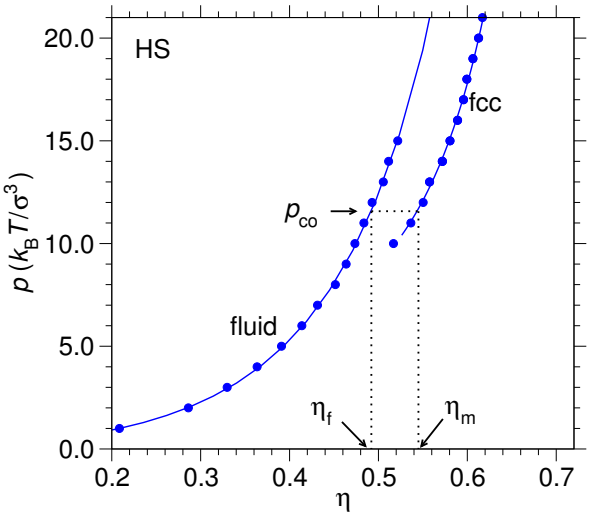

FIGURE 8.1: The phase diagram for the hard sphere system taken from [ZT10] [η is the packing density $\eta = \pi\sigma_0^3 N/(6V)$]. Dots correspond to simulation data and lines are analytical expression estimates for the fluid and the solid branches. The coexistence pressure is designed by p_{co}. Note the presence of metastable liquid and solid branches.

8.3

Prelude

In this Section we shall discuss some of the preliminary approaches that were crucial to end up with the tethered strategy that will be explained in Section 8.5.

The simplest possible simulation study of this transition would be, for instance, to use standard MC moves at constant pressure. However, reaching the equilibrium within a NpT simulation in the vicinity of the coexistence pressure, p_{co} (see Figure 8.1) is even harder that what was discussed for soft polydisperse spheres in the previous chapters. Although at a given pressure both the fluid and the FCC phase are metastable, one does not find *flip-flops* between these two phases (one needs to reduce the system size below $N \sim 30$, to find any), even after a relatively long simulation time. Indeed, if the simulation started in the fluid phase, it would stay forever there. Or even worse, it might form a metastable BCC crystal, but not a FCC. The situation is not better when one starts from a perfect FCC lattice, the stochastic dynamics is not able to melt the crystal structure.

We have tried to use more sophisticated ensembles, for instance, the microcorical one (see Appendix D.5). The situation is exactly as before, at a given volume, we find both crystal and fluid depending on the starting configuration: the FCC structures do not melt, and the random initial configurations crystallize to another metastable defective crystal structure. Among all the observables computed during the simulation, only the ones related to the crystalline structure (Q_6 or the number of neighbors) seem to really distinguish the three phases involved here: fluid, FCC and BCC.

Then, we thought of using crystalline parameters as reaction coordinates. We

started with just one order parameter, in particular, with Q_6 defined in Section 6.3. The goal was then to control the growth of the crystalline domains by tuning the value of Q_6.[1] This idea of using Q_6 to govern the crystallization process in a MC simulation is not new, in fact [Wol95, Moro5, Choo6] are well examples of works exploiting that idea. Previous works constrain the value of Q_6 using the umbrella sampling technique [Tor74]. This method, broadly used in the chemical physics community, consists on "pressing" the usual NpT probability used for the Metropolis test with a weight associated with the order parameter. With this idea, one can reconstruct an effective free energy by means of

$$G(Q_6) = \text{const} - k_B T \log\left[P(Q_6)\right], \tag{8.2}$$

with $P(Q_6)$ the probability to find the order parameter around a given value of Q_6. This probability can be measured directly from the simulation history by making histograms of the instantaneous $Q_6(t)$. Nearby the transition one expects to find two minima in $G(Q_6)$ and the phase coexistence is then identified when the two minima are equally deep.

In this work we are using the tethered MC method (see [Fero9b, MM11] and Appendix D.6.1) rather than umbrella sampling to constrain the bond-order parameters. This method is a refinement over the umbrella sampling. It was initially proposed in a different context, but formally, when applied to crystallization, the tethered ensemble leads to the same MC weights than umbrella sampling when concerning the simulation method in this problem. The differences between both methods appear in the way of analyzing the simulation data. Indeed, in the tethered formalism, the effective free energy is obtained in a simpler way using a fluctuation-dissipation formalism [MMo7] and time averages of Q_6. This simplification has strong consequences in the precision for magnitudes such as the p_{co} or the surface tension achievable with the same set of simulation data. In fact, the precision in the histograms of Q_6 is very crude, and because of that, previous works [Wol95, Moro5, Choo6] are more centered on studying the structure on the crystalline grains than in determining precisely the coexistence point. The situation is even worse when one constrains more than one order parameter [Moro5]

[1] Q_6 was defined in Section 6.3 but for the technical definition of nearest neighbor. This definition is taken here different to the one discussed for polydisperse systems in Section 7.2.1.3. Two particles i and j are considered neighbors iff $r_{ij} < 1.5\ \sigma$. This choice ensures that we enclose only the first-neighbors shell in the FCC structure, for all the densities of interest here. Indeed, we need a radius that includes all the first nearest neighbors and excludes the second nearest ones in the FCC structure. The theoretical radius of the perfect lattice depends on the total volume it takes up. However, the total volume fluctuates in our simulations, but we need a fixed value for the definition of the crystalline parameters. Nevertheless, in a perfect FCC, the first and second nearest neighbors shell in a lattice of volume V are placed at a distance (in units of σ)

$$R^{(1)}_{\text{FCC}} = \sqrt{2}\left(\frac{V}{2N}\right)^{1/3},\ R^{(1)}_{\text{FCC}} = 2\left(\frac{V}{2N}\right)^{1/3}.$$

Then, we seek for a value of the radius that defines $N_b(i)$ that is always in between these two values for all the volumes studied, and 1.5 does fulfill this requirement.

using umbrella sampling approach. The method implies computing bidimensional histograms which damages notably the accuracy. On the contrary, as we shall see, the tethered approach is not hampered by the number of constraints one wants to impose.

8.3.1 Tethered in Q_6

Our first step was then to perform MC simulations in the $\hat{Q}_6 NpT$ ensemble (see Appendix D.6.1). We shall see that this constraint $\hat{Q}_6$ is not sufficient to avoid metastabilities in all the range of parameters. We will devote this section to justify why it does not. Since it will not be our final approach, we will not describe here all the formalism and technical simulation details, but just the necessary tools to give the reader a clear idea of the problem we encountered.

Thus we employ the tethered ensemble described in Appendix D.6.1 for an arbitrary magnitude $O(\boldsymbol{R})$. In this case we constrain Q_6. In this ensemble, we let the instantaneous value of the bond-order parameter fluctuate around a fixed value $\hat{Q}_6$, and the constraint tries to loosely impose $\langle Q_6 \rangle \approx \hat{Q}_6$. This can be done in a simulation using the tethered weight

$$\omega_N(\boldsymbol{R}, V; p, \hat{Q}_6) = \sqrt{\frac{\alpha N}{2\pi}} H(\boldsymbol{R})\ \mathrm{e}^{-\beta p V - \frac{\alpha N}{2}\left[\hat{Q}_6 - Q_6(\boldsymbol{R})\right]^2}, \tag{8.3}$$

for the MC updates, which is equivalent to say that the tethered mean values for a given couple of simulation points $(\hat{Q}_6, p)$ are given by

$$\langle O \rangle_{\hat{Q}_6, p} = \frac{\int_0^\infty db \int \mathrm{d}\boldsymbol{R}\ O(\hat{Q}_6, p; V, \boldsymbol{R})\, \omega_N(\boldsymbol{R}, V; p, \hat{Q}_6)}{\int_0^\infty db \int \mathrm{d}\boldsymbol{R}\ \omega_N(\boldsymbol{R}, V; p, \hat{Q}_6)}. \tag{8.4}$$

With this idea, we run simulations at a pressure nearby the freezing transition in a mesh of values of $\hat{Q}_6$ in between the fluid expectation value, $\hat{Q}_6^{\text{fluid}} \sim 1/\sqrt{N}$, and the perfect crystal equilibrium phase (in hard spheres a FCC lattice), $\hat{Q}_6^{\text{FCC}} = 0.574$. In order to check the thermalization, as we did before, we run two simulations at each $\hat{Q}_6$ value, one starting from a random particle configuration and other from a perfect FCC lattice. If the approach succeeds, both simulations should converge in a very few steps to the same structure. The method works for most of the $\hat{Q}_6$ points. The $\hat{Q}_6$ value forces one single phase (in fact, the pdf, $p(\hat{Q}_6)$, is unimodal) and no difference between the two starts in the measured mean values is observed (within the errors). Let us point out that it is already a great advance from all our previous approaches, in fact we were not ever able to synthesize a FCC from a fluid nor with NpT nor with $N\hat{V}T$, and now it forms spontaneously just imposing its mean Q_6 value. However, there are some points (in the solid phase) at which both simulation runs do not converge to the same structure (see, for instance, the evolution of $Q_6(\boldsymbol{R}, t)$ in Figure 8.2). The situation is less dramatic than it was before, the $Q_6(\boldsymbol{R}, t)$ values obtained are very similar thought not equal. The problem is clarified by the

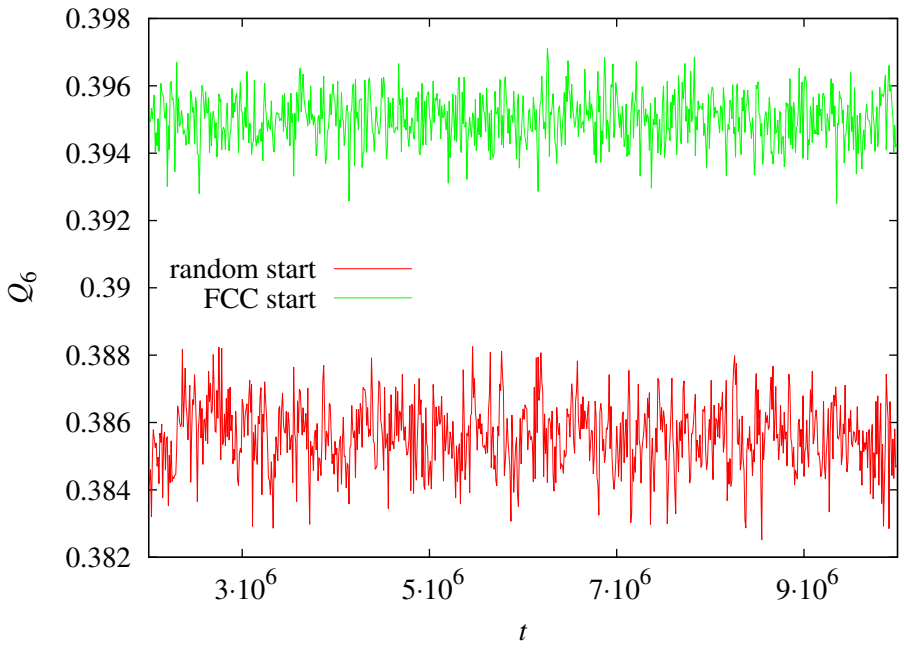

FIGURE 8.2: Snatch of the evolution of $Q_6(\boldsymbol{R}, t)$ in a $\hat{Q}_6 NpT$ MC simulation (for $\hat{Q}_6 = 0.394$, $N = 256$, $p = 11.224$). Time is measured in units on a elementary MC step: N particles moves, followed by a volume update. The two lines correspond to two identical Markov chains that started from (green) FCC or (red) random configurations.

snapshot in Figure 8.3, the two solid structures are FCC-like. However, the FCC-start simulations lead to a defective FCC with the planes parallel to the simulation box walls. On the other hand, the random start freezes in a helicoidal almost-FCC crystal allowed by the periodic boundary conditions whose planes are misaligned. Since our simulation box is finite, and cubic, a FCC can only be accommodated perfectly with the planes parallel to the cube faces, which makes this configuration the most stable one. However, the chances of a FCC grain to start to grow in a fluid with the axis on the right orientation are minimal. Indeed, since the Q_6 magnitude is rotationally invariant, we have no tool to force a particular orientation, only the kind of crystal structure.

The straightforward solution would be to consider another bond-orientational parameter but with cubic symmetry instead of rotationally symmetric one.

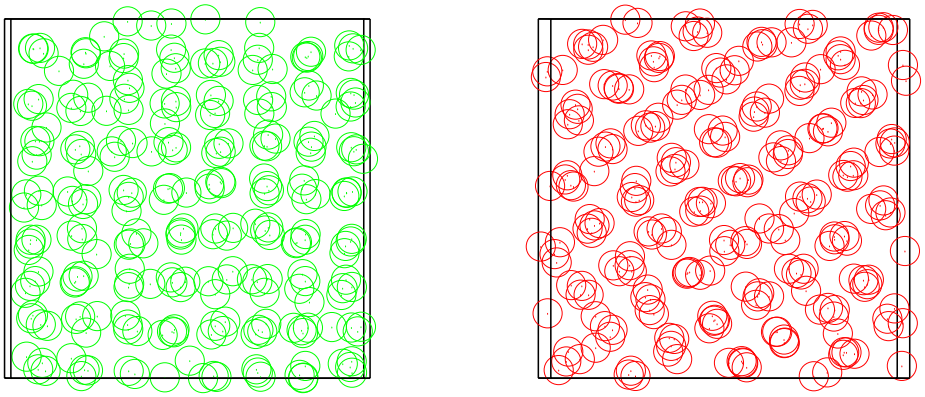

FIGURE 8.3: Bidimensional projection of the typical configurations found from (green) FCC or (red) random start in Q_6NpT simulations.

8.4

The second bond-order parameter: avoiding rotational symmetry

As justified in the previous section, we need to define a second order parameter with only cubic symmetry. Such a parameter was recently proposed [AU10]:

$$C = \frac{2288}{79} \frac{\sum_{i=1}^{N} \sum_{j=1}^{N_b(i)} c_\alpha(\hat{\boldsymbol{r}}_{ij})}{\sum_{i=1}^{N} N_b(i)} - \frac{64}{79}, \tag{8.5}$$

where

$$c_\alpha(\hat{\boldsymbol{r}}) = x^4y^4(1-z^4) + x^4z^4(1-y^4) + y^4z^4(1-x^4)\,. \tag{8.6}$$

Again, $N_b(i)$ represents the number of neighbors of the ith particle, here defined as the number of particles j that fulfill $|\boldsymbol{r}_j - \boldsymbol{r}_i| < 1.5$.[2] Within this definition of nearest neighbors, the expectation value for C in the different phases is the following: 0.0 in the fluid, 1.0 in the ideal FCC crystal, perfectly aligned with the simulation box, and -0.26 in the perfectly aligned ideal BCC. We include the calculation of C in a perfect lattice in Appendix F. The difference with the quoted value in Ref. [AU10] for the perfect BCC crystal is due to our smaller threshold for neighboring particles.

[2] See Footnote 1 in this Chapter.

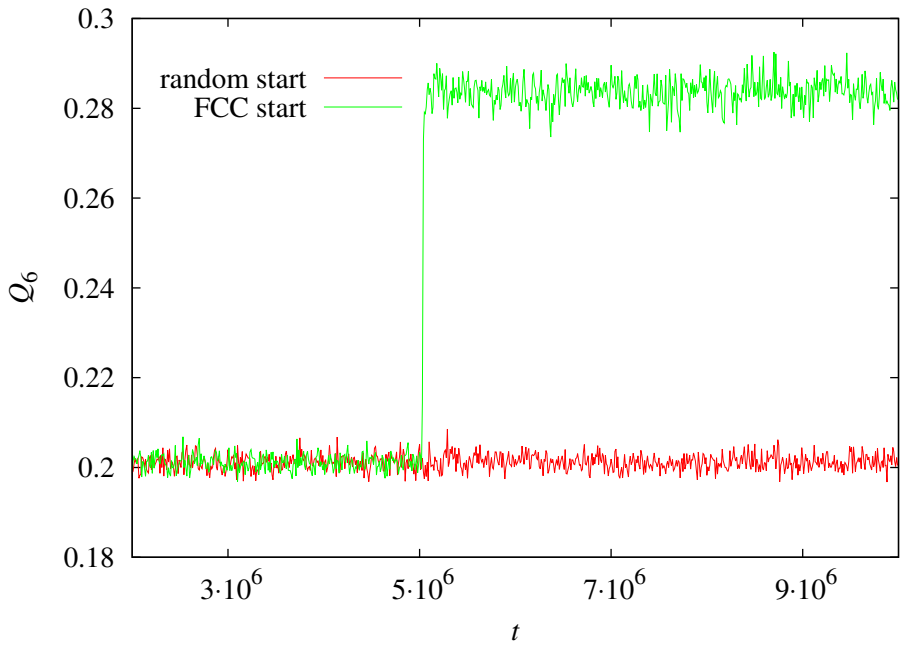

FIGURE 8.4: History of $Q_6(\boldsymbol{R}, t)$ in a $\hat{C}NpT$ MC simulation (for $\hat{C} = 0.3$, $N = 256$, $p = 11.224$). Time is measured in units on a elementary MC step: N particles moves, followed by a volume update.

For defective structures, we must expect values for Q_6 and $|C|$, lower than the ones quoted here for perfect lattices.

Following the previous discussion, we can repeat the previous study but this time fixing this parameter instead of Q_6. As expected, the problem with rotated FCC lattices does not appear anymore. However, for intermediate values of $\hat{C}$ we find metastabilities in the simulation history, $C(\boldsymbol{R})$ is not able to differentiate misaligned crystals and some mixtures of fluid and crystal. We can distinguish these two phases by looking at Q_6, which is rotationally invariant. We show this $Q_6(\boldsymbol{R}, t)$ history in Figure 8.4. Nevertheless, the region at which these flip-flops appear in the $\hat{C}NpT$ simulation is not the same one where the $\hat{Q}_6NpT$ fails to thermalize. This last fact made us wonder what would happen if we fixed Q_6 and C parameters at the same time. We shall see that with this idea we fulfill our expectations: the runs starting from different configurations converge quickly and we are finally able to avoid phase coexistence with its corresponding exponential dynamic slowing down.

8.5

Tethered formalism for a hard sphere system

As discussed in Section 8.3, the cure for the EDSD seems to be constraining simultaneously the values of two bond-order parameters, Q_6 and C. We use the tethered ensemble for two parameters, described in Appendix D.6.2. With it, the *tethered averages* of a generic observable $O(\boldsymbol{R}, V, p)$ are defined as

$$\langle O \rangle_{\hat{Q}_6,\hat{C},p} = \frac{\int dV \mathrm{d}\boldsymbol{R}\; O(\boldsymbol{R}, V, p)\; \omega_N(\boldsymbol{R}, V; \hat{Q}_6, \hat{C}, p)}{\int \mathrm{d}V \mathrm{d}\boldsymbol{R}\; \omega_N(\boldsymbol{R}, V; \hat{Q}_6, \hat{C}, p)}, \tag{8.7}$$

with,[3]

$$\omega_N(\boldsymbol{R}, V; \hat{Q}_6, \hat{C}, p) \;\; = \tfrac{N\alpha}{2\pi} H(\boldsymbol{R}) \mathrm{e}^{-\beta p V} \mathrm{e}^{-\frac{\alpha N}{2}\left[\hat{Q}_6 - Q_6(\boldsymbol{R})\right]^2} \mathrm{e}^{-\frac{\alpha N}{2}\left[\hat{C} - C(\boldsymbol{R})\right]^2}. \tag{8.8}$$

The Metropolis MC simulation of this weight requires two types of moves: single particle displacements, as well as changes in the volume of the simulation box. We shall use the short hand Elementary Monte Carlo Step (EMCS) to the combination of N consecutive single-particle displacements attempts, followed by a change attempt in the simulation box volume. For the particle displacements we pick at random a particle-index, say i, and try $\boldsymbol{r}_i \to \boldsymbol{r}_i + \boldsymbol{\delta}$ with $\boldsymbol{\delta}$ chosen with uniform probability within the sphere of radius Δ. We tune Δ to keep the acceptance above 30%. We recast ω in Eq. (8.8) as the Boltzmann factor for HS at fixed pressure with a *fictive* potential energy $k_{\mathrm{B}} T N \alpha \left[(\hat{Q}_6 - Q_6(\boldsymbol{R}))^2 + (\hat{C} - C(\boldsymbol{R}))^2\right]/2$. Since $Q_6(\boldsymbol{R})$ and $C(\boldsymbol{R})$ are built out of sums of local terms, the number of operations needed to compute their changes after a single-particle displacement does not grow with N.

As it is discussed in Appendix D.6.2, the Helmholtz effective potential is here given by

$$\mathrm{e}^{-N\Omega_N(\hat{Q}_6,\hat{C},p)} = \frac{\beta p}{N!\Lambda^{3N}} \frac{\alpha N}{2\pi} \int \mathrm{d}V \int \mathrm{d}\boldsymbol{R}\, \mathrm{e}^{-\beta p V}\, \mathrm{e}^{-\beta U(\boldsymbol{R})}\, \mathrm{e}^{-\frac{\alpha N}{2}\left[\left\{\hat{Q}_6 - Q_6(\boldsymbol{R})\right\}^2 + \left[\hat{C} - C(\boldsymbol{R})\right]^2\right]}. \tag{8.9}$$

Then, it is clear that the ensemble equivalence with the NpT (in particular Eq. (8.1)) is obtained by integrating over all the range of parameters,

$$Y_{NpT} = e^{-N g_N(p,T)} = \int \mathrm{d}\hat{Q}_6\, \mathrm{d}\hat{C}\; e^{-N\Omega_N(\hat{Q}_6,\hat{C},p)}\,. \tag{8.10}$$

[3]The reader may notice that the ω presented here is very different to the weight deduced in the original work in the Tethered method [Fero9b]. The explanation regards on our definition for the tethered variables. Indeed, in the ensemble definition we add the demons linearly, $\hat{T} = T + \frac{1}{\alpha N}\sum_{i=1}^{\alpha N} \eta_i$, whereas in the original work, the demons were added quadratically, i.e. $\hat{T} = T + \frac{1}{2}\sum_{i=1}^{\alpha N} \eta_i^2$, as an analogy to the momenta in the microcanonical ensemble [MM07] (used in Chapter 7). These quadratic sums, introduce a Heaviside step function that forbids trial moves with $\hat{Q}_6 > Q_6(\boldsymbol{R})$ and $\hat{C} > C(\boldsymbol{R})$. Note that ascertaining thermalization is an issue in crystallization studies. It is very important to compare the outcome of simulations with widely differing starting configurations. In this respect, the constraints are a major problem, as they prevent us from using the ideal FCC crystal as starting configuration. This problem is directly erased if one adds the demons linearly as we do here.

We shall need to consider the dependency with p in the mean values (8.7). We could do it by running many simulations at different pressures, or alternatively, by taking advantage of our lack of metastabilities, and using the histogram reweighting method [Fal82, Fer88]. Indeed, this method let us to extrapolate mean values at $p + \delta p$ using simulation data obtained at p using the following equality:

$$\langle O \rangle_{\hat{Q}_6,\hat{C},p+\delta p} = \frac{\langle O\, \mathrm{e}^{-\beta\delta p V} \rangle_{\hat{Q}_6,\hat{C},p}}{\langle \mathrm{e}^{-\beta\delta p V} \rangle_{\hat{Q}_6,\hat{C},p}}. \tag{8.11}$$

Although this equation is formally exact, our simulation data is finite and the stochastic path visits mainly only the volume region relevant for pressure p. The extrapolation will be safe as long as the probability distribution functions for the specific-volume, $v = V/N$, at both pressures overlap (thus having sampled some of the relevant region for $p + \delta p$). Then, we can compute the maximum safe extrapolation, δp, making quantitative this idea. Indeed, this condition is roughly equivalent to the following statement. The displacement $\delta v = \langle v \rangle_{p+\delta p} - \langle v \rangle$ should be smaller than the mean deviation of v, i.e.

$$\delta v < \sqrt{\langle v^2 \rangle_{\hat{Q}_6,\hat{C},p} - \langle v \rangle^2_{\hat{Q}_6,\hat{C},p}}\,. \tag{8.12}$$

Besides, since the distribution of volumes is unimodal, we can assume that the response is linear

$$\delta v = \frac{\partial v}{\partial p}\, \delta p = \chi_p\, \delta p, \tag{8.13}$$

and the compressibility, χ_p, can be obtained using the *fluctuation-dissipation* theorem

$$\chi_p = \left.\frac{\partial \langle v \rangle}{\partial p}\right|_{(\hat{Q}_6,\hat{C},p)} = N\left[\langle v^2 \rangle_{\hat{Q}_6,\hat{C},p} - \langle v \rangle^2_{\hat{Q}_6,\hat{C},p}\right]. \tag{8.14}$$

Then, we should restrict ourselves to

$$\delta p \lesssim \frac{1}{\sqrt{N\chi_p}}\,. \tag{8.15}$$

Hence, it is crucial that the pdf for v be unimodal (i.e. single-peaked), and with an N-independent χ_p, for all points considered here. In other words, it is important that the integration path (see Section 8.6) to be free of metastabilities. This condition holds very well as shown in Figure 8.5, then, we can be confident to use extrapolated data. We include the actual δp we used for our computations in Table 8.1.

We summarize the simulation technical details in Table 8.1. N_S accounts for the number of $(\hat{Q}_6, \hat{C})$ points simulated (S is the line parameter of the integration curve that joins the fluid with the solid phases, as we shall see in Section 8.6). We run simulations at a central pressure p_{sim}, and we extrapolate data to $p \pm \delta p$. We also include in the table the (Q_6, C) mean values expected for the FCC and fluid phases. We will refer to these points as the *saddle points* later on, and their technical computation will be explained in Section 8.6.2.

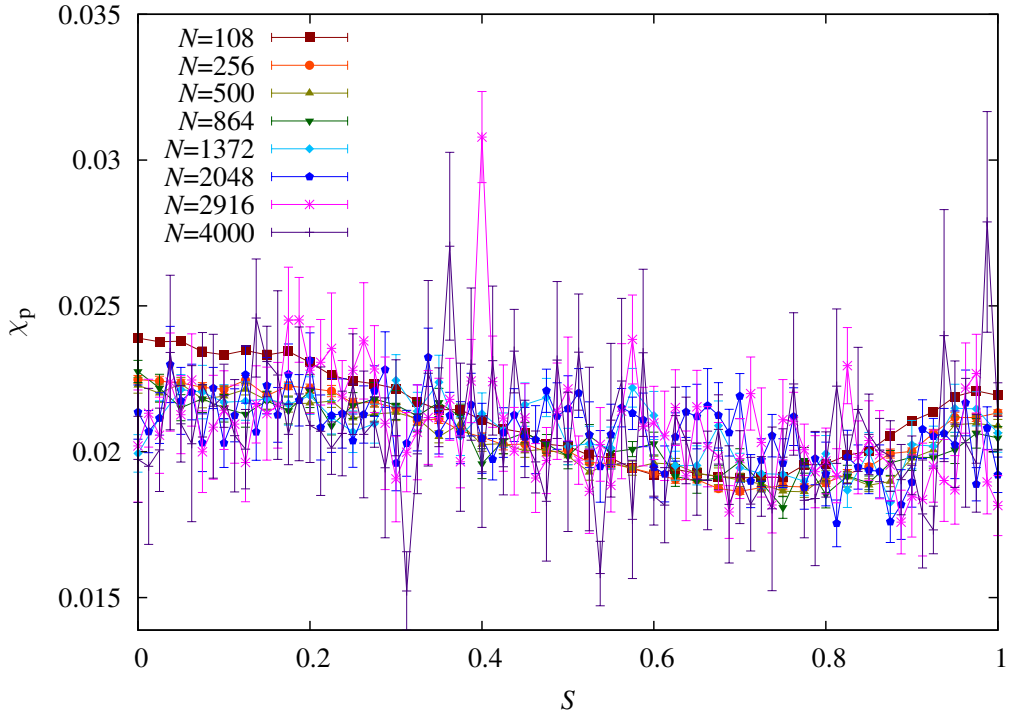

FIGURE 8.5: Compressibility of the system at different system sizes as a function of S. $S(\in [0,1])$ is the line parameter that covers all the $(\hat{Q}_6, \hat{C})$ points simulated in this work, it will be introduced in Section 8.6.

N	N_S	$N_{\text{sim}} \times t_{\text{max}}$	p_{sim}	δp	$\hat{Q}_6^{\text{FCC}}$	$\hat{Q}_6^{\text{fluid}}$	$\hat{C}^{\text{FCC}}$	$\hat{C}^{\text{fluid}}$
108	42	2×10^6	10.920	0.40	0.3997998	0.0746256	0.6640012	−0.0076329
256	42	2×10^6	11.224	0.40	0.399293	0.0486370	0.662729	0.0007850
500	42	2×10^6	11.363	0.24	0.3993689	0.0349778	0.6627378	−0.0000134
864	42	2×10^6	11.441	0.16	0.3995549	0.0268013	0.6629474	−0.0009323
1372	42	2×10^6	11.487	0.16	0.3996055	0.0213669	0.6630886	−0.0005104
2048	82	2×10^6	11.514	0.08	0.3997456	0.0175258	0.6633223	−0.0002546
2916	82	2×10^6	11.529	0.08	0.3997110	0.0146926	0.6632560	−0.0001866
4000	82	4×10^6	11.540	0.08	0.3997886	0.0125658	0.6633856	−0.0001238

TABLE 8.1: Technical details of the simulations. The length of each simulation, t_{max}, is measured in units of EMCS (N attempts of particle displacements followed by a change attempt of the simulation volume). N_S represent the number of $(\hat{Q}_6, \hat{C})$ points studied and N_{sim} the amount of independent runs we studied at each $(\hat{Q}_6, \hat{C})$-point. In all cases but $N = 4000$, $N_{\text{sim}} = 2$, which corresponds a start from a random and from a perfect FCC configuration. In the case of $N = 4000$, three independent runs began from a random configuration.

8.6

The coexistence pressure: computing differences in the effective potential

The tethered approach, at variance with the umbrella sampling, presents a direct way to obtain the effective potential by means of a thermodynamic integration using only mean values. In this section we explain step by step how to use this approach to obtain the coexistence pressure $p_{\rm co}$.

We start with the relationship between the effective potential, $\Omega_N(\hat{Q}_6, \hat{C}, p)$, and the Gibbs free-energy. The Eq. (8.10) can be simplified using a saddle-point approximation,

$$g_N(p,T) = \Omega_N(\hat{Q}_6^*, \hat{C}^*, p) + O(1/N)\,, \tag{8.16}$$

where $(\hat{Q}_6^*, \hat{C}^*, p)$ is the p-dependent absolute minimum of $\Omega_N(\hat{Q}_6, \hat{C}, p)$, regarded as a function of $\hat{Q}_6$ and $\hat{C}$. Coordinates $(\hat{Q}_6^*(p), \hat{C}^*(p))$ are then located in Section 8.6.2 through $\boldsymbol{\nabla}\Omega_N = 0$.

Therefore, up to corrections vanishing as $1/N$, the chemical potential $\beta g(p,T)$ is the absolute minimum of $\Omega_N(\hat{Q}_6, \hat{C}, p)$, see (8.16). Yet, close to phase coexistence, Ω_N has two relevant minima (i.e. the fluid and the FCC crystal). Therefore, the coexistence pressure $p_{\rm co}^{(N)}$ follows from $\Omega_N^{\rm fluid} = \Omega_N^{\rm FCC}$ (i.e. the standard condition of equal chemical potential).

Now, this gradient of the Helmholtz effective potential, $\Omega_N(\hat{Q}_6, \hat{C}, p)$, is obtained by taking derivatives in (8.9). Using a Fluctuation-Dissipation formulae, it leads to

$$\begin{aligned}\boldsymbol{\nabla}\Omega_N(\hat{Q}_6, \hat{C}, p) &= \left(\frac{\partial \Omega_N(\hat{Q}_6, \hat{C})}{\partial \hat{Q}_6}, \frac{\partial \Omega_N(\hat{Q}_6, \hat{C})}{\partial \hat{C}} \right) \\ &= \left(\left\langle \alpha \left(\hat{Q}_6 - Q_6 \right) \right\rangle_{\hat{Q}_6, \hat{C}, p}, \left\langle \alpha \left(\hat{C} - C \right) \right\rangle_{\hat{Q}_6, \hat{C}, p} \right).\end{aligned} \tag{8.17}$$

Furthermore, the differences in effective potential between to points, $\Omega_N(\hat{Q}_6^b, \hat{C}^b) - \Omega_N(\hat{Q}_6^a, \hat{C}^a)$ at fixed p are computed as the line integral of this $\boldsymbol{\nabla}\Omega_N$ along any convenient path joining $(\hat{Q}_6^a, \hat{C}^a, p)$ with $(\hat{Q}_6^b, \hat{C}^b, p)$ in the $(\hat{Q}_6, \hat{C})$ plane. Then, the coexistence pressure, $p_{\rm co}$, follows from the difference in effective potential between the pressure-dependent coordinates of the coexisting pure phases:

$$\Delta\Omega_N(p) = \Omega_N\big(\hat{Q}_6^{\rm FCC}(p), \hat{C}^{\rm FCC}(p), p\big) - \Omega_N\big(\hat{Q}_6^{\rm fluid}(p), \hat{C}^{\rm fluid}(p), p\big)\,. \tag{8.18}$$

The scope of the game is finding the coexistence pressure, $p_{\rm co}^N$, such that $\Delta\Omega_N(p_{\rm co}^N) = 0$. Indeed, the saddle-point condition (8.16), tells us that, at $p_{\rm co}^N$, the chemical potential for the two phases coincides.

Our framework is illustrated in Fig. 8.6, where we show $\boldsymbol{\nabla}\Omega_N(\hat{Q}_6, \hat{C})$ at $p = p_{\rm co}^{(N)}$. We identify two local minima where $\boldsymbol{\nabla}\Omega_N = 0$ (the fluid, close to $(\hat{Q}_6, \hat{C}) =$

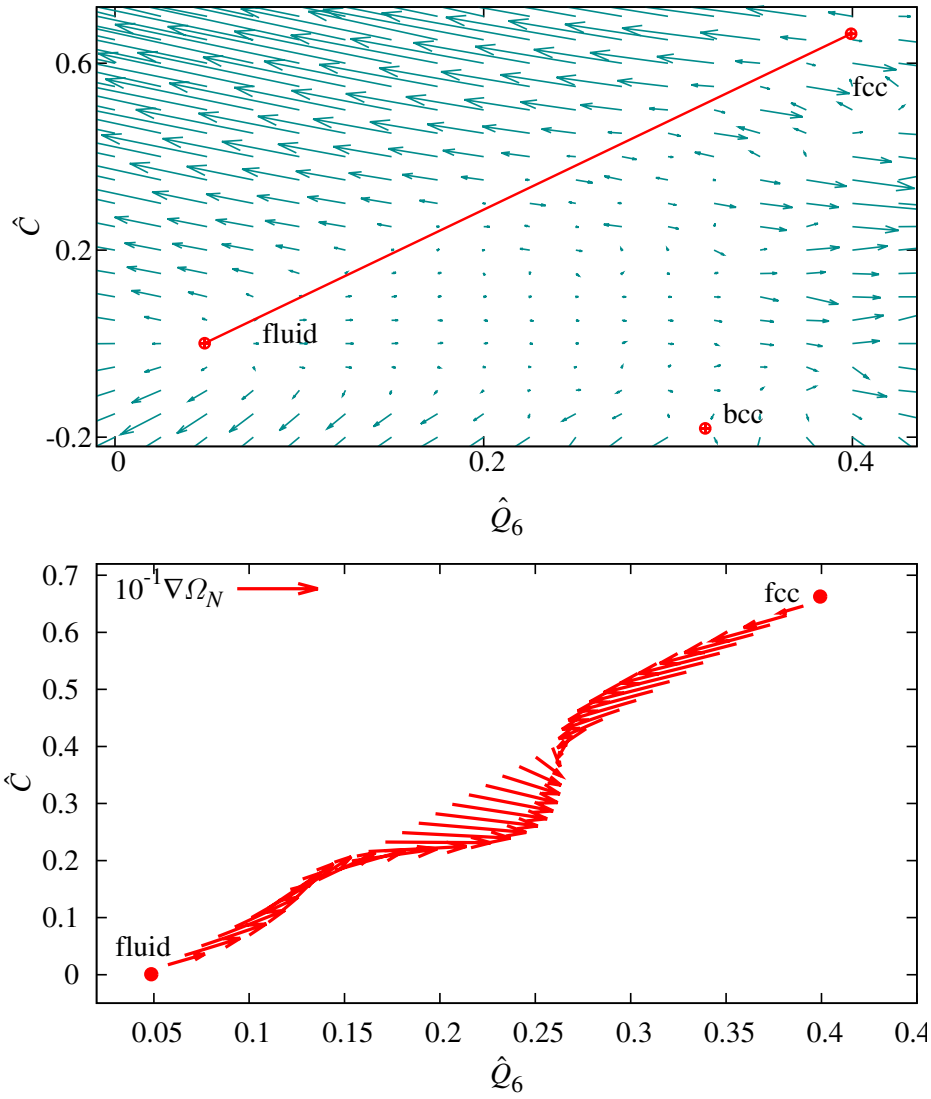

FIGURE 8.6: **Top:** map of the gradient field $\boldsymbol{\nabla}\Omega_{N=256}$, including the points corresponding to the fluid, FCC and BCC potential minima. For the sake of visibility we have divided the gradient by a factor $\alpha = 200$. **Bottom:** $\boldsymbol{\nabla}\Omega_{N=256}$, as computed from Eq. (8.17) for $N = 256$ hard spheres, along the straight path that joins the fluid and the FCC minima of the effective potential. To improve visibility, we have divided $\boldsymbol{\nabla}\Omega_{N=256}$ by a factor of 10 (mind the different normalization as compared with the top panel). The simulation pressure is the phase-coexistence one for both figures.

$(1/\sqrt{N}, 0)$, and the FCC minimum where both parameters are positive, and are summarized in Table 8.1). Note their distance to other local minima of Ω_N, such as the body centered cubic (BCC).

Our main goal is to compute $\Delta\Omega(p) = \Omega^{\text{FCC}} - \Omega^{\text{fluid}}$, choosing the straight segment in Fig. 8.6 as integration path. The path is parameterized by our *reaction coordinate*, S ($S=0$: fluid, $S=1$: FCC). Actually, due to the *additivity* of Q_6 and C,[4] choosing this segment is a must if we are to compute the interfacial free energy. Indeed, physical fluid-solid coexistence is a convex combination of the two pure phases [Rue69], which provides a physical interpretation for S as the fraction of particles in the coexisting solid phase: in the large N limit, v, C and Q_6 vary linearly with S (see Fig. 8.7—bottom).

Our simulation set up is as follows. We start by locating $(\hat{Q}_6, \hat{C})$ for the FCC and liquid minima at $p \approx p_{\text{co}}^{(N)}$. The first guess is obtained from NpT simulations with crystalline/disordered starting configurations. We later refine by solving for $\boldsymbol{\nabla}\Omega_N = 0$ as we will discuss it in detail in Section 8.6.2.

Now, at variance with umbrella sampling, $\Delta\Omega_N$ follows from the integral

$$\Delta\Omega_N = \int_{\mathcal{C}} \boldsymbol{\nabla}\Omega_N \cdot \mathrm{d}\boldsymbol{l} = \int_0^1 \boldsymbol{\nabla}_S \Omega_N \, \mathrm{d}S, \tag{8.19}$$

with $\boldsymbol{\nabla}_S\Omega_N$, the projection of $\boldsymbol{\nabla}\Omega_N$ along the straight-line, Fig. 8.7—top. In addition, we use (8.11) to extrapolate $\boldsymbol{\nabla}\Omega_N$ to different pressures, which allow us to obtain $\Delta\Omega(p)$ as a function of pressure. Then, it is easy to locate $p_{\text{co}}^{(N)}$, Fig. 8.8. Statistical errors are estimated using standard Jack-Knife blocks [Ami05].

In order to compute p_{co}^{N}, we may initially neglect the pressure dependence of the end points for the integration path in Fig. 8.6. One may easily correct for end-points displacements, as explained in Sect. 8.6.2, which induces a correction in p_{co}^{N} negligible with respect to our statistical errors.

The problem of thermalization is fully tackled in Appendix E, nonetheless we give here a few strokes of the brush about how we can be confident of it. We introduce a uniform S grid on the liquid-FCC line and perform *independent* simulations at fixed $(\hat{Q}_6, \hat{C}, p)$ (see Table 8.2 for simulation details). As a test for equilibration, achieved for all N but $N = 4000$, every run was performed twice (starting from an ideal gas and from an ideal FCC crystal). Furthermore, our runs for $N \leq 2916$ are, at least, 100τ long (τ is the integrated autocorrelation time [Sok97], computed for Q_6 and v). For $N = 2916$, but only at $S = 0.4$, we find metastability with

[4] A magnitude A is *additive* if NA is extensive: gluing together systems 1,2 (with $N^{(i)}$ particles and $A = A^{(i)}$, $i = 1,2$), results in a total system with $N = N^{(1)} + N^{(2)}$ particles and $NA = N^{(1)}A^{(1)} + N^{(2)}A^{(2)}$. C is additive to a great accuracy for coexisting fluid and FCC phases, because the average number of neighbors N_b is very similar in both phases (5% difference, with negligible effects on additivity in our N range, as compared with surface effects $\sim 1/N^{1/3}$). Q_6 is additive only if one of the subsystems, say $i = 1$, is a liquid so that $Q_6^{(1)} \sim 1/\sqrt{N^{(1)}}$ (Q_6 is a pseudo-order parameter, i.e. a strictly positive quantity which is of order $1/\sqrt{N}$ in a disordered phase). For studies of interfaces on larger systems, it would be advisable to choose exactly additive order parameters.

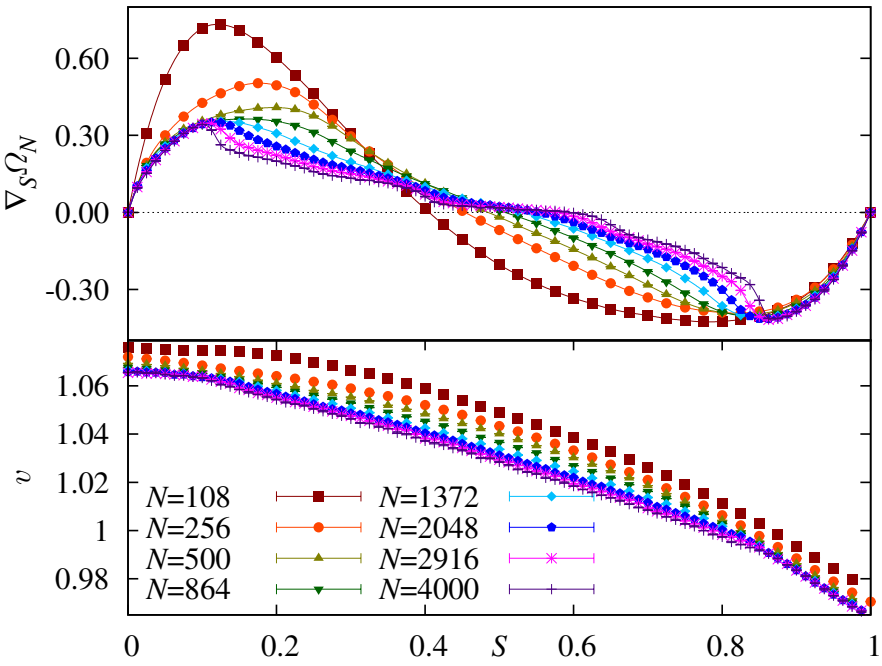

FIGURE 8.7: (**Top**) $\boldsymbol{\nabla}\Omega_N$ projected over the fluid-FCC line, $\boldsymbol{\nabla}_S\Omega_N$, vs. the line parameter S ($S = 0$: fluid, $S = 1$: FCC), for all our system sizes at the simulation pressures. (**Bottom**) Specific volume $v = V/N$ as a function of line parameter S. At large N, v becomes a linear function, as expected for a convex combination of pure phases [Rue69].

a helicoidal configuration (however, its contribution to final quantities is smaller than statistical errors). Metastabilities arise often for $N = 4000$, at intermediate S (yet, a careful selection of starting configurations yields a $\boldsymbol{\nabla}\Omega_N$ with smooth S dependency).

8.6.1 Results

By now, we have all the tools to compute $\Delta\Omega_N(p)$. These potential differences as a function of p are shown in Figure 8.8. Once this effective potential is known, $p_{\text{co}}^{(N)}$ is obtained as the pressure at which $\Delta\Omega_N\left(p_{\text{co}}^{(N)}\right) = 0$. We show in Table 8.2 and Figure 8.9 the results for each system size. As usually, we are interested in the large N limit p_{co}^{∞}. Figure 8.9 suggests that we need a second order polynomial to fit the data $p_{\text{co}}^{(N)}$. We try a fit $p_{\text{co}}^{(N)} = p_{\text{co}}^{\infty} + a_1/N + a_2/N^2$ [Bor92] for $256 \leq N \leq 2916$ (fitting data and curve are also in Table 8.2 and Figure 8.9), obtaining

$$p_{\text{co}}^{\infty} = 11.5727(10)\,.$$

For this extrapolation, we left out the $p_{\text{co}}^{N=4000}$ value because of the doubtful thermalization. Nevertheless, we would like to point out that the $p_{\text{co}}^{N=4000}$ is compatible with the fitted curve.

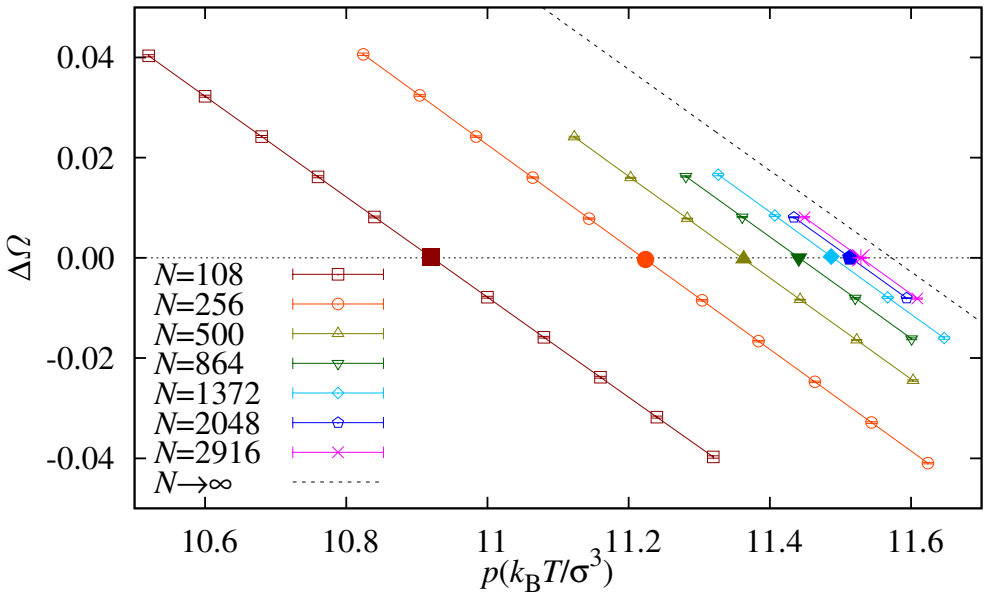

FIGURE 8.8: Effective-potential difference $\Delta\Omega(p) = \Omega^{\mathrm{FCC}} - \Omega^{\mathrm{fluid}}$, as a function of pressure. At p_{co}^N, $\Delta\Omega_N = 0$. The large N limit stems from Eq. (8.22). The simulated pressures (see Table 8.1) correspond to the larger, filled symbols.

	This work	[Wil00]	[Err04]	[ZT10]	[Veg07]
N	p_{co}	Phase switch		Direct coexistence	E. M.
108	10.9216(18)	10.94(4)	11.00(6)		11.02(5)
256	11.2209(13)	11.23(4)	11.25(1)		11.26(5)
500	11.3607(8)		11.34(1)		11.35(3)
864	11.4416(13)				
1372	11.4897(13)				11.50(3)
2048	11.5146(7)				11.52(3)
2916	11.5311(15)				
4000	11.5452(11)				
∞	11.5727(10)	11.49(9)	11.43(2)	11.576(6)	11.54(4)
χ^2/dof	2.61/3				

TABLE 8.2: For each N, we report the phase-coexistence pressure p_{co}^N in units of $k_{\mathrm{B}}T/\sigma^3$ (which is compared with work by other authors using different methods: phase switch Monte Carlo, the non-equilibrium direct coexistence method, and the Einstein Molecule approach).

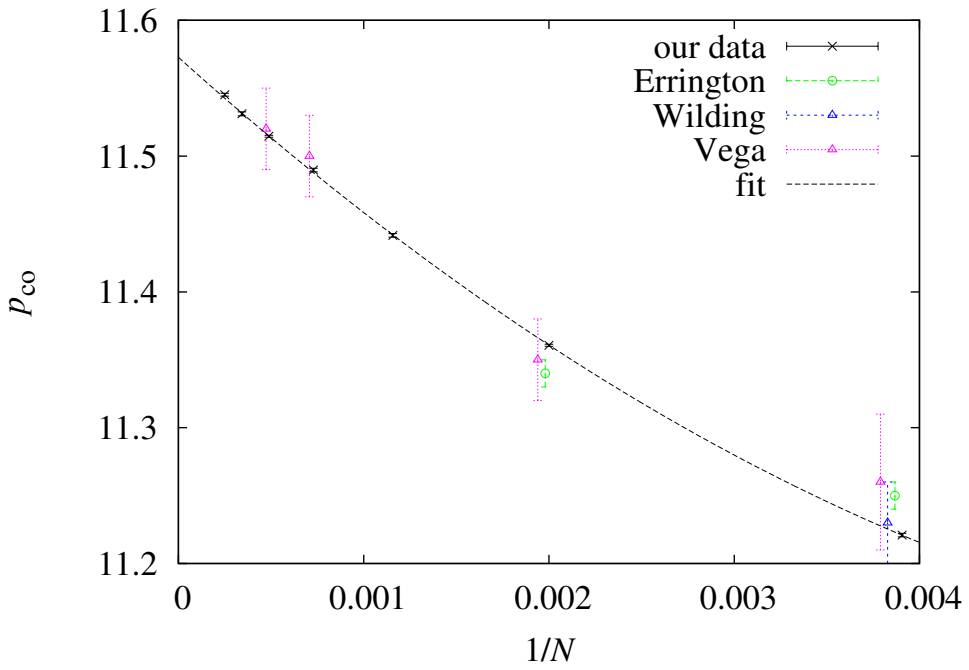

FIGURE 8.9: Finite size estimations of p_{co} plotted vs. $1/N$ obtained in this work, together with previous determinations using phase-switch MC, Errington [Erro4] and Wilding [Wiloo], and Einstein molecule method, Vega [Vego7]. To improve visibility, estimations by other authors are slightly displaced to the left. We plot as well the quadratic fit of our data.

N	$\langle v \rangle^{\text{FCC}}$	$\langle v \rangle^{\text{fluid}}$
108	0.97580(7)	1.07611(8)
256	0.97049(6)	1.07202(7)
500	0.96796(10)	1.06932(7)
864	0.96796(10)	1.06932(7)
1372	0.96549(14)	1.06659(13)
2048	0.96500(14)	1.06577(15)
2916	0.96468(14)	1.06545(19)
4000	0.96461(13)	1.06556(15)
∞	0.96405(3)	1.06448(10)
χ^2/dof	0.32/3	0.61/2
N_{min}	256	500
N_{max}	2916	2916

TABLE 8.3: Specific-volumes of the FCC crystal and the fluid phase as function of the system size. We include the extrapolation to $N = \infty$ together with the details of the linear fit to $v^{\infty} + a_1/N$.

We compare our results in Table 8.2 and Figure 8.9 with previous estimates. They are more precise (and compatible with) independent determinations by other authors, both at finite and in the large N limit. The best previous equilibrium estimate seems to be the rather crude $p_{\text{co}}^{\infty} = 11.50(9)$ [Wiloo], obtained using phase-switch Monte Carlo. In fact, the only previous method accurate enough to provide a meaningful comparison is the non-equilibrium direct-coexistence: $p_{\text{co}}^{\infty} = 11.576(6)$ [ZT10]. Note, however, that in order to achieve such a small error (but still six times larger than the error in our tethered computation), systems with up to $N = 1.6 \times 10^5$ particles were simulated [ZT10].

In addition, we can compute the specific volumes for the fluid and the FCC phase averaging the volume data at $S = 0$ and 1 respectively (the saddle points quoted in Table 8.1). We show the results obtained in Table 8.3 together with an extrapolation in $1/N$.

Finally, the reader might wonder about the linear relation of $\Delta\Omega$ vs. p in Figure 8.8. It follows from Eq. (8.16). The potential at each extrema is $\Omega^*(p) = g(p) + O(1/N)$, where $g(p)$ is the Gibbs free-energy density. Then, its derivate is

$$\left.\frac{\partial \Omega}{\partial p}\right|_* = \frac{\partial g}{\partial p} + O(1/N) = v_* + O(1/N), \tag{8.20}$$

where v_* is the intrinsic volume at the extremal point. Thus, the effective potential at p close to p^*, is:

$$\Omega(p) = \Omega^* + v^*(p - p^*) + O\left((p - p^*)^2\right) + O(1/N), \tag{8.21}$$

and since the effective potential at the extremal points must be equal in the two phases at the coexistence pressure, p_{co}, the difference in effective potential between

the fluid and the FCC phase at p, will be determined by

$$\Omega_{\rm FCC}(p) - \Omega_{\rm f}(p) = (v_{\rm FCC} - v_{\rm fluid})(p - p_{\rm co}) + O(1/N), \tag{8.22}$$

and thus, presents a linear dependency in p. We include in Fig. 8.8 the prediction for the thermodynamic limit that follows from this last relation using the large-N extrapolations for the specific volume displayed in Table 8.3.

8.6.2 Calculation of the extremal points and corrections

We had postponed the discussion about the computation of the extremal points shown in Table 8.1, as well as the issue of considering the same integration curve for all values of p. We devote this section to both problems.

We need to locate the two extremal points in the straight path in Fig. 8.6, which correspond to the fluid or to the FCC crystal. The two points are local minima of Ω_N, regarded as a function of $\hat{Q}_6$ and $\hat{C}$ but at fixed pressure. Our procedure has been as follows.

We first obtain a crude estimate from standard simulations in the NpT ensemble (without any constrain in the crystal parameters). Note that the autocorrelation time for such simulations is unknown, but larger than any simulation performed to date. Hence, these standard simulations get stuck at the local minimum of Ω_N which is most similar to their starting configuration. Starting the simulation either from an ideal gas, or from a perfect FCC crystal, we approach the pure-phases we are interested in. The Monte Carlo average of $Q_6(\boldsymbol{R})$ and $C(\boldsymbol{R})$ provides our first guess.

To refine the search of either of the two local minima $(\hat{Q}_6^*, \hat{C}^*)$, we note that, up to terms of third order in $\hat{Q}_6 - \hat{Q}_6^*$ or $\hat{C} - \hat{C}^*$,

$$\Omega_N(\hat{Q}_6, \hat{C}) = \Omega_N^* + \frac{A_{QQ}}{2}(\hat{Q}_6 - \hat{Q}_6^*)^2 + A_{QC}(\hat{Q}_6 - \hat{Q}_6^*)(\hat{C} - \hat{C}^*) + \frac{A_{CC}}{2}(\hat{C} - \hat{C}^*)^2 \,. \tag{8.23}$$

The shorthand Ω_N^* stands for $\Omega_N(\hat{Q}_6^*, \hat{C}^*)$. Incidentally, Eq. (8.23) tells us that the computation in Sect. 8.6 is intrinsically stable. An error of order ϵ in the location of $(\hat{Q}_6^*, \hat{C}^*)$ will result in an error of order ϵ^2 in the coexistence pressure.

Yet, the tethered computation does not give us access to Ω_N, but to its gradient:

$$\boldsymbol{\nabla}\Omega_N(\hat{Q}_6, \hat{C}) = \big(A_{QQ}(\hat{Q}_6 - \hat{Q}_6^*) + A_{QC}(\hat{C} - \hat{C}^*), A_{CC}(\hat{C} - \hat{C}^*) + A_{QC}(\hat{Q}_6 - \hat{Q}_6^*)\big) \,. \tag{8.24}$$

Eq. (8.24) holds up to corrections quadratic in $\hat{Q}_6 - \hat{Q}_6^*$ or $\hat{C} - \hat{C}^*$. We thus compute the expectation value of the field $\boldsymbol{\nabla}\Omega_N$, in a grid of nine points $(\hat{Q}_6, \hat{C})$ that surround our first guess for $(\hat{Q}_6^*, \hat{C}^*)$, and fit the results to Eq. (8.24). We iterate this procedure until an accuracy $\sim 10^{-6}$ in both coordinates $(\hat{Q}_6^*, \hat{C}^*)$ is reached.

Actually, Eq. (8.11), shows how one extrapolates the expectation values for the gradient field from the simulated pressure, p to a nearby $p + \delta p$. The corresponding fit to Eq. (8.24) provides the new coordinates $\big(\hat{Q}_6^*(p + \delta p), \hat{C}^*(p + \delta p)\big)$.

At this point, one could worry because the integration path in Fig. 8.6 is no longer appropriate at pressure $p + \delta p$. In fact, the extremal points in the integration path are pressure-dependent. However, some reflection shows that this is not a real problem. In fact,

$$\Delta\Omega_N(p + \delta p) = \Delta^{\text{FCC}}(p, p + \delta p) + \Delta^{\text{path}}(p, p + \delta p) - \Delta^{\text{fluid}}(p, p + \delta p)\,. \qquad (8.25)$$

The different pieces in Eq. (8.25)

$$\begin{aligned} \Delta^{\text{FCC}}(p, p + \delta p) &= \Omega_N\big(\hat{Q}_6^{\text{FCC}}(p + \delta p), \hat{C}^{\text{FCC}}(p + \delta p);\, p + \delta p\big) - \\ &- \Omega_N\big(\hat{Q}_6^{\text{FCC}}(p), \hat{C}^{\text{FCC}}(p);\, p + \delta p\big)\,, \end{aligned} \qquad (8.26)$$

the correction due to the shift of order δp in the coordinates of the FCC minimum,

$$\begin{aligned} \Delta^{\text{path}}(p, p + \delta p) &= \Omega_N\big(\hat{Q}_6^{\text{FCC}}(p), \hat{C}^{\text{FCC}}(p);\, p + \delta p\big) - \\ &- \Omega_N\big(\hat{Q}_6^{\text{fluid}}(p), \hat{C}^{\text{fluid}}(p);\, p + \delta p\big)\,, \end{aligned} \qquad (8.27)$$

the line-integral sketched in Fig. 8.6 as computed at pressure $p + \delta p$, and

$$\begin{aligned} \Delta^{\text{fluid}}(p, p + \delta p) &= \Omega_N\big(\hat{Q}_6^{\text{fluid}}(p + \delta p), \hat{C}^{\text{fluid}}(p + \delta p);\, p + \delta p\big) - \\ &- \Omega_N\big(\hat{Q}_6^{\text{fluid}}(p), \hat{C}^{\text{fluid}}(p);\, p + \delta p\big)\,, \end{aligned} \qquad (8.28)$$

the correction due to the shift in the coordinates of the fluid minimum.

Now, one expects that the pressure-induced changes in the minima coordinates as well as on the coefficients A_{QQ}, $A_{Q,C}$ and A_{CC} will of order δp. Hence, Eq. 8.23 implies that both $\Delta^{\text{FCC}}(p, p + \delta p)$ and $\Delta^{\text{fluid}}(p, p + \delta p)$ are of order $(\delta p)^2$. This is the rationale behind the simplifying assumption made in Sect. 8.6.

At any rate, $\Delta^{\text{FCC}}(p, p + \delta p)$ and $\Delta^{\text{fluid}}(p, p + \delta p)$ can be numerically computed from Eq. 8.23. For all values of N simulated, their combined effect on the determination of the coexistence pressure turns out to be smaller than 1% of the statistical error bars as shown in Table 8.4. Then, at least in our systems, this kind of refinement seems not to be necessary (partly because we did short simulations that yielded working estimates of $p_{\text{co}}^{(N)}$).

However, we cannot forget that before running simulations we had an idea of the value of the coexistence pressure for each system size, and we did not need to displace too much in p, but this is not the normal case in the most interesting systems, and these corrections might become important as long as one gets further away from the simulation pressure.

N	p_{co}	$p_{\text{co}}^{\text{corrected}}$	$(p_{\text{co}} - p_{\text{co}}^{\text{corrected}})/error$
108	10.9216(18)	10.9216(18)	-0.0046
256	11.2209(13)	11.2209(13)	-0.0106
500	11.3607(8)	11.3607(8)	-0.0132
864	11.4416(13)	11.4416(13)	-0.0018
1372	11.4897(13)	11.4897(13)	-0.0062
2048	11.5146(7)	11.5146(7)	-0.0020
2916	11.5311(10)	11.5311(10)	-0.0082

TABLE 8.4: Study of the effect of the corrections in the determination of p_{co}^N.

8.7 Geometric transitions and the interfacial free-energy

The interfacial free energy is the free-energy cost per unit area of a liquid-to-crystal interface. Its computation has been rather difficult for hard spheres. In fact, different authors finding mutually incompatible results [Dav00, Mu05, Dav10].

As for the interfacial free energy, γ, he difficulties are due to the need of considering inhomogeneous configurations. [5] In a system with periodic boundary conditions, geometrical transitions arise when the line parameter S varies from the liquid to the solid. In fact, the system struggles to minimize the surface energy while respecting the global constraints for Q_6 and C. Depending on the fraction of crystal phase, which is fixed by S, the minimizing geometry can be either a bubble, a cylinder or a slab of liquid in a crystal matrix (or vice versa). An example of each type of configuration is displayed in Fig. 8.10. As S varies, the minimizing geometry changes at definite S values. This phenomenon is named *geometric transition*, and has been previously studied in simpler models (for instance, first-order transitions in lattice magnetic systems [MM07], or fluid-gas phase-coexistence [Mac06, Bin11]). These transitions result in the cusps and steps that appear for large N in $\boldsymbol{\nabla}_S \Omega_N$, Fig. 8.7—top.

The physical situation is as follows. When we go from the liquid to the solid, Fig. 8.6, the homogeneous fluid becomes unstable at a value of the linear coordinate $S \propto N^{-1/(D+1)}$, which means that a macroscopic droplet of crystal forms. This has been established for all types of first-order phase transitions [Bis02, Bin03, Mac04, Nuß06], and explicitly verified for crystallization here. As S grows the mass of the crystal droplet increases, which costs surface energy. At a certain point, the periodic boundary conditions allow reducing the surface energy by turning the crystal droplet onto a crystal cylinder. At still larger S, the cylinder becomes a slab. Of

[5] The tethering approach does not induce artificial interfaces. In fact, mathematically, the interfacial free-energy is defined though the ratio of two partition functions with different boundary conditions. But the tethered potential does not change the partition function [with any boundary conditions, see Eq. (8.10)].

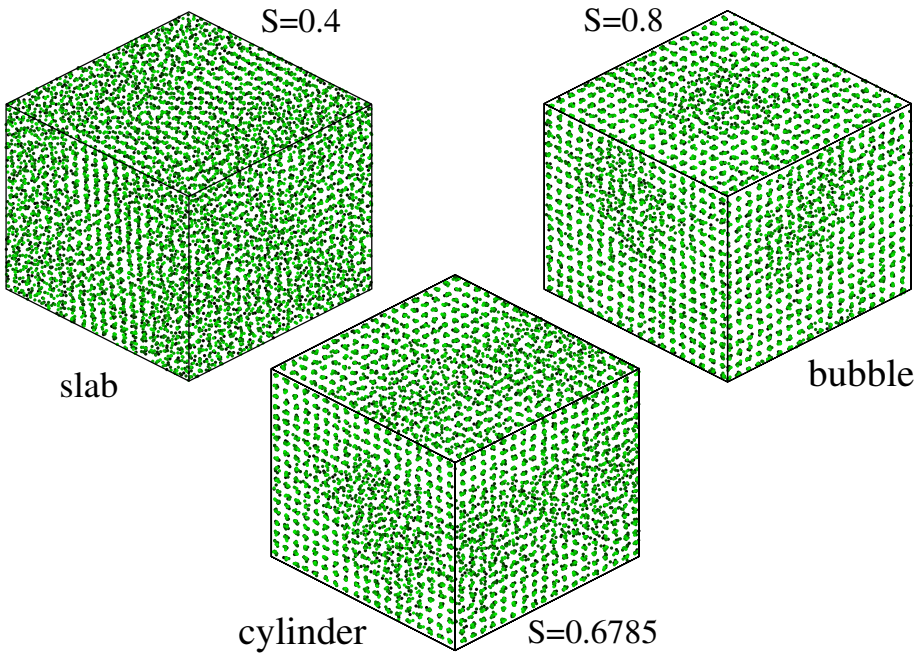

FIGURE 8.10: Snapshots of mixed configurations for $N = 2916$ particles found as the line parameter S varies. We present projections in the three Cartesian directions. To improve visibility, the radii are a fraction of the real ones, and the darkness is an increasing function of the distance to the projection plane.

course another three analogous geometrical transitions arise when S keeps increasing as we approach the FCC minimum. All six geometric transitions appeared in our simulations of large enough hard-spheres systems. We are interested in identifying systems large enough to form a slab of crystal surrounded by fluid to be able to compute the interfacial free-energy.

In order to follow these geometrical transitions, it is useful to look at the inhomogeneity of the system. As shown in Figure 8.10, we deal with phase separation between fluid and FCC crystal, then it is interesting to consider the particle-density fluctuations (recall Section 7.2.1.2) quantified through

$$\mathcal{F}(\boldsymbol{q}) = \frac{1}{N^2}\left|\sum_{i=1}^{N} \mathrm{e}^{\mathrm{i}\boldsymbol{q}\cdot\boldsymbol{r}_i}\right|^2, \tag{8.29}$$

As we are interested in the largest wavelength, we consider the smallest $\boldsymbol{q}$ allowed by periodic boundary conditions, $\|\boldsymbol{q}\| = 2\pi/L$, where L is the linear size of the simulation box. There are three such minimal wave vectors in a cubic box, $(2\pi/L, 0, 0)$, $(0, 2\pi/L, 0)$ and $(0, 0, 2\pi/L)$. Given a particle configuration, we define $\mathcal{F}_1$ as the maximum over the three directions, $\mathcal{F}_3$ as the minimum, and $\mathcal{F}_2$ as the intermediate one. As the droplet, cylinder and slab geometries have different symmetries the natural order parameters are

- Whenever the system is phase separated, $(\mathcal{F}_1 + \mathcal{F}_2 + \mathcal{F}_3)/3$ is of order 1, (order $1/N$ otherwise).

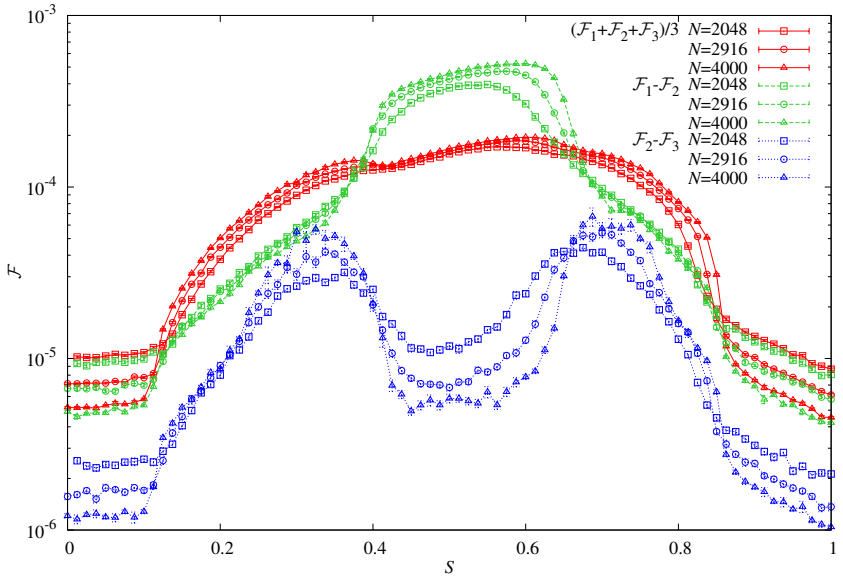

FIGURE 8.11: For systems of N hard spheres at their phase-coexistence pressure, we show, as a function of the line parameter S, different linear combinations of the particle-density fluctuations, Eq. (8.29), computed for the minimal wave vectors allowed by periodic boundary conditions and ordered in such a way that $\mathcal{F}_1 > \mathcal{F}_2 > \mathcal{F}_3$. For the phase-separated states all three $\mathcal{F}$ are of order 1 (order $1/N$ for homogeneous systems). The slab phase is the only one with $\mathcal{F}_1 - \mathcal{F}_2$ of order one. The cylinder phase is identified by $\mathcal{F}_2 - \mathcal{F}_3$ of order one.

- For a cylinder, two of the $\mathcal{F}$'s are of order 1, while the $\mathcal{F}$ along the cylinder axis is small. Hence, $\mathcal{F}_2 - \mathcal{F}_3$ is of order 1 in the cylinder phase, but it vanishes (for large N) both in the droplet and the slab phase.

- For a slab the only $\mathcal{F}$ of order 1 is that transversal to it. Hence $\mathcal{F}_1 - \mathcal{F}_2$ is of order 1 for a slab, but not for the cylinder nor the droplet.

All these behaviors are identified in Fig. 8.11. We thus conclude that $N \geq 2048$ is sufficient to attempt a computation of the interfacial free-energy.

The effective potential has a local maximum along the line that joins the FCC and the fluid (the solution of $\boldsymbol{\nabla}_S \Omega_N = 0$ at $S^* \approx 0.5$, Fig. 8.7—top). The excess free energy is due to the *two* interfaces that the fluid presents with a crystalline slab parallel to the simulation box ($\{100\}$ planes). Then the interfacial free energy at $p_{\text{co}}^{(N)}$ is

$$\gamma_{\{100\}}^{(N)} = k_{\text{B}} T \, N \left(\Omega_{s^*} - \Omega_{\text{FCC}} \right) / \left(2 \left\langle N v \right\rangle_{S^*}^{2/3} \right). \tag{8.30}$$

The $\gamma_{\{100\}}^{(N)}$ (listed in Table 8.5) are extrapolated as [Bil94]

$$\frac{\gamma_{\{100\}}^{(N)} \sigma^2}{k_{\text{B}} T} = \frac{\gamma_{\{100\}} \sigma^2}{k_{\text{B}} T} + \frac{a_2 - \log N}{6 N^{2/3}} + \frac{a_3}{N} + \frac{a_4}{N^{4/3}} + \dots \tag{8.31}$$

N	$\gamma_{\{100\}}$
108	0.4063(12)
256	0.4243(8)
500	0.4798(8)
864	0.5285(12)
1372	0.5611(14)
2048	0.5832(10)
2916	0.5971(12)
4000	0.607(2)
∞	0.636(11)
χ^2/dof	0.14/2

TABLE 8.5: For each N, we report {100} interfacial free energy $\gamma_{\{100\}}$ (in $k_B T/\sigma^2$ units). The large-N limit is obtained using (8.31).

A fit for $256 \leq N \leq 2916$ yields $\gamma_{\{100\}} = 0.636(11)$ in units of $k_B T/\sigma^2$ ($\chi^2 = 0.14$ for two degrees of freedom). We remark that the difference among the fit and $\gamma_{\{100\}}^{(N=4000)}$ (not included in the fit) is one fifth of the error bar. Also, the extrapolation for $500 \leq N \leq 2916$ merely doubles the final error estimate. Our result is compatible with $\gamma_{\{100\}} = 0.64(2)$ [Muo5], $\gamma_{\{100\}} = 0.619(3)$ [Caco3] and $\gamma_{\{100\}} = 0.639(11)$ [Här12], but not with $\gamma_{\{100\}} = 0.5820(19)$ [Dav10]. A peculiarity of the tethered approach is that one may control the dependence of the estimate of γ_{100} on the actual estimate used for the coexistence pressure. One simply computes γ_{100} as a function of pressure, using (8.30), as it is shown in Fig. 8.12. It turns out that the slope of the curve is of order 0.4, hence an error of order ϵ in the determination of $p_{\rm co}^{\infty}$ results in an error of order $\sim 0.4\epsilon$ in γ_{100}. To our knowledge, such effects have not been taken into account in previous computations [Davoo, Muo5, Dav10]. In fact, in recent works [Här12] using the coexistence method, the interfacial free-energy was computed at the coexistence pressure $p_{\rm co}^{\infty} = 11.576(6)$ [ZT10] very close to our own computation. Not surprisingly, these authors obtain an almost identical interfacial free energy.

A final warning is in order. Not much is known about the effect of the cusps and steps in $\boldsymbol{\nabla}_S \Omega_N$, Fig. 8.7—top, in the large-N extrapolation $\gamma_{\{100\}}^{(N)} \to \gamma_{\{100\}}$. This non-smoothness is a consequence of the geometric transitions that arise in our larger systems. However, as far as the $p_{\rm co}^{(N)} \to p_{\rm co}$ extrapolation is concerned, the analogy with simpler models [MM07] (e.g. the $D = 2$ Potts model, where comparison with exact solutions is possible), strongly suggests that these cusps and steps are inconsequential.

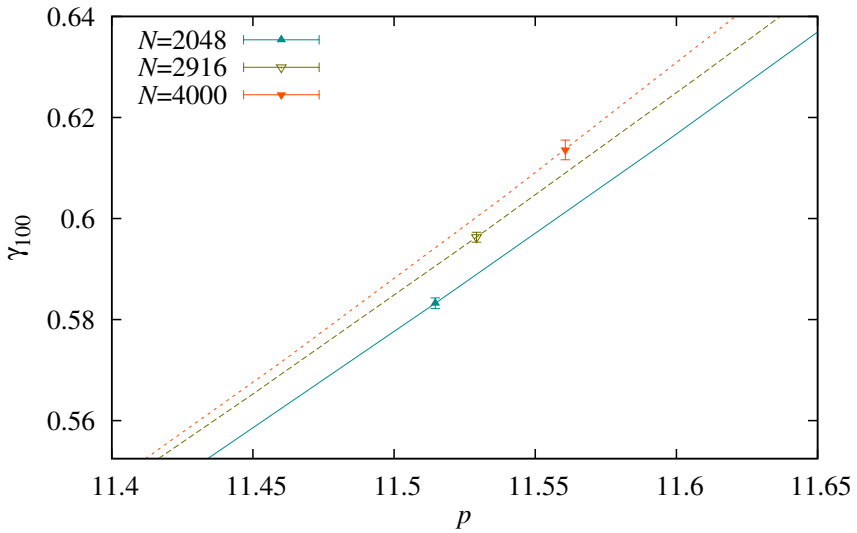

FIGURE 8.12: Interfacial free-energy for the (100) lattice crystalline direction $\gamma_{\{100\}}$ as a function of pressure, for a system of N hard-spheres, for $N = 2048, 2916$ $N = 4000$. We estimated $\gamma_{\{100\}}$ from Eq. 8.30

Part III

Quantum Annealing

CHAPTER IX

Many-body transverse interactions in the quantum annealing

9.1 Introduction

In all previous chapters, our initial objective was to reach the equilibrium configuration given certain conditions. This is nothing but an optimization problem: the task of finding the configuration that optimizes a given free-energy (or cost in a more general problem) function $\mathcal{H}(\{S_i\})$ dependent on a large number N of variables $S_1, \ldots, S_N$ (often subjected to constraints). This kind of question appears often in physics when one wonders about equilibrium or ground states, but it is a whole research field by itself, common to many fields in science. Finding the minimum energy or cost often becomes a hard task when the constraints in the system, or the interactions between variables, induce frustration because there is no way to find a minimum configuration that minimizes the problem locally (we discussed the concept of frustration in spin glasses in Figure 3.1). As we have discussed all over this thesis, the frustration leads to a rugged free-energy landscape of many relative minima, and an exhaustive search for the absolute minimum is just not feasible for the interesting sizes (the dimension of the system often grows exponentially with N). As examples of these optimization problems, one can cite the traveling sales problem [Pap98] or the k-SAT problem [Gar79] in computer science, or finding the equilibrium configuration in a glass, as we tried in this thesis.

Complexity in optimization problems is commonly classified as P if an algorithm is known to solve the problem in a time that grows polynomially with N. On the contrary, if it is not the case, and the time scales faster with N, these problems are labeled NP and considered as hard problems. Among all the NP problems, there is a subgroup named NP complete so that any possible NP problem can be reduced to one of them by means of a polynomial algorithm. Thus, if one algorithm

were found that solved polynomically an NP complete problem, the whole family of problems would also become easy. The problems mentioned above belong all to the NP-complete class.[1]

Statistical mechanics, based on physical intuition, has contributed a lot in the development of new strategies for optimization problems: parallel tempering or replica exchange [Huk96], and simulated annealing [Kir83] are the two popular and widely used examples even outside the physics' world. We have also studied and introduced here new algorithms like the microcanonical or tethered algorithms in Part II of this thesis with the same aim. For the algorithm we are studying in this Chapter, the quantum annealing, it is interesting to first discuss the the temperature annealing, its classical counterpart. In this method, fluctuations are introduced in the problem through a ficticious temperature. This temperature favors the jump over barriers and thus encourages the system to visit other possible minima. The system is then simulated at a temperature $T(t)$ that decreases slowly with time until it is finally switched off at the end of the simulation. We will refer to this simulated annealing as classical annealing (CA) in contrast to the quantum annealing (QA) [Kad98, Fin94, Das08, San06], where fluctuations are induced also in the system but this time quantum ones. Quantum perturbations allow tunneling effects, and thus, if narrow enough, barriers can be crossed instead of surpassed.

In the traditional QA formulation, a time-dependent Hamiltonian is introduced

$$\hat{H}(t) = s(t)\hat{H}_0 + [1 - s(t)]\,\hat{V}, \tag{9.1}$$

where $\hat{H}_0$ is the target Hamiltonian (or the cost function that one wants to minimize) and $\hat{V}$ represents the quantum perturbations. In the field we are working in, the Hamiltonian $\hat{H}_0$ represents the magnetic interaction between spins. For the sake of simplicity, we will consider that $\hat{H}_0$ only depends on the z components of the Pauli matrix $\hat{\sigma}_i^z$, where $i(= 1, \ldots, N)$ labels the index of each spin in the system. As normally, we are interested in finding the lowest energy spin configuration, i.e. the ground state. Now we introduce the quantum fluctuations through a spin driver term $\hat{V}$. In principle, this term is arbitrary, as long as it does not commute with $\hat{H}_0$. In addition, we impose that $\hat{V}$ has a single, trivial ground state. A typical example of a driver Hamiltonian is the transverse-field operator

$$\hat{V}_{\mathrm{TF}} \equiv -\sum_{i=1}^{N} \hat{\sigma}_i^x, \tag{9.2}$$

where the $\hat{\sigma}_i^x$ $(i = 1, \ldots, N)$ are the x components of the Pauli matrix. This perturbation is very intuitive, since it represents nothing but the interaction with a magnetic field along the x direction that induces quantum transitions between the eigenstates of $\hat{\sigma_i^z}$, whose modulus is tuned through the control parameter $s(t)$. Initially, at $t = 0$, the control parameter $s(t)$ starts at $s(0) = 0$, with $\hat{H}(0) = \hat{V}$, and

[1] With the exception of the 2-SAT problem and the $2D$ Ising spin glass [Bar12] that can be solved polynomically.

increases monotonically with time until it reaches unity at time τ and $\hat{H}(\tau) = \hat{H}_0$. Let us choose the simplest possible scheme where the control parameter grows linearly with time, i.e. $s(t) = t/\tau$.

The evolution of the system, $|\Phi(t)\rangle$, is determined by the Schrödinger equation,

$$\mathrm{i}\frac{\mathrm{d}}{\mathrm{d}t}|\Phi(t)\rangle = \hat{H}(t)\,|\Phi(t)\rangle\,,\ 0 \leq t \leq \tau. \tag{9.3}$$

The initial state $|\Phi(0)\rangle$ is the ground state of the driver Hamiltonian $\hat{V}$ and is thus known. If the parameter $s(t)$ is changed very slowly (τ is very long), the state will be at every time very close to the instantaneous ground state. If it so, by tuning the parameters, one will move adiabatically from the initial ground state to the ground state of $\hat{H}_0$.

The adiabatic theorem states that the system stays close to the instantaneous ground state as long as $\tau \gg \Delta_{\min}^{-2}$ where $\Delta_{\min}$ is the minimum energy gap from the ground state. Of course, in order for the above argument to be of general use, this $\Delta_{\min}$ cannot decrease with N too fast. In fact, if the energy gap decays exponentially with the system size, as happens generally in first-order transitions, the running time will increase exponentially with N and the QA would not help to solve the problem efficiently.

This vanishing exponential gap present in many first-order transitions is sometimes considered to be one of the most important drawbacks of quantum annealing. Its presence was somehow shadowed for certain time by the preasymptotic behavior displayed in the small system sizes feasible in simulations [Far01, Hog03, You08]. Indeed, in the last years, an increasing number of first-order transitions in the annealing parameters are being found [You10, Hen11, Jör08, Jör10a, Jör10b]. It has thus been suggested that the presence of these quantum first-order transitions when tuning the transverse field is an intrinsic property of the systems with complicate free energy landscape, i.e. the hard problems, leading a pessimistic scenario for the QA algorithm [You10, Hen11, Jör08, Jör10a, Jör10b].

Recently, it was found that the ferromagnetic p-spin model, a model without disorder and with a simple free energy landscape, also suffers from this kind of first-order transition [Jör10a]. Due to its simplicity, this model constitutes a perfect benchmark to study the QA performance. Indeed, it was recently shown [Sek12] that, at least for finite values of p and $p \neq 3$, it is possible to avoid this first-order transition by appending an additional antiferromagnetic driver term and performing the annealing along a curve in a space of two annealing parameters instead of just one. This study changes the paradigm about first-order transitions in QA, since the failure of QA strategies observed up to now could be a failure of the standard formulation of QA with a transverse field, not a failure of the algorithm itself.

Here we go deeper into this problem, studying a family of alternative driver terms, displaying different symmetries. We show analytically the existence of paths that cross only a second-order transition and thus the speed of QA is not exponentially damped. Indeed, in a second order transition the gap vanishes only

polinomially with the number of particles, which must be compared with the exponential damping observed in the first order transition. The solution to the problem is not unique and we study the properties of these new driver terms, reaching the conclusion that the structure of the ground state of the additional Hamiltonians is not the main important feature that makes the whole algorithm success as argued in [Bap12].

9.2

Problem

Our starting point is the ferromagnetic p-spin model ($p = 2, 3, 4 \ldots$)

$$\hat{H}_0 = -N \left(\frac{1}{N} \sum_{i=1}^{N} \hat{\sigma}_i^z \right)^p . \tag{9.4}$$

The ground state for this model, $|\Phi_0\rangle$, corresponds to the state of all the spins aligned along the z direction. In order to avoid the degeneracy of the up and down configurations present in even powers of p, we consider here only the odd values of p and $p \geq 3$. In the limiting $p \to \infty$ case, this model is nothing but the Grover problem [Jör10a, Gro97]. Although the Grover's quantum algorithm, whose reformulation in quantum annealing is given in [Rol03], is considered a success of the quantum algorithm (provides a square-root gain with respect to the classical search [Gro96]) it remains being a hard problem even with quantum algorithms. Now we consider the problem of finding this already known ground state $|\Phi_0\rangle$ of (9.4) with the QA algorithm using two driving terms.

As usual, we consider the traditional transverse field operator,

$$\hat{V}_{\mathrm{TF}} \equiv -\sum_{i=1}^{N} \hat{\sigma}_i^x , \tag{9.5}$$

whose ground state, $|\Phi^{\mathrm{TF}}\rangle$, is the one where all the N spins are pointing to the positive direction along the x axis. We next introduce a second Hamiltonian inspired in the antiferromagnetic interaction suggested in [Sek12],

$$\hat{V}_k = +N \left(\frac{1}{N} \sum_{i=1}^{N} \hat{\sigma}_i^x \right)^k , \tag{9.6}$$

that depends on a parameter $k(> 1)$. When $k = 2$, we recover the antiferromagnetic interaction studied in [Sek12]. The ground state for this Hamiltonian, namely $|\Phi_k\rangle$, depends on the value of the power k. When k is odd, the energy is minimum when all spins are aligned along the x axis but pointing to the negative direction. On the contrary, when k is even, the ground state corresponds to the state with

total $\sum_{i=1}^{N}\sigma_i^x = 0$ if N is even, or $\sum_{i=1}^{N}\sigma_i^x = \pm 1$ for N odd. One of the goals of the present paper is to clarify whether the value $k = 2$ is essential to avoid the first-order transition.

If we sum up (9.1), (9.5) and (9.6), the new Hamiltonian of the problem reads as

$$\hat{H}(s,\lambda) = s\left[\lambda\hat{H}_0 + (1-\lambda)\hat{V}_k\right] + (1-s)\hat{V}_{\mathrm{TF}}. \tag{9.7}$$

Here there are two annealing parameters, s and λ. These parameters will be tuned slowly during the annealing process so that, at the final time, τ, $s(\tau) = \lambda(\tau) = 1$ and the target Hamiltonian (9.4) is thus recovered. In that way, one can explore the annealing process following infinitely different paths. It might resemble the idea of nondeterministic Turing machines, but one must always keep in mind that, even though many paths are possible, only one is chosen in each particular realization.

The traditional QA is one of the infinite possible paths in (9.7). In fact, one can remove the influence of $\hat{V}_k$, just by fixing $\lambda(t) = 1$. Then, the annealing is performed by tuning s from 0 to 1. If one looks at the configurations, at $t = 0$ all spins should be aligned with the x axis, and at the end, with the z axis. In this case, we know that the system suffers from a quantum first-order phase transition between these two states. This transition ruins the efficiency of the algorithm as it becomes exponential [Jör10a]. The idea of introducing this two-parameter space (λ, s) is precise to try avoid this transition by following an alternative route. Seki and Nishimori succeeded in finding ingenious paths [Sek12] with antiferromagnetic interactions, and here, we generalize that method to check how the value of k affects the conclusion.

9.3

Analysis by a semi-classical approach

The QA strategy will succeed if we are able to find a path in the space of parameters (λ, s) that avoids crossing any first-order transition. With this aim, we compute in this section the phase diagram correspondent to the new Hamiltonian (9.7), as a function of the parameter k. The $N \to \infty$ limit can be computed analytically using a semi-classical approximation (method to be explained below) or the Trotter-Suzuki decomposition formula [Suz76] and the static approximation (see Appendix G), leading to equivalent results.

9.3.1 General Properties

As a starting point, let us rewrite the Hamiltonian (9.7) in terms of the total spin variables ($S^\alpha = \frac{1}{2}\sum_{i=1}^{N}\sigma_i^\alpha$ with $\alpha = x$, y and z),

$$\hat{H}(s,\lambda) = -s\lambda N\left(\frac{2}{N}S^z\right)^p + s\,(1-\lambda)N\left(\frac{2}{N}S^x\right)^k - 2(1-s)S^x. \tag{9.8}$$

This Hamiltonian commutes with the total squared spin, S^2. Since the total spin is conserved and the initial state in the annealing process is the one with all spins aligned with the x axis, we are only interested in studying the maximum possible S value, i.e. $S = N/2$.

Now, consider the normalized variables $m^\alpha = S^\alpha/S$, with $\alpha = x$, y and z. The commutation relations for these variables are

$$[m^x, m^y] = \mathrm{i}\frac{2}{N}m^z, \tag{9.9}$$

and cyclic permutations. The normalized variable m^α can take $N+1$ values within the interval $[-1, 1]$. Thus, in the large N limit, these variables commute, and we can consider them as the components of a classical unit vector, i.e. $\boldsymbol{m} = (\cos\theta, \sin\theta\sin\varphi, \sin\theta\cos\varphi)$, being θ the polar angle measured from the x axis, and φ the azimuthal one measured from the z axis.

Considering the system now as classic, we can write the energy per spin as

$$e = -s\lambda(\sin\theta\cos\varphi)^p + s\,(1-\lambda)\cos^k\theta - (1-s)\cos\theta. \tag{9.10}$$

The equilibrium state will be determined by the minimum of e. Since p is odd, the minimum lies on the plane with $\varphi = 0$, which we call XZ^+ plane. The energy on this plane is labeled only by the polar angle θ

$$e = -s\,\lambda\sin^p\theta + s\,(1-\lambda)\cos^k\theta - (1-s)\cos\theta. \tag{9.11}$$

We search the $\theta_0 \in [0, \pi]$ that minimizes (9.11)[2]. The condition for the minimum is

$$\frac{\partial e}{\partial\theta_0} = -p\,s\,\lambda\sin^{p-1}\theta_0\cos\theta_0 - k\,s\,(1-\lambda)\cos^{k-1}\theta_0\sin\theta_0 + (1-s)\sin\theta_0 = 0, \tag{9.12}$$

whose solutions are the angles θ_0 that satisfy either $\sin\theta_0 = 0$ or

$$p\,s\,\lambda\sin^{p-2}\theta_0\cos\theta_0 + k\,s\,(1-\lambda)\cos^{k-1}\theta_0 - 1 + s = 0. \tag{9.13}$$

These two equations have more than one solution, and each one corresponds to a different phase. We will consider them as ferromagnetic if $m^z(=\sin\theta_0) > 0$, and quantum paramagnetic if $m^z = 0$. The most stable one at each point (λ, s) will be the absolute minimum of e.

We begin with the quantum paramagnetic solutions. The equation $\sin\theta_0 = 0$ is satisfied for $\theta_0 = 0$ or π. The case $\theta_0 = 0$ corresponds to positive x magnetization, $m^x = 1$. We name this phase QP^+. Its energy is obtained by inserting this angle in (9.11),

$$e_{\mathrm{QP}^+}(s, \lambda) = s(1-\lambda) - 1 + s. \tag{9.14}$$

[2]Negative magnetizations along z axis have always higher free energy due to the change of sign in the $\sin^p\theta$ term in (9.11) (remember that we only consider the p odd case in this work).

The other paramagnetic solution, $\theta_0 = \pi$, corresponds to negative magnetization, $m^x = -1$. We call this phase QP^-. This phase is only stable for odd values of k and its energy is

$$e_{\mathrm{QP}^-}(s,\lambda) = -s(1-\lambda) + 1 - s. \tag{9.15}$$

This phase will not appear in the phase diagrams for k even, since its energy is always positive in the range of parameters $0 \leq s, \lambda \leq 1$.

We consider next the ferromagnetic solutions ($\theta_0 > 0$). The purely ferromagnetic solution $\sin\theta_0 = 1$ is only a valid solution on the line $s = 1$. Apart from this line, equation (9.13) cannot be explicitly solved for any value of p, but it can be done in the $p \to \infty$ limit. We study below all the solutions for this limit and discuss their validity for p finite.

9.3.2 Phase diagram for $p \to \infty$

In this limit, (9.13) has two possible ferromagnetic solutions. The parameter p appears in (9.13) through $p \sin^{p-2}\theta_0$. We consider the two possible limits for the sine power, $\sin^{p-2}\theta_0 \to 1$ (for the F phase) and 0 (for the F′ phase), always keeping $\theta_0 > 0$.

We begin the discussion with the F phase. With this aim, we assume

$$\sin^p\theta_0 \to 1, \tag{9.16}$$

and substitute it in (9.13),

$$p\,s\,\lambda\cos\theta_0 + k\,s\,(1-\lambda)\cos^{k-1}\theta_0 - 1 + s = 0. \tag{9.17}$$

In the $p \to \infty$ limit, this equation can only be satisfied if either the cosine vanishes, i.e. $\theta_0 = \pi/2$ (but only on the line $s = 1$), or $p\cos\theta_0$ tends to a constant. Let us investigate this second case. We consider $\cos\theta_0 = c/p$, with c a p-independent constant, and introduce it in (9.17), and taking the $p \to \infty$ limit, the equation reads

$$s\,\lambda\,c - 1 + s = 0, \tag{9.18}$$

whose solution is $c = (1-s)/s\lambda$. Thus,

$$\cos\theta_0 = \frac{1-s}{s\,p\,\lambda} \to 0, \tag{9.19}$$

is a solution to (9.13). Still we need to check that this θ_0 agrees with the initial assumption (9.16). Indeed,

$$\lim_{p\to\infty} \sin^{p-2}\theta_0 = \lim_{p\to\infty}\left[1 - \left(\frac{1-s}{2\,s\,p\,\lambda}\right)^2\right]^p = 1.$$

We obtain the energy for this phase introducing (9.19) in (9.11)

$$e_{\mathrm{F}}(s,\lambda)^k\Big|_{p\to\infty} = -s\,\lambda. \tag{9.20}$$

On the other hand, the F′ solution is obtained assuming the opposite limit,

$$p \sin^p \theta_0 \to 0. \tag{9.21}$$

Under this assumption, (9.13) reduces to

$$k\, s\, (1-\lambda) \cos^{k-1} \theta_0 - 1 + s = 0, \tag{9.22}$$

whose solution is

$$\cos \theta_0 = \left[\frac{1-s}{k\, s\, (1-\lambda)} \right]^{\frac{1}{k-1}}. \tag{9.23}$$

Note that if k is odd, the negative solution for the cosine is also a valid solution. However, it has always higher energy than its positive counterpart, so we will not consider it for further discussions.

The energy for the F′ phase when $p \to \infty$ is

$$e_{\mathrm{F}'}(s,\lambda)|_{p\to\infty} = -\frac{k-1}{k} \left[\frac{1-s}{k\, s\, (1-\lambda)} \right]^{\frac{1}{k-1}} (1-s). \tag{9.24}$$

Up to this point, we have obtained all the possible solutions to (9.13) in the $p \to \infty$ limit: three (for even k) and four (for odd k) phases. We can use the energies to determine which phase is the most stable at each point (λ, s). We show in figure 9.1 several phase diagrams for $k = 2$, 3, 4 and 5. Let us analyze the nature of each transition. We begin with the transition line between the F′ and QP^+ phases. This line is obtained by solving $e_{\mathrm{F}'} - e_{\mathrm{QP}} = 0$ using the expressions (9.24) and (9.14). This equality is fulfilled on the line $s = 1/[1 + k(1-\lambda)]$. On this line, $m^x = \cos\theta_0 = 1$ in both phases, which corresponds to a second-order transition. On the other hand, the transition between the F and the QP^+ phases lies on the $s = 1/2$ line and, since magnetization is discontinuous, it is first-order. The second-order transition extends from $(\lambda, s) = (0, 1/(k+1))$ to $(\lambda, s) = ((k-1)/k, 1/2)$, the point where these two kinds of transitions cross. According to that, the higher k is, the broader the second-order line and the smaller the QP^+ region are. Furthermore, in the $k \to \infty$ limit, the QP^+ region completely disappears.

Still there is a first-order transition between the F and F′ phases, determined by the solution of $e_{\mathrm{F}'} - e_{\mathrm{F}} = 0$ using (9.24) and (9.20). We solve this equation numerically and obtain the curve displayed in figure 9.1. On this line, the magnetizations are discontinuous but at the point $(\lambda, s) = (0, 1)$ where they two become equal, $m^z = \sin\theta_0 = 1$. The transition is then first-order, but in the mentioned point, where it would be second-order.

Up to this point, the discussion is common for even and odd values of k. However, in this latter case the QP^- phase also exists. Thereby, two additional transitions between F or F′ phases and the QP^- phase appear. In both cases the x magnetization changes the sign on the transition, and then, they are first-order. The transition lines are obtained by solving the equations $e_{\mathrm{QP}^-} - e_{\mathrm{F}} = 0$, leading

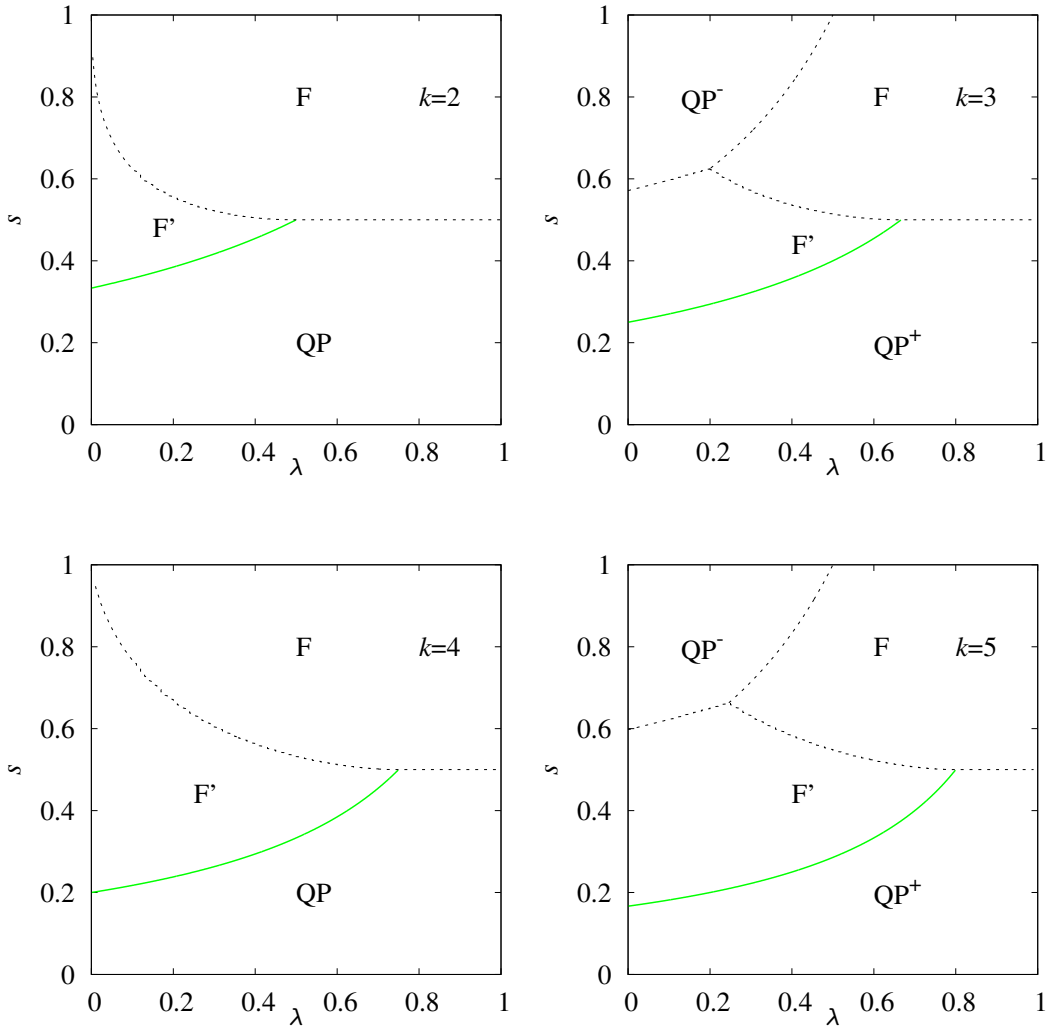

FIGURE 9.1: Phase diagram for $p \to \infty$. Dashed black lines represent first-order transitions, whereas the solid line in light green accounts for the second-order transition.

to $s = 1/(2(1-\lambda))$, and $e_{\mathrm{QP}^-} - e_{\mathrm{F}'} = 0$ which must be solved numerically. We display all the transition lines in figure 9.1.

According to these results, when we consider the $p \to \infty$ limit, there is only one single path that succeeds in avoiding first order transitions. This is the straight line that joins the initial point $(\lambda, s) = (0, 0)$ with the left upper corner, $(0, 1)$, and the final state $(1, 1)$. However, even though this path only crosses second order transitions, along this way there is no quantum annealing process, as can be seen by an insertion of these parameter values into the Hamiltonian (9.7), and thus this path is meaningless.

9.4

Phase Diagram

The phase diagram for finite p is different. Now, there appear regions where first-order transitions disappear, leaving more space for annealing trajectories. We display the corresponding diagrams in figures 9.2, 9.3, 9.4 and 9.5 for $k = 2$, 3, 4 and 5, respectively. Again, the shape of the phase diagram strongly depends on whether k is even or odd. In the former, there are only three phases and in the latter the extra QP^- phase appears. Besides, the higher k is, the longer is the second-order transition line.

The picture of the ferromagnetic phase for finite p is rather complicated. When one solves numerically (9.13) and looks at the $\theta_0 > 0$ solutions, the situation is the following: in a wide region, one finds two possible alternative solutions that look very much alike to the F and F′ phases discussed for the $p \to \infty$ limit. However, near the left and upper corner in the phase diagram, there is one single ferromagnetic solution which is neither F nor F′ but something intermediate. In fact, for k even, one can find paths through which the magnetization evolves continuously from the F′ to the F magnetizations without crossing any transition on the way, see figure 9.6. However, when p is high and k is odd, transitions between the F and F′ phases cannot be avoided, see figures 9.5, 9.6 and 9.7.

All this effect can be understood quantitatively coming back to the discussion of the $p \to \infty$ ferromagnetic solutions. Each of the phases were derived using the assumptions (9.16) for the F phase, and (9.21) for the F′ phase. Now we discuss the validity of these approximations for p finite.

We begin with the F phase. This phase was obtained by introducing (9.16) in (9.13). Since this equality is not strictly true, we introduce it as an approximation $\sin^{p-2}\theta_0 \approx 1$, thus obtaining a new approximate equation

$$p\, s\, \lambda \cos\theta_0 + k\, s\, (1-\lambda) \cos^{k-1}\theta_0 - 1 + s \approx 0. \tag{9.25}$$

If we assume $\cos\theta_0 \ll 1$, the solution is

$$\cos\theta_0 \approx \frac{1-s}{s\,[p\,\lambda + k(1-\lambda)]}, \tag{9.26}$$

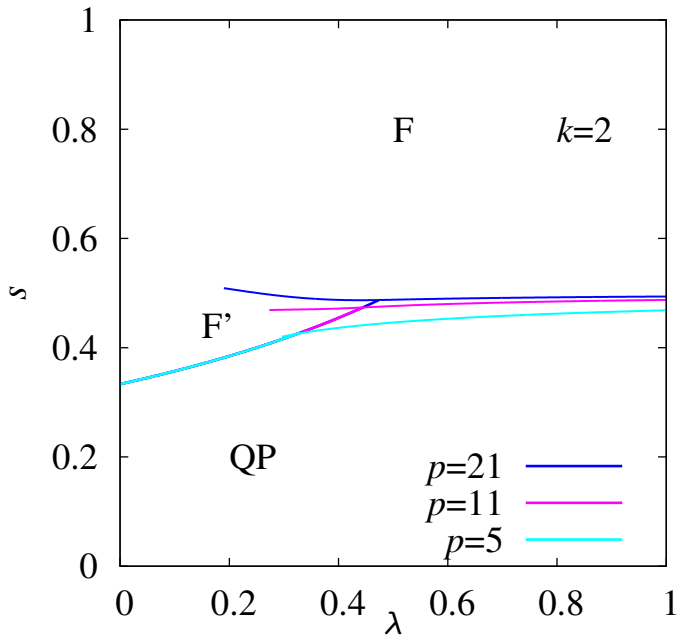

FIGURE 9.2: Phase diagram for $k = 2$. This is the same phase diagram as in reference [Sek12]. The transition between the F′ and QP phases is of second order, and the F-QP and F-F′ transitions are of first order.

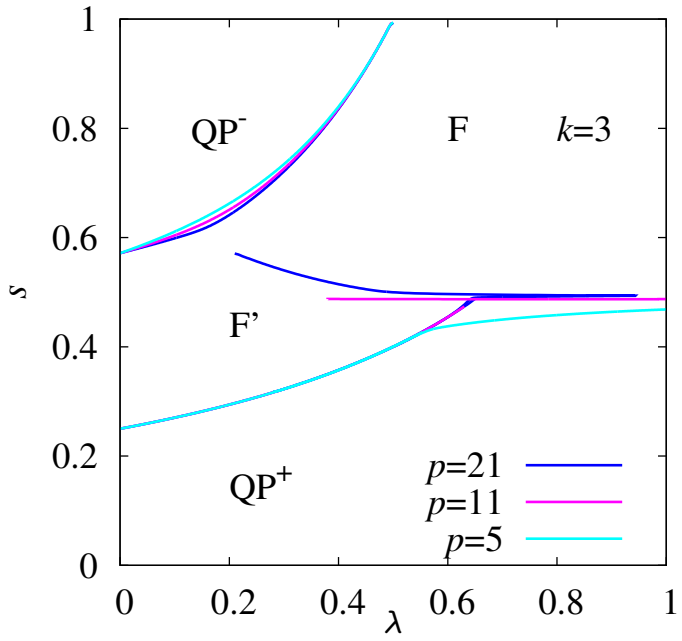

FIGURE 9.3: Phase diagram for $k = 3$. Only the F′-QP$^+$ transition is of second order.

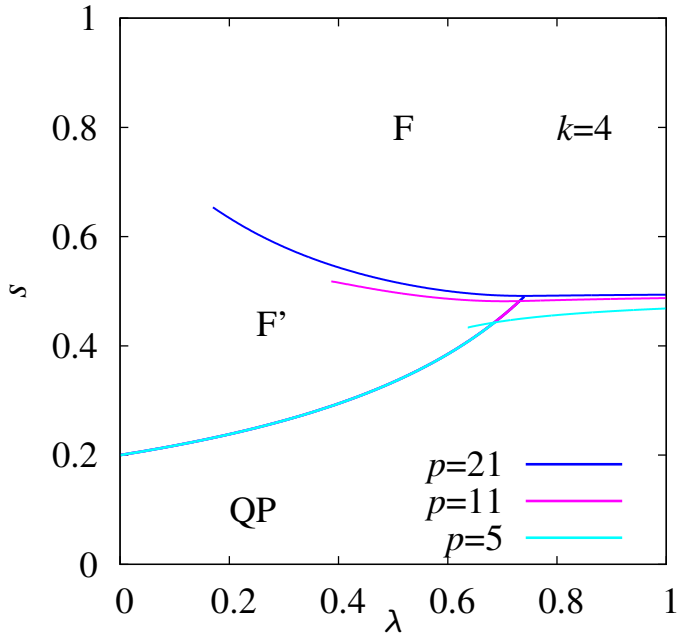

FIGURE 9.4: Phase diagram for $k = 4$. The structure is qualitatively the same as for $k = 2$.

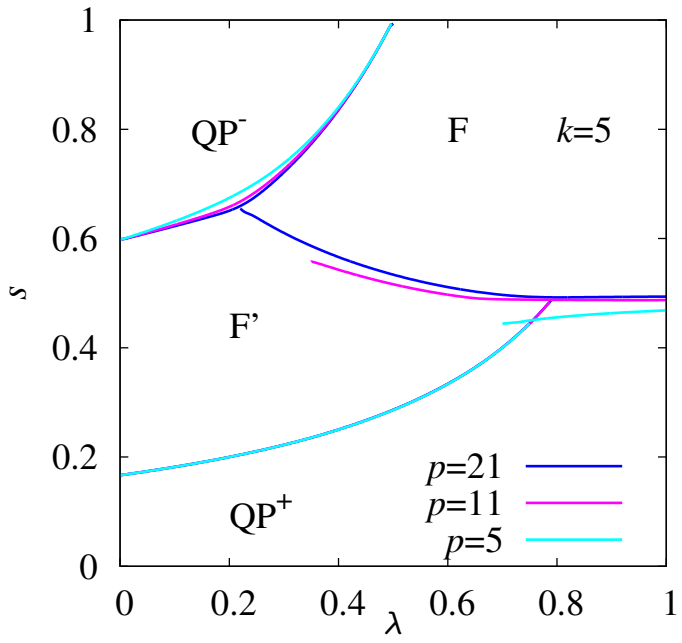

FIGURE 9.5: Phase diagram $k = 5$. The F′-QP$^+$ transition is of second order, and the other transitions are all of first order.

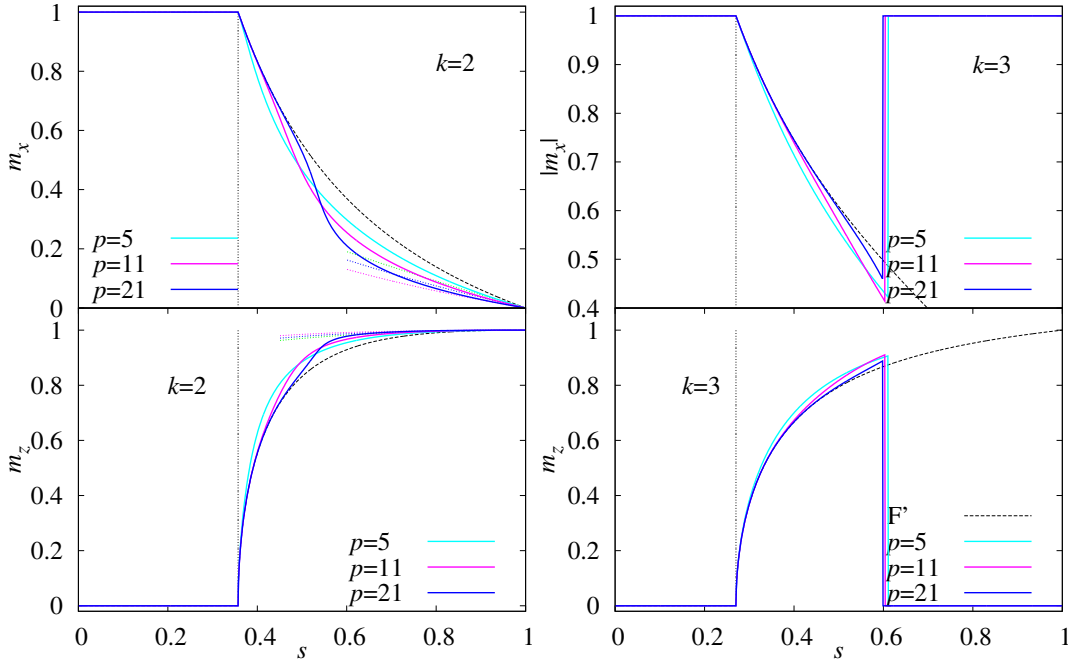

FIGURE 9.6: Magnetization obtained with the semi-classical approach as a function of s for $\lambda = 0.1$ and for $k = 2$ and 3. The dashed lines correspond to the analytical predictions for the QP$^{\pm}$, F (9.26) and F′ (9.32) solutions.

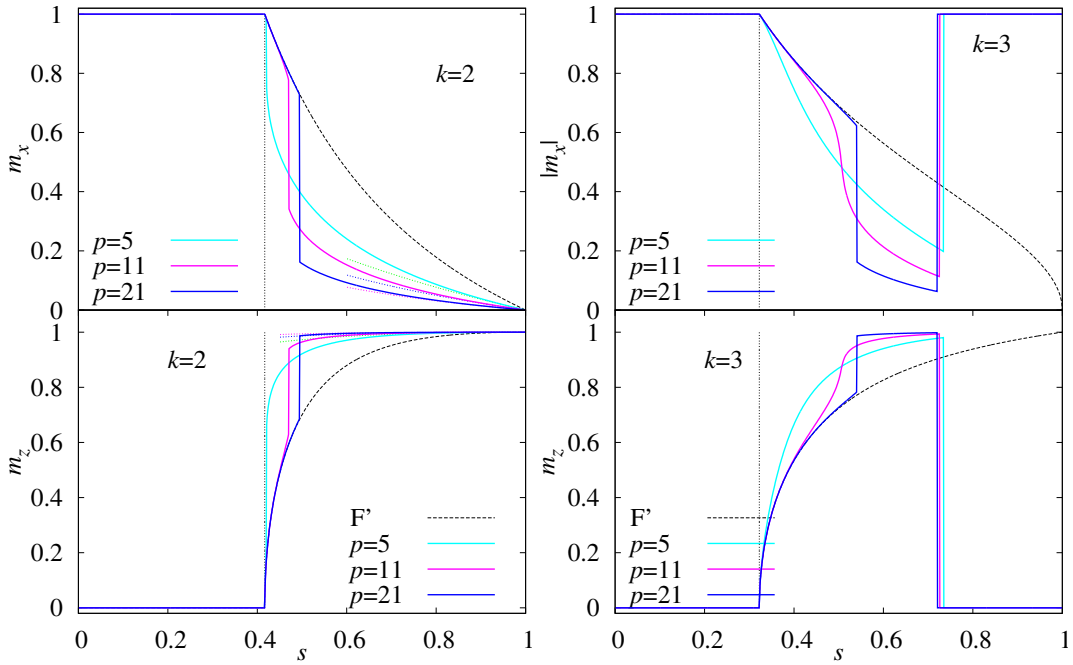

FIGURE 9.7: Magnetization obtained with the semi-classical approach as a function of s for $\lambda = 0.3$ for $k = 2$ and 3. The dashed lines correspond to the analytical predictions for the QP$^{\pm}$, F (9.26) and F′ (9.32) solutions.

for $k = 2$, and

$$\cos\theta_0 \approx \frac{1-s}{s\,p\,\lambda}, \tag{9.27}$$

for $k > 2$. That means, that the F solution found for the $p \to \infty$ limit also appears for finite p whereas $\cos\theta_0 \ll 1$, or

$$\frac{1-s}{s\,p\,\lambda} \ll 1. \tag{9.28}$$

In particular, the smaller this quotient (9.28) is, the better approximation the F solution is. We can obtain the energies for finite p by introducing this solution in (9.11). For $k = 2$,

$$\begin{aligned} e_{\rm F}^{k=2}(s,\lambda) \approx -s\,\lambda\left[1-\left(\frac{1-s}{s\,[p\,\lambda+2\,(1-\lambda)]}\right)^2\right]^{\frac{p}{2}-1} \\ +s\,(1-\lambda)\left(\frac{1-s}{s\,[p\,\lambda+2\,(1-\lambda)]}\right)^k-(1-s)\left(\frac{1-s}{s\,[p\,\lambda+2\,(1-\lambda)]}\right), \end{aligned} \tag{9.29}$$

and for $k > 2$

$$\begin{aligned} e_{\rm F}^{k}(s,\lambda) \approx -s\,\lambda\left[1-\left(\frac{1-s}{s\,p\,\lambda}\right)^2\right]^{\frac{p}{2}-1} \\ +s(1-\lambda)\left(\frac{1-s}{s\,p\,\lambda}\right)^k-(1-s)\left(\frac{1-s}{s\,p\,\lambda}\right). \end{aligned} \tag{9.30}$$

Next we study the F′ solution. We consider the following approximation

$$p\sin^{p-2}\theta_0 \approx 0. \tag{9.31}$$

As before, if this is a good approximation,

$$\cos\theta_0 \approx \left[\frac{1-s}{k\,s\,(1-\lambda)}\right]^{\frac{1}{k-1}} \tag{9.32}$$

is one solution to (9.13). This solution is equal to the one obtained for $p \to \infty$, (9.23). In other words, at this order of approximation, the solution is exact at this limit.

We briefly discuss the range of validity of this F′ solution (9.32) for p finite. The approximation (9.31) is valid for small values of θ_0. With this idea we expand separately the two terms in (9.13) around $\theta_0 = 0$, the first term being

$$\sin^{p-2}\theta_0\cos\theta_0 \;=\; p\,s\,\lambda\,\theta_0^{p-2}\left[1-\frac{p+1}{6}\theta_0^2+O(\theta_0^4)\right],$$

and the second term

$$\begin{aligned} & k\,s\,(1-\lambda)\cos^{k-1}\theta_0 - 1 + s \\ = k\,s\,(1-\lambda) & \left[1 - \frac{k-1}{2}\theta_0^2 + O(\theta_0^4)\right] - 1 + s. \end{aligned} \tag{9.33}$$

The dependency on θ_0 in the first term becomes irrelevant when $p > 3$, thus recovering the F′ solution (9.32). When $p = 3$, the lowest power of θ_0 appears in the first term, leading to a different ferromagnetic solution, but not the F′. Clearly, the higher p (and the smaller θ_0) is, the better is approximation (9.31).

In general, for intermediate values of s and λ, the higher p is, the more exact the two ferromagnetic solutions, F and F′, are. Then, since both approximations represent opposite cases in the value of m^x (or m^z), a new first-order transition between both phases will appear on the line when their two free energies become equal. However, for low values of p, or alternatively for $s \to 1$ or 0, there will only be one ferromagnetic solution, somewhere in between these two F and F′ phases. This idea is well ilustrated in figures 9.6 and 9.7, where both the numerical solution to (9.13) and the analytical predictions (9.26) and (9.23) are displayed.

This has straightforward consequences on the performance of the quantum annealing algorithm: the higher p is, the narrower will be the region where annealing paths can avoid a first-order transition. In the limit of $p \to \infty$, as was discussed before, there will be only one possible path, but not effective as quantum annealing.

Concerning the transitions between the QP and ferromagnetic phases, we can distinguish two kinds of transitions. First of all, the transitions between the F and $\mathrm{QP}^{\pm}$ phases will be first order, since the F phase is characterized by a high value of m^z whereas the paramagnetic solution has $m^z = 0$. On the other hand, there is another transition between the F′ and QP phases that lies on the line where their two free energies become equal, i.e. $s = 1/[1 + k(1-\lambda)]$. On this line, $m^x = 1$ ($m^z = 0$) for the two phases. Furthermore, the F′ solution is exact for $m^x = 1$. Since the magnetizations are continuous on this line, the transition between F′ and QP is of second order. Besides, it can be checked that there is a wide range of this line where $e_{\mathrm{F}'} < e_{\mathrm{F}}$. Thus, this phase is the stable one in the ferromagnetic phase. This second-order transition does not hamper the QA performance and gives us a way to avoid the F-QP phase transition that appeared when using the traditional QA approach. It is important to point out that this second-order transition appears for any value of k.

In Appendix G, we describe a different, quantum-mechanical method to derive the same results.

9·5

Energy gap

As discussed in Introduction, the efficiency of the QA algorithm is closely related to the behavior of the gap between the ground and first excited states. As usual, this gap can be computed by direct diagonalization of the problem Hamiltonian (9.7). Indeed, since the total spin $\boldsymbol{S}$ is conserved during the evolution, the dimension of the problem is $N+1$. That means that the diagonalization matrixes grow polynomially with the system size instead of exponentially as for generic quantum problems. However, still computer resources limit this computation to moderate sizes although such computations are useful for some purposes [Sek12, Jör10a]. Here, we adopt an alternatively approach, this gap can be computed in the thermodynamic limit $N \to \infty$ by the method described in [Fil11]. The main idea is to extend the semi-classical scheme for the ground state by the consideration of quantum fluctuations around the classical ground state. It is important to point out that this method can only be applied in the case of finite gaps in the thermodynamic limit, as it is the case away from the transition points themselves. In case of exponentially small ones, other methods such as instantonic or WKB methods should be used [Jör10a, Bap12].

It is most convenient to rotate the system by an angle θ_0 around the y axis in order to bring the x axis parallel to the semi-classical magnetization, i.e.

$$\begin{pmatrix} S_x \\ S_y \\ S_z \end{pmatrix} = \begin{pmatrix} -\sin\theta_0 & 0 & \cos\theta_0 \\ 0 & 1 & 0 \\ \cos\theta_0 & 0 & \sin\theta_0 \end{pmatrix} \begin{pmatrix} \tilde{S}_x \\ \tilde{S}_y \\ \tilde{S}_z \end{pmatrix}. \tag{9.34}$$

We rewrite the Hamiltonian (9.8) in terms of these new variables $\tilde{S}^\alpha$, obtaining

$$\begin{aligned} \hat{H}(s,\lambda) = &-s\,\lambda\,N\left[\tfrac{2}{N}\left(\cos\theta_0\,\tilde{S}_x + \sin\theta_0\,\tilde{S}_z\right)\right]^p \\ &+s\,(1-\lambda)\,N\left[\tfrac{2}{N}\left(-\sin\theta_0\,\tilde{S}_x + \cos\theta_0\,\tilde{S}_z\right)\right]^k \\ &-2\,(1-s)\left(-\sin\theta_0\,\tilde{S}_x + \cos\theta_0\,\tilde{S}_z\right). \end{aligned} \tag{9.35}$$

Now, we add quantum fluctuations to the system by means of the Holstein-Primakoff transformation

$$\tilde{S}_z = \frac{N}{2} - a^\dagger a, \qquad \tilde{S}_+ = (N - a^\dagger a)^{1/2} a = \tilde{S}_-^\dagger, \tag{9.36}$$

where a is a boson annihilation operator that satisfies $[a, a^\dagger] = 1$. When quantum fluctuations are small relative to the classical state, i.e. for $N \gg \langle a^\dagger a \rangle$, we can use a simpler expression

$$\tilde{S}_x \approx \frac{\sqrt{N}}{2}(a + a^\dagger). \tag{9.37}$$

We introduce these transformations into the Hamiltonian (9.35) and expand the three different terms in powers of $1/N$. Thanks to the previous rotation, the coefficient in $1/\sqrt{N}$ vanishes. We keep terms up to $1/N$ and group together all the

coefficients with the same power of N. The result is

$$H(\gamma,\delta) = N\,e + \gamma + \gamma\left[(a^\dagger)^2 + a^2\right] + \delta a^\dagger a. \tag{9.38}$$

The term for N^1 is nothing but the ground energy obtained before in (9.11),

$$e \equiv -s\lambda \sin^p\theta_0 + s(1-\lambda)\cos^k\theta_0 - (1-s)\cos\theta_0. \tag{9.39}$$

The coefficients δ and γ are given as

$$\begin{aligned}\delta &\equiv -s\,\lambda\left[p(p-1)\sin^{p-2}\theta_0\cos^2\theta_0 - 2\,p\,\sin^p\theta_0\right]\\ &+ s\,(1-\lambda)\left[k(k-1)\sin^2\theta_0\cos^{k-2}\theta_0 - 2\,k\,\cos^k\theta_0\right] + 2(1-s)\cos\theta_0,\end{aligned} \tag{9.40}$$

and

$$\gamma \equiv -\frac{s\,\lambda\,p(p-1)}{2}\sin^{p-2}\theta_0\cos^2\theta_0 + s\,(1-\lambda)\frac{k(k-1)}{2}\sin^2\theta_0\cos^{k-2}\theta_0. \tag{9.41}$$

We need to diagonalize this Hamiltonian in order to compute the first excited state by the Bogoliubov transformation

$$a = \cosh\frac{\Theta}{2}\,b + \sinh\frac{\Theta}{2}\,b^\dagger, \quad a^\dagger = \cosh\frac{\Theta}{2}\,b^\dagger + \sinh\frac{\Theta}{2}\,b, \tag{9.42}$$

where b is a new bosonic annihilation operator satisfying $[b, b^\dagger] = 1$. Using this transformation, we can eliminate the coefficient of $\left[(b^\dagger)^2 + b^2\right]$ by choosing the angle Θ as

$$\tanh\Theta = -\frac{2\gamma}{\delta} \equiv \epsilon.$$

With this choice, the Hamiltonian can be written as

$$H(\gamma,\delta) = N\,e + \gamma + \frac{\delta}{2}\left(\sqrt{1-\epsilon^2} - 1\right) + \Delta\; b^\dagger b, \tag{9.43}$$

with

$$\Delta = \delta\sqrt{1-\epsilon^2}. \tag{9.44}$$

The Hamiltonian is diagonal in $b^\dagger b$. The energy gap in the $N \to \infty$ limit between the ground and first excited states is Δ.

Using the values θ_0 previously obtained solving (9.13), we can compute the energy gap for our system. We show the data for $p = 11$ and $\lambda = 0.1$ and 0.3 for different values of k in figure 9.8. As was suggested in the magnetization data in the previous section for $\lambda = 0.1$ (figures 9.2 to 9.5), no first-order transition F-F′ is observed through the energy gap. The gap vanishes continuously on the second-order transition line but present no further jumps later, but the ones related to the

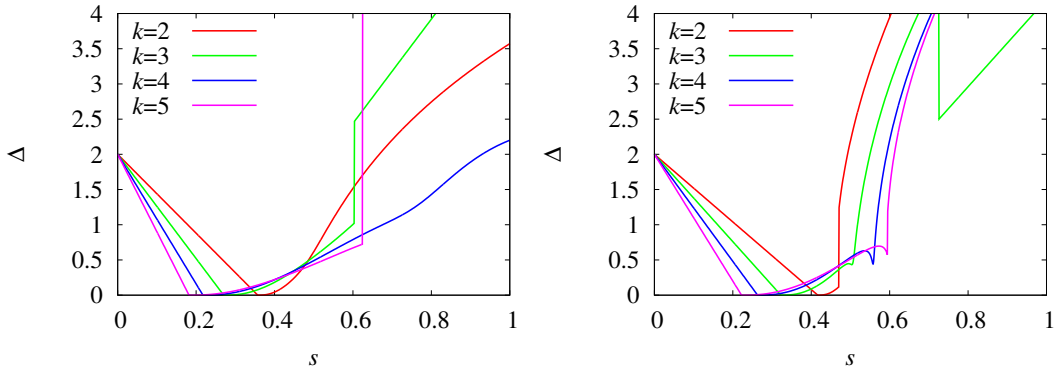

FIGURE 9.8: Energy gap for $p = 11$ as a function of s for $\lambda = 0.1$ (left) and $\lambda = 0.3$ (right) for several values of k.

F-QP$^-$ that always take place in the odd-k cases. On the contrary, when $\lambda = 0.3$, the jumps in the gap appear for all the k's at the place where we observed the F-F′ transition before.

In the thermodynamic limit, the gap vanishes at a single point of first-order transition and remains finite away from this point. The single point of vanishing gap is hard to see by the present method, which results in an apparent simple jump in the gap at a first-order transition as seen in figure 9.8.

9.6

Overlap of the ground-state wave functions

It has been suggested in [Bap12] that the reason for the antiferromagnetic interaction, the $k = 2$ case in (9.6) introduced by Seki and Nishimori in [Sek12], to work better than the transverse field interaction only is related to the large overlap between the ground states of the Hamiltonians $\hat{V}_{k=2}$ and $\hat{H}_0$. In this section, we will discuss the properties of these different states, concluding that, even thought the overlap is important, it is not the decisive factor that makes the strategy to succeed.

The ground state of $\hat{V}_{\mathrm{TF}}$ is the one where all the spins are aligned along the x axis, $|\phi_{\mathrm{TF}}\rangle = \otimes_{i=1}^{N} |\uparrow\rangle_i^x$. If we denote the ground state of $\hat{H}_0$, as $|\phi_0\rangle = \otimes_{i=1}^{N} |\uparrow\rangle_i^z$, the overlap between $|\phi_{\mathrm{TF}}\rangle$ and $|\phi_0\rangle$ decreases exponentially with N as 2^{-N}, as can easily be seen from the elementary relation $|\uparrow\rangle_i^x = \left(|\uparrow\rangle_i^z + |\downarrow\rangle_i^z\right)/\sqrt{2}$.

The overlap computation becomes a little more complicated for the ground state of $\hat{V}_k$. The ground state for this term depends on the value of k. Indeed, if k is odd, the ground state is the one where all the spins are aligned along the x axis, but towards the negative direction, i.e. $\otimes_{i=1}^{N} |\downarrow\rangle_i^x$. Then, the overlap with $|\phi_0\rangle$ for the k odd case will be exponentially suppressed as 2^{-N} as in the case of $\hat{V}_{\mathrm{TF}}$. Thus, the argument in [Bap12] does not apply directly since we can avoid first-order transitions even in this case of k odd, in spite of the very small overlap of the ground state for $\hat{H}_0$ and $\hat{V}_k$.

The ground state for the k even case needs some care to be analyzed. We compute it in Appendix H. We show there that that the overlap is indeed higher for k even. The antiferromagnetic interations is a particular case, $k = 2$. In fact, the overlap displays an algebraic decay as the system size increases, i.e. $\sim 1/\sqrt{N}$.

We conclude that the overlap is not the main ingredient that makes the present method to succeed.

Part IV

Conclusions

CHAPTER X

Conclusions

In this thesis, we have tackled the general problem of describing complex systems. The name complex refers to a large amount of degrees of freedom and the difficulty of finding simple recipes to describe them. The extremely large amount of possible states draws a complex free energy landscape, which has a common consequence for many diverse systems: an excessive slow dynamics. This sluggish evolution has a direct consequence in experiments: these systems must be regarded to be always out of equilibrium. Finding a rational way to approach this kind of problems is one of the central problems in the modern theory of condense matter physics.

As discussed many times in this dissertation, nature lives in a nonequilibrium world, which crashes with the standard theoretical approach, that needs equilibrium in order to cancel out the chaotic individual behavior. For this reason, computer simulations are requested to establish a bridge between these two worlds. Besides, in the last years it has been proposed a novel approach that provides a quantitative relation between both worlds by interchanging some degrees of freedom that one can control in a computer: finite times in nonequilibrium simulations with finite sizes in equilibrium simulations. Indeed, what was regarded as an annoying inconvenience for many years can be used now for writing a real dictionary between the theoretical calculations based on an equilibrium eternally unachievable and experiments that last finite times.

In this thesis we have focused on this final goal, with emphasis on one of the two parts, that is, on laying the foundations of this dictionary by characterizing precisely the equilibrium phase at finite system sizes. Due to the extreme slowness of the dynamics, this mission is extraordinarily complex and we had to face it by considering several perspectives:

1. By model building. Indeed, as theoretical physicists, it is of major importance to find models simple enough to allow some analytical predictions but complex enough to still suffer the phenomenon we are interested on.

2. By brute force, that is, by means of large-scale simulations, with the help of

large computational facilities.

3. By the design of optimized algorithms that allow us to explore the topography of the complex landscape. This approach offers as well a major practical advantage. It helps us to find the flattest simulation path that allows us to speed the simulation.

Regarding the definition of new models, we presented in Chapter 4 a new mean field model, which at variance with the rest of this kind, allows a natural definition of distance. Then, being mean field, it provides a direct way of investigating the coarsening process in a replica symmetry breaking scenario, with magnitudes that can be compared with experiments, like the magnetic domain's size.

Concerning the extensive simulations, let us note that the results presented all over the thesis demanded large computational facilities (conventional computer clusters, supercomputing facilities and dedicated computers) as well as the implementation of modern simulation techniques like multispin coding. It specially remarkable, that for the temperature chaos work (Chapter 5), we reanalyzed data obtained with one year of non-stop production of Janus, a special-purpose computer many thousands faster than a conventional computer. These brute-force simulation gave us access to unprecedently large configurations in the $3D$ Edwards-Anderson model thermalized up to very low temperatures, which was crucial to identify without any doubt the temperature chaos effect in a simulation, as well as to lay the foundations for the size dependency characterization.

Apart from large computation facilities, we also followed an alternative approach to speed up the simulations: to design clever optimized algorithms that speed up the dynamics. The key lies precisely on the rugged free-energy landscape. Then, if one were able to identify the topography this landscape, one could find the best path to go from one minimum to the other. This was precisely our aim in all Part II of the thesis and in work on the quantum annealing algorithm described in Chapter 9.

Indeed, when we started working with colloids, about the beginning of my PhD, our objective was to describe the phase diagram of highly polydisperse systems. Previous works had failed in characterizing the disordered solid equilibrium phase, and our idea was to apply the successful microcanonical algorithm [MM07] to this problem (this approach was described in Chapter 7). Initially, the we thought that the difficulty was the glass transition, but after some months of intense simulation, we identified another harder problem and unsolved in the literature, the free-energy barriers in first order transitions in off-lattice systems. With this idea in mind, we moved back to the simplest possible system of this kind, to identify the order parameters that could allow us to explore softly the free-energy landscape, and thus, to find a flat trajectory free from metastabilities. Our successful solution to the problem was discussed in Chapter 8 in the context of hard spheres crystallization, a simpler model but carrying still the same problem.

The problem with the quantum annealing algorithm is rather different but still very related to the rest of the thesis. The main problem to build a quantum com-

puter based on this kind of computation is precisely the adiabaticity condition of the algorithm. Indeed, the times needed to keep the system permanently in equilibrium grow exponentially with the system size if a quantum first order transition is found on the annealing trajectory. This problem with the adiabatic condition is the same problem considered all along the rest of the thesis when talking about thermalization times. The solution, this time, was to add an additional driver term, and control the trajectory with two parameters. With this idea, we could map the free energy, and show the existence of annealing trajectories that avoids the first order transition.

After this general discussion, we extend separately in the following sections the conclusions for each of the chapters presented in this dissertation.

10.1

Spin Glasses

10.1.1 Hypercube model

We have studied a spin glass model in the D-dimensional unit hypercube in the limit of large D, but with finite coordination number. We have shown that any short range model in such a lattice will behave as a mean field model in the thermodynamic limit (that coincides with the large D limit). An important advantage of this model is that it has a natural notion of spatial distance.

We have argued that any statistical mechanics model on the hypercube with random connectivity would be afflicted by huge finite size effects, for purely geometrical reasons. The obvious cure has consisted in restricting the connectivity graphs to those with a fixed number of neighbors. Unfortunately, constructing such graphs is far from trivial. We have generated a subset of them by means of a simple dynamic Monte Carlo. In this way, we obtain sets of graphs that are isotropic. We have checked that the Edwards-Anderson model defined over these finite connectivity hypercubes verify some consistency checks, including comparison with the analytically computable correlation function in the paramagnetic phase.

We have numerically studied the nonequilibrium dynamics in the spin glass phase. The three main features found were: (i) aging dynamics consists in the growth of a coherence length, much as in 3D systems, (ii) the scaling of the two times correlation function implies infinitely many time-sectors, and (iii) the p^4 propagator has been observed. In addition, we have studied the finite size effects in our model, finding that a naive finite size scaling ansatz accounts for our data.

From the static point of view, it is most probable, almost a theorem, that our model suffers replica symmetry breaking. Hence, it provides an interesting playground to study nonequilibrium dynamics on RSB systems. An interesting possible extension of the present study would be the computation of quantities that are di-

rectly measurable in experiments, and/or of experimental cooling protocols.

10.1.2 Temperature chaos

We have characterized the temperature chaos in the $D = 3$ Ising spin glass as a rare-event driven phenomenon. When it occurs, its effects are strong, and can be felt even at the shortest length scales, as confirmed by the two-temperatures spatial correlation function. We argue that this characterization was inaccessible to the statistical analysis employed in previous works. In fact, two ingredients were crucial to obtain this conclusion. First, the JANUS supercomputer gave us access to unprecedentedly large configurations, well thermalized up to very low temperatures (remarkable both for system sizes up to $L = 32$ and for the low temperatures [ÁB10a, ÁB10b]). And second, we introduce new tools of statistical analysis, based on a large-deviations functional.

With this approach, we were able to quantify the size-dependencies using this large-deviation functional. This step is crucial to find a time-length dictionary [Fra98, ÁB10a, ÁB10b, Bar01] for temperature-varying protocols, which paves the way to design a protocol that allows to detect the temperature chaos in a real experiment.

A surprising outcome of our finite size analysis is that the chaotic length scales with system size as $\xi_C \propto L^a$, with $a \approx 0.4$: divergent in the thermodynamic limit, yet much smaller than L. This duality will probably be important to interprete the somehow contradictory memory and rejuvenation effects [Jon98]. In fact, although the $\xi_C \propto L^a$ scaling follows from a $L \to \infty$ extrapolation (which is tricky even in mean-field) we now know that the extrapolation relevant for experiments is rather to $L \sim 100$ lattice spacings [ÁB10a].

10.2

Colloids

10.2.1 Polydisperse soft spheres

We have studied in the microcanonical ensemble a soft-spheres model for liquids and colloids with a 24% polydispersity. Extrapolating by finite size scaling (FSS) to the thermodynamic limit the results obtained from the Maxwell construction in finite systems, we show that the critical temperature for the amorphous-crystal phase-separation is *below* the dynamic glass transition, which makes dynamically difficult (although not impossible [Zac09a]) to observe such phase-separation.

At low temperatures the system divides spatially into an amorphous and a crystalline part, in agreement with previous findings [Fer07b]. The phase-separated amorphous is a stable fluid *below its dynamic glass temperature,* which is an optimal candidate to suffer a thermodynamic glass transition. On the other hand, the

phase-separated solid displays crystalline order. Polydispersities on the coexisting amorphous and solid are smaller than in the fluid. In fact, particles distribute spatially according to their size following a complex pattern not described by any fractionation scenario known to us.

We were able to obtain the equilibrium solid phase, but only for smaller system sizes that what we were seeking. Indeed, we applied the microcanonical algorithm with the hope of avoiding metastabilities, but the existence of phase separation ruined our approach. In fact, it was precisely the solution to this problem which encouraged our research on hard spheres crystallization.

10.2.2 Hard spheres crystallization

We have introduced a tethered MC [Fer09b, MM11] approach to HS crystallization. We go continuously from the fluid to the crystal by varying a reaction coordinate (a blend of two *global* bond-orientational order parameters). Tethered MC provides a major simplification to umbrella sampling, which makes it possible to study multi-constrained free energies. At variance with previous methods, our simulations equilibrate (i.e. we find results independent of the starting particle configuration), not only for the formation of the space-filling crystal, but even for the more difficult case of mixed states with fluid-crystal interfaces. Our estimation of the coexistence pressure is, by far, the most accurate to date. That of the interfacial free energy is compatible with most (but not all) recent determinations. Should one wish to reach larger N, the tethered strategy would easily accommodate additional order parameters. The method can also be generalized to other simple liquids, or to investigate the glass transition.

10.3

Quantum Annealing

We have analyzed the reason for the failure of the traditional annealing with a transverse-field term in the infinite-range ferromagnetic p-spin model. We have shown that it is possible to find annealing trajectories that avoid the crossing of first-order transitions thanks to the introduction of a second driver term in the problem, which may be due to the multiple spin flips in the z-basis caused by the second term as was the case in [Suz07]. This additional term favors the appearance of a second-order transition that does not hamper the annealing performance. A whole family of possible candidates has been studied and we conclude that the solution to the problem presented by Seki and Nishimori [Sek12] is a special case of a more general additional quantum term. The main properties of these additional terms have also been discussed with the conclusion that the properties of the ground states of the diverse terms in the Hamiltonian are not a decisive factor to make the quantum annealing fail or succeed.

Part V

Appendices

APPENDIX A

Analytical calculations on the hypercube

A.1

On the Bethe approximation in a ferromagnet

A.1.1 The Bethe approximation

The Bethe approximation is a refinement over the mean field, for this reason, we will begin the discussion applying the MF approximation to an Ising ferromagnet.

In the standard MF approximation, spins are assumed to be uncorrelated. The probability distribution function is thus factorized ($m_i \equiv \langle S_i \rangle$)

$$P(S) = \prod_i P_{m_i}(S_i), \tag{A.1}$$

where

$$P_{m_i}(S) = \frac{1+m_i}{2}\,\delta_{S,1} + \frac{1-m_i}{2}\,\delta_{S,-1}. \tag{A.2}$$

As usual, the equilibrium solution will be the one that minimizes the free-energy functional, defined as follows ($\beta = 1/T$)

$$\Phi[P] = \langle H \rangle_P - \frac{S[P]}{\beta}, \tag{A.3}$$

where

$$\langle H \rangle_P = -J \sum_{<i.j>} m_i m_j, \tag{A.4}$$

and

$$S[P] = -\langle \ln P(S) \rangle_P = -\sum_i \langle \ln P_i(S) \rangle_P = -\sum_i s(m_i), \tag{A.5}$$

with

$$s(m_i) = \frac{1+m_i}{2} \ln \frac{1+m_i}{2} + \frac{1-m_i}{2} \ln \frac{1-m_i}{2}. \tag{A.6}$$

Note that the entropy (A.5) is additive because the probability (A.1) is factorized.

The condition for minima leads us to

$$\frac{\partial \Phi}{\partial m_i} = 0 \;\Rightarrow\; m_i = \tanh\left(\beta \sum_j J_{ij}\, m_j\right). \tag{A.7}$$

In an Ising ferromagnet, the J_{ij} are equal to J if spins i and j are nearest neighbors and zero elsewhere. The actual minimum of Φ corresponds to constant magnetization $m_i = m$ for all spins i. Then, the magnetization satisfies the equation

$$m = \tanh\left(\beta J z m\right), \tag{A.8}$$

where z is the coordination number. This equation predicts a a transition at the critical point $\beta_c = 1/z$. However, this solution is not very satisfactory since it predicts a phase transition no matter the dimension of the system, and we know that there is no transition in the one dimensional Ising model.

This problem can be surpassed by looking at the system locally and applying the cavity approach. The magnetization of spin σ can be computed as a function of the nearby spins τ_i, $i = 1, \ldots, n$, being n the coordination number of σ. Let us remove the spin σ. There is now a cavity in the system surrounded by the spins τ. We assume that the spins are not correlated (which is the Bethe approximation) and the magnetization in the cavity, m_C, is obtained with (A.2). Now, we add back the spin σ. Thus, the probability for this spin is given by

$$P(\sigma) = \frac{F(\sigma)}{F(1) + F(-1)}, \tag{A.9}$$

where

$$F(\sigma) = \sum_{\{\tau\}} P_{m_C}[\tau] e^{\beta J \sigma \sum_{i=1}^{z} \tau_i} = \left[\cosh(\beta J \sigma) + m_C \sinh(\beta J \sigma)\right]^n. \tag{A.10}$$

The probability (A.9) is of the form (A.2). Hence, it suffices to compute $\langle \sigma \rangle$. Since $\sigma = \pm 1$ in the Ising model,

$$\cosh(\beta J \sigma) + m_C \sinh(\beta J \sigma) = \cosh(\beta J) \frac{e^{\sigma A(\beta, J, m_C)}}{\cosh A(\beta, J, m_C)}, \tag{A.11}$$

where

$$A(\beta, J, m_C) = \tanh^{-1}\left[\tanh(\beta J) m_C\right]. \tag{A.12}$$

Thereby, the magnetization of spin σ can be obtained as usual

$$m = \langle \sigma \rangle = \tanh\left[n A(\beta, J, m_C)\right] = \tanh\left\{n \tanh^{-1}\left[\tanh\left(\beta J\right) m_C\right]\right\}. \tag{A.13}$$

If we now increase the cavity removing one more spin, τ_i, keeping fixed the magnetization to m_C and still considering the spins uncorrelated, we can obtain a relation for m_C using eq. (A.13) and imposing a self-consistent condition

$$m_C = \tanh\left\{(n-1) \tanh^{-1}\left(\tanh\left(\beta J\right) m_C\right)\right\}. \tag{A.14}$$

Once m_C is known, m can be calculated by means of (A.13). (A.14) is more satisfactory than (A.8), in fact, it predicts no transition in one dimension (if the connectivity is $n = 2$, no β would ever satisfy eq. (A.14)).

We can now come back to the previous discussion on distance between spins, see eq. (4.9). It now becomes clear that the Bethe approximation is correct for the hypercubes (and for random Poisson lattices). Then, in the paramagnetic phase, once a bond has been removed, the two neighboring nodes are separated by a large distance, i.e. $O(D)$. In fact, it becomes exact when $D \to \infty$ since both spins are infinitely far away and are statistically uncorrelated.

A.1.2 Calculation of the critical temperature K_c

We fix the starting point in eq. (A.14), $(K \equiv \beta J)$

$$m_C = \left\langle \tanh\left\{ (n-1) \tanh^{-1}\left(\tanh\left(K_c\right) m_C\right)\right\}\right\rangle_1, \tag{A.15}$$

where the $\langle\ \rangle_1$ refers to an average over the coordination number (remember that n is not necessarily fixed in our model). We seek solutions for m_C. These solutions must be around $m_C \to 0$ we can expand the right-hand side term in powers of m_C. Introducing

$$\tanh x = x + \mathcal{O}(x^3) \quad \text{and} \quad \tanh^{-1} x = x + \mathcal{O}(x^3), \tag{A.16}$$

in (A.15), we get

$$m_C \approx\ m_C(\langle n\rangle_1 - 1) \tanh K_c. \tag{A.17}$$

This equation can be solved, leading to

$$K_c = \tanh^{-1}\left(\frac{1}{\langle n\rangle_1 - 1}\right). \tag{A.18}$$

Although it seems really counterintuitive, $\langle n\rangle_1$ is different in the two sets of graphs we have been discussing. While in the fixed-n graphs it is 6, in the random-n graphs it is function of D, let us explain why.

A.1.2.1 Random connectivity graphs

In order to compute $\langle n\rangle_1$, let us describe carefully how eq. (A.14) was obtained. We picked one spin and selected one of its neighbors. Hence, we are asking which is the mean number of neighbors of a spin of which we happen to know for sure that it has a particular neighbor. We write down these ideas in the following way: the coordination number is given by

$$n = 1 + m, \tag{A.19}$$

D	K_c
6	0.20273
8	0.19283
10	0.18735
12	0.18386
14	0.18145
16	0.17969
18	0.17834
⋮	⋮
∞	0.16824

TABLE A.1: Values for K_c for certain dimensions D obtained using the Bethe approximation.

where m is the number of active links among the $D-1$ remaining ones. Thereby the coordination number n is necessarily higher or equal to one. The distribution function of m is then

$$p(m) = \left(\begin{array}{c} D-1 \\ m \end{array} \right) \left(\frac{z}{D}\right)^m \left(1 - \frac{z}{D}\right)^{D-1-m}, \tag{A.20}$$

where $z = 6$. One can average n using this probability distribution function, getting:[1]

$$\langle n \rangle_1 (D) = 1 + \overline{m} = 1 + (D-1)\frac{z}{D} = z + 1 - \frac{z}{D}. \tag{A.21}$$

Now we have all the necessary ingredients to calculate K_c for a given dimension D, just plugging the value for $\langle n \rangle_1 (D)$ in eq. (A.18) one gets

$$K_c(D) = \tanh^{-1}\left(\frac{D}{z\,(D-1)}\right). \tag{A.22}$$

We present values of K_c for certain dimensions in Table A.1.[2]

One must recall that relation (A.14) is only exact for infinite dimension. Since correlations between spins vanish with $O\left(D^{-1}\right)$, we must expect corrections of the same order to eq. (A.14). Then there will also be additional corrections to $K_c^\infty = \tanh(1/z)$ with D than those presented in (A.22) and Table A.1. Then, it would be certainly more appropriate to work with the following expression for K_c instead

$$K_c(D) = K_c^\infty + \frac{a_1}{D} + \frac{a_2}{D^2} + \cdots. \tag{A.23}$$

[1]Note that, in the large D limit, the number of neighbors of a site picked at random is $\langle n \rangle = 6$, yet for one of its neighbors is $\langle n \rangle_1 = 7$.

[2]Note that if we had chosen $\langle n \rangle_1 = 6$, the transition should be in $K_c(D) = 0.20273$ for all D. Then, both connectivity descriptions, as far as K_c^∞ is concerned, are not equivalent in the thermodynamical limit.

If we notice that dimension is related to the number of spins by means of

$$D = \frac{\log N}{\log 2}, \tag{A.24}$$

we realize that we must expect logarithmic corrections to K_c^∞ in the number of spins N. This problem is then really hard. Depending on the actual values of coefficients a_i these corrections can be huge. Then, this random connectivity model suffers from such strong finite size effects that make it not suitable for numerical computations at finite D.

A.1.2.2 Fixed connectivity graphs

This strong dependency of K_c with D in the random connectivity graphs is the reason that encouraged us to study the systems within the n-fixed ensemble, although its graphs are more difficult to generate. In these graphs $n = z$ and then eq. (A.18) reads as

$$K_c = \tanh^{-1}\left(\frac{1}{z-1}\right), \tag{A.25}$$

if $z = 6$, we get $K_c \approx 0.20273$. This means that the expectation number for K_c provided by the Bethe approximation does not depend on D. For this reason, we should expect less corrections with D in K_c^∞ than in the previous case. In fact, we should only find corrections associated to the validity of the Bethe approximation for finite D. In other words, the corrections are only due to the short loops.

A.2

High temperature expansion

For sake of clarity, we will firstly discuss the calculations for the random connectivity hypercube. Results for the fixed connectivity model will be then obtained by minor changes.

Using the identity ($\beta = 1/T$)

$$e^{\beta J_{xy}\sigma_x\sigma_y} = \cosh\beta\left(1 + J_{xy}\sigma_x\sigma_y\tanh\beta\right), \tag{A.26}$$

we can write the partition function and the spin propagator as (N_l is the total number of links in the graph):

$$\begin{aligned}
\frac{Z}{2^N(\cosh\beta)^{N_l}} &= \sum_{\{\sigma\}}\prod_{\langle zw\rangle}\left(1+J_{zw}\sigma_z\sigma_w\tanh\beta\right), \\
\left\langle\sigma_x\sigma_y\right\rangle &= \frac{\displaystyle\sum_{\{\sigma\}}\sigma_x\sigma_y\prod_{\langle zw\rangle}\left(1+J_{zw}\sigma_z\sigma_w\tanh\beta\right)}{\displaystyle\sum_{\{\sigma\}}\prod_{\langle zw\rangle}\left(1+J_{zw}\sigma_z\sigma_w\tanh\beta\right)}.
\end{aligned} \tag{A.27}$$

The high-temperature expansion (see, for instance [Par88]), expresses the propagator as a sum over lattice paths that join the points $\boldsymbol{x}$ and $\boldsymbol{y}$, $\gamma_{\boldsymbol{x}\to\boldsymbol{y}}$:

$$\left\langle \sigma_{\boldsymbol{x}}\sigma_{\boldsymbol{y}}\right\rangle = Z^{-1}\sum_{\gamma_{\boldsymbol{x}\to\boldsymbol{y}}} Z_\gamma J(\tanh\beta)^{l_\gamma}, \tag{A.28}$$

where l_γ represents the length of the path $\gamma_{\boldsymbol{x}\to\boldsymbol{y}}$, J is the product of the couplings, J_{zw}, along the path, and Z_γ is a restricted partition function obtained by summing only over all closed paths that do not have any common link with the path $\gamma_{\boldsymbol{x}\to\boldsymbol{y}}$.

However, when averaging over disorder, due to the randomness in the coupling signs, $\overline{\left\langle \sigma_{\boldsymbol{x}}\sigma_{\boldsymbol{y}}\right\rangle} = 0$. The spin glass propagator is obtained instead by averaging over disorder $\overline{\left\langle \sigma_{\boldsymbol{x}}\sigma_{\boldsymbol{y}}\right\rangle^2}$. Clearly, the sum will be dominated by those diagrams where the go and return path are the same (thus, $J_{zw}^2 = 1$):

$$\overline{\left\langle \sigma_{\boldsymbol{x}}\sigma_{\boldsymbol{y}}\right\rangle^2} = Z^{-2}\sum_{\gamma_{\boldsymbol{x}\to\boldsymbol{y}}} Z_\gamma^2\left[\tanh^2\beta\right]^{l_\gamma} = Z^{-2}\sum_{\gamma_{\boldsymbol{x}\to\boldsymbol{y}}} \kappa^{l_\gamma} Z_\gamma^2, \tag{A.29}$$

where $\kappa = \tanh^2\beta$. In Bethe lattices, due to their cycle-less nature, $Z_\gamma^2/Z^2 = 1$ in the thermodynamic limit. Hence, we are left with the problem of counting the average number of paths of length l_γ that join $\boldsymbol{x}$ and $\boldsymbol{y}$, $p(l_\gamma)$. From it, we obtain

$$\hat{C}_4(r) = \binom{D}{r}\sum_{l_\gamma\geq r} p(l_\gamma)\kappa^{l_\gamma}. \tag{A.30}$$

The sum is restricted to $l_\gamma \geq r$ because the length of the shortest path that joins $\boldsymbol{x}$ and $\boldsymbol{y}$ is given by their postman distance r.

In order to count the average number of paths, $p(l_\gamma)$, let us distinguish two cases: $l_\gamma = r$ and $l_\gamma > r$. The first will give the leading contribution in the large D limit.

The number of paths joining $\boldsymbol{x}$ and $\boldsymbol{y}$ in precisely r steps is $r!$, because the r steps are all taken along different directions and in a random order. For a given path, the probability of all the r links be active is $(z/D)^r$. Hence

$$p\left(l_\gamma = r\right) = \frac{z^r}{D^r} r!\,. \tag{A.31}$$

Note that the D^{-r} factor compensates exactly the divergence of the $\binom{D}{r}$ in (A.30) (for large D).

In the case of $l_\gamma > r$, one has $l_\gamma = r + 2k$, with $k > 0$. Note that when $l_\gamma = r$ the path contains r different directions (namely, the Euclidean components in which $\boldsymbol{x}$ and $\boldsymbol{y}$ differ). Each of these directions appear only once. However, when $l_\gamma > r$, other directions must be included, we call them unnecessary. Note that, if the path is to end at the desired point, any unnecessary step must be undone later on. Hence, $l_\gamma - r$ is always an even number $2k$. Clearly, the number of such paths is bounded by $\Gamma\left(r,k\right)D^k$, where $\Gamma\left(r,k\right)$ is a D-independent amplitude. On the other

hand, the probability of finding all the links active is $(z/D)^{r+2k}$. Thus, we conclude that

$$p\left(l_\gamma = r + 2k\right) = O\left(\frac{1}{D^{k+r}}\right), \tag{A.32}$$

that results in a $O\left(D^{-k}\right)$ contribution to $\hat{C}_4(r)$.

Then, in the large D limit we obtain ($A = z\kappa$):

$$\hat{C}_4(r) = A^r = e^{r \log A}, \tag{A.33}$$

with finite size corrections of $O\left(D^{-1}\right)$. Thus, we encounter an exponential decay with an exponential correlation length given by

$$\xi^{\text{exp}} = \frac{1}{|\log A|}. \tag{A.34}$$

Summing all up, we can compute the spin-glass susceptibility for the large D limit:

$$\chi = \sum_{r=0}^{\infty} \hat{C}_4(r) = \sum_{r=0}^{\infty} A^r = \frac{1}{1-A}. \tag{A.35}$$

We see that when $A = 1$ the correlation no longer decays with distance, and the susceptibility diverges. Of course, one gets $A = 1$ precisely at the critical temperature, T_c, reported in (4.11).

The computation for the fixed connectivity model is very similar. One only needs to notice that, whereas the probability for the first link in a lattice path to be active is z/D, the probability for the next link is roughly $(z-1)/D$ (this is only accurate for large D). It follows that, again, the $l_\gamma = r$ paths are the only relevant paths in the high temperature expansion. We find that

$$p(l_\gamma = r) = \begin{cases} 1 & \text{if } r = 0, \\ \frac{z}{D}\left(\frac{z-1}{D}\right)^{r-1} r! & \text{if } r > 0. \end{cases} \tag{A.36}$$

Again, we can use it to compute $\hat{C}_4(r)$. In the large D limit, up to corrections of $O\left(D^{-1}\right)$, it is given by:

$$\hat{C}_4(r) = \begin{cases} 1 & \text{if } r = 0, \\ \frac{z}{z-1}\left[(z-1)\,\kappa\right]^r & \text{if } r > 0, \end{cases} \tag{A.37}$$

which, taking $\tilde{A} = (z-1)\kappa$, also shows an exponential decay with

$$\xi^{\text{exp}} = \frac{1}{|\log \tilde{A}|}. \tag{A.38}$$

Using this spatial correlation function, we can either compute the SG-susceptibility in the fixed connectivity hypercube,

$$\chi = \sum_{r=0}^{\infty} \hat{C}_4(r) = 1 + \frac{z}{z-1}\frac{\tilde{A}}{1-\tilde{A}}, \tag{A.39}$$

or the integral correlation length, defined as (4.21),

$$\xi = \frac{\sum_{r=0}^{\infty} r\,\hat{C}_4(r)}{\sum_{r=0}^{\infty} \hat{C}_4(r)} = \frac{\chi - 1}{\chi}\frac{1}{1-\tilde{A}}\,. \tag{A.40}$$

Again, when $\tilde{A} = 1$, we find a critical point. The corresponding T_c matches (4.11). The critical exponents, $\gamma = 1$, $\nu = 1$, can be read directly from (A.39) and (A.40). The reader might be puzzled by a mean field model with $\nu \neq 1/2$. The solution to the paradox is in our chosen metrics. Recall that the postman distance in the hypercube is the square of the Euclidean one. Hence, the correlation length in (A.40) is the *square* of the Euclidean correlation length.

APPENDIX B

Multi-spin coding

In this appendix, we discuss the multispin techniques used in Chapters 4 and 5.

B.1

The computer code for the hypercube model

Multi-spin coding is a kind of parallel computation that codes independent systems on each one of the bits in a computer word. The fixed-connectivity hypercube displays two features that allows for efficient multi-spin coding. First, spins are located in the nodes of a unit hypercube, that means that, in a D-dimensional hypercube, each spin position can be encoded in a word of D-bits, and the same for the links. And second, both the spins and the couplings are binary variables, and thus, can be codified in one bit. This last property allow us to simulate many systems in parallel. Indeed, since bitwise operations in a computer act at the same time over all the bits in a word, using multi-spin coding, one can simulate 64 systems (encoding spins in an `unsigned long long` variable)[1] at the same time, thus multiplying the efficiency by almost this factor.

In this appendix we will discuss, first, some technical details about the implementation of the hypercube in a computer using C language, discussing the graph generation, and second, we will explain how to implement the Metropolis algorithm taking full advantage of multi-spin coding.

B.1.1 Bitwise operations

Before anything else, it is interesting to discuss the bitwise operations we need to use in the program. We begin with the simplest one, the NOT operator (`!` in C). Its

[1] Indeed, the traditional natural processor word is 64-bit-long. However, although we did not use them, we cite that the SSE lets to work with 128 or even 256 (in the newest computers) bits words.

0&0=0	0|0=0	0^0=0
0&1=0	0|1=1	0^1=1
1&0=0	1|0=1	1^0=1
1&1=1	1|1=1	1^1=0

TABLE B.1: Truth tables for **(left)** AND (&), **(center)** OR (|) and **(right)** XOR (^) operator.

effect is inverting the bit, i.e. $!0 = 1$ and $!1 = 0$. We also need the AND operator (& in C), the OR operator (| in C) and the exclusive OR or XOR (^ in C). We present their truth tables in Table B.1. It is interesting to note that the XOR operator leaves unchanged the second bit in case the first one is a 0, and behaves like the NOT operator in the case it is a 1.

In addition, we will use the shifts operators » and «. They shift bits to the right or to the left.

Now that we have defined all the operators we are going to need, we can use them to move along the hypercube or the different samples. We begin with the implementation of the hypercube in a computer.

B.1.2 The hypercube in a computer

Being our problem an unit hypercube, its spatial coordinates are $\boldsymbol{x} = (x_1, \ldots, x_D) = (\{0,1\}, \ldots, \{0,1\})$ and then, can be directly coded in a D-bit word (let us call this word `site`) just writing the i-th coordinate (x_i) as the i-th bit ($\texttt{site}^i$) in the word. One can easily recover the x_i coordinate by performing the following operation

```
(site» i)& 1,
```

that is, the bit located in the i-th bit of `site` is obtained by displacing the bits in `site` by i bits, and finally recovered by means of an AND operator with 1.

In the hypercube, the nearest neighbors of spin in $\boldsymbol{x}$ are located in $\boldsymbol{x} + \hat{\boldsymbol{\mu}}$ where $\hat{\boldsymbol{\mu}}$ are the Cartesian unit vectors in a D-dimensional space. Again, we can write these unit vectors using D-bit words [all bits will be zero but the one located in the `mu`$(= 0, \ldots, D-1)$ position]. Then, using bitwise operations, and taking into account the periodic boundary conditions, the nearest neighbor of `site` in direction $\hat{\boldsymbol{\mu}}$ will be given by

```
site^(1«mu).
```

As an example, let us consider a $D = 4$ dimensional hypercube and the spin located in site 14. The spatial representation in bits is thus $(1,1,1,0)$. The first neighbor in the 0 direction is the $(1,1,1,1) = 15$-th spin. Note that the Euclidean coordinates are written from right to left (on the opposite than usually) to keep the equivalence with the binary representation. Thereby, the first neighbor in direction 3 is the $(0,1,1,0) = 6$, while the first neighbor along direction 2 is $(1,0,1,0) = 10$.

B.1.3 Connectivity matrix

In the next section, we will explain how to parallelize the Metropolis algorithm to simulate 64 samples at the same time. However, for practical reasons, we need to consider the same connectivity matrix, $n_{x,\hat{\mu}}$ in (4.6), for all the samples. The difference between samples within the same simulation is thus introduced only through the randomness of the couplings $J_{x,\hat{\mu}}$. That means that the configuration of interacting neighbors will be same at each run, but the nature of the interaction between spins, will not.

We include here a simplified version for the program used to generate the fixed connectivity graphs. In Listing B.1 we detail the dynamic Monte Carlo program used to simulate the fixed connectivity graph, based on the plaquette transformation, written in Listing B.2. This transformation was explained in detail in Section 4.2.2 and schematized in Figure 4.3.

As one can read in Listing B.1, we have defined some vectors. First, we introduce the connectivity matrix, $\{n_{x,\hat{\mu}}\}$ as a N-dimensional vector. The index `site` labels the starting vertex in the hypercube, and the direction of the link is encoded in the first D bits of the word. The link between the spin located at $x \equiv$ `site` with its neighbor in direction $\hat{\mu} \equiv$ `mu` is stored in `n[site^(1<<mu)]`, and will be 1 if the two spins are connected and 0 otherwise. In addition, since the interaction is very diluted, in order to speed the simulation, we store in vector `neighbor_list[site*6+mu]`, where `mu` labels the 6 neighbors of the spin in `site`.

Listing B.1: hypercube connections

```
void hypercube_connections(void)
{
  unsigned n_ini;
  int i,k,site,dir1,dir2,mu,indice;

  n_ini=63;                                  // initial configuration
                                             // of links
                                             // 0-5  = active   = 1
                                             // 6-.. = inactive = 0
  for (i=0;i<N;i++)                          // only N/2 will be used
    n[i]=n_ini;                              // (but copies are retained
                                             // to simplify the code)

  //  Start Monte Carlo

  for (k=0;k<100;k++){                       // run the plaquete
    for (i=0;i<N;i++){                       // transformations k*N times
      site=MYRANDOM>>(64-D);                 // the D most significant bits
      dir1=MYFRANDOM*D;                      // a random direction
      while ((dir2=MYFRANDOM*D)==dir1); // a different (random)
         direction
      permut_links(site,dir1,dir2);          // plaquette transformation
    }
```

```
    }

    for (site=0;site<V;site++){
      indice=0;
      for(mu=0;mu<D;mu++){
        if((n[site]>>mu)&1){              // stores which are the
    neighbor_list[site*6+indice]=site^(1<<u);
    indice++;                          // neighbors of
                                       // the spin in site
        }
      }
    }
  }
```

Listing B.2: plaquette transformation

```
  void permut_links(int i, int mu, int nu)
  {
    int J1,J2,J3,J4;
    int mask;
    //                                 Boundary conditions
    //  i+nu i+nu,mu  i+mu+nu          'i+mu'=i^(1<<mu)
    //       * ------ *
    //       |   J3   |
    // i,nu |J4    J2| i+mu,nu
    //       |   J1   |
    //       * ------ *
    //    i    i,mu    i+mu

    J1=(n[i]>>mu)&1;
    J4=(n[i]>>nu)&1;

    if (J1^J4){ // links are different

      J2=(n[i^(1<<mu)]>>nu)&1;
      J3=(n[i^(1<<nu)]>>mu)&1;

      if (J2^J3 && J1^J2){ // also are different
        // 8 bits are changed (4 original and 4 copies)
        mask=(1<<mu)|(1<<nu);
        n[i]^=mask;
        n[i^(1<<mu)]^=mask;
        n[i^(1<<nu)]^=mask;
        n[i^mask]^=mask;
      }
    }
  }
```

B.1.4 Multi-spin coding

As we briefly discussed before, it is possible to take benefit of the simultaneity of the bitwise operations to simulate at the same time many systems if they are all coded together in the same word. With this aim, we define a vector of `unsigned long long` variables of N spins, `S[N]`. In this scheme, each bit in the word `S[site]` accounts for the spin state placed at `site` in each of the 64 samples simulated.

As an example, using the operations discussed above, the spin placed in position $\boldsymbol{x} = (0, \ldots, 0, 1, 1)$ of the 10-th sample, for instance, would be recovered with

```
(S[3]»9)&1,
```

i.e. the position in the hypercube is recovered by considering the coordinates of the vector $\boldsymbol{x}$ as the bits of the word `site`, then `site=0`$\cdots$`11` $\equiv 3$. `S[3]` is an `unsigned long long` variable where each of its 64 bits represent the state of the spin placed at $\boldsymbol{x}$ in each sample. In order to extract the corresponding bit of the 10-th sample, we displace all the bits of `S[3]`, $10 - 1 = 9$ positions, and then perform and `&` with 1 to isolate this value.

Before entering in the algorithm, we need to establish an equivalence between bits and spins or couplings. For the spins we consider the following change of variables:

$$\sigma = +1 \to s = 1, \quad \text{and,} \quad \sigma = -1 \to s = 0. \tag{B.1}$$

In the same way that we did with the spins, we also need to encode the active coupling constants $J_{\boldsymbol{x},\hat{\mu}} = \pm 1$ of the 64 samples also in a `unsigned long long` vector. Since each spin is connected always with only 6 spins, the dimension of this vector will be $6N$ (one per site in the lattice and one per occupied link). We choose the equivalence between the coupling variables and the bits in the opposite way than before

$$J = +1 \to j = 0, \quad \text{and,} \quad J = -1 \to j = 1. \tag{B.2}$$

The reason for this arbitrary election is to absorb the negative sign in the definition of the Hamiltonian (4.6). Indeed, using these transformations, the logic operation (using the $\{0, 1\}$ basis)

```
s1^j^s2,
```
(B.3)

and the product of the original $\{-1, +1\}$ variables,

$$-J\sigma_1\sigma_2, \tag{B.4}$$

leads to the same result [using the spin transformation (B.1)], as is shown in Table B.2. Summing up, with this election, sample to sample (or bit to bit), the result will be 0 if the coupling is satisfied, and 1 if it is unsatisfied. Since the bitwise operations act over all the bits in a word at the same time, this product is computed for the 64 samples at once.

J	σ_1	σ_2	$-J\sigma_1\sigma_2$	s1	j	s2	j^ s2	s1^ j^ s2
-1	1	1	+1	1	1	1	0	1
-1	1	-1	-1	1	1	0	1	0
-1	-1	1	-1	0	1	1	0	0
-1	-1	-1	+1	0	1	0	1	1
+1	1	1	-1	1	0	1	1	0
+1	1	-1	+1	1	0	0	0	1
+1	-1	1	+1	0	0	1	1	1
+1	-1	-1	-1	0	0	0	0	0

TABLE B.2: Comparison between the product (B.4) and the logic operation (B.3).

At usual, for the Metropolis test, we need to compute the energy gain or lost of flipping one selected spin, σ_i. We only consider nearest neighbor interactions with exactly 6 neighbors, then, the energy difference will be

$$\Delta E = -2\sigma_i \sum_{j-\text{neighbor}}^{6} J_j\sigma_j, \tag{B.5}$$

where the sum on $j-$neighbor runs only over the 6 connected spins in the graph. In the $\{-1,+1\}$ basis, this ΔE can only take 7 different values -12, -8, -4, 0, $+4$, $+8$, $+12$. Then, the flip will be directly accepted if $\Delta E \leq 0$ or with probability $\exp(-\beta\Delta E)$ if $\Delta E > 0$.

Now, we need to compute this ΔE in the bit basis. If we consider the equivalence between operations discussed before, for each sample, the flip will be directly accepted if the number of unsatisfied couplings, n_{unsat}, is higher or equal to 3. The ΔE, (B.5), is thus recovered using the relation $\Delta E = 12 - 2n_{\text{unsat}}$.

The problem now is how to compute this ΔE and to perform the Metropolis test without breaking the parallelism between samples. The idea is to store bit by bit the energy for each sample. The maximum number of unsatisfied couplings is 6 per sample, in binary representation `100`, which means that we need three bits per sample to store it. Thus, we introduce three `unsigned long long` variables: `bit2`, `bit1` and `bit0`, so that the number of unsatisfied couplings for the i-th sample will be the binary number composed by the $\texttt{bit2}^i\texttt{bit1}^i\texttt{bit0}^i$, where $\texttt{bit}^i$ represents the i-th bit of word `bit` (representing the i-th sample).

The process to compute the number of unsatisfied links for each samples would be the following:

1. Select one spin in `site`, `S[site]`.

2. Select its *first* connected neighbor. Its position was stored in the vector `neighbor_list` defined in Section B.1.3. Then, its position is

   ```
   site_0=neighbor_list[site*6+0],
   ```

and the coupling,

`J_0=J[site*6+0].`

3. Compute `link0=S[site]^J_0^S[site_0]`. It is the first link we count so the total number of unsatisfied couplings can only be 0 or 1 so far. We only need one bit to keep it, so

   `bit0=link0.`

4. Select the *second* neighbor. As before,

   `site_1=neighbor_list[site*6+1],`

   `J_1=J[site*6+1].`

   And compute `link1=S[site]^J_1^S[site_1]`. The total number of unsatisfied couplings can be, so far, 0, 1 or 2 (in binary `00`, `01` and `10`). The possible combinations of `bit0` and `link1` are

bit0	link1	bit1_new	bit0_new
0	0	0	0
0	1	0	1
1	0	0	1
1	1	1	0

   Then,

   `bit1_new=bit0&link1,`

   and

   `bit0_new=bit0^link1.`

5. Select the *third* neighbor. Again,

   `site_2=neighbor_list[site*6+2],`

   `J_2=J[site*6+2],`

   and `link2=S[site]^J_2^S[site_2]`. The total number of unsatisfied couplings can be now 0, 1, 2 or 3 (in binary `00`, `01`, `10` and `11`). The possible combinations are now

bit1	bit0	link2	bit0&link2	bit1_new	bit0_new
0	0	0	0	0	0
0	0	1	0	0	1
0	1	0	0	0	1
0	1	1	1	1	0
1	0	0	0	1	0
1	0	1	0	1	1

Then,

`bit1_new=bit1^(bit0&link2)`,

and

`bit0_new=bit0^link2`.

6. Select the *forth* neighbor. Again,

   `site_3=neighbor_list[site*6+3]`,

   `J_3=J[site*6+3]`,

   and `link3=S[site]^J_3^S[site_3]`. The total number of unsatisfied couplings can be now 0, 1, 2, 3 or 4 (in binary `000`, `001`, `010`, `011` and `100`). Now we need three bits to store all. As before, the possible combinations are now

bit1	bit0	link3	bit0&link3	bit2_new	bit1_new	bit0_new
0	0	0	0	0	0	0
0	0	1	0	0	0	1
0	1	0	0	0	0	1
0	1	1	1	0	1	0
1	0	0	0	0	1	0
1	0	1	0	0	1	1
1	1	0	0	0	1	1
1	1	1	1	1	0	0

   Then, `bit2_new=bit1&(bit0&link3)`,

   `bit1_new=bit1^(bit0&link3)`,

   and

   `bit0_new=bit0^link3`.

7. Select the *fifth* neighbor. Again,

   `site_4=neighbor_list[site*6+4]`,

   `J_4=J[site*6+4]`,

   and `link4=S[site]^J_4^S[site_4]`. The total number of unsatisfied couplings can be now 0, 1, 2, 3, 4 or 5 (in binary `000`, `001`, `010`, `011`, `100` and `101`). Now both `bit0` and `bit1` can saturate, for the sake of abbreviation we name `A=bit0&link4` and `B=bit1&(bit0&link4)=bit1&A`,

bit2	bit1	bit0	link4	A	B	bit2_new	bit1_new	bit0_new
0	0	0	0	0	0	0	0	0
0	0	0	1	0	0	0	0	1
0	0	1	0	0	0	0	0	1
0	0	1	1	1	0	0	1	0
0	1	0	0	0	0	0	1	0
0	1	0	1	0	0	0	1	1
0	1	1	0	0	0	0	1	1
0	1	1	1	1	1	1	0	0
1	0	0	0	0	0	1	0	0
1	0	0	1	0	0	1	0	1

Then, `bit2_new=bit2^[bit1&(bit0&link4)]`,

`bit1_new=bit1^(bit0&link4)`,

and

`bit0_new=bit0^link4`.

8. Finally we select the *sixth* neighbor. Again,

   `site_5=neighbor_list[site*6+5]`,

   `J_5=J[site*6+5]`,

   and `link5=S[site]^J_4^S[site_4]`. The total number of unsatisfied couplings can be now 0, 1, 2, 3, 4, 5 or 6 (in binary `000`, `001`, `010`, `011`, `100`, `101` and `110`). Again, we abbreviate `A=bit0&link5` and `B=bit1&A`,

bit2	bit1	bit0	link5	A	B	bit2_new	bit1_new	bit0_new
0	0	0	0	0	0	0	0	0
0	0	0	1	0	0	0	0	1
0	0	1	0	0	0	0	0	1
0	0	1	1	1	0	0	1	0
0	1	0	0	0	0	0	1	0
0	1	0	1	0	0	0	1	1
0	1	1	0	0	0	0	1	1
0	1	1	1	1	1	1	0	0
1	0	0	0	0	0	1	0	0
1	0	0	1	0	0	1	0	1
1	0	1	0	0	0	1	0	1
1	0	1	1	1	0	1	1	0

Then, `bit2_new=bit2^[bit1&(bit0&link5)]`,

`bit1_new=bit1^(bit0&link5)`,

and

`bit0_new=bit0^link5`.

Up to this point, we know the amount of unsatisfied links for each sample (and then the energy difference) we need to decide whether the flips of the spins in `S[i]` are accepted or not, but for all the 64 samples at the same time.

The instruction for inverting one spin is equivalent to make an XOR with `1` (indeed, `1^0=1` and `1^0=1`). On the contrary, the spin will be unaltered if the XOR is made with a `0` in the first place (i.e. `0^0=0` and `0^1=1`). With this idea in mind, we define a new `unsigned long long` variable, called `flip`, that carries in each of its bits the information about flipping the spin in each of the samples. That is, for example, if its 10-th bit is `1`, the spin in sample 10, will be inverted. On the contrary, if it is `0`, it will continue as it was. We have to find a way to store the information about flipping all the samples at once.

We come back to the number of unsatisfied links and its equivalent energy barrier. The possible results are

ΔE	n_{unsat}	`bit2`	`bit1`	`bit0`
-12	6	1	1	0
-8	5	1	0	1
-4	4	1	0	0
0	3	0	1	1
4	2	0	1	0
8	1	0	0	1
12	0	0	0	0

The flip of `S[site]`^{i} is directly accepted if $\Delta E \leq 0$. In terms of `bit2`^{i}`bit1`^{i}`bit0`^{i}, this will occur whereas `bit2`$^i = 1$ (for the negative values of ΔE) or if `bit0`^{i}`&bit1`^{i} `=1` (for the $\Delta E = 0$ case). In the rest of cases, the flip will be accepted conditioned to the Metropolis test.

Nevertheless, even though many flips will be accepted directly, it is presumably that the flip will not be accepted simultaneously for all the 64 samples in the simulation, then, we always need to through a random number, $0 \leq R < 1$, and to check if $R < \exp(-\beta\Delta E)$ is fulfilled for each sample to accept the change. If we use the same random number for all the samples, we can check if it surpass or not a barrier of $\exp(-4\beta)$, $\exp(-8\beta)$ or $\exp(-12\beta)$ at once. With this aim, we define another three `unsigned long long` variables, `jump4`, `jump8` and `jump12` that will be a variable with 64 bits equal to `1` (`!0` in C, the highest possible number) if the barrier is surpassed, or all them equal to `0` if it is not. Clearly if `jump12=!0`, all samples will be flipped (if jumped the highest barrier, jumped all). If not, we must decide which samples are updated and which not. For this aim, it is useful

to check this other combination of variables

ΔE	n_{unsat}	bit1	bit0	jump4	jump8	Accept
4	2	1	0	1	1	Y
				1	0	Y
				0	0	N
8	1	0	1	1	1	Y
				1	0	N
				0	0	N

Then, when `jump16=0`, if `jump8=!0` only the samples with $\texttt{bit0}^i$=1 be updated. On the contrary, if `jump8=0`, but `jump4=!0`, the flipped ones will be only the ones with $\texttt{bit1}^i = 1$. If none of the `jump` variables is `!0`, no spin will be updated.

Summing all the conditions up, the variable `flip` will be given by

```
flip=bit2|(bit1&bit0)|jump12|(jump8&bit0)|(jump4&bit1)
```

Finally, the whole collection of samples will be updated at once by means of the instruction

```
S[site]^=flip.
```

B.2

Multi-spin coding for correlation functions

In this appendix, we face up the technical problem of computing an extremely large number of overlaps in a reasonable computer time. Indeed, all the study performed in Chapter 5 involves computing overlaps for N_s samples, with 4 independent sets of equilibrium configurations of $V = L^3$ spins each (obtained with independent Monte Carlo simulations) at N_T different temperatures. In addition, we consider for the equilibrium mean values, $N_t = 100$ independent times, evenly spaced in the whole Monte Carlo time. The data for each system size was summarized in Table 5.1.

That means that, in order to compute the averaged $\left\langle q^2_{T_1,T_2}\right\rangle_J$ for each sample and couple of temperatures $\{T_1, T_2\}$, we need to average over all the

$$q^{(a,b)}_{T_1,T_2}(t_A, t_B; J) = \frac{1}{V}\sum_{\boldsymbol{x}} s^{(a),T_1}_{\boldsymbol{x}}(t_A)\, s^{(b),T_2}_{\boldsymbol{x}}(t_B)\,, \tag{B.6}$$

$12N_t^2$ overlaps. Indeed, since the temperatures are different, there are $N_r(N_r-1) = 12$ ways of combining two replicas a and b, and N_t^2 pairs of times. In addition, we need to compute overlaps for $N_T^2/2$ couples of temperature (choosing $T_1 \leq T_2$) and N_s samples. Summing all up, we need to compute $6N_sN_t^2N_T^2$ overlaps, which only for $L = 32$ is 46240000000 L^3 operations. The situation is even worse if we consider the spatial correlation function $c_4(\boldsymbol{r})$ since, in addition, we must consider

all the possible displacements. Clearly, a direct computation would take months if no parallelization is considered.

Our solution to the problem was again to use multispin coding, as we did for the Hypercube model and detailed in this appendix in Section B.1. Indeed, if the L^3 spin variables, and overlap fields are coded in words of 64 bits, we can reduce the total time by a factor 64. We will discuss here only the ideas necessary for the parallelization, not the whole analysis program.

The approach is analogous to the one discussed in Section B. That is, to code the $\{-1, +1\}$ spin or overlap values in the $\{0, 1\}$ bits of a 64-bit word, and to take advance of the simultaneously of the bitwise operations to parallelize the problem. This time, instead of considering different systems coded in the same word, we will locate all the N spins sequentially in different size words, as we will explain below.

The spin configurations from JANUS were written in the following format

```
char u[Nr][NT][Nt][V8],
```

where the indexes `Nr`, `NT` and `Nt` refers to N_r, N_T and N_t respectively. Not as clear is the meaning of this `V8`. First, `V8` means $V/8$, which is always an integer since our system sizes have all even L. The reason for this division by 8 is that we are using `char` variables, which are 8-bit words. Then, we can pack the V spins in $V/8$ groups of 8 spins each coded together in the bits of the same word. Concerning this packing, we need to discuss how to move along the lattice points, indeed, for the spatial correlations functions we will need to now the spatial position $\boldsymbol{x}$ of each spin. According to our program the spin at $\boldsymbol{x} = (\mathtt{x}, \mathtt{y}, \mathtt{z})$ is recovered (leaving aside the indexes for replicas, temperatures or times) as

```
(u[z*S8+y*L8+x/8]»(x&7))&1
```
(B.7)

As before, `S8` and `L8` mean $L^2/8$ and $L/8$ respectively. An explanation of the bitwise operations can be found in Section B.1.1. This relation is valid for all our values of L but $L = 12$.[2]

Now, the process to compute the overlap field (3.58) between the configurations `u[ir][iT1][it]` and `u[ir2][iT2][it2]` (`ir`, `iT` and `it` accounts for the replica, temperature and iteration indexes) is summarized in List B.3.

Listing B.3: Overlap field calculation

[2]Indeed, the $L = 12$ case is more difficult since L is not divisible by 8. Packing is then a bit less straight-forward. We will not fully discuss this case here because the ideas are exactly the same but the calculations are more tedious. The underlying idea is that, although a whole row in each plane does not hold exactly in an even number of 8-bit words (as happens in the other system sizes), two neighboring rows do fit perfectly in 2 words. Then, if one wants to sum over all the row, must take into account whether the index is even or odd. In the case the index is even, one can sum all the bits in the word without worries because they belong to the same row. In the case it is odd, only 4-bits in the word belong to the desired row.

```
  char overlap[V8];
3
  conf1=u[ir][iT1][it];
  conf2=u[ir2][iT2][it2];

  calcula_overlap(conf1, conf2,overlap);
8
  ...


  void calcula_overlap(char *u1,char *u2, char *q)
13 {
    int i;
    long long *ul1,*ul2,*ql;

    ul1=(long long *)u1;
18  ul2=(long long *)u2;
    ql=(long long *)q;


    for (i=0;i<V64;i++){
23    ql[i]=ul1[i]^ul2[i];
    }

  }
```

Indeed, $V/8$ groups of 8 bits can be always be packed in $V/64$ (=`V64`) groups of 64 and thus parallelize the computation. This is, as displayed, just performed by a changing the word type. As seen, the exclusive OR bitwise operator (see Table:xor) is used for computing the spin multiplications. Indeed, as discussed in Section B it has the same multiplication table using bits, than the multiplication of signs.

Up to this point, we only computed the overlap field, in order to compute the whole overlap we need to sum up all the components. Since the computation is linear, it can be directly obtained by counting the number of bits equal to `1` in `overlap`, and returning to the original $\{-1, +1\}$ basis, see List B.4

Listing B.4: Total overlap sum

```
    long long *miq=(long long *) overlap;
    q12=0;
    for (i=0;i<V64;i+=1)
4     q12+=SUM_64BITS(miq[i]);

  //return to the original {+1,-1} basis
    mq12=(1.-2.*q12/(double)V);
```

For the summing bits' function `SUM_64BITS(x)` one can use, either the built-in function `_mm_popcnt_u64(x)` or a table initialized at the beginning of the program counting the amount of bits `1` for all long long numbers.

The computation for the spatial correlation function is a bit more complicated. To illustrate it we begin with the simplest case, when displacements are only con-

sidered along the z-axis, i.e. $\boldsymbol{r} = (0, 0, r)$. Note that the `z` coordinates are the first indexes in the overlap field `overlap` just computed, then, computing sums between the different planes is straight-forward as explained in List B.5.

Listing B.5: Spatial correlation function for displacements in z

```
1
  for(z=0;z<L;z++)
    for(zp=0;zp<=L/2;zp++){
      new_z=(zp+z)%L;
      corr=1.-2.*corr_points(&overlap[z*S8],&overlap[new_z*S8])/(double)
         S;
6     my_corr[zp]+=corr;
    }

  ...

11 int corr_points(char *q1,char *q2)
  {
      int i;
      int sum;
      long long *ql1,*ql2;
16    long long l;

      sum=0;
      ql1=(long long *)q1;
      ql2=(long long *)q2;
21    for (i=0;i<S64;i++)
        {
    l=ql1[i]^ql2[i];
    sum+=SUM_64BITS(l);
        }
26    return sum;
  }
```

Now, the idea is to compute the other two directions in the same way. In order to do it so, we need to rewrite the configurations so that the x or alternatively the y coordinate are placed on the first index, as z was in (B.7). We thus define two alternative rotated configurations

```
char uY[Nr][2][NT][V8],
```

with where coordinates $\boldsymbol{r} = (\mathtt{x}, \mathtt{y}, \mathtt{z})$ are recovered as

```
(uY[y*S8+z*L8+x/8]>>(x&7))&1.
```

And

```
char uX[Nr][2][NT][V8],
```

where the indexes run, this time, as follows

```
(uX[x*S8+y*L8+z/8]>>(z&7))&1.
```

Interchanging $y \leftrightarrow z$ is very easy, since there is no spin coding and only implies a change of variables. In order to get the variable x we need to decode it from the bits and afterwards to encode z in its place. We present in List B.6 the two different rotations we need.

Listing B.6: Rotations for the spatial correlation function

```
  //first we rotate the spin configurations for each couple of
     temperatures
  for(ir=0; ir< Nr; ir++)
3   for(it=0; it < NT ; it++)
      {
        rotate_conf_yz(u[ir][ibeta1][it],uY[ir][0][it]);
        rotate_conf_xz(u[ir][ibeta1][it],uX[ir][0][it]);

8       rotate_conf_yz(u[ir][ibeta2][it],uY[ir][1][it]);
        rotate_conf_xz(u[ir][ibeta2][it],uX[ir][1][it]);
      }

  ...
13



  void rotate_conf_yz(char *u1, char *u2) // interchange (y<->z)
  {
18  int x8,y,z,i1,i2;
    bzero(u2,V8);

    for (z=0;z<L;z++)
      for (y=0;y<L;y++){
23      i1=y*L8+z*S8;  //we just put y in the old place of z
        i2=z*L8+y*S8;
        for (x8=0;x8<L8;x8++){
    u2[i2]=u1[i1];
    i1++;
28  i2++;
        }
      }
  }


33
  void rotate_conf_xz(char *u1, char *u2) // interchage (x<->y)
  {
      int x,y,z,i1,i2,shift1,shift2,bit;
      bzero(u2,V8);
38
      for (z=0;z<L;z++)
    for (y=0;y<L;y++){
        shift2=z&7;
        for (x=0;x<L;x++){
43    i1=x/8+y*L8+z*S8;
      i2=z/8+y*L8+x*S8;
      shift1=x&7;
```

```
      bit=(u1[i1]>>shift1)&1;
      u2[i2]|=bit<<shift2;
48      }
    }
  }
```

Once rotated the configurations, the computation for the overlap follows from B.5.

APPENDIX C

Scaling and dynamic ultrametricity in the hypercube model

As in (4.28), let us assume that the spin time correlation function behaves for large t_w as

$$C(t, t_w) = f\left(\alpha(t, t_w)\right) , \quad \alpha(t, t_w) = \log t / \log t_w , \tag{C.1}$$

where the scaling function f is smooth and monotonically decreasing. From now on, we shall refer to this scaling as BB scaling (after Bertin-Bouchaud).

Let us see under which conditions BB scaling implies the ultrametricity property

$$C(t_1 - t_3, t_3) = \min\left\{C(t_1 - t_2, t_2), C(t_2 - t_3, t_3)\right\} , \tag{C.2}$$

where $t_1 \gg t_2 \gg t_3$ and t_3 tends to infinity.

The natural time dependency is a power law choice

$$t_1 = t_3 + A t_3^{\mu_1}, \tag{C.3}$$

$$t_2 = t_3 + B t_3^{\mu_2}, \tag{C.4}$$

with $\mu_1 > \mu_2$. In that case, the large t_3 limit for the argument of the scaling function are: $\alpha(t_1 - t_3, t_3) = \mu_1$, $\alpha(t_2 - t_3, t_3) = \mu_2$ and $\alpha(t_1 - t_2, t_2) = \mu_1$ if $\mu_2 < 1$ and $\alpha(t_1 - t_2, t_2) = \mu_1/\mu_2$ if $\mu_2 > 1$. Then, the condition (C.2) is only satisfied in case $\mu_2 < 1$. If, as it is the case for the critical trap model [Bero2b], $f(\alpha > 1) =$ constant, [1] the BB scaling would imply dynamic ultrametricity. This is not the case for a general scaling function f such as, for instance, the one we get in Figure 4.16. Nevertheless, although this analysis implies that the dynamic ultrametricity is only present in our model in some range of parameters, let us try a more straight approach.

We consider a fixed value for the correlation function, q. On the view of the previous considerations and of Figure 4.16, we should expect ultrametricity only

[1] Weak ultrametricity breaking implies that $f(\alpha > 1) = 0$.

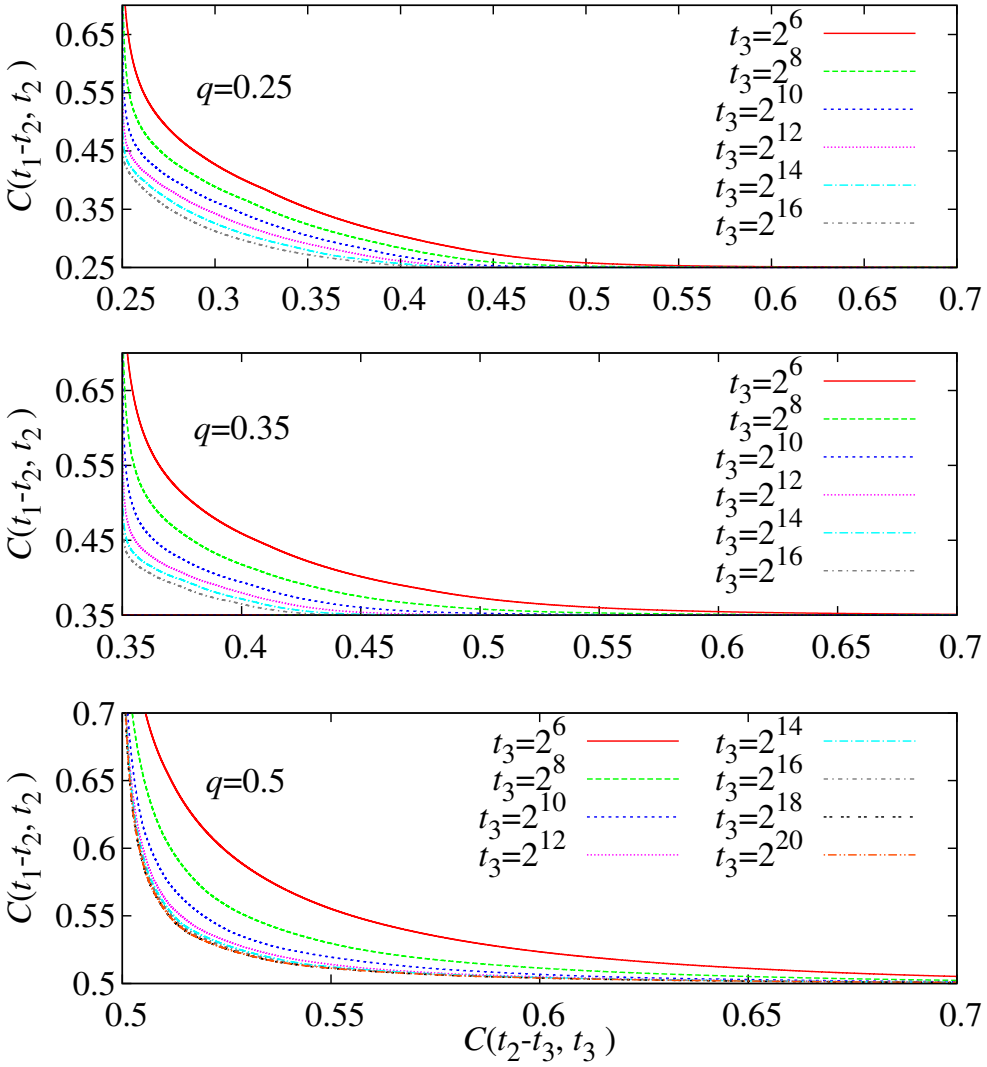

FIGURE C.1: Parametric plot $[x(t_2), y(t_2)] = [C(t_1 - t_2, t_2), C(t_2 - t_3, t_3)]$, $t_1 > t_2 > t_3$ with t_1 fixed by the condition $C(t_1 - t_3, t_3) = q$ and different t_3. In the presence of dynamic ultrametricity, (C.2), the parametric plot should tend for large t_3 to the union of $x = q$ and $y = q$. The panels correspond to $q = 0.25$ (**top**, nice BB scaling but no ultrametricity expected), $q = 0.35$ (**middle**, nice BB scaling and ultrametricity expected) and $q = 0.5$ (**bottom**, supposedly ultrametric but poor BB scaling). Note that there are not qualitative differences between $q = 0.25$ and $q = 0.35$.

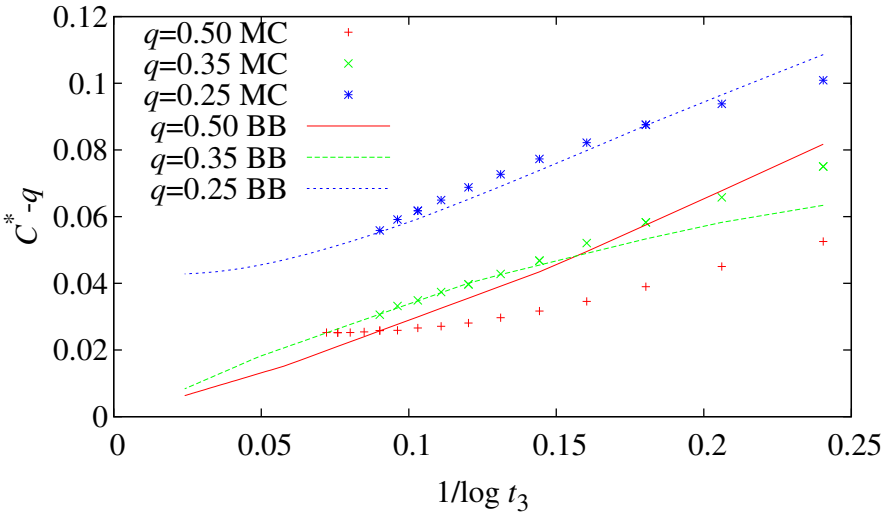

FIGURE C.2: **Dots:** For each q and t_3, as in Figure C.1, we take the intercept with $x = y$, i.e. $C^* = C(t_1 - t_2, t_2) = C(t_2 - t_3, t_3)$, and represent $C^* - q$ as a function of $1/\log t_3$. **Lines:** analogous plot for the toy model described in the text, where the BB scaling is exact.

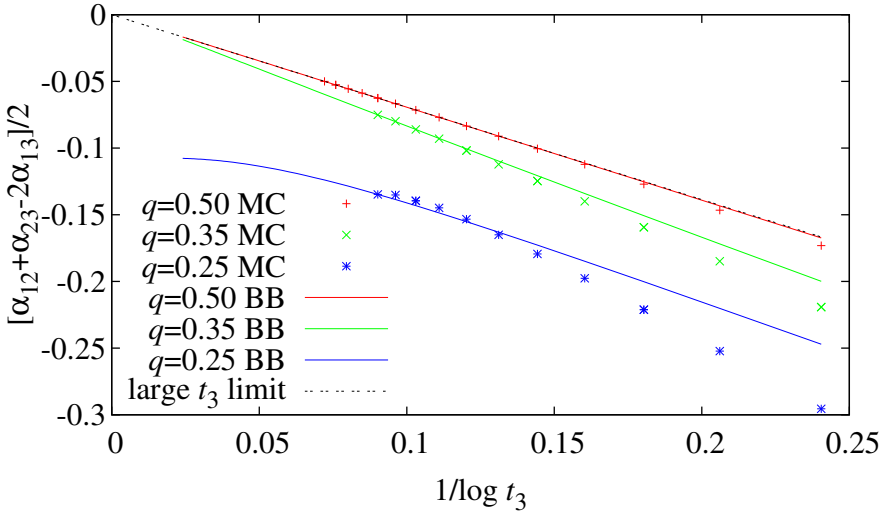

FIGURE C.3: For the data in Figure C.2, we represent $[\alpha(t_1, t_2) + \alpha(t_2, t_3)]/2 - \alpha(t_1, t_3)$ vs. $1/\log t_3$. The dashed line corresponds to (C.5).

for $q > f(\alpha = 1) \approx 0.35$. Now, for each t_3, we find t_1 such that $C(t_1 - t_3, t_3) = q$. Then, we perform a parametric plot of $C(t_1 - t_2, t_2)$ vs. $C(t_2 - t_3, t_3)$, for $t_3 < t_2 < t_1$. Ultrametricity predicts that, in the large t_3 limit, the curves should tend to a half square (e.g. the intersection of the straight lines $x = q$ and $y = q$) and, in particular, when $C(t_1 - t_2, t_2) = C(t_2 - t_3, t_3) = C^*$, C^* should tend to q.

We present in Figure C.1 results for three different values of q: 0.5 (ultrametric region, but in our range of t_w data do not scale according BB), 0.35 (ultrametric region and good BB scaling) and 0.25 (non ultrametric region but BB scaling works nicely). At the qualitative level, the parametric curves seem to tend to a corner (but $q = 0.5$), but the convergence is slow. Furthermore, there are no clear differences between the curves with $q > f(\alpha = 1)$ and those with $q < f(\alpha = 1)$. Hence, due to the failure of this qualitative approach, we may try a more quantitative analysis.

We obtain numerically C^*, the point where $C^* = C(t_1 - t_2, t_2) = C(t_2 - t_3, t_3)$, and study $C^* - q$ as function of $1/\log t_3$. This choice is due to the fact that in the ultrametric region BB scaling predicts

$$\alpha(t_1 - t_2, t_2) = \alpha(t_1 - t_3, t_3) - \frac{\log 2}{\log t_3} + \dots . \tag{C.5}$$

Hence, we expect that $C^* - q$ will be of order $1/\log t_3$ if ultrametricity holds. Let us sketch the proof. We define $y = f^{-1}(q) = \alpha(t_1 - t_3, t_3)$ (recall that $y < 1$ in the ultrametric region). Hence, the three times are

$$t_1 = t_w + t_w^y , \tag{C.6}$$
$$t_2 = t_w + A(t_w) t_w^y , \tag{C.7}$$
$$t_3 = t_w . \tag{C.8}$$

The hierarchy of time scales, $t_1 > t_2 > t_3 \gg 1$, implies that, for large t_w, $A(t_w)$ is bounded. The condition $\alpha(t_1 - t_2, t_2) = \alpha(t_2 - t_3, t_3)$ translates to

$$\frac{y \log t_w + \log\left[1 - A(t_w)\right]}{\log t_w + \log\left[1 + A(t_w) t_w^{y-1}\right]} = y + \frac{\log A(t_w)}{\log t_w} . \tag{C.9}$$

The above equation can be solved asymptotically for $A(t_w)$ in the limit of large t_w as (recall that $y < 1$)

$$A(t_w) = \frac{1}{2} - \frac{y}{8} t_w^{y-1} + \dots . \tag{C.10}$$

To obtain (C.5), one just notes that $\alpha(t_1 - t_2, t_2)$ is equal to the right hand side of (C.9).

The MC numerical data in Figure C.2 confirm the expectation of $C^* - q = O(1/\log t_3)$ only partly. For $q = 0.35$ the results are as expected, yet for $q = 0.25$ the difference is decreasing fast as t_3 grows and it is hard to tell whether the extrapolation will be zero or not. For $q = 0.5$ (where BB scaling is not working for our numerical data) the behavior is non monotonic.

To rationalize our finding, we consider a simplified model, where the BB scaling is supposed to hold exactly. The master curve $f(\alpha)$ is taken from the numerical data for $C(t, t_3 = 2^{16})$ for $D = 22$. This toy model allows us consider ridiculously large values of t_3. As we see in Figure C.2, the peculiarities of the master curve cause a non monotonic behavior in q for an ample range of t_3.

The lack of monotonicity in q makes also on interest to focus on α, rather than on the correlation function. With this aim, we consider the time t_2 where $C(t_1 - t_2, t_2) = C(t_2 - t_3, t_3) = C^*$, and compute $\frac{1}{2}\left[\alpha(t_1 - t_2, t_2) + \alpha(t_2 - t_3, t_3)\right] - \alpha(t_1 - t_3, t_3)$. BB scaling and ultrametricity combined, see (C.5), imply that this quantity should be of order $1/\log t_3$ (in the non ultrametric region, it should be of order one). Our results in Figure C.3 basically agree with these expectations.

APPENDIX D

Statistical ensembles

In this Appendix we summarize the statistical ensembles we used along Part II of the thesis. We focus on the uncommon ones. The standard ensembles will be only named and its defining equations will be defined only as a help to understand the new ensembles.

D.1

Common definitions

We consider N particles, each at the position $\boldsymbol{r}_i$ with $i = 1, \ldots, N$ in a cubic volume $V = L^3$ with periodic boundary conditions. Let U be the total potential energy of our system,

$$U(\{\boldsymbol{r}_i\}) = \sum_{i<j} \mathcal{U}(|\boldsymbol{r}_i - \boldsymbol{r}_j|)\,, \ (u \equiv U/N)\,, \tag{D.1}$$

with $\mathcal{U}(r)$ the pairwise interaction potential. From now on, we will use the shortcut $\boldsymbol{R} \equiv \{\boldsymbol{r}_i\}$.

As it is common in the literature, we label the different ensembles by their conserved magnitudes. For instance, NVT accounts for the statistical collectivity with conserved number of particles, N, volume, V, and temperature, T.

D.2

Canonical ensemble (NVT)

The partition function is ($\beta = 1/(k_{\mathrm{B}}T)$)

$$Z_N(V,T) = \mathrm{e}^{-\beta F_N(V,T)} = \frac{1}{N!\Lambda^{3N}} \int \mathrm{d}\boldsymbol{R}\, \mathrm{e}^{-\beta U(\boldsymbol{R})}, \tag{D.2}$$

where $F_N(V,T)$ is the Helmholtz free-energy, $f(v,T) = F_N(V,T)/N$ the free-energy density and Λ the de Broglie thermal wavelength (an irrelevant constant to make Z_N adimensional).

The canonical average of a generic observable $O(\boldsymbol{R})$ is

$$\langle O \rangle_\beta = \frac{\int \mathrm{d}\boldsymbol{R}\, O(\boldsymbol{R})\, \mathrm{e}^{-\beta U(\boldsymbol{R})}}{\int \mathrm{d}\boldsymbol{R}\, \mathrm{e}^{-\beta U(\boldsymbol{R})}}. \tag{D.3}$$

D.3 Isobaric ensemble (NpT)

If the pressure p is fixed, the volume fluctuates. The partition function is

$$\Upsilon_N(p,T) = \mathrm{e}^{-\beta G_N(p,T)} = \frac{p\beta}{N!\Lambda^{3N}} \int \mathrm{d}V \mathrm{e}^{-\beta pV} \int \mathrm{d}\boldsymbol{R}\, \mathrm{e}^{-\beta U(\boldsymbol{R})}, \tag{D.4}$$

with $G_N(p,T)$ the Gibbs free-energy and $Z_N(V,T)$ the NVT partition function defined in (D.2). The chemical potential is $g(p,T) = G_N(p,T)/N$.

Again, the isobaric average at fixed p of a function of V and the particle positions, $O(V,\boldsymbol{R})$, is

$$\langle O \rangle_p = \frac{\int \mathrm{d}V\, \mathrm{e}^{-\beta pV} \int \mathrm{d}\boldsymbol{R}\, O(\boldsymbol{R})\, \mathrm{e}^{-\beta U(\boldsymbol{R})}}{\int \mathrm{d}V\, \mathrm{e}^{-\beta pV} \int \mathrm{d}\boldsymbol{R}\, \mathrm{e}^{-\beta U(\boldsymbol{R})}}. \tag{D.5}$$

The overlap equivalence is obtained from (D.4). We rewrite it in terms of Helmholtz free-energy density, $f(v,T)$, and the intrinsic volume $v = N/N$

$$\mathrm{e}^{-\beta N g(p,T)} = p\beta N \int \mathrm{d}v\, \mathrm{e}^{-N\beta[pv+f(v,T)]}. \tag{D.6}$$

Then, using a saddle point approximation, we can relate the pressure in the NpT ensemble with NVT averages.

$$p = -\left.\frac{\partial f(v,T)}{\partial v}\right|_\beta \tag{D.7}$$

$$= \frac{1}{v}\left(k_\mathrm{B}T + \frac{1}{3N}\left\langle \sum_i \boldsymbol{r}_i \cdot \boldsymbol{\nabla}_{\boldsymbol{r}_i} U(\boldsymbol{R}) \right\rangle_\beta\right) \tag{D.8}$$

D.4 Microcanonical ensemble (NVE)

In this ensemble, we want to constrain the value of the energy of the system. Finding standard MC moves that satisfy this constraint is rather difficult. Instead, our

proposal is to add a trivial Gaussian bath to the potential energy, and to conserve the "total" joint energy. In order to do so, we extend the configuration space with N additional momenta p_i (normal variables, they are simply a conceptual device to introduce the ensemble [Lus98]). Thus, our total energy is

$$E = U + K\,,\ (e \equiv E/N)\,. \tag{D.9}$$

where

$$K = \sum_{i=1}^{N} p_i^2/2 \tag{D.10}$$

is the kinetic energy associated to the conjugated momenta $\{p_j\}$. In the canonical ensemble, these p_i are a Gaussian bath decoupled from the particles. Here, we are considering just one conjugated momentum per particle, we will see in Section D.6.1 that this is not necessarily the best choice. In particular $\langle e\rangle_\beta = \langle u\rangle_\beta + 1/(2\beta)$. As the kinetic energy is non-negative by definition, we should have $E \geq U$.

A quantity of major importance in the microcanonical ensemble is the entropy density, $s_N(e)$:

$$\exp[Ns_N(e)] \;=\; \int_\infty^\infty \prod_{i=1}^{N} \mathrm{d}p_i \int \mathrm{d}\boldsymbol{R}\ \delta(Ne - E).$$

The conjugated momenta are explictly integrated out using the Dirac's delta function,

$$\exp[Ns_N(e)] \;=\; \frac{(2\pi N)^{N/2}}{N\Gamma(N/2)} \int \mathrm{d}\boldsymbol{R}\ (e-u)^{\frac{N}{2}-1}\theta(e-u)\,.$$

The Heaviside step function, $\theta(e-u)$, enforces $e > u$. The microcanonical average of an arbitrary function of the particle positions $\boldsymbol{R}$ and of the energy density e, $O(\boldsymbol{R};e)$ is defined as

$$\langle O\rangle_e \;\equiv\; \frac{\int \mathrm{d}\boldsymbol{R}\, O(\boldsymbol{R};e)\omega_N(\boldsymbol{R};e)}{\int \mathrm{d}\boldsymbol{R}\,\omega_N(\boldsymbol{R};e)}\,, \tag{D.11}$$

where,

$$\omega_N(\boldsymbol{R};e) \;=\; (e-u)^{\frac{N}{2}-1}\theta(e-u)\,. \tag{D.12}$$

The canonical partition function (but for irrelevant constants) can be recovered from the entropy density $s_N(e)$

$$Z_N(V,T) = \int \mathrm{d}e\, \mathrm{e}^{N[s_N(e)-\beta(e)e]}. \tag{D.13}$$

Then, using the saddle-point approximation gives us a condition for the inverse temperature

$$\beta(e) = \frac{\mathrm{d}s_N(e)}{\mathrm{d}e}\,, \tag{D.14}$$

which leads to a microcanonical expectation value at fixed energy e:

$$\beta(e) \equiv \langle \hat{\beta} \rangle_e, \quad \hat{\beta} = \frac{N-2}{2N(e-u)}. \tag{D.15}$$

D.5

Microcorical ensemble ($N\hat{V}T$)

This ensemble is analogous to the microcanonical ensemble, but less intuitive. Now we let the volume fluctuate but constrain it as well. It is then very similar to the NVT ensemble, but gives us more control of the simulation.

The fluctuations in the volume are introduced via N Gaussian demons η_i analogous to the momenta in the microcanonical approach, that is

$$\hat{V} = V + \sum_{i=1}^{N} \eta_i^2/2, \ (\hat{v} = \hat{V}/N). \tag{D.16}$$

As we did with the entropy, we compute the number of states that fulfill the imposed condition $V + \sum_{i=1}^{N} \eta_i^2/2 = \hat{V}$,

$$\hat{Z}_N(\hat{v}, T) = \int \mathrm{d}V Z_N(V, T) \int \prod_{i=1}^{N} \mathrm{d}\eta_i \, \delta \left(N\hat{v} - V - \sum_{i}^{N} \eta_i^2/2 \right). \tag{D.17}$$

Again, these demons are decoupled from the rest of variables and can be integrated out (now the trick is even clearer than in the microcanonical case),

$$\hat{Z}_N(\hat{V}, T) = \mathrm{e}^{-N\beta \hat{f}_N(\hat{v},T)} = \frac{(2\pi)^{N/2}}{\Gamma(N/2)} \int \mathrm{d}V Z_N(V, T) \left(N\hat{v} - V\right)^{N/2-1} \Theta\left(N\hat{v} - V\right). \tag{D.18}$$

This $\hat{f}_N(\hat{v}, T)$ is our new Helmholtz free-energy density.

The microcorical average of an arbitrary function of the particle positions $\boldsymbol{R}$ and of the $\hat{v}$, $O(\{\boldsymbol{r}\}_i; \hat{v})$ is

$$\langle O \rangle_{\hat{v}} \equiv \frac{\int \mathrm{d}\boldsymbol{R} \, O(\boldsymbol{R}; \hat{v}) \omega_N(\boldsymbol{R}; \hat{v})}{\int \mathrm{d}\boldsymbol{R} \, \omega_N(\boldsymbol{R}; \hat{v})}, \tag{D.19}$$

with

$$\omega_N(\boldsymbol{R}; \hat{v}) = \left(N\hat{v} - V\right)^{\frac{N}{2}-1} \theta(N\hat{v} - V). \tag{D.20}$$

We can relate this ensemble with the NpT one just integrating over all the $\hat{v}$. Then, the partition function is recovered

$$Y_N(p, T) = \int \mathrm{d}\hat{v} \, \mathrm{e}^{-N\beta[p(\hat{v})\hat{v} - \hat{f}_N(\hat{v},T)]}. \tag{D.21}$$

Again, the saddle point approximation lets us to compute the pressure

$$p(\hat{v}) = \frac{\mathrm{d}f_N(\hat{v}, T)}{\mathrm{d}\hat{v}}, \tag{D.22}$$

which gives us the microcorical expectation value at fixed $\hat{v}$:

$$p(\hat{v}) \equiv \langle \hat{p} \rangle_{\hat{v}}, \quad \hat{p} = \frac{N-2}{2(N\hat{v} - V)}. \tag{D.23}$$

D.6

Tethered ensemble

D.6.1 For one magnitude O ($\hat{O}NpT$)

The tethered ensemble allows us to build an ensemble constraining the mean value of any desired quantity. Here we develop the formalism for an arbitrary magnitude $O(\boldsymbol{R}) = No(\boldsymbol{R})$ keeping fixed N, p and T.

We first note that in the NpT ensemble, the probability of getting certain value o for the observable $o(\boldsymbol{R})$ at a given pressure p is

$$p_1(o, p) \propto \int_0^\infty \mathrm{d}V \, \mathrm{e}^{-\beta p V} \int \mathrm{d}\boldsymbol{R} \, \mathrm{e}^{-\beta U(\boldsymbol{R})} \, \delta\left(o - o(\boldsymbol{R})\right). \tag{D.24}$$

On the other hand, we consider a Gaussian bath of αN demons.[1] The probability of $\sum_{i=1}^{\alpha N} \eta_i / \alpha N$ to be equal to s is

$$p_2(s) \propto \int_{-\infty}^{+\infty} \prod_{i=1}^{\alpha N} \mathrm{d}\eta_i \, \mathrm{e}^{-\sum_{i=1}^{\alpha N} \eta_i^2 / 2} \, \delta\left(s - \frac{1}{\alpha N} \sum_{i=1}^{\alpha N} \eta_i\right). \tag{D.25}$$

We introduce a new variable

$$\hat{o} = o + s. \tag{D.26}$$

The probability distribution function for $\hat{o}$ can be obtained with the convolution of these two last probabilities

$$p(\hat{o}, p) = \int_0^{+\infty} \mathrm{d}o \int_0^{+\infty} \mathrm{d}r \; p_1(o, p) \; p_2(s) \; \delta\left(\hat{o} - o - s\right). \tag{D.27}$$

[1] In the previous works to this thesis on this algorithm [Fero9b, MMo9], α was taken always equal to 1. However, previous works were performed always in spin systems where the normal system sizes simulated are far larger than in colloidal systems, which is the case we are interested in applying the method. Indeed, the tethered method is introduced via a convolution of the physical ensemble probability with a Gaussian of weight $1/\sqrt{\alpha N}$, see Eq. (D.27). For the system sizes we studied in Chapter 8 ($N \leq 4000$) these Gaussian were too broad to resolve the different peaks if one took $\alpha = 1$. The problem could be directly solved by reducing this Gaussian weight, or in other words, increasing the amount of demons.

As above, in the microcorical case, the demons can be integrated out. Then, the tethered mean value of a generic observable $A(\boldsymbol{R})$ fixed $\hat{o}$ is then given by

$$\langle A \rangle_{\hat{o}} \equiv \frac{\int \mathrm{d}V \int \mathrm{d}\boldsymbol{R}\, A(\boldsymbol{R}) \omega_N(\boldsymbol{R}, p; \hat{o})}{\int \mathrm{d}V \int \mathrm{d}\boldsymbol{R}\, \omega_N(\boldsymbol{R}, p; \hat{o})}, \tag{D.28}$$

where,

$$\omega_N(\boldsymbol{R}, p; \hat{o}) = \sqrt{\frac{\alpha N}{2\pi}}\, \mathrm{e}^{-\beta p V}\, \mathrm{e}^{-\beta U(\boldsymbol{R})} \mathrm{e}^{-\frac{\alpha N}{2}[\hat{o} - o(\boldsymbol{R})]^2}. \tag{D.29}$$

In close analogy with the other ensembles, we can define a Helmholtz effective potential

$$\mathrm{e}^{-N\Omega_N(\hat{o},p)} = \frac{\beta p}{N!\Lambda^{3N}} \sqrt{\frac{\alpha N}{2\pi}} \int \mathrm{d}V \int \mathrm{d}\boldsymbol{R}\, \mathrm{e}^{-\beta p V}\, \mathrm{e}^{-\beta U(\boldsymbol{R})}\, \mathrm{e}^{-\frac{\alpha N}{2}[\hat{o} - o(\boldsymbol{R})]^2}. \tag{D.30}$$

The most important tethered average is the $\hat{o}$-derivative of this effective potential, the tethered field,

$$\frac{\partial \Omega_N}{\partial \hat{o}} = \left\langle \hat{h} \right\rangle_{\hat{o}}, \tag{D.31}$$

with

$$\hat{h} = \alpha \left[\hat{o} - o(\boldsymbol{R})\right]. \tag{D.32}$$

D.6.2 For several conserved magnitudes

In the previous section, we considered an ensemble with just one tethered quantity. However, as we discuss in Chapter 8, sometimes it is necessary to consider several reaction coordinates at the same time. The construction of the ensemble is analogous to what described for one coordinate. We start by coupling the observables $O_i(\boldsymbol{R}) = N o_i(\boldsymbol{R})$, with $i = 1, \ldots, n$, with αN demons each,

$$\hat{o}_1 = o_1 + s_1, \quad \ldots, \quad \hat{o}_n = o_n + s_n, \tag{D.33}$$

and then follow the same steps of Section D.6.1. As a consequence, we have now a n-dimensional effective potential $\Omega_N(\hat{\boldsymbol{o}})$,

$$\mathrm{e}^{-N\Omega_N(\hat{\boldsymbol{o}},p)} = \frac{\beta p}{N!\Lambda^{3N}} \left(\frac{\alpha N}{2\pi}\right)^{n/2} \int \mathrm{d}V \int \mathrm{d}\boldsymbol{R}\, \mathrm{e}^{-\beta p V}\, \mathrm{e}^{-\beta U(\boldsymbol{R})}\, \mathrm{e}^{-\frac{\alpha N}{2}\left[\sum_i [\hat{o}_i - o_i(\boldsymbol{R})]^2\right]}. \tag{D.34}$$

Now, the gradient field is given by

$$\boldsymbol{\nabla} \Omega_N(\hat{\boldsymbol{o}}, p) \equiv \left(\frac{\partial \Omega_N(\hat{\boldsymbol{o}}, p)}{\partial \hat{o}_1}, \ldots, \frac{\partial \Omega_N(\hat{\boldsymbol{o}}, p)}{\partial \hat{o}_n} \right) = \tag{D.35}$$

$$= \left(\langle \alpha\, (\hat{o}_1 - o_1) \rangle_{\hat{\boldsymbol{o}}}, \ldots, \langle \alpha\, (\hat{o}_n - o_n) \rangle_{\hat{\boldsymbol{o}}} \right). \tag{D.36}$$

APPENDIX E

Thermalization checks in the hard spheres crystallization

In this appendix, we tackle the problem of thermalization of the systems we worked with in Chapter 8.

E.1

Time-autocorrelation functions

We will begin the discussion studying briefly the time-autocorrelation functions. These functions carry the information about the time it takes the system to forget a particular configuration. For an observable $O(t)$, it is defined as

$$\rho_O = \frac{C_{OO}(t)}{C_{OO}(0)} \quad \text{with} \quad C_{OO}(t) = \langle O_s O\,(s+t)\rangle - \langle O\rangle^2 . \tag{E.1}$$

One should like to consider the time autocorrelation functions for the components of the gradient field, $\boldsymbol{\nabla}\Omega_N$. Yet, its definition (8.17) tells us that these correlation functions are identical to those of $Q_6(\boldsymbol{R})$ and $C(\boldsymbol{R})$. Eq. (8.11) suggests as well that the time autocorrelation function for the specific volume v is of interest. An example of these autocorrelation functions is shown in Fig. E.1, for the $S = 0$ point (recall Figs. 8.6 and 8.7). We note that v plays the role of the algorithmic slow mode, with a strong N dependence. On the other hand, the autocorrelation function for Q_6 decreases very fast, and it is barely N-dependent. The autocorrelation function for C is qualitatively identical to that of Q_6, and will thus be skipped.

The analysis is made quantitative by considering the integrated autocorrelation times,

$$\tau_{\text{int},O} = \frac{1}{2} + \sum_{t=1}^{\infty} \rho_{OO}(t), \tag{E.2}$$

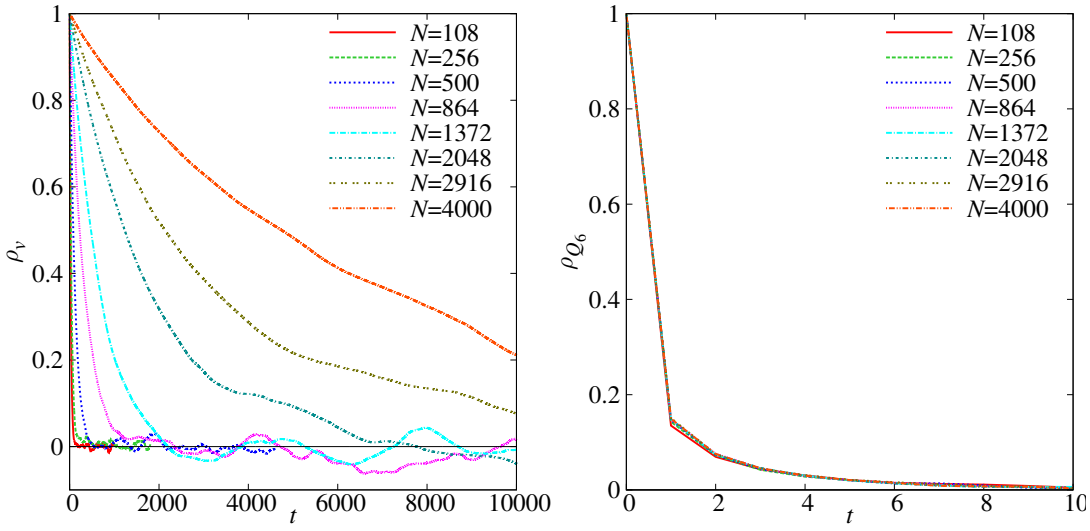

FIGURE E.1: Normalized time autocorrelation function, Eq. E.1, for the specific volume (left) and the crystal order parameter (right), as computed for a system of N hard spheres, in the fluid minimum of the effective potential (labeled $S = 0$). Time is measured in units of EMCS (see text). Mind the different time scale for the left and right panels. Each value of N was simulated very close to (but not precisely at) its phase-coexistence pressure $p_{\rm co}^N$ obtained in Section 8.6.1.

see Fig. E.2.[1] We notice that the dynamics of v is considerable slower than that of Q_6, and featureless as a function of S. Data for the specific volume scales as $\tau_v \sim N^{5/3}$ (quite worse than standard critical slowing down in three dimensions, $\tau \sim N^{2/3}$, yet much better than exponential dynamic slowing-down). There is a clear anomaly in the behavior of τ for a single simulation point in $N = 2916$. We will discuss this point in Section E.3, where we focuss on the $N = 4000$ and 2916 systems.

Using these tools, we can be confident that all simulations were, at least, 100τ long. Besides, all simulations were performed twice, with different starting configurations (either an ideal FCC crystal, or an ideal gas). We check systematically the compatibility between the two sets of investigations in the next section.

[1] In practical situations, when times become long in comparison with this $\tau_{\rm int}$ itself, the signal-to-noise in function ρ_{OO} becomes low, which results in large contributions to the sum (E.2) from very noisy data. The solution to this problem, is to establish a large-time cutoff and determine $\tau_{{\rm int},O}$ self-consistently. In our particular calculation, we replaced the ∞ by $6\tau_{{\rm int},O}$.

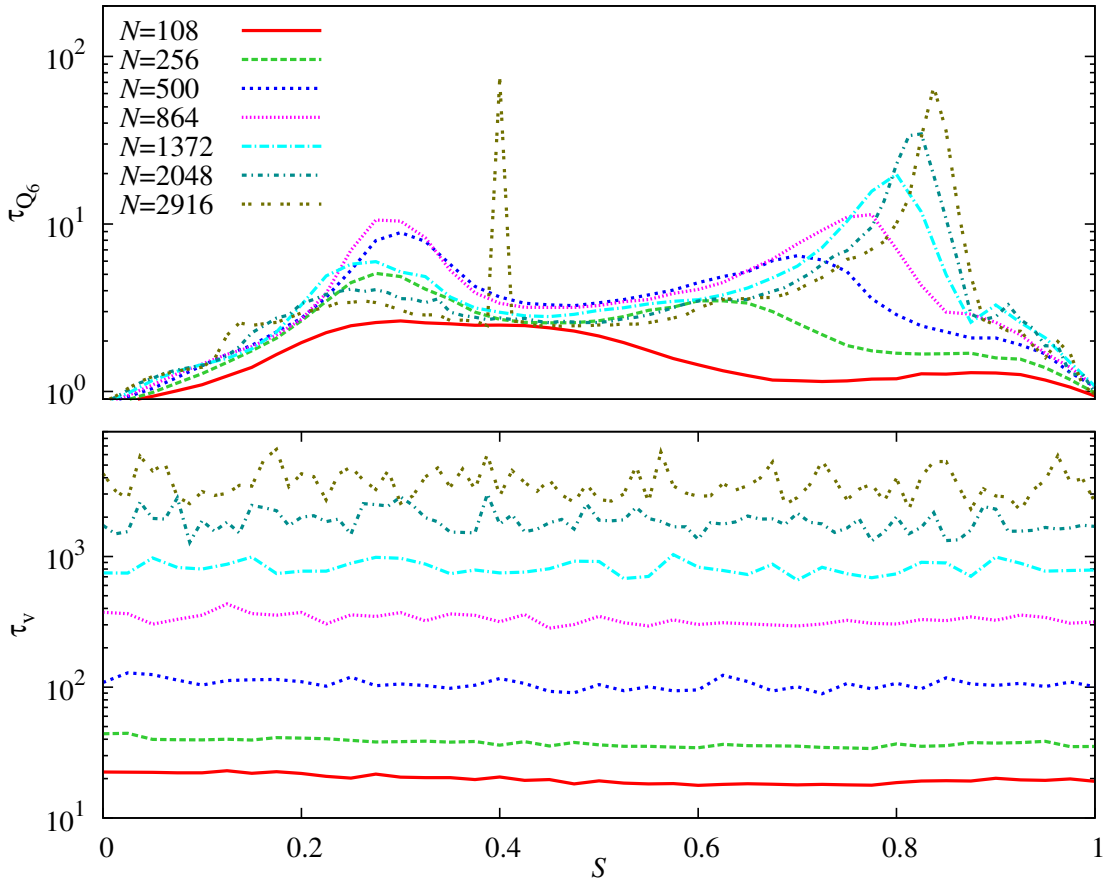

FIGURE E.2: Integrated autocorrelation times, defined in (E.2), for Q_6 (top) and v (bottom), as a function of S (the linear coordinate that labels the integration path in Fig. 8.6, where $S = 0$ stands for the fluid minimum and $S = 1$ represents the homogeneous FCC phase). Time is measured in units of EMCS.

E.2

Independence of results from different runs

Precisely to control the system equilibration, we run two independent simulations, each starting from a completely different configuration: one ordered, which is, in addition, the stable one in the crystal region, and one disordered, the stable one in the fluid region. We can be confident about the equilibration of the system if after certain time, we obtain the same mean values (within error bars) with both startings. Thus, checking that the two simulations are compatible is the goal of this section.

We can perform a systematic study of this compatibility through the $\boldsymbol{\nabla}_S\Omega_N$, obtained as the proyection of (8.17) on the simulated straight line in Figure 8.6, which is central in the calculation of the main quantities obtained in this work: p_{co} and $\gamma_{\{100\}}$. The procedure is following: we obtain this $\boldsymbol{\nabla}_S\Omega_N$ separately in simulations starting from a random configurations, namely, $\boldsymbol{\nabla}_S\Omega_N^{\text{fluid}}$ and from FCC configurations, namely, $\boldsymbol{\nabla}_S\Omega_N^{\text{FCC}}$, and we compute the following quotient,

$$y_S = \frac{\boldsymbol{\nabla}_S\Omega_N^{\text{FCC}} - \boldsymbol{\nabla}_S\Omega_N^{\text{fluid}}}{\sqrt{\sigma^2_{\boldsymbol{\nabla}_S\Omega_N^{\text{FCC}}} + \sigma^2_{\boldsymbol{\nabla}_S\Omega_N^{\text{fluid}}}}}. \tag{E.3}$$

Since the two $\boldsymbol{\nabla}_S\Omega_N$ variables are mean values obtained from a Monte Carlo simulation, they are Gaussian distributed with the same mean (if the simulation is ergodic). Then, the expected quotient y_S should be normal distributed. In particular, $\langle y_S\rangle = 0$, $\langle y_S^2\rangle = 1$ and $\langle y_S^4\rangle = 3$. We can check if this is the case or not.

We start by studying if the mean of these y_S values is indeed 0 for all S-points. With this aim we perform a χ^2 test to check this assumption. We present in the first columns of Table E.1, the χ^2 per degrees of freedom (dof), obtained as,

$$\chi^2 = \sum_{i=1}^{N_S} y_S^2, \tag{E.4}$$

with N_S degrees of freedom (dof in the Table). As usually, if data y_S are indeed normally distributed, χ^2/dof should be close to 1. In addition, we compute the probability of obtaining (for a set of N_S perfect normal distributed variables) a higher value of χ^2/dof than χ_0^2 (the value quoted in the table). We refer to this probability as Q, and it is defined as

$$\begin{aligned} Q &= p(\chi^2 > \chi_0^2) = \tfrac{1}{\Gamma(N_S/2)} \textstyle\int_{\sum_i y_i^2 > \chi_0^2} \prod_j \mathrm{d}y_j \, \mathrm{e}^{-\frac{1}{2}\sum_j y_j^2} = \\ &= \frac{1}{\Gamma\left(N_S/2\right)} \int_{\chi_0^2/2}^{\infty} \mathrm{e}^{-u} u^{N_S-1} \mathrm{d}u, \end{aligned} \tag{E.5}$$

where Γ is the Euler gamma-function.

N	χ^2/dof	Q	$y^{\min}$	$y^{\max}$	$p(y^{\min}, y^{\max})$	$N^{1\sigma}$	$N^{2\sigma}$	$N^{3\sigma}$	$N^{>3\sigma}$
108	48.09/41	0.21	-2.88	2.49	0.71	25(28.0)	39(39.1)	41(40.9)	0(0.1)
256	42.40/41	0.41	-2.42	2.37	0.50	29(28.0)	37(39.1)	41(40.9)	0(0.1)
500	47.85/41	0.21	-2.79	1.95	0.31	27(28.0)	39(39.1)	41(40.9)	0(0.1)
864	57.84/41	0.04	-2.84	2.94	0.85	27(28.0)	38(39.1)	41(40.9)	0(0.1)
1372	37.62/41	0.6	-2.77	1.56	0.07	29(28.0)	40(39.1)	41(40.9)	0(0.1)
2048	85.77/81	0.34	-2.66	2.28	0.29	53(55.3)	77(77.3)	81(80.8)	0(0.2)
2916	97.25/81	0.11	-1.53	6.24	0.01	65(55.3)	78(77.3)	80(80.8)	1(0.2)

TABLE E.1: Study of the distribution function of y_S.

The $N = 2916$ data is presented separately because the integrated correlation times (plotted in Figure E.2) cast some doubts about its thermalization. The data for $N = 4000$ is not included in this study, since from direct visualization we can see it is not thermalized (see Figure E.3 below).

One naive approach to the numbers shown in Table E.1 might lead to a wrong feeling about the compatibility of mean values for $N \leq 2048$. But this idea does not survive a deeper inspection. Indeed, in statistics the rare events (in the sense that they have low probability to occur) must appear, one must worry about them if they happen too often. Let us discuss the worst χ^2 test case (anagously for the other cases). For $N = 864$ we get a very low value Q, in fact, there is only a 4% probability of getting a worst test. However, one must recall that we computed 7 values of χ^2 here. Thus, the probability for the lowest Q being 4% or smaller, becomes as large as 25%. This is equivalent to say that if we performed this very same study 4 times, such a bad result should be expected to occur at least once. Because of that, we are not concerned by the thermalization of the system of $N = 864$. Besides, this "bad" result was obtained for a middle-sized system, in a region of N where we can be confident about having a many exponential times in the simulation.

However, if we are not confident enough, the χ^2 test is not the only check we can perform about the normality of the data. If the y_S are indeed normal distributed, we can compute the theoretical probability that all the y_S points lied in the interval in between the minimum and the maximum y_S obtained for each N, i.e.

$$p(y_{\min} < y_i < y_{\max}) = \left[\frac{1}{\sqrt{2\pi}} \int_{y_{\min}}^{y_{\max}} \mathrm{e}^{-y^2/2} \mathrm{d}y \right]^{N_S} . \tag{E.6}$$

We present these values also in Table E.1, in the second block of columns.

Finally, we also can compute the number of y_S values we got separated from the zero mean value by less than one, two and three mean deviations, as well as the number of data we got beyond 3 sigmas. We can compare these numbers with the theoretical predictions of a normal distribution computed as (E.6) (see third block of columns in Table E.1, numbers in between parenthesis represent the theoretical predictions).

As a summary of all the numbers presented in this table, we can conclude that fluctuations in y_S seem to be completely Gaussian for $N \leq 2048$, the two starting

N	p_{co}^{FCC}	p_{co}^{fluid}	$(p_{co}^{FCC} - p_{co}^{ran})$/error
108	10.9222(22)	10.9206(26)	0.4828
256	11.2192(16)	11.2225(18)	-1.4081
500	11.3628(13)	11.3589(15)	2.0350
864	11.4399(13)	11.4429(18)	-1.3450
1372	11.4910(16)	11.4886(16)	1.0530
2048	11.5151(12)	11.5143(14)	0.4228
2916	11.5267(12)	11.5329(19)	-2.7624

TABLE E.2: Comparison between the p_{co}^{N} estimations for simulations starting from a random distribution or a FCC perfect lattice.

points seem to lead to same mean results, which make us feel confident about the correct thermalization of our samples. In addition, concerning the case of $N = 2916$, all results shown in the table seem reasonable but the $\boldsymbol{\nabla}_S\Omega_N$ point where the prediction for the random start and the ordered start differed by $y_S = 6.26$ (we know there is only one point with $|y_S| > 3$). This fact makes us feel confident about that the problem in thermalization of $N = 2916$ is restricted a single S value.

A different check regards the computation of p_{co}^{N}. Indeed, we can check that its determination does not depend on the initial configuration. We compute the difference between the two estimations of p_{co}^{N} and divide this number by its error (see Table E.2). The differences between the two estimations are very reasonable, but for the $N = 2916$ point, where it is far too large. We will devote next section to the study of this problem.

Finally, the reader might have noticed that, although both kind of simulations have exactly the same length, the errors of p_{co} in Table E.2 are systematically larger when the simulation started from a fluid configuration. This fact stems from the maximum change in volume, δv, allowed for the Metropolis test. Indeed, quite annoyingly, this δv depended on the kind of start we were considering since it was assotiated to the initial density in the computer program.[2]

E.3

$N = 2916$ and $N = 4000$ particle systems

The anomaly at $S = 0.4$ for $N = 2916$ in Figure E.2 is due to the emergence of a metastability. At this point, we expected to find a spatially segregated state (a slab of FCC crystal in a liquid matrix). This state appeared indeed, but the simulation tunnels back and forth from it to an helicoidal crystal (a similar crystal to the one

[2]Technically, the random configuration was obtained in a larger simulation box (very low density), in order to minimize the number of particles whose radius supperposed after proposing random positions for each particle. With such a density, the FCC lattice would melt instantaneously, thus running the simulations from the fluid phase as well.

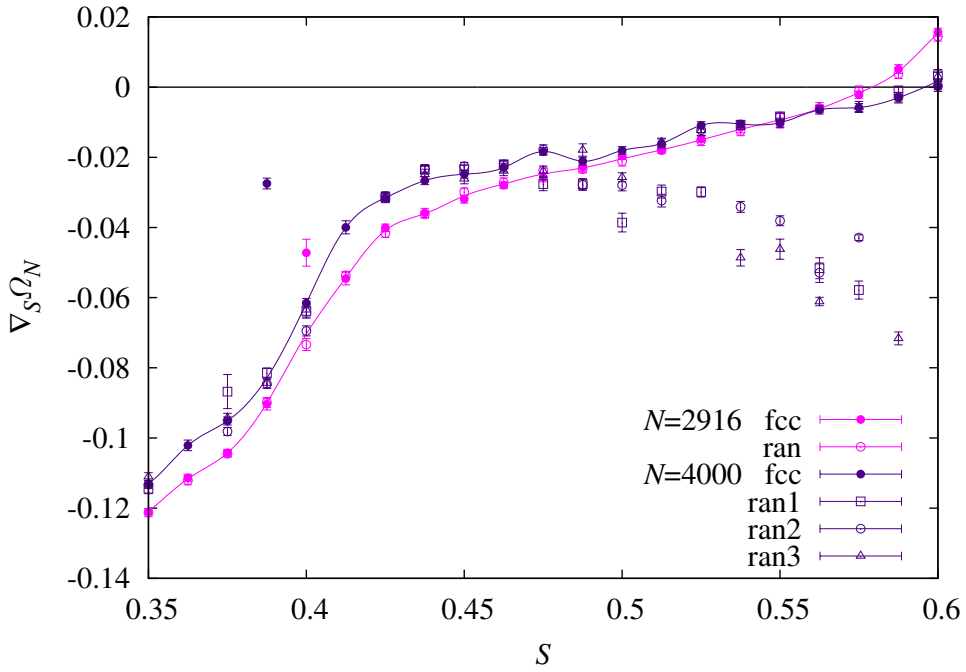

FIGURE E.3: Enlarged central part of the spinodal curve for the two biggest system sizes, $N = 2916$ and 4000.

illustrated in Fig. 8.3–right, when we tethered only Q_6).

We show in Fig. E.3 both $\nabla_S \Omega_N$ for the two independent runs in $N = 2916$ and in $N = 4000$ particles. From the figure, it is clear that these helicoidal crystals appear much more often for $N = 4000$ and intermediate S. Nevertheless, selecting carefully the starting particle configuration for the simulation at each S, one may obtain a gradient field with a smooth S-dependency (represented in a solid line in Fig. E.3). However, it is clear that these $N = 4000$ results, although plausible, cannot be regarded as well equilibrated. For this reason, although we presented results in the Tables all over the Chapter 8, we did it just as a hint, in the sense that these values are not used for any large-N extrapolation.

The situation is more subtle for $N = 2916$ particles, because the metastabilities are only observed at $S = 0.4$. At this point, both runs find a solid-fluid mixed state, as happens at nearby points. However, for the simulation starting from a FCC we find a metastability of this mixed state with an helicoidal crystal, with significantly higher Q_6 and C. Although we extended the lenght of this random-start run, this crystal was never found. In order to check how important this new phase was, we ran some extra new independent simulations (from both kind of startings) at this point but no one but the original FCC-starting one visited this phase. In other words, this phase seemed to be very rare. However, even being rare, we cannot be suer about its statistical weight, it could be the most stable phase at this point. With the aim of refusing this hypothesis, we also ran some new simulations starting from one of the configurations corresponding to this phase (using different random numbers). In all the cases, all the runs "fell-back" after some time to the mixed state

Percentage	$p_{\rm co}^N$	γ_{100}^N
$p_{0\%}$	11.5314(10)	0.5972(10)
$p_{10\%}$	11.5311(9)	0.5971(10)
$p_{20\%}$	11.5305(9)	0.5968(10)
$p_{50\%}$	11.5292(10)	0.5963(10)
$p_{100\%}$	11.5283(11)	0.5959(11)

TABLE E.3: Comparison between the $p_{\rm co}^N$ and γ_{100} between the three different ways of mixing the conflicting point.

found in the rest of runs.

Now, after being sure that this helicoidal crystal is not the most stable state, we can try to delimit its probability of appearance, and mix the data for $\boldsymbol{\nabla}\Omega_N$ coming from the different runs, according to their relative probability, to obtain the equilibrium estimate. This we can do it using the detailed balance condition. Indeed, if we have two states i and j,

$$W_{j\to i}\; p_j = W_{i\to j}\; p_i \tag{E.7}$$

where $W_{i\to j}$ is the probability of hopping from state i to state j, and p_i the probability of being at state i. That means that one can compute the relative probability between these two phases by computing the flip-flop probabilities. With this idea, and our numerous simultions with jumps in both directions, we could estimate that the probability of the helicoidal phase was upperbounded by 10%. Our number of runs is limited, thus, in order to not understimate this phase we also include an error in the determination of the probability of roughly 10%, which we know for sure that is an upper-estimation.

We now mix the values of $\boldsymbol{\nabla}\Omega_N$ obtained in each of the two phases accordingly to their relative probability. Afterwards, we obtain $p_{\rm co}$ following the same procedure all over the Chapter 8.

In Table E.2 we obtained incompatible values for $p_{\rm co}$ obtained with the different runs. Now, mixing the data of both simulations only at $S = 0.4$, we see that the origin of this divergence was nothing but this described metastability. In order to justify this statement, we mix the data at $S = 0.4$ for $\boldsymbol{\nabla}\Omega_N$ from the two phases using different relative probabilities. For the rest of the points we mix the data in the same way done all over the Chapter, that is $50\% - 50\%$ from the two starts's simulations. After obtaining the whole $\boldsymbol{\nabla}\Omega_N(S)$ curve with this procedure, we can compute $p_{\rm co}$. We display these $p_{\rm co}$ values in Table E.3. Clearly, the differences found in Table E.2 are a direct consecuence of the lack of thermalization in $S = 0.4$.

Finally, the estimations of $p_{\rm co}^{(2916)}$ quoted in Table 8.2 and $\gamma_{\{100\}}^{(2916)}$ in Table 8.5 are obtained with a relative mixture of 10% helicoidal crystal at $S = 0.4$. In addition, the error is taken as the sum of each inner statistical error plus a systematic error coming from our uncertainty in the determination of the probability of the helicoidal crystal. We consider this error as the difference between $p_{10\%}$ and $p_{20\%}$.

APPENDIX F

C values in a perfect lattice

At variance with Q_6, it is very easy to obtain the C (defined in (8.5)) for a perfect lattice. We compute here the predictions for the two phases of interest, namely the FCC and the BCC.

F.1

FCC

We consider a perfect FCC lattice. In it, each particle $\boldsymbol{r}_0$ has twelve possible nearest-neighbors at positions $\boldsymbol{r}_i$. In units of the characteristic length of the lattice, the 12 neighbors are placed at

$$\begin{gathered}(\boldsymbol{r}_i-\boldsymbol{r}_0)=\left(0,\frac{1}{2},\pm\frac{1}{2}\right),\left(0,-\frac{1}{2},\pm\frac{1}{2}\right),\left(\frac{1}{2},0,\pm\frac{1}{2}\right),\\ \left(-\frac{1}{2},0,\pm\frac{1}{2}\right),\left(\frac{1}{2},\pm\frac{1}{2},0\right),\left(-\frac{1}{2},\pm\frac{1}{2},0\right).\end{gathered} \tag{F.1}$$

Then, plugging these positions in the definition of $c_\alpha(\boldsymbol{r})$ given in (8.6), we obtain for all of them,

$$c_\alpha(\boldsymbol{r})=\frac{1}{(1/\sqrt{2})^8}\frac{1}{2^4}\frac{1}{2^4}=\frac{1}{16}. \tag{F.2}$$

As mentioned, $N_b=12$ for all particles. Then,

$$C=\frac{2288}{79}\frac{1}{16}-\frac{64}{79}=1. \tag{F.3}$$

F.2

BCC

We perform the same calculation for the BCC structure. In this case all particles have 8 nearest neighbors, located at

$$(\boldsymbol{r}_i - \boldsymbol{r}_0) = \left(\pm\frac{1}{2}, \pm\frac{1}{2}, \pm\frac{1}{2}\right). \tag{F.4}$$

Then $r = \sqrt{3}/2$ in all the cases, and

$$c_\alpha(\boldsymbol{r}) = 3\frac{1}{2^8}\left(1 - \frac{1}{9}\right) \Big/ \frac{3^4}{2^8} = \frac{2^3}{5^5}. \tag{F.5}$$

We introduce this result in (8.5),

$$C = \frac{2288}{79}\frac{2^3}{5^5} - \frac{64}{79} = 0.143\cdots. \tag{F.6}$$

This last result is the one reported in [AU10]. However, in Section 8.4, we discussed the notion of nearest neighbor for our systems. We did it terms of the FCC radius only. Indeed, we wanted a definition that could guaratee that we only counted the first shell of neighbors in this case, no matter the total volume of our simulation box. It turns out, that the actual definition reaches the second shell of neighbors in the case of a perfect BCC. Then, we need to include 6 extra neighbors in the calculus, placed at

$$(\boldsymbol{r}_i - \boldsymbol{r}_0) = (\pm 1, 0, 0), (0, \pm 1, 0), (0, 0, \pm 1). \tag{F.7}$$

It turns out that $c_\alpha(\boldsymbol{r})$ is zero for all these vectors, but still we need to average over all the neighbors

$$\frac{\sum_{i=1}^{N}\sum_{j=1}^{N_b(i)} c_\alpha(\hat{\boldsymbol{r}}_{ij})}{\sum_{i=1}^{N} N_b(i)} = \frac{6\cdot 0 + 8\cdot\frac{8}{3^5}}{8+6} = \frac{2^5}{3^5\cdot 7}, \tag{F.8}$$

which results in the final value

$$C = -0.2657\cdots. \tag{F.9}$$

APPENDIX G

Analysis with the Suzuki-Trotter formula

We investigate the properties of $\hat{H}(s,\lambda)$, defined in (9.7), the phase diagram in particular, using the decomposition formula [Suz76] and the static approximation. This approach, although quantum, leads to the same results as the semi-classical method described in section 9.3. The method here is analogous to the one explained in detail in [Sek12, Jör10a], but we leave the power k as a free parameter in all the calculus. The purpose of this appendix is to confirm consistency between the method of the main text and that in [Sek12, Jör10a].

The starting point is the partition function,

$$Z = \mathrm{Tr} e^{-\beta \hat{H}(s,\lambda)}. \tag{G.1}$$

We use the decomposition formula to express it as

$$\begin{aligned} Z &= \lim_{M\to\infty} Z_M \equiv \lim_{M\to\infty} \mathrm{Tr}\left\{ e^{-\frac{\beta}{M} s\lambda \hat{H}_0} e^{-\frac{\beta}{M}\left[s(1-\lambda)\hat{V}_{\mathrm{AFF}} + (1-s)\hat{V}_{\mathrm{TF}}\right]} \right\}^M \\ &= \lim_{M\to\infty} \sum_{\{\sigma^z\}} \langle\{\sigma^z\}| \left\{ \exp\left[\frac{\beta s\lambda N}{M} \left(\frac{1}{N}\sum_{i=1}^{N} \hat{\sigma}_i^z \right)^p \right] \right. \\ &\quad \left. \times \exp\left[-\frac{\beta s(1-\lambda)N}{M} \left(\frac{1}{N}\sum_{i=1}^{N} \hat{\sigma}_i^x \right)^k + \frac{\beta(1-s)}{M} \sum_{i=1}^{N} \hat{\sigma}_i^x \right] \right\}^M |\{\sigma^z\}\rangle, \end{aligned} \tag{G.2}$$

where $\sum_{\{\sigma^z\}}$ refers to the summation over all the 2^N possible spin configurations in the z basis, and $|\{\sigma^z\}\rangle \equiv \otimes_{i=1}^{N} |\sigma_i^z\rangle$.

We introduce M closure relations, each one labeled by $\alpha (= 1, \ldots, M)$,

$$\hat{\mathbb{I}}(\alpha) \equiv \sum_{\{\sigma^z(\alpha)\}} |\{\sigma^z(\alpha)\}\rangle \langle\{\sigma^z(\alpha)\}| \times \sum_{\{\sigma^x(\alpha)\}} |\{\sigma^x(\alpha)\}\rangle \langle\{\sigma^x(\alpha)\}|, \tag{G.3}$$

just before the αth exponential operator involving $\hat{\sigma}_i^x$ in (G.2). The trace over the product of quantum operators is thus reduced to the product of numbers that commute and can be reordered,

$$\begin{aligned} Z_M &= \prod_{\alpha=1}^{M} \sum_{\{\sigma^z(\alpha)\}} \sum_{\{\sigma^x(\alpha)\}} \exp\left[\frac{\beta s \lambda N}{M}\left(\frac{1}{N}\sum_{i=1}^{N}\sigma_i^z(\alpha)\right)^p\right] \\ &\quad \times \exp\left[-\frac{\beta s(1-\lambda)N}{M}\left(\frac{1}{N}\sum_{i=1}^{N}\sigma_i^x(\alpha)\right)^k + \frac{\beta(1-s)}{M}\sum_{i=1}^{N}\sigma_i^x(\alpha)\right] \\ &\quad \times \prod_{i=1}^{N} \langle \sigma_i^z(\alpha) \,|\sigma_i^x(\alpha)\rangle \langle \sigma_i^x(\alpha) \,|\sigma_i^z(\alpha+1)\rangle\,, \end{aligned} \tag{G.4}$$

where $|\sigma_i^z(M+1)\rangle \equiv |\sigma_i^z(1)\rangle$.

We write the product in terms of the total x and z magnetizations in each copy of the system, i.e. $m^x(\alpha) \equiv \frac{1}{N}\sum_{i=1}^{N}\sigma_i^x(\alpha)$ and $m^z(\alpha) \equiv \frac{1}{N}\sum_{i=1}^{N}\sigma_i^z(\alpha)$, using the integral definition of the delta distribution

$$f\left(\frac{1}{N}\sum_{i=1}^{N}\sigma_i(\alpha)\right) = \int \mathrm{d}m\, \delta\left(m(\alpha) - \frac{1}{N}\sum_{i=1}^{N}\sigma_i(\alpha)\right) f\left(m(\alpha)\right). \tag{G.5}$$

After a few simplifications, we introduce the static approximation to remove the α dependence of the magnetizations. Under this approximation, we can compute the $M \to \infty$ limit using again the decomposition formula. The partition function (G.1) then reduces to

$$Z = \int \mathrm{d}m^z\, \mathrm{d}m^x\, \exp\left[-N\beta\, f(\beta, s, \lambda; m^z, m^x)\right], \tag{G.6}$$

where $f(\beta, s, \lambda; m^z, m^x)$ is the pseudo free-energy defined as follows:

$$\begin{aligned} f(\beta, s, \lambda; m^z, m^x) &= (p-1)\, s\, \lambda (m^z)^p - (k-1)\, s\, (1-\lambda)(m^x)^k \\ -\frac{1}{\beta}\log\left\{2\cosh\beta\sqrt{\left[p\, s\, \lambda\, (m^z)^{p-1}\right]^2 + \left[1-s-s\,(1-\lambda)\,k\,(m^x)^{k-1}\right]^2}\right\}. \end{aligned} \tag{G.7}$$

Again, one can apply the saddle-point method, obtaining two self-consistent equations for the two magnetizations,

$$\begin{aligned} m^z &= \frac{p\, s\, \lambda\, (m^z)^{p-1}}{\sqrt{\left[p\, s\, \lambda\, (m^z)^{p-1}\right]^2 + \left[1-s-s\,(1-\lambda)\,k\,(m^x)^{k-1}\right]^2}} \\ &\quad \times \tanh\beta\sqrt{\left[p\, s\, \lambda\, (m^z)^{p-1}\right]^2 + \left[1-s-s\,(1-\lambda)\,k\,(m^x)^{k-1}\right]^2}, \end{aligned} \tag{G.8}$$

$$\begin{aligned} m^x &= \frac{1-s-s\,(1-\lambda)\,k\,(m^x)^{k-1}}{\sqrt{\left[p\, s\, \lambda\, (m^z)^{p-1}\right]^2 + \left[1-s-s\,(1-\lambda)\,k\,(m^x)^{k-1}\right]^2}} \\ &\quad \times \tanh\beta\sqrt{\left[p\, s\, \lambda\, (m^z)^{p-1}\right]^2 + \left[1-s-s\,(1-\lambda)\,k\,(m^x)^{k-1}\right]^2}. \end{aligned} \tag{G.9}$$

In this work we are only interested in the purely quantum transitions, not in the thermodynamical ones. For this reason, and with the sake of simplification, we remove the dependence of physical quantities on β from now on by considering the low-temperature limit, $\beta \to \infty$. In this limit, if $\left[p\,s\,\lambda\,(m^z)^{p-1}\right]^2 + \left[1-s+s\,(1-\lambda)\,k\,(m^x)^{k-1}\right]^2 \neq 0$, the hyperbolic tangent in (G.8) and (G.9) tends to unity, and thus the self consistent equations simplify

$$m^z = \frac{p\,s\,\lambda\,(m^z)^{p-1}}{\sqrt{\left[p\,s\,\lambda\,(m^z)^{p-1}\right]^2 + \left[1-s-s\,(1-\lambda)\,k\,(m^x)^{k-1}\right]^2}}, \tag{G.10}$$

$$m^x = \frac{1-s-s\,(1-\lambda)\,k\,(m^x)^{k-1}}{\sqrt{\left[p\,s\,\lambda\,(m^z)^{p-1}\right]^2 + \left[1-s-s\,(1-\lambda)\,k\,(m^x)^{k-1}\right]^2}}. \tag{G.11}$$

The magnetization lies on the unit radius circumference, i.e. $(m^x)^2 + (m^z)^2 = 1$. This result agrees with the approach in section 9.3, where the magnetization was a unit vector constrained to the XZ plane. The pseudo free energy (G.7) becomes

$$f(\beta, s, \lambda; m^z, m^x) = (p-1)\,s\,\lambda (m^z)^p - (k-1)\,s\,(1-\lambda)(m^x)^k - \sqrt{\left[p\,s\,\lambda\,(m^z)^{p-1}\right]^2 + \left[1-s-s\,(1-\lambda)\,k\,(m^x)^{k-1}\right]^2}. \tag{G.12}$$

Equations (G.10) and (G.11) have ferromagnetic (F) solutions with $m^z > 0$ and quantum paramagnetic (QP) ones satisfying $m^z = 0$ and $m^x \neq 0$. Let us begin with the latter case.

G.1

Paramagnetic solutions

Substituting $m^z = 0$ in (G.11), we get

$$m^x = \frac{1-s-k\,s\,(1-\lambda)(m^x)^{k-1}}{|1-s-k\,s\,(1-\lambda)(m^x)^{k-1}|}, \tag{G.13}$$

which leads to $m^x = \pm 1$. The solution $m^x = -1$ is obtained if the numerator in (G.13) is negative, that is, if $1-s-k\,s\,(1-\lambda)(-1)^{k-1} < 0$, which, in the range of parameters $0 \leq s \leq 1$ and $0 \leq \lambda \leq 1$ considered, can only be satisfied if k is odd and in the region $1/[1+k(1-\lambda)] < s \leq 1$. This phase is precisely the QM^- phase discussed in the text. Its free energy is

$$f_{\mathrm{QP}^-}(s, \lambda) = 1 - 2s + s\lambda, \tag{G.14}$$

which coincides with equation (9.15).

The other quantum paramagnetic solution with $m^x = +1$ (the QP^+ phase) can be satisfied only if the numerator is positive, i.e. if $1-s-k\,s\,(1-\lambda) \geq 0$, which can

be fulfilled for any value of k as long as s lies in the region $0 \leq s \leq 1/[1+k(1-\lambda)]$. The free energy of this phase is

$$f_{\mathrm{QP}^+}(s,\lambda) = -1 + 2s - s\lambda, \tag{G.15}$$

and is also equal to (9.14).

There is still one additional paramagnetic solution. In order to obtain it, we need to come back to the discussion about the $\beta \to \infty$ limit. The hyperbolic tangent in (G.8) and (G.9) could tend to a finite value in the $\beta \to \infty$ limit, as long as the term in the square root vanishes. Mathematically,[1]

$$\lim_{\beta\to\infty} \tanh\beta\sqrt{\left[p\,s\,\lambda\,(m^z)^{p-1}\right]^2 + \left[1-s-s\,(1-\lambda)\,k\,(m^x)^{k-1}\right]^2} = \tanh c, \tag{G.16}$$

when

$$m^z \to 0, \quad m^x \to \left[\frac{1-s}{k\,s\,(1-\lambda)}\right]^{\frac{1}{k-1}}. \tag{G.17}$$

In order to find a non-trivial solution, it is also necessary in this limit that m^z tends to zero faster than the bracketed term of m^x in (G.9), i.e.

$$\frac{p\,s\,\lambda(m^z)^{p-1}}{1-s-k\,s\,(1-\lambda)(m^x)^{k-1}} \to 0. \tag{G.18}$$

Under these assumptions, (G.8) and (G.9) imply $m^z = 0$ and $m^x = \tanh c$, where $\tanh c = [(1-s)/k\,s\,(1-\lambda)]^{\frac{1}{k-1}}$, in order to be consistent with the limit (G.17). This correspondence determines the region in the space where this phase can appear. In fact, as any hyperbolic tangent, $|\tanh c| \leq 1$, which is true only if $1/[1+k\,(1-\lambda)] \leq s \leq 1$. Besides, the condition (G.18) forces $p > 3$.[2]

Since the magnetization in the z direction vanishes, we call this phase QP2. The free energy is obtained with (G.7),

$$f_{\mathrm{QP2}}(s,\lambda) = -\frac{k-1}{k}\left[\frac{1-s}{k\,s\,(1-\lambda)}\right]^{\frac{1}{k-1}}(1-s). \tag{G.19}$$

This last phase was not predicted by the semi classical approach. However, we will see below that it is irrelevant to the problem, since the F′ phase has always a smaller value of the free energy.

[1] In the k-odd case, the limit

$$m^z \to 0,\ m^x \to -\left[\frac{1-s}{k\,s\,(1-\lambda)}\right]^{\frac{1}{k-1}}$$

also makes the square root in (G.16) vanish, but it leads to a positive free energy in (G.19), and thus it is not relevant.

[2] Indeed, using $(m^x)^2 + (m^z)^2 = \tanh^2 c = [(1-s)/k\,s\,(1-\lambda)]^{\frac{2}{k-1}}$ and computing the limit (G.17) when $m^x \to \tanh c$, one can check that it vanishes only as long as $p > 3$.

G.2

Ferromagnetic solutions

We next consider the possible solutions with $m^z > 0$.[3] As before, the ferromagnetic solutions cannot be computed explicitly for a given value of p but for certain limiting cases.

The solution $m^z = 1$ (and $m^x = 0$) is exact only on the line $s = 1$. However, we can see that an approximate solution $m^z \approx 1$ and $m^x \approx 0$ is valid in a wider space of parameters. Indeed, the solution

$$m^x = \frac{1-s}{s\,p\,\lambda}, \quad \text{and} \quad m^z = \sqrt{1-\left(\frac{1-s}{s\,p\,\lambda}\right)^2} \tag{G.20}$$

fulfills (G.10) and (G.11) when $(1-s)/p\,s\,\lambda \to 0$. This is the F phase we obtained before in equation (9.30). The free energy is obtained plugging these values into equation (G.12). For the $p \to \infty$ limit,

$$f_{\mathrm{F}}(s,\lambda)|_{p\to\infty} = -s\lambda. \tag{G.21}$$

We consider an alternative solution for $0 < m^z < 1$. With this aim, we rewrite (G.10) in the following way

$$\left[(m^z)^2 - 1\right]\left[p\,s\,\lambda (m^z)^{p-1}\right]^2 + \left\{m^z\left[1 - s - s(1-\lambda)k(m^x)^{k-1}\right]\right\}^2 = 0. \tag{G.22}$$

In the $p \to \infty$ limit, $p(m^z)^{p-1} \to 0$, and

$$m^x = \left[\frac{1-s}{k\,s\,(1-\lambda)}\right]^{\frac{1}{k-1}} \quad m^z = \sqrt{1-\left[\frac{1-s}{k\,s\,(1-\lambda)}\right]^{\frac{2}{k-1}}} \tag{G.23}$$

is an exact solution to (G.22), and similarly of (G.11), as long as $(1-s)/k\,s\,(1-\lambda) < s \leq 1$, or $1/[1+k\,(1-\lambda)] < s < 1$.[4] This is precisely the F′ phase discussed in section 9.3. Again, we compute the free energy by plugging the solution (G.23) in (G.12) and taking the $p \to \infty$ limit

$$f_{\mathrm{F}'}(s,\lambda)|_{p\to\infty} = -\frac{k-1}{k}\left[\frac{1-s}{k\,s\,(1-\lambda)}\right]^{\frac{1}{k-1}}(1-s), \tag{G.24}$$

which is exactly equal to the one obtained for the QP2 phase (G.19).

The solution (G.23) is also a good approximate solution for p finite (but $p > 3$) when $(m^z)^p \to 0$. The free energy for this phase is

$$f_{\mathrm{F}'}(s,\lambda) \approx -s\,\lambda\left[1-\left(\frac{1-s}{s\,k\,(1-\lambda)}\right)^{\frac{2}{k-1}}\right]^p - \frac{k-1}{k}\left[\frac{1-s}{k\,s\,(1-\lambda)}\right]^{\frac{1}{k-1}}(1-s), \tag{G.25}$$

[3] No negative value for m^z can satisfy (G.10) for odd values of p.

[4] Again, the negative solution for m^x is also a valid solution in the odd k case but has a higher free energy than (G.23) due to the change of sign in the $(m^x)^k$ term in (G.12).

which, for finite p, is always smaller than f_{QP2}. According to this observation, except for the $p \to \infty$ limit, the F′ phase is always stabler than the QP2 phase.

We have therefore reproduced the results of section 9.3 by a completely different method. The present method is nevertheless better suited for generalizations to more complicate problems where the target Hamiltonian $\hat{H}_0$ cannot be expressed in terms of simple total spins.

APPENDIX H

Ground state of $\hat{V}_k$ and its overlap with the ground state of $\hat{H}_0$

In this Appendix, we derive the properties of the ground state of $\hat{V}_k$, defined in (9.6), for k even. Let us first consider the case with N even. The ground state of $\hat{H}_0$, $|\phi_0\rangle = \otimes_{i=1}^{N} |\uparrow\rangle_i^z$, can be expressed as

$$\begin{aligned} |\phi_0\rangle &= \otimes_{i=1}^{N} \left(|\uparrow\rangle_i^x + |\downarrow\rangle_i^x \right)/\sqrt{2} \\ &= \frac{1}{2^{N/2}} \Big(|\uparrow\rangle_1^x |\uparrow\rangle_2^x \cdots |\uparrow\rangle_N^x + |\uparrow\rangle_1^x |\uparrow\rangle_2^x \cdots |\uparrow\rangle_{N-1}^x |\downarrow\rangle_N^x \\ &\quad + \cdots + |\downarrow\rangle_1^x |\downarrow\rangle_2^x \cdots |\downarrow\rangle_N^x \Big). \end{aligned} \tag{H.1}$$

This last expression has 2^N terms, in which the partial sum of terms with a half of the sites having $|\uparrow\rangle_i^x$ and the other half $|\downarrow\rangle_i^x$ is nothing but the ground state of $\hat{V}_k$ in the $S = N/2$ sector $|\phi_k\rangle$, up to a normalization,

$$\begin{aligned} |\phi_k\rangle &= a \Big(|\uparrow\rangle_1^x |\uparrow\rangle_2^x \cdots |\uparrow\rangle_{N/2}^x |\downarrow\rangle_{N/2+1}^x \cdots |\downarrow\rangle_N^x \\ &\quad + \cdots + |\downarrow\rangle_1^x |\downarrow\rangle_2^x \cdots |\downarrow\rangle_{N/2}^x |\uparrow\rangle_{N/2+1}^x \cdots |\uparrow\rangle_N^x \Big). \end{aligned} \tag{H.2}$$

It is easy to check from the number of terms in the above equation that the normalization condition is $a^2 \binom{N}{N/2} = 1$. We thus have

$$\langle \phi_0 | \phi_k \rangle = \frac{a}{2^{N/2}} \binom{N}{N/2} = \frac{1}{2^{N/2}} \sqrt{\binom{N}{N/2}}. \tag{H.3}$$

For large N,

$$\log |\langle \phi_0 | \phi_k \rangle|^2 = \log \left[2^{-N} \frac{N!}{\left(\frac{N}{2}!\right)^2} \right] \approx -\frac{1}{2} \log N + \log \sqrt{\frac{2}{\pi}}, \tag{H.4}$$

which means that the overlap decreases only polynomically with N as $\sim N^{-1/2}$.

The case of odd N can be analyzed similarly but in this case $\binom{N}{N/2}$ is replaced by $\binom{N}{(N+1)/2}$ or $\binom{N}{(N-1)/2}$.

APPENDIX I

Resumen de la tesis en castellano

I.1

Introducción General

La física ha avanzado durante siglos gracias a la estrategia de "divide y vencerás": separar el sistema total en muchas pequeñas partes e inferir el comportamiento global a partir del de ellas. Sin embargo en la naturaleza hay muchos sistemas que, bien porque sus constituyentes están fuertemente correlacionados, o porque son muy complejos, no pueden explicarse a partir de la suma de sus partes. De hecho, hay muchos comportamientos que son puramente colectivos, como los terremotos, las redes neuronales, el plegamiento de proteínas, la turbulencia, los vidrios...

La investigación en este tipo de problemas ha sufrido un impulso radical con la aparición y desarrollo de los ordenadores. De hecho, ha sido gracias a las simulaciones numéricas cuando por primera vez se ha podido tanto reproducir el comportamiento colectivo de sistemas relativamente grandes, como predecir el efecto de tipos complicados de interacción o de desorden en el sistema. Además, los ordenadores también han traído consigo la posibilidad de analizar enormes cantidades de datos, no sólo de simulaciones, sino también de experimentos. Por esta razón, los sistemas complejos se han convertido en los últimos años en un campo de investigación por sí mismo, pero un campo pluridisciplinar compartido por físicos, matemáticos, biólogos...

La mecánica estadística tradicional trata el problema de explicar el estado de equilibrio de un sistema compuesto por un gran número de partículas. En esta teoría se asume que, de forma efectiva, los comportamientos caóticos de cada uno de los componentes del conjunto, se anulan entre sí en el equilibrio, conduciendo a un estado global extremadamente simple. Sin embargo, ¿qué ocurre si la evolución es tan lenta que el régimen relevante para un experimento es el de fuera del equilibrio? En este caso, las nociones tradicionales de termodinámica fallan y aparecen toda una colección de comportamientos nuevos y sorprendentes. Los parámetros

de control habituales, tal como la temperatura o la presión, dejan de describir el sistema por ellos mismos. De hecho, no sólo hace falta contabilizar el tiempo durante el que transcurre un experimento, sino que también necesitamos conocer la edad del sistema en su fase "complicada". La evolución del sistema está condicionada por toda su historia anterior, lo que tiene consecuencias bastante llamativas: un objeto material (un vidrio de espín, por ejemplo) envejece, rejuvenece o incluso tiene memoria. Además reacciona drásticamente a cambios minúsculos de ciertas condiciones externas, fenómeno conocido como caos (véase el Capítulo 5 de esta tesis).

Llegado este punto, el estudio de estos materiales podría parecer inabordable, pues todo es nuevo. Sin embargo, este tipo de materiales presentan cierta ventaja: el comportamiento colectivo de estos "sistemas complejos" parece satisfacer cierta universalidad. De hecho, las mismas recetas sirven por igual para sistemas radicalmente distintos, sin importar las características individuales de los componentes que los conforman. La física que acabamos de describir se comprende mejor si pensamos en ejemplos concretos.

Un ejemplo cotidiano de sistema complejo es el vidrio. Macroscópicamente se comporta como un sólido, mientras que microscópicamente parece un líquido. Como estos últimos, no presenta ningún tipo de orden de largo alcance. Sin embargo, sus partículas están tan juntas entre sí que no pueden moverse, lo que resulta en un flujo de materia neto extremadamente pequeño. Los vidrios se obtienen habitualmente enfriando muy rápidamente fluidos que, de hacerlo lentamente, formarían cristales. Es sorprendente que, incluso después de miles de años fabricando y manipulando vidrios, no entendamos bien la naturaleza de esta fase. De hecho, responder a la pregunta de si la transición vítrea es una transición real o no, es uno de los principales problemas de la física del estado sólido. La fase vítrea se caracteriza por una enorme viscosidad que crece dramáticamente al disminuir la temperatura. Con el aumento de la viscosidad, las partículas se quedan sin espacio para desplazarse, y como consecuencia, los tiempos característicos de difusión se disparan. El sistema pasa a evolucionar tan lentamente en torno a la transición (definida dinámicamente como el punto en el cual la viscosidad alcanza los 10^{13} poises) que debemos considerar estos materiales como permanentemente fuera del equilibrio.

Sin embargo, este comportamiento tan lento de las variables dinámicas de un sistema no aparece sólo en las posiciones de las partículas que forman estos vidrios cotidianos (nos referiremos a ellos como estructurales). De hecho, algunas aleaciones magnéticas (conocidas como vidrios de espín, véase la Parte I de la tesis) presentan un comportamiento similar en la evolución de sus momentos magnéticos, que parecen congelados. La fase vidrio de espín (en ausencia de campo magnético) se caracteriza por una nula magnetización total como ocurre en la fase paramagnética. Sin embargo, al contrario de esta última, cada espín en la red parece congelado en el tiempo siguiendo un patrón espacial aparentemente aleatorio. Los vidrios de espín comparten una multitud de fenómenos con los vidrios estructurales, aunque son de naturaleza totalmente diferente: en un caso hablamos

de interacciones magnéticas y en el otro de difusión de partículas.

Al contrario que los vidrios estructurales, los vidrios de espín son, al menos por ahora, materiales sin aplicaciones conocidas. Sin embargo, aunque ambos comparten los mismos fundamentos de una fase vítrea, los vidrios de espín son más accesibles a una descripción analítica. De hecho, puesto que la difusión no es importante, los espines se pueden colocar en los nodos de una red, lo que facilita notablemente los cálculos. Por esta razón, aunque los vidrios estructurales tendrían más interés práctico, los vidrios de espín son actualmente el banco de pruebas habitual para investigar el comportamiento complejo, y mucha de nuestra intuición sobre vidrios proviene de los estudios de vidrios de espín.

Esta tesis está centrada en el estudio numérico de sistemas complejos. Como hemos mencionado antes, la diversidad de problemas es inagotable, aunque tanto el mecanismo interno, como las herramientas necesarias para estudiarlos son bastante intercambiables de un sistema a otro. Por esta razón, hemos trabajado tanto en vidrios de espín (Parte I de esta tesis) como en sistemas coloidales formadores de vidrios (Parte II). Como veremos, normalmente estaremos interesados en estudiar las propiedades de equilibrio, lo que, presenta un gran problema de tiempos cuando hablamos de simulaciones en un ordenador. Como ya mencionamos antes, la principal característica de la transición vítrea es una divergencia de los tiempos de difusión de las partículas, que en una simulación numérica es equivalente a tiempos de autocorrelación tan largos, que la termalización se vuelve inalcanzable en tiempos humanos incluso para sistemas relativamente pequeños. No obstante, hemos justificado que en estos materiales el régimen relevante en un experimento es el de fuera del equilibrio, ¿por qué preocuparnos entonces por el equilibrio? La respuesta es sencilla: los escasos resultados analíticos que tenemos a nuestro alcance corresponden casi exclusivamente al equilibrio. Es en este punto donde las simulaciones numéricas se hacen cruciales. Con una simulación podemos estudiar ambos regímenes simultáneamente en el mismo modelo, lo que nos permite inferir cuáles serían las consecuencias del comportamiento de equilibrio (para el cuál tenemos predicciones o teorías) en un experimento.

La transición vítrea no es el único problema con el que nos enfrentamos en una simulación. De hecho, el estudio numérico de cualquier transición de fase lleva asociada una divergencia de los tiempos característicos con el número de partículas N (relacionada con el crecimiento de una fase dentro de la otra). Este hecho limita enormemente el tamaño de sistema accesible para una simulación numérica. En los problemas que vamos a considerar en esta tesis, tendremos que lidiar con ambos efectos, los dinámicos de la transición vítrea asociados al desorden, y los propios de una transición de fase tradicional. Por esta razón, estos problemas pertenecen a los llamados computacionalmente difíciles en ciencias de la computación (véase el Capítulo 9). Esta dificultad nos obliga a acompañar nuestro estudio de la física del problema con el desarrollo e investigación de nuevos algoritmos numéricos que nos permitan acelerar la dinámica del sistema.

Aproximadamente la mitad de esta tesis está dedicada al desarrollo de nuevas técnicas y algoritmos de computación. Este énfasis en el ámbito computacional

es menos patente en la parte dedicada a vidrios de espín (Parte I), ya que los algoritmos de Montecarlo utilizados son bastante comunes y el progreso de nuestro trabajo ha estado más relacionado con la implementación del *multispin coding* (véase Apéndice B) o con el superordenador JANUS. Por el contrario, la Parte II dedicada a los coloides polidispersos está casi exclusivamente enfocada en este problema. En estos capítulos, tenemos que lidiar simultáneamente con una transición vítrea y una de primer orden en una región muy pequeña del espacio de parámetros. Las transiciones de primer orden llevan asociada una divergencia de tiempos (exponencial en el número de partículas N) que se vuelve especialmente nociva en sistemas topológicamente desordenados (es decir, sin el soporte geométrico de un retículo). Por esta razón, nuestros esfuerzos han estado dedicados principalmente a combatir este problema introduciendo nuevos algoritmos. Más adelante, continuando con la estrategia de buscar algoritmos optimizados para simular vidrios, en los últimos meses de la tesis nos movimos hacia la computación cuántica y las nuevas oportunidades que ofrece. En particular, comenzamos a trabajar en uno de los principales problemas del algoritmo de "quantum annealing" (también conocido como computación cuántica adiabática).

La mayoría de los resultados de esta tesis han sido publicados en revistas y presentados en conferencias internacionales. Aprovechamos para resumirlos aquí. Comenzamos con la Parte I dedicada a vidrios de espín. La introducción general a los vidrios de espín presentada en el capítulo 3 está basada en las Refs. [ÁB10a, ÁB10b] (trabajos de las Janus collaboration a la que pertenezco). Sin embargo, no presentamos trabajo original de esta tesis en este capítulo. Por otro lado, el Capítulo 4 está basado en [Fer10a]. Tuve la oportunidad de presentar este trabajo en una ponencia en la conferencia más importante del campo, en *STATPHYS 24, the XXIV International Conference on Statistical Physics* en Cairns (Australia) en Julio de 2010. También tuve una charla sobre este modelo en *CompPhys09, 10th International NTZ-Workshop on New Developments in Computational Physics* en Leipzig (Alemania) en Noviembre de 2009. El Capítulo 5 está basado en [Fer12a] (actualmente en proceso de revisión). Por otro lado, la Parte II está dedicada a sistemas coloidales. Dentro de ella, el Capítulo 7 está basado en [Fer10b]. Presenté este trabajo en ponencias de los congresos *the XII International Workshop on Complex Systems* en Andalo (Italia) en Marzo de 2010 y en *the International Workshop on Complex Energy Landscapes* en Zaragoza (España) en Junio de 2010. Por otro lado, el Capítulo 8 está basado en [Fer12b, MM11]. Presenté estos dos trabajos conjuntamente en una ponencia en el encuentro satélite del STATPHYS 24, *Monte Carlo Algorithms in Statistical Physics* en Melbourne (Australia) en Julio de 2010, y en un póster en la conferencia *Viscous Liquids III* en Roma (Italy) en Marzo de 2011. Finalmente, el capítulo de quantum annealing (Capítulo 9) está basado en [Seo12], y lo he presentado recientemente con un póster en la conferencia *Quantum Information meets Statistical Mechanics* en Innsbruck (Austria) en Septiembre de 2012.

Por último, me gustaría agradecer el apoyo económico a este trabajo llevado a cabo por el MECCD (España) por medio del programa FPU, así como por el MICINN (España) a través del contrato Nº FIS2009-12648-C03.

I.2

Resumen de los resultados más importantes de la tesis

El resumen está estructurado siguiendo los diferentes capítulos de la tesis que contienen resultados originales. Como en el resto del texto, discutimos primero los dos trabajos en vidrios de espín, continuamos con dos de coloides y terminamos resumiendo el de quantum annealing.

I.2.1 El modelo del hipercubo

La mayoría de la intuición que tenemos hoy en día sobre vidrios de espín proviene de resultados analíticos obtenidos gracias a la aproximación de campo medio. Entre todos los modelos de campo medio disponibles en la literatura, el modelo de Sherrington-Kirkpatrick (SK) [She75] es sin lugar a duda el modelo históricamente más relevante. Al contrario de lo que ocurre con la aproximación de campo medio en un ferromagneto, la solución emergente del modelo de SK es altamente no trivial. De ella obtenemos una imagen de una estructura intrincada para la fase de vidrio de espín caracterizada por una infinidad de estados de equilibrio organizados entre sí de forma ultramétrica.

Los modelos de campo medio permiten un alto grado de desarrollo analítico pero casi todos los resultados disponibles hasta la fecha corresponden al equilibrio. Por el contrario, los vidrios de espín reales viven permanentemente fuera del equilibrio, y entendemos muy poco de este régimen aún incluso en modelos de campo medio. De hecho, el tratamiento analítico del envejecimiento es extremadamente difícil ya para el protocolo experimental más simple, por lo que reproducir analíticamente los efectos provenientes de protocolos mucho más complicados, como los experimentos de memoria o rejuvenecimiento [Jon98] está, hoy por hoy, totalmente fuera de nuestro alcance. Por esta razón, las simulaciones de Montecarlo en modelos de campo medio, es todavía importante puesto que permite estudiar el comportamiento fuera del equilibrio de modelos cuyo equilibrio es bastante conocido (algo que no podemos afirmar sobre modelos más realistas).

En el modelo de SK la interacción entre espines tiene alcance infinito, por lo que todos los espines interaccionan entre sí. Esta falta de noción de vecinos o de distancia entre espines aleja bastante este modelo de cualquier vidrio de espín real, dónde los espines están bien localizados en una red y dónde la interacción entre ellos tiene un alcance finito. Por otro lado, a nivel computacional, esta propiedad conlleva cálculos de la energía para las actualizaciones de Metropolis de orden $\mathcal{O}(N^2)$, donde N es el número de espines, lo que hace muy complicado estudiar sistemas grandes mediante una simulación de Montecarlo. Como solución conjunta a estos dos problemas, en los últimos años se han introducido toda una nueva familia de modelos de campo medio con una conectividad finita entre espines [Par06, Méz01]. Entre todos ellos, se han vuelto muy populares aquellos formulados sobre grafos (árboles de Cayley, grafos de Erdos-Renyi o redes de Bethe, por ejemplo).

En todos estos grafos, cada espín interacciona sólo con un número finito de espines elegidos aleatoriamente entre todos los posibles. Esta condición introduce una noción de vecindad en el sistema, pero la falta de una estructura espacial clara no permite definir una distancia. La existencia de esta distancia es vital para estudiar la física fuera del equilibrio. Hoy en día sabemos que el envejecimiento en vidrios de espín se explica a partir de un crecimiento de dominios magnéticos. Las distintas teorías difieren mucho en sus predicciones para estos dominios. En campo medio conocemos bien la estructura de estos dominios en equilibrio, puesto que la teoría de la ruptura de la simetría de las réplicas (RSB, en sus siglas en inglés) se cumple por encima de $D = 6$ dimensiones. Por lo tanto, si somos capaces de definir un modelo que combine campo medio con distancia, tendremos una herramienta para estudiar la dinámica en un problema puramente RSB.

En esta tesis hemos propuesto un modelo que combina justamente estas dos características. En particular, introducimos un nuevo modelo de campo medio también formulado sobre un grafo aleatorio, pero esta vez sobre un hipercubo de D dimensiones. Este nuevo modelo combina una definición clara de primeros vecinos con una estructura espacial que permite definir una distancia.

Nuestra alternativa consiste en colocar $N = 2^D$ espines sobre los vértices $\boldsymbol{x}$ de un hipercubo unitario de D dimensiones. Así los acoplamientos entre espines están definidos sobre las aristas $\{\boldsymbol{x}, \hat{\boldsymbol{\mu}}\}$, donde $\hat{\boldsymbol{\mu}}$ etiqueta a los D posibles vectores unitarios en el espacio D-dimensional. Además consideramos condiciones de contorno periódicas, por lo que cada espín puede estar conectado a lo sumo con $D = \log_2 N$ espines. Esta construcción permite definir una distancia como el número de aristas que separan a un espín de otro.[1] En este modelo, la energía de interacción está dada por

$$\mathcal{H} = -\frac{1}{2} \sum_{\boldsymbol{x},\hat{\boldsymbol{\mu}}} J_{\boldsymbol{x},\hat{\boldsymbol{\mu}}} n_{\boldsymbol{x},\hat{\boldsymbol{\mu}}} s_{\boldsymbol{x}} s_{\boldsymbol{x}+\hat{\boldsymbol{\mu}}} \,, \tag{I.1}$$

donde $J_{\boldsymbol{x},\hat{\boldsymbol{\mu}}}$ indica la naturaleza de la interacción tomando $+1$ (ferromagnética) o -1 (antiferromagnética) con idéntica probabilidad. Por otro lado, $n_{\boldsymbol{x},\hat{\boldsymbol{\mu}}} = 1$ si los espines $s_{\boldsymbol{x}}$ y $s_{\boldsymbol{x}+\hat{\boldsymbol{\mu}}}$ interactúan, y $n_{\boldsymbol{x},\hat{\boldsymbol{\mu}}} = 0$ si no lo hacen.

Para terminar la definición del modelo, nos falta explicar cómo construir la matriz de conectividad $\{n_{\boldsymbol{x},\hat{\boldsymbol{\mu}}}\}$. Comenzamos con un grafo Poissoniano de conectividad aleatoria. Activamos cada uno de los posibles links (es decir, tomamos $n_{ik} = 1$) con probabilidad z/D. De esta manera cada espín estará conectado en media con z espines. Se puede demostrar que este tipo de grafos no presenta árboles locales, lo que hace exacta la aproximación de Bethe en el límite de $D \to \infty$. Esta aproximación permite calcular el inverso de la temperatura crítica en un ferromagneto de forma sencilla (véase el Apéndice A.1) o incluso en un vidrio de espín [Tho86]

$$K_{\mathrm{c}}^{\mathrm{FM}} = \operatorname{atanh} \frac{1}{\langle n \rangle_1 - 1} \;,\; K_{\mathrm{c}}^{\mathrm{SG}} = \operatorname{atanh} \frac{1}{\sqrt{\langle n \rangle_1 - 1}} \,, \tag{I.2}$$

[1] Este tipo de distancia se conoce como la distancia del cartero, y es esencialmente equivalente a la métrica Euclidiana (entre dos mismos puntos, está última está dada por la raíz cuadrada de la distancia del cartero).

donde $\langle n\rangle_1 = 1 + z - \frac{z}{D}$, representa la conectividad media de un espín del que sabemos que uno concreto de sus enlaces está activo. Por lo tanto, directamente de la aproximación de Bethe podemos concluir que la conectividad fluctuante inherente a nuestra definición del grafo, introduce correcciones de volumen finito enormes [$\mathcal{O}(1/\log N)$ dado que $D = \log_2 N$]. La cura directa para este problema es bastante obvia: quedarnos sólo con el subconjunto de estos grafos cuya conectividad es igual para todos los espines. En general tomaremos $z = 6$ para imitar lo máximo posible a sistemas tridimensionales y nos referiremos a este subgrupo como hipercubos de conectividad fija. Por supuesto, obtener este conjunto de grafos no es trivial. Nosotros asumimos un enfoque operacional y obtenemos al menos una buena parte de ellos gracias a un algoritmo dinámico de Montecarlo discutido en la Sección 4.2.2.

Puesto que todas las variables necesarias para definir este modelo, tanto las dinámicas (los espines), como las *quenched* (los acoplamientos $\{J_{x,\hat{\mu}}\}$ y la matriz de conectividad $\{n_{x,\hat{\mu}}\}$) son binarias, pueden ser codificados en los bits de una palabra computacional. Este método se conoce como *multispin coding* y nos permite simular al mismo tiempo tantas muestras como bits tenga la palabra básica con la que trabajemos (en nuestro caso utilizamos variables de 64 bits). Este método nos ha permitido alcanzar una velocidad de 0.29 ns/*spin-flip* con un Intel i7 at 2.93GHz (en Ref. [Haso8a] se hablaba de $\sim$1.2 ns/*spin-flip* en un Opteron a 2.0 GHz).

Para evitar las fuertes correcciones de escala, trabajamos siempre sobre el subgrupo de hipercubos de conectividad fija. Este modelo se pueden obtener muchos resultados analíticos en equilibrio, lo que nos permite realizar bastantes checks de consistencia, así como asegurarnos que el conjunto de grafos de conectividad fija accesibles con el algoritmo de Montecarlo es suficientemente grande para no introducir sesgos detectables. Una vez entendido el equilibrio, resumimos aquí los resultados más importantes que hemos obtenido estudiando la dinámica fuera del equilibrio en este modelo.

Comenzamos con la estructura del envejecimiento isotérmico. En una simulación podemos estudiar los efectos de envejecimiento en las funciones de correlación temporal de los espines a dos tiempos

$$C(t, t_{\rm w}) = \frac{1}{N}\overline{\sum_i c_i(t, t_{\rm w})}\,, \quad \text{con} \quad c_i(t, t_{\rm w}) = s_i^{(1)}(t + t_{\rm w}) s_i^{(1)}(t_{\rm w})\,. \tag{I.3}$$

Las medidas obtenidas en experimentos de la imanación (que es esencialmente esta función) sugieren un colapso de estas funciones si se representan frente al cociente $t/t_{\rm w}$ al menos para $10^{-3} < t/t_{\rm w} < 10$ y $t_{\rm w}$ dentro del rango 50s—10^4s [Rodo3]. Este fenómeno se conoce como *Full Aging*. Nuestros datos sugieren una violación clara de este comportamiento, como podemos ver en la Figura I.1. Este scaling está relacionado con la existencia de sólo dos escalas de tiempo relevantes en el sistema, a tiempos muy cortos, en los que la función de correlación es aproximadamente 1, y a tiempos $t \gg t_{\rm w}$ en la que se hace cero. La imagen que tenemos del envejecimiento en modelos de campo medio sugiere la necesidad de considerar más sectores de tiempo [Cug94], y nuestros datos muestran exactamente la misma conclusión. Más

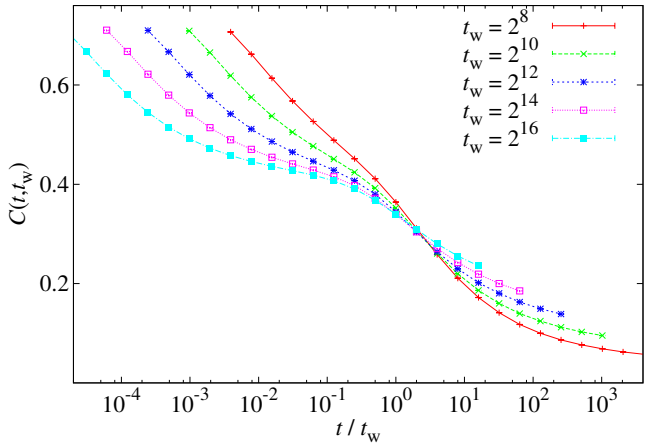

FIGURE 1.1: Función de correlación $C(t, t_w)$ frente a t/t_w para $D = 22$ y $T = 0.7T_c$.

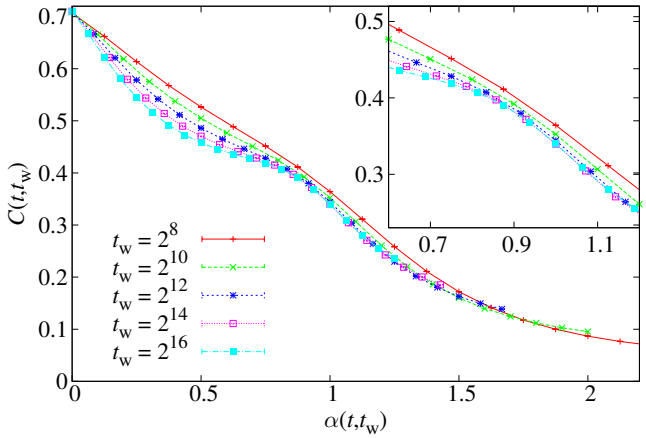

FIGURE 1.2: Mismos datos que en la Figura 1.1, pero representados como función de $\alpha(t, t_w)$, definida en (1.4). La ventana es una amplificación de la región de interés.

aún, si probamos el scaling de Bertin-Bouchaud [Bero2b]

$$C(t, t_w) = f\left(\alpha(t, t_w)\right), \quad \alpha(t, t_w) = \log t / \log t_w, \tag{1.4}$$

observamos que los datos colapsan sorprendentemente bien. Este scaling indica que $C(t, t_w)$ tiende a una constante (en el límite de $t_w \to \infty$) para cualquier rango finito de la variable t/t_w, lo que sugiere la existencia de un número infinito de sectores de tiempo.

También podemos estudiar los efectos del envejecimiento en la función de correlación de enlaces

$$C_{\text{link}}(t, t_w) = \frac{1}{zN} \overline{\sum_{ik} n_{ik}\, c_i(t, t_w) c_k(t, t_w)}, \tag{1.5}$$

con $c_i(t, t_w)$ definido en (1.3). Si la representamos frente a $C^2(t, t_w)$, como mostramos en la Figura 1.3, obtenemos una relación lineal entre los dos, que implica equivalencia entre overlaps, como esperamos en un sistema RSB. El hecho de que el

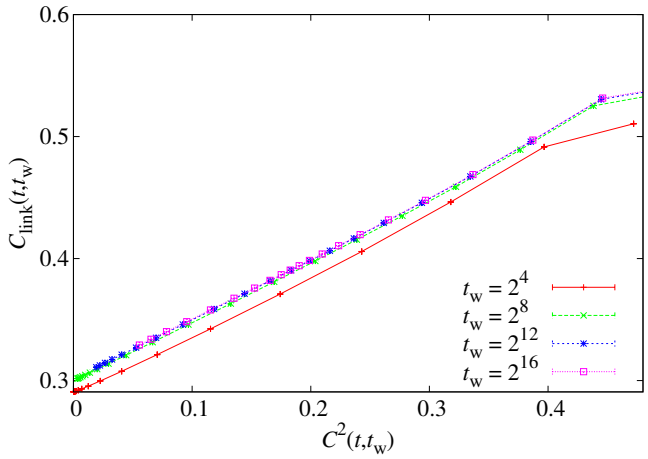

FIGURE I.3: $C_{\rm link}$ frente a $C^2(t,t_{\rm w})$ para diferentes $t_{\rm w}$ a $T=0.7T_{\rm c}$ y para $D=22$.

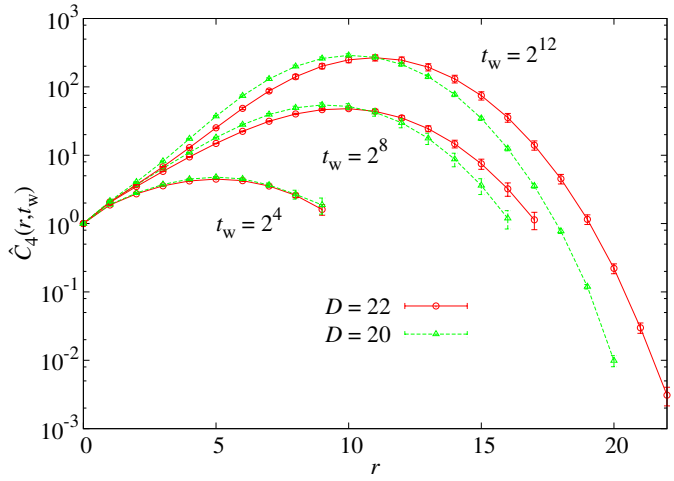

FIGURE I.4: $\hat{C}_4(r,t_{\rm w})$, (I.6), para $D=20$ y 22, para $t_{\rm w}=2^4$, 2^8 y 2^{12} a $T=0.7T_{\rm c}$.

distribución de $C_{\rm link}(t,t_{\rm w})$ no se haga trivial con el tiempo, indica que el cociente superficie-volumen de los dominios magnéticos no se anula, lo que tiene consecuencias directas en la estructura de éstos: son fractales y ocupan todo el espacio.

Como ya destacamos anteriormente, una de las principales ventajas de este modelo es que nos ha permite estudiar funciones de correlación espacial y caracterizar el crecimiento de dominios magnéticos. De hecho, en nuestras muestras podemos calcular explícitamente la función de correlación

$$\hat{C}_4(r,t_{\rm w}) = \sum_{\boldsymbol{r},|\boldsymbol{r}|=r} c_4(\boldsymbol{r},t_{\rm w})\,, \quad c_4(\boldsymbol{r},t_{\rm w}) = \tfrac{1}{N}\overline{\textstyle\sum_{\boldsymbol{x}} q_{\boldsymbol{x}}(t_{\rm w})q_{\boldsymbol{x}+\boldsymbol{r}}(t_{\rm w})}\,. \tag{I.6}$$

Representamos estas funciones para diferentes tiempos de espera, $t_{\rm w}$, en la Figura I.4. $\hat{C}_4(r,t_{\rm w})$ presenta un máximo que se desplaza con el tiempo hacia valores de r

mayores.[2] Podemos utilizar este hecho para estimar una longitud de coherencia por medio de un estimador integral

$$\xi_{0,1}(t_{\mathrm{w}}) = \frac{\int_0^\infty \mathrm{d}r\; r\; \hat{C}_4(r, t_{\mathrm{w}})}{\int_0^\infty \mathrm{d}r\; \hat{C}_4(r, t_{\mathrm{w}})}\,. \tag{I.7}$$

Representamos estas longitudes de coherencia en la Figura I.5–arriba, como función del tiempo. Identificamos una longitud que crece con t_{w} pero sólo hasta aproximadamente $D/2$. Como cabría esperar, esta magnitud tiene que sufrir efectos de volumen finito puesto que no puede crecer indefinidamente en un hipercubo de tamaño finito. De todas formas, a tiempos cortos, cuando los dominios aún no sienten que el tamaño es finito, crecen aparentemente como $\log t_{\mathrm{w}}$. Este comportamiento nos lleva a proponer que $\xi_{D=\infty}(t_{\mathrm{w}}) \propto \log t_{\mathrm{w}}$. Con esta idea, probamos un scaling de tamaño finito ξ_D/D frente a $\log t_{\mathrm{w}}/D$. La intuición se confirma en la Figura I.5–abajo, donde observamos un colapso espectacular de los datos. Este mismo scaling vale para los datos de la transformada de Fourier de $\hat{C}_4(r)$ designada aquí por $G(k)$. De hecho, si representamos el coeficiente adimensional $G(k)/G(0)$ frente a $\log t_{\mathrm{w}}/D$, como hacemos en la Figura I.6, observamos también un colapso extremadamente bueno.

También podemos estudiar la dependencia de $G(k)$ con k. Ciertas descripciones teóricas [Dom93, Dom98, Dom06] predicen que el propagador debería ir con $1/p^4$ ($p = k/D$) en el rango $1/\xi(t_{\mathrm{w}}) \ll p \ll 1$, aunque, por lo menos hasta dónde sabemos, este comportamiento no se ha observado nunca en un estudio numérico. Puesto que nosotros hemos trabajado siempre con la métrica del cartero, que es el cuadrado de la Euclidiana habitual, el comportamiento que debemos esperar en nuestro modelo, con nuestra métrica, es $1/p^2$. Dado que en nuestro rango de tiempos $\xi(t_{\mathrm{w}}) \sim \log t_{\mathrm{w}}$, esta predicción implicaría que $G(k)\left(p^2 + 1/\log^2 t_{\mathrm{w}}\right)$ debería hacerse constante según D crece. Vemos en la Figura I.7 que así es, lo que supone la primera observación de este comportamiento en una simulación numérica.

I.2.2 Caos en temperatura

El caos en temperatura se refiere a la fragilidad del estado de equilibrio de un vidrio de espín frente a cambios mínimos de temperatura. Este efecto ha sido predicho por las diferentes teorías de vidrios de espín, aunque todavía no ha sido comprobado directamente en ningún experimento. La principal dificultad para diseñar un experimento es que los vidrios de espín reales viven fuera del equilibrio, por lo que sólo podemos medir las consecuencias indirectas de esta fragilidad en protocolos fuera del equilibrio. De hecho, en los últimos años el caos en temperatura ha acaparado gran interés precisamente porque ha sido propuesto como una de las

[2] $\hat{C}_4(r, t_{\mathrm{w}})$ no presenta un decaimiento monótono con r como suele ocurrir en las funciones de correlación. Sin embargo, en el capítulo extendido de la tesis justificamos detalladamente que esta es la definición correcta.

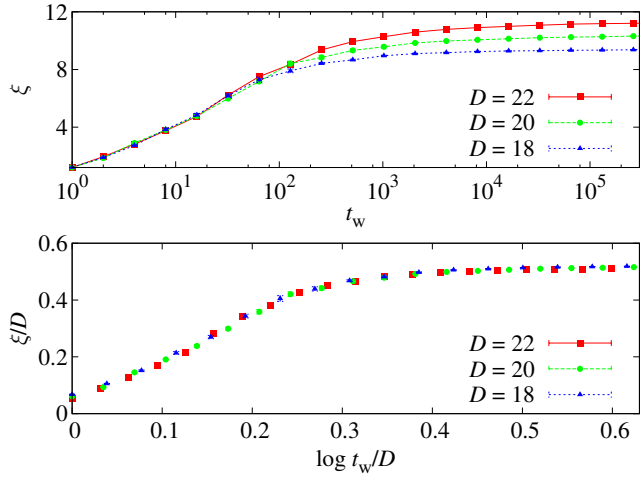

FIGURE I.5: **(Arriba)** Longitud de coherencia ξ en la fase vidrio de espín a $T = 0.7T_c$ frente a t_w para diferentes tamaños. **(Abajo)** mismos del panel de arriba pero reescalados por D como función de $\log t_w/D$.

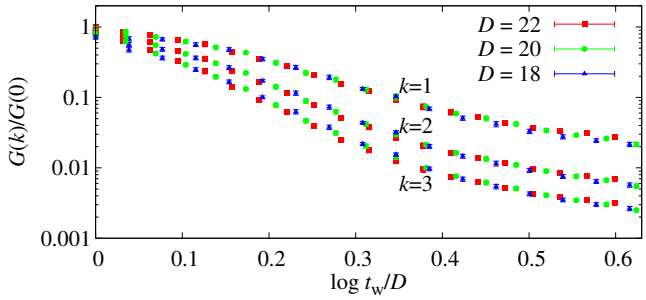

FIGURE I.6: Transformada de Fourier $G(k)$ de $\hat{C}_4(r)$ en unidades de $G(0)$ como función de $\log t_w/D$ para bastantes valores de D y k a $T = 0.7T_c$. Para cada valor de k se observan diferentes funciones de escala.

posibles explicaciones para los sorprendentes experimentos de rejuvenecimiento y memoria [Jon98]. En efecto, si los estados de equilibrio a dos temperaturas T_1 y T_2 ($T_2 < T_1$) estuvieran totalmente descorrelacionados, la susceptibilidad no debería verse afectada por la relajación que tuvo lugar a T_1, lo que explica directamente el rejuvenecimiento. La memoria estaría luego relacionada con la separación de escalas de los *dominios fantasma* en la teoría de las droplets [Yos03, Jön04] o alternativamente, con la organización jerarquizada de estados de la teoría RSB [Mar00].

El caos en temperatura fue predicho inicialmente en [Bra87] y desde entonces ha sido buscado numéricamente sin mucho éxito tanto en modelos de campo medio [Bil00, Bil02] como en modelos más realistas [NN97, NN98, Asp02, Riz03, Krz04, Sas05, Kat07]. El resultado hasta ahora ha sido siempre el mismo, se detectan signos de caos, pero siempre extremadamente débiles. En particular, todos los trabajos concluyen que o bien el efecto es muy débil o tiene lugar escalas espa-

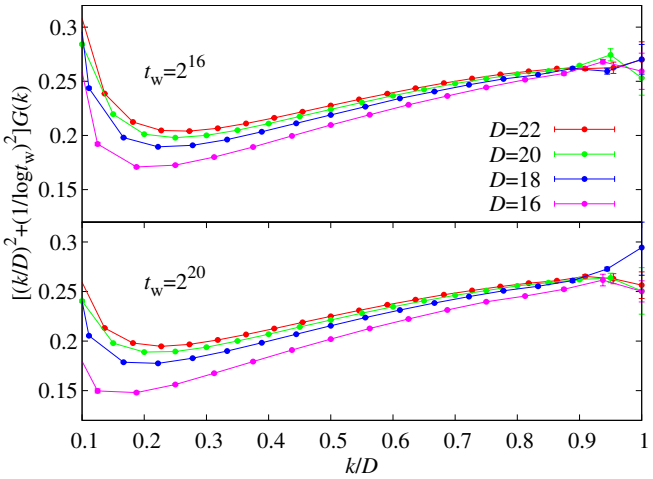

FIGURE 1.7: Transformada de Fourier $G(k)$, en unidades del propagador $[(p^2 + 1/\xi^2(t_w))^{-1}]$ [Dom93, Dom98, Dom06] como función de p, donde el momento con dimensiones es $p = k/D$ y $\xi(t_w) \sim \log t_w$. Recuerde que estamos trabajando en la métrica del cartero, por lo que lo que para nosotros es p^2, se transforma a p^4 en la métrica Euclídea. Mostramos resultados para dos tiempos de espera: $t_w = 2^{16}$ **(arriba)** y $t_w = 2^{20}$ **(abajo)**.

ciales demasiado grandes para ser detectado en toda su magnitud en los tamaños alcanzables por nuestras simulaciones numéricas. De acuerdo con ésto, el caos en temperatura no debería ser el causante de los efectos experimentales de memoria y rejuvenecimiento, ya que estos aparecen a escalas menores y son muy fuertes.

Hoy en día, existen dos imágenes diferentes para explicar el caos:

- Por un lado, desde la teoría de las droplets, el caos surge de forma muy sencilla. En este marco, los dominios magnéticos compactos (droplets) podrían invertirse frente a un cambio infinitesimal de temperatura debido a un balance muy delicado entre la energía libre y la entropía. Según esta teoría, los estados de equilibrio a T_1 y T_2 deberían diferir completamente a escalas superiores a cierta longitud de caos dada por

$$\xi_C(T_1, T_2) \propto |T_2 - T_1|^{-1/\zeta}, \tag{1.8}$$

  donde ζ es el *exponente caótico*.

- Por otro lado, el caos en temperatura aparece de forma mucho más rigurosa en desarrollos en modelos campo medio [Bilo2, Rizo3, Par10] donde la teoría RSB es exacta. Aquí se puede estudiar analíticamente la energía libre, constreñida a un valor dado del overlap a dos temperaturas, en términos de un funcional de grandes desviaciones.

Hasta ahora, casi sin excepción, los datos de simulaciones numéricas han sido analizados siguiendo la primera imagen. En casi todos estos estudios se justifica la

existencia de caos de manera indirecta gracias cierta renormalización fenomenológica. Los overlaps se superponen sorprendentemente bien utilizando dependencia funcional (I.8) para la longitud de caos, y los exponentes ζ que se obtienen son compatibles con los que predice la teoría. Sin embargo, estos cálculos presentan un fuerte problema, ya que el colapso tiene lugar tanto en la fase vidrio de espín (donde debería haber caos) como en la fase ferromagnética (donde no lo hay). Este hecho muestra que sea cuál sea el efecto que se está detectando, no puede ser el caos en temperatura.

Llegados a este punto, y dado que teníamos a nuestra disposición, gracias al superordenador JANUS, configuraciones termalizadas del modelo de Edwards-Anderson en $D = 3$ mucho más grandes y a temperaturas mucho menores que todo lo estudiado hasta la fecha (donde los efectos de caos deberían ser notablemente más fuertes), decidimos reenfocar el trabajo [Kat07]. Bajo nuestro punto de vista, el análisis realizado anteriormente estaba subestimado el caos en temperatura y queríamos entender por qué.

El primer paso fue determinar qué observable era el más adecuado para detectar los efectos de caos, y nuestra idea fue buscarlo en la dinámica de Parallel Tempering (PT). Durante las simulaciones, nos encontramos que los tiempos exponenciales de autocorrelación, τ_{exp}, fluctuaban en un rango de varios órdenes de magnitud de una muestra a otra, y nuestra apuesta fue que este hecho estaba fuertemente relacionado con los efectos de caos. En efecto, si las configuraciones de equilibrio fueran radicalmente diferentes de una temperatura a otra (como predice el caos), los updates de PT entre ambas se aceptarían con muy baja probabilidad.

El punto de partida es el denominado *parámetro de caos* para cada muestra (J) [NN97]

$$X^J_{T_1,T_2} = \frac{\left\langle q^2_{T_1,T_2} \right\rangle_J}{\sqrt{\left\langle q^2_{T_1,T_1} \right\rangle_J \left\langle q^2_{T_2,T_2} \right\rangle_J}}, \tag{I.9}$$

donde $\left\langle q^2_{T_1,T_2} \right\rangle_J$ se refiere al promedio temporal del overlap entre dos temperaturas en cada muestra. Al estudiar la relación entre esta magnitud y τ_{exp} pudimos ver que ambas estaban fuertemente correlacionadas. No obstante, la correlación era aún mayor si en vez de estudiar $X^J_{T_1,T_2}$, estudiábamos su integral con respecto a una de las temperaturas

$$I = \int_{T_1}^{T_{\max}} X^J_{T_1,T_2} \, \mathrm{d}T_2. \tag{I.10}$$

Mostramos el diagrama de dispersión junto con el valor del coeficiente de correlación en la Figura I.8.

De acuerdo con esta figura, las muestras con I pequeña, aquellas en el que $X^J_{T_1,T_2}$ ha caído a valores bajos a temperaturas cercanas a T_1 (como esperaríamos en caso de existir caos) se corresponden con las muestras donde $\tau_{\exp}$ es mayor. Este hecho sugiere introducir el concepto de *evento caótico*, así como abandonar la idea de un

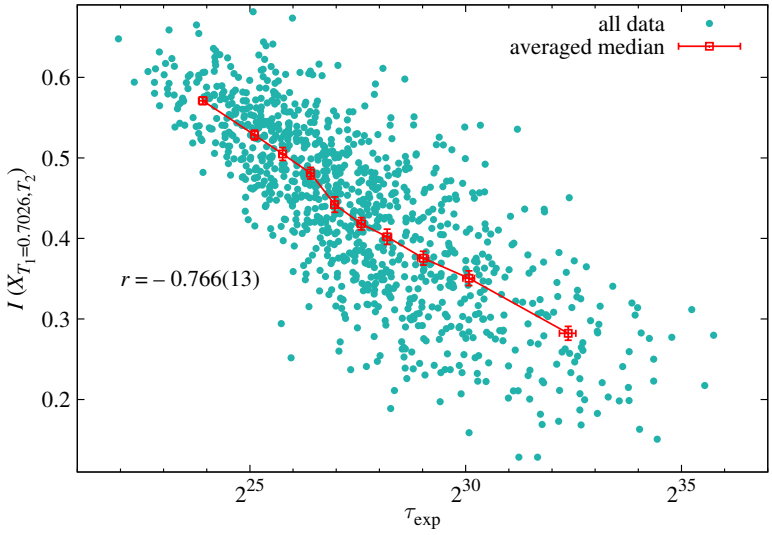

FIGURE 1.8: Diagrama de dispersión de $I = \int_{T_1}^{T_{\rm max}} X^J_{T_1,T_2}\, {\rm d}T_2$, frente a $\tau_{\rm exp}$ [$X^J_{T_1,T_2}$ en (1.9), $T_1 = T_{\rm min} = 0.7026$, $T_{\rm max} = 1.549$, datos para $L = 32$]. Para calcular la línea roja se ordenaron los datos por $\log \tau_{\rm exp}$ creciente y se hicieron grupos de 100 muestras cada uno. Dentro de cada grupo, se calculó la mediana (los errores se obtuvieron con el método del boostrap).

análisis tradicional basado en promedios entre muestras.

Este cambio de paradigma queda mucho mucho más claro en la Figura 1.9. En el panel superior se muestra el promedio muestral de $X^J_{T_1,T_2}$ como función de T_2. Como también se observaba en los trabajos anteriores [NN97, NN98, Kato7], nuestras muestras están aún muy lejos del límite de gran L, dónde la media de $X^J_{T_1,T_2}$ debería anularse si $T_2 \neq T_1$. Por el contrario, nuestras curvas describen un comportamiento muy suave sin ningún cambio apreciable una vez sobrepasado $T_{\rm c}$. No obstante, si en vez de representar la media, consideramos por separado las curvas correspondientes a cada una de las muestras (en el panel central de la Figura 1.9) observamos que algunas muestras sí que caen abruptamente en valores bien determinados de T_2. A esto es a lo que llamaremos *evento caótico*. Como podemos ver, en muchas muestras esto no ocurre nunca. De todas formas, el porcentaje de muestras que sufren eventos caóticos aumenta a medida que también lo hace L. Esta idea la podemos cuantificar estudiando la dispersión entre muestras para cada tamaño, véase el panel inferior de la Figura 1.9. Como podemos observar, esta dispersión tiende al valor $1/\sqrt{12}$ (la dispersión de una variable aleatoria distribuida uniformemente entre 0 y 1) en la fase vidrio de espín, mientras que tiende a cero cuando $T_2 > T_{\rm c}$. Esto supone un logro destacable: es la primera vez que somos capaces de identificar un comportamiento diferente entre la fase vidrio de espín y la paramagnética, (es evidente que no esperamos caos en temperatura en la fase paramagnética). La conclusión de esta figura es clara, el promedio entre muestras anula la información sobre caos en temperatura. En su lugar, este efecto ha de estudiarse como un fenómeno de eventos raros. El caos está ahí, cuando ocurre sus efectos son muy fuertes, pero para los tamaños que estamos estudiando ocurre con

relativamente poca frecuencia.

Esta fuerte dispersión entre muestras nos lleva a aplicar los funcionales de grandes desviaciones utilizados en los estudios de campo medio [Bilo2, Rizo3, Par10]. De esta forma, introducimos un potencial de grandes desviaciones, $\Omega^L_{T_1,T_2}(\varepsilon)$, por medio de

$$\text{Probabilidad}[X^J_{T_1,T_2} > \varepsilon] = \mathrm{e}^{-L^D \Omega^L_{T_1,T_2}(\varepsilon)} . \tag{I.11}$$

Este concepto sólo es útil si este $\Omega^L_{T_1,T_2}(\varepsilon)$ se hace independiente de L para tamaños moderados de L. Vemos en la Figura I.10 que así es. Además, éste describe un comportamiento lineal en ε^2. Si ajustamos los datos de $\Omega^L_{T_1,T_2}(\varepsilon)$ (véase Figura I.11) fijando $\beta = 2$ en

$$\Omega^L_{T_1,T_2}(\varepsilon) = A(T_1,T_2)\varepsilon^\beta, \quad \beta \approx 2, \quad \text{con } A(T_1,T_2) \propto |T_2 - T_1|^b, \tag{I.12}$$

podemos obtener el factor $A(T_1,T_2)$. Observamos dos regímenes bien diferenciados. Por un lado, para pequeñas diferencias de temperaturas, $b \sim 2.8$, mientras que para mayores, $b \sim 1.16$. Retornaremos a estos valores más adelante.

Puesto que todos los trabajos anteriores utilizaban promedios muestrales para el análisis, tiene sentido plantearnos si las longitudes tan grandes de correlación que obtenían [Aspo2] son verdaderamente las escalas espaciales en las que aparece el caos. Con nuestras configuraciones podemos calcular explícitamente las funciones de correlación espacial

$$C^J_{T_1,T_2}(r) = \frac{1}{3V} \sum_{\boldsymbol{r}=r\boldsymbol{e}_{x,y,z}} \sum_{\boldsymbol{x}} \left\langle s^{T_1}_{\boldsymbol{x}} s^{T_2}_{\boldsymbol{x}} s^{T_1}_{\boldsymbol{x}+\boldsymbol{r}} s^{T_2}_{\boldsymbol{x}+\boldsymbol{r}} \right\rangle_J , \tag{I.13}$$

y tratar de calcular directamente estas longitudes de correlación. Dado que como discutimos previamente, sólo un pequeño porcentaje de muestras sufre eventos caóticos, estudiamos separadamente el promedio de $C^J_{T_1,T_2}(r)$ sobre las muestras más caóticas y menos caóticas. Elegimos como caóticas al 10% de las muestras con menor $X^J_{T_1,T_2}$ y como no caóticas al 10% con mayor valor de $X^J_{T_1,T_2}$. Consideramos también el promedio sobre el total de las muestras. Mostramos estas curvas en la Figura I.12.

A primera vista, el comportamiento es cualitativamente diferente en la curva caótica, mientras que no se observa demasiada diferencia entre la curva promediada a todas las muestras y la no caótica. A la vista de los datos, la afirmación de que la longitud característica del caos es muy grande es falsa, los efectos de caos se detectan a longitudes muy cortas comparadas con el tamaño del sistema.

Podemos hacer esta discusión cuantitativa ajustando las curvas a un decaimiento exponencial de la forma

$$C_{T_1,T_2}(r) \sim \sum_{i=1,2} A_i \left(\mathrm{e}^{-r/\xi_i} + \mathrm{e}^{-(L-r)/\xi_i}\right), \tag{I.14}$$

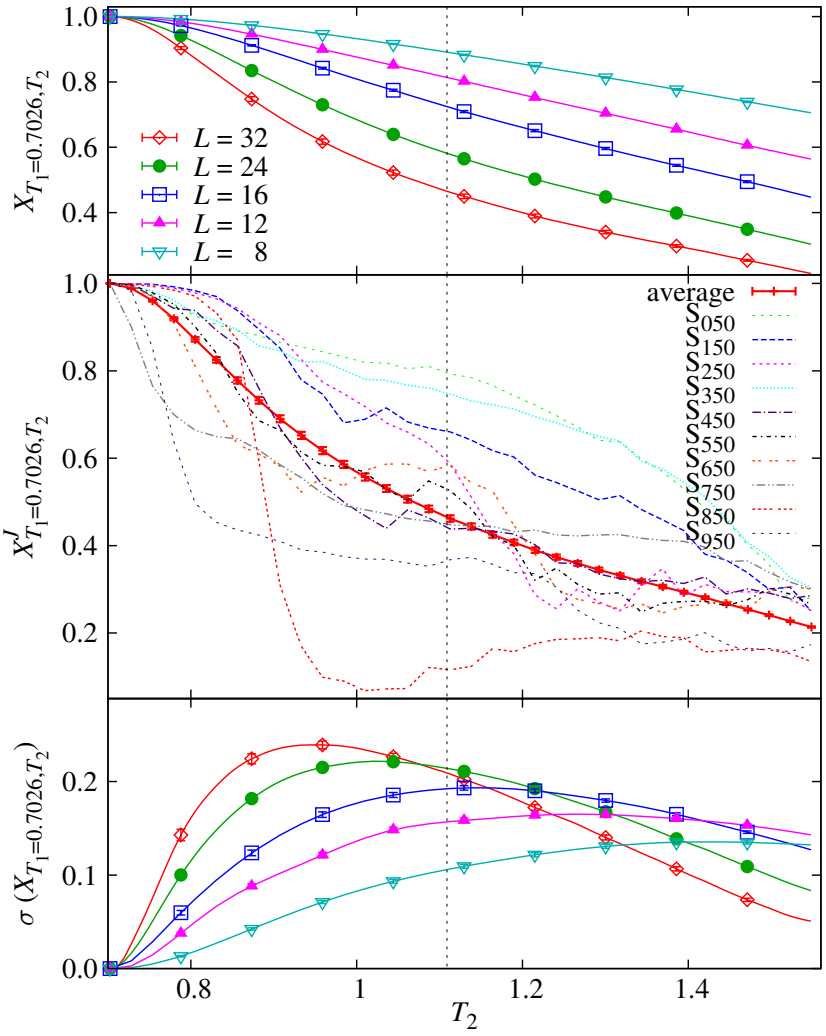

FIGURE 1.9: Diferentes vistas de $X^J_{T_1,T_2}$, (1.9), como función de T_2 ($T_1 = 0.7026$, la línea vertical muestra $T_2 = T_c$). **(Arriba)** promedio entre muestras de $X^J_{T_1,T_2}$ para todos los tamaños. **(Centro)** para $L = 32$, mostramos $X^J_{T_1,T_2}$ para diez muestras escogidas espacialmente de una lista de muestras ordenadas por valor creciente de τ_{exp}, recuerde la Fig. 1.8. **(Abajo)** para todos los tamaños de sistema, mostramos la dispersión (la raíz de la varianza sobre las muestras) de $X^J_{T_1,T_2}$.

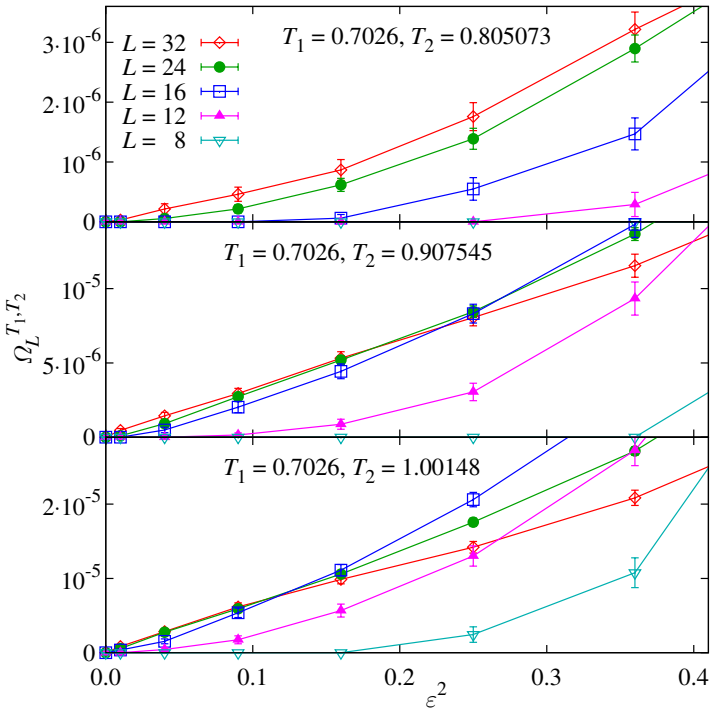

FIGURE I.10: Potencial de grandes desviaciones para $T_1 = 0.7026$ y **(arriba)** $T_2 = 0.805703$, **(centro)** $T_2 = 0.907545$ y **(abajo)** $T_2 = 1.00148$.

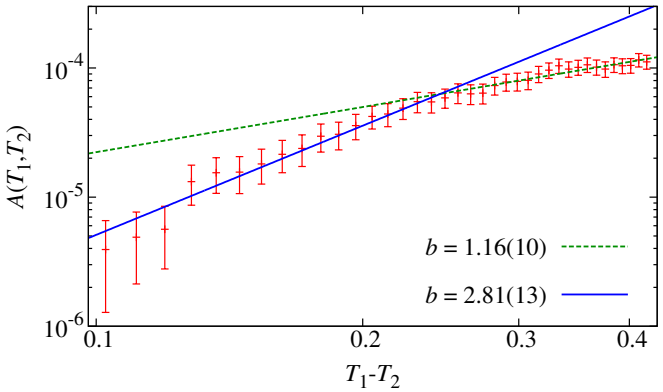

FIGURE I.11: Cálculo del exponente b. Los puntos rojos representan $A(T_1, T_2)$, mientras que las líneas azules y verdes se corresponden con ajustes a valores pequeños o grandes de T_2. Los resultados del ajuste se muestran en la figura.

en el rango $2 \leq r \leq L/2$, véase la Figura 1.12. Obtenemos ajustes muy buenos, a la vista de los valores de χ^2/dof (menores que $1/10$)[3].

Como resumen de los ajustes, en las muestras no caóticas obtenemos $\xi_{\text{NC}} \approx L/2$, mientras que en las caóticas, $\xi_{\text{C}} \approx 6$ para $L = 32$ (o $\xi_{\text{C}} \approx 4$ para $L = 24$). Dada la disparidad de escalas, no nos parece obvio el cómo estimar una única longitud de caos con promedios muestrales.

Una consecuencia reseñable de la ecuación (1.12) (véase la discusión en el capítulo), es que la ξ_{C} se hace infinita en el límite termodinámico, aunque pequeña comparada con el tamaño del sistema. En el capítulo completo discutimos que nuestros datos son consistentes con $\xi_{\text{C}} \sim L^{0.4}$, aunque tal vez estemos hablando de un comportamiento transitorio para sistemas pequeños.

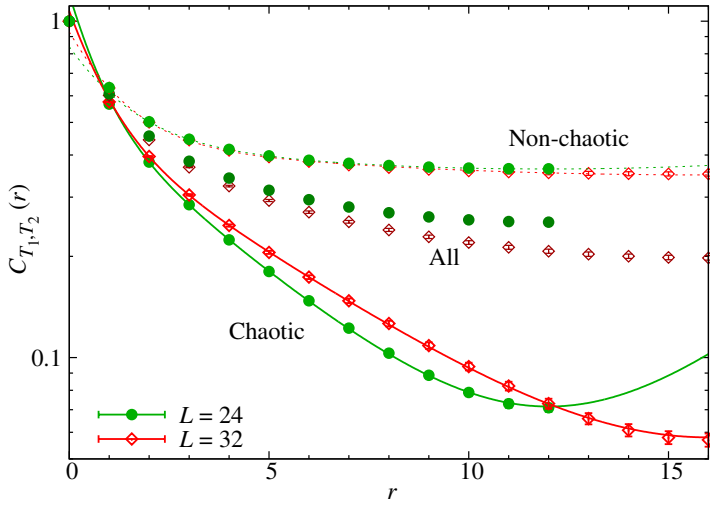

FIGURE 1.12: Función de correlación espacial (1.13) para $T_1 = 0.70260$ y $T_2 = 0.90318$, mediada sobre diferentes conjuntos de muestras: todas las muestras, las muestras no caóticas ($X_{T_1,T_2} > 0.93$) y las muestras caóticas ($X_{T_1,T_2} \leq 0.33$). Las líneas representan los ajustes de estas funciones a $\sum_{i=1,2} A_i \left(\mathrm{e}^{-x/\xi_i} + \mathrm{e}^{-(L-x)/\xi_i}\right)$. Para cada ajuste, la longitud de correlación fue $\xi_{\text{C}}^{L=32} = 5.69(2)$, $\xi_{\text{C}}^{L=24} = 4.447(15)$, $\xi_{\text{NC}}^{L=32} = 23.7(7)$, $\xi_{\text{NC}}^{L=24} = 18.9(3)$.

Ahora bien, si nuestra longitud de correlación no escala con L (al menos para nuestros tamaños), ¿cuál es el significado del exponente ζ de la ecuación (1.8) calculado en los trabajos anteriores [Sas05, Kat07]? Como argumentamos en el capítulo, se trata de $\zeta = D/b$ donde b está definido en (1.12). De acuerdo con esto, el exponente ζ no tendría ninguna relación con el caos en temperatura. Desarrollemos esta idea reproduciendo el análisis de [Kat07].

La renormalización fenomenológica se puede expresar de la siguiente manera. Primero, identificamos una $T_2(L)$ tal que la distribución de probabilidad de $X^J_{T_1,T_2(L)}$ sea independiente de L, véase el panel superior de la Figura 1.13. En este caso, el

[3]Recuérdese que para estos ajustes consideramos la χ^2 diagonal aunque los datos para las diferentes r están fuertemente correlacionados.

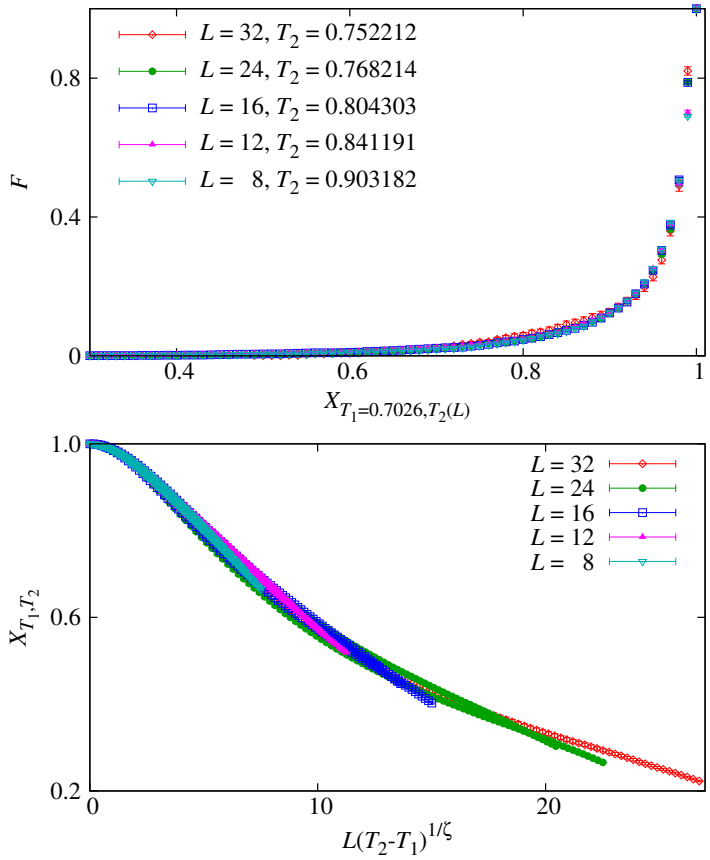

FIGURE I.13: **(Arriba)** Renormalización fenomenológica: para cada L, buscamos $T_2(L)$ de forma que la función de distribución $p\left(X^J_{T_1=0.7026,T_2(L)} \leq \varepsilon\right)$ más se parezca a la de $L = 8$ para $T_1 = 0.7026$ y $T_2 = 0.90318$. **(Abajo)** Promedio de muestras de $X^J_{T_1,T_2}$ frente a $L(T_1 - T_2)^{1/\zeta}$ utilizando $\zeta = 1.06$ (datos para $T_1 = 0.7026$ y cuando $L \leq 24$, también para $T_2 = 0.625$). El colapso de los datos se obtiene tanto para $T_2 < T_c$ como para T_2 en la fase paramagnética.

exponente ζ calculado en [Kato7] se obtiene a partir $L \propto |T_1 - T_2(L)|^{1/\zeta}$. Podemos ajustar nuestros datos a

$$T_1 - T_2(L) \propto 1/L^{\zeta}, \tag{I.15}$$

con lo que obtenemos $\zeta = 1.02(3)$ (para $L \leq 32$, $T_1 = 0.7026$ y $T_2(L = 8) = 0.90318$, con $\chi^2/\text{dof} = 3.57/3$) o $\zeta = 1.07(2)$ (para $L \leq 24$, $T_1 = 0.625$ y $T_2(L = 8) = 0.815$, con $\chi^2/\text{dof} = 1.77/2$). Mostramos estos ajustes en el panel inferior de la Figura I.13. Estos resultados son compatibles con el exponente $\zeta \approx 1.07$ calculado en [Kato7].

Pero por otro lado, si consideramos el scaling propuesto para $\Omega^L_{T_1,T_2}(\varepsilon)$, la condición que hemos impuesto para colapsar las curvas es equivalente a

$$L^D |T_1 - T_2(L)|^b = \text{constante}, \tag{I.16}$$

lo que conduce a $\zeta = D/b$.

Previamente obtuvimos b mediante los ajustes de la Figura I.11. Entonces discutimos que existían dos regímenes. Para $|T_1 - T_2(L)| < 0.25$ obtuvimos $b = 2.81(13)$,

lo que conduce directamente a $\zeta = 1.07(5)$, compatible con el exponente de [Kato7] y con el ajuste que acabamos de discutir. Sin embargo, das las diferencias de temperaturas a las que se refiere este cálculo, estos datos se corresponden con intervalos en los que no observamos casi ningún evento caótico.

I.2.3 Coloides

El objetivo de la Parte II de la tesis era estudiar el diagrama de fase en un modelo de esferas blandas polidispersas. En un primer trabajo [Fero7b] anterior a mi tesis, se había caracterizado el diagrama de fases como función de la polidispersidad, δ, demostrando que aunque una polidispersidad muy alta inhibe la formación de cristales, para todo valor de δ aparece una transición fluido-sólido amorfo. Las características del posible sólido han sido muy discutidas, pasando desde sólidos amorfos, como sugería este trabajo, a patrones de fractonización, donde el sólido estaría formado por muchos cristales de la misma clase pero cada uno construido sólo con partículas de tamaños similares.

Estudiar la región de alta polidispersidad con una simulación numérica es extremadamente complicado. El principal problema proviene de que conviven dos tipos de transiciones en un rango muy pequeño de temperaturas. Por un lado, las partículas sufren la transición vítrea, lo que dispara los tiempos de difusión (las partículas quedan encerradas y apenas se desplazan), y por el otro lado tenemos la transición fluido-sólido. Las transiciones de primer orden en una simulación convencional vienen acompañadas de una divergencia exponencial de los tiempos característicos con el número de partículas, N, que en la práctica hace casi imposible la termalización incluso para tamaños relativamente pequeños. Como consecuencia de estos dos efectos, los tiempos de termalización se hacen monstruosos incluso para sistemas muy pequeños ($N \sim 500$ partículas). Por esta razón, la búsqueda de nuevas estrategias computacionales para tratar este tipo de sistemas fuera del retículo es fundamental en este campo. En efecto, el número de métodos eficientes disponibles en la literatura es muy reducido si lo comparamos con los problemas análogos en el retículo. Nosotros hemos dedicado la mayoría de nuestros esfuerzos precisamente en proponer nuevos algoritmos para el estudio de este tipo de sistemas.

Comenzamos con el problema que planteábamos antes, la estructura del sólido estable a muy alta polidispersidad. Mediante simulaciones canónicas en [Fero7b] sólo fue posible termalizar en la fase fluida, gracias a la utilización del algoritmo de *swap* [Grio1a, Fero6b, Fero7a]. Ni siquiera se intentó alcanzar el equilibrio en la fase sólida. Este era precisamente nuestro objetivo en [Fer10b]: estudiar la estructura de equilibrio de la fase sólida a muy alta polidispersidad.

I.2.3.1 Enfoque microcanónico

Para termalizar en esta región, necesitamos encontrar algún algoritmo que nos permita evitar la divergencia exponencial con N asociada a la transición de primer or-

den. La divergencia de tiempos aparece siempre que una o más fases son metaestables durante una misma simulación, como consecuencia del coste de energía libre asociado a la creación de interfaces entre dos fases. De esta manera, nuestra estrategia para sortear este efecto es proponer una colectividad en la que el fluido y el sólido no sean metaestables una vez fijados los parámetros de cada simulación. Nuestra apuesta fue aplicar el método microcanónico [MM07] que se resultado muy útil en transiciones de primer orden en sistemas magnéticos. De hecho, en este tipo de problemas en el retículo, la energía distinguía perfectamente las diferentes fases, era una buena coordenada de reacción.

Llegado a este punto, estudiamos numéricamente con el método microcanónico la transición fluido-sólido (referimos al lector al Capítulo 7 para detalles sobre el algoritmo o los métodos de simulación). Desde el primer momento uno observa que la energía no es capaz de evitar metaestabilidad, nuestras historias presentan *flip-flops* (saltos entre dos fases) y los tiempos de termalización crecen exponencialmente al aumentar el tamaño del sistema. Por lo tanto, desde el punto de vista de la colectividad, con la microcanónica no conseguimos un salto cualitativo con respecto a los tamaños estudiados en [Fer07b]. Sin embargo, gracias a la combinación de este método, con un algoritmo de Parallel Tempering en energías, fuimos capaces de termalizar en la fase sólida y obtener así la inversa de la temperatura de transición ($\beta_c = 1/T_c$) con mucha precisión, así como la estructura de la fase desordenada.

Una de las ventajas del método microcanónico, es que nos permite obtener $\beta(e)$ como función de la energía de forma muy precisa a partir de promedios temporales. Mostramos estas curvas en la Figura I.14. Más adelante podemos utilizar la falta de monotonicidad de estas curvas para definir una temperatura crítica (inversa), β_c^N, como la β a la cuál las dos fases coexisten con el mismo peso termodinámico. De esta manera, obtenemos β_c^N por medio de la construcción de Maxwell

$$0 = \int_{e_N^S(\beta_c^N)}^{e_N^L(\beta_c^N)} \mathrm{d}e \, \left(\beta(e) - \beta_c^N\right) , \tag{I.17}$$

donde las energías $e_N^L(\beta_c^N)$ ($e_N^S(\beta_c^N)$) corresponden cada una a la raíz más a la derecha (izquierda) de la ecuación $\beta(e) = \beta_c^N$ (véase el inset de la Figura I.14). Una vez obtenido β_c^N para varios tamaños podemos extrapolar el valor en el límite termodinámico, obteniendo $\beta_c = 4.626(2)$.

Finalmente estudiamos la estructura de la fase sólida. Presentamos en el panel superior izquierdo Figura I.15 una configuración típica de $N = 864$ partículas para baja energía. A primera vista las partículas siguen un patrón de fractonización muy complejo. Las 400 partículas de radio más pequeño (que se corresponden con las de índice $i < 400$ dado que en nuestro modelo el radio de cada partícula crece linealmente con i), junto con algunas de tamaño intermedio ($i \in [600, 725]$) no muestran ningún tipo de orden (panel de abajo). Por el contrario, las partículas con $i > 725$ y $i \in [400, 600]$ forman planos cristalinos bien definidos (panel superior derecho). Además, las partículas ordenadas y las desordenadas ocupan diferentes

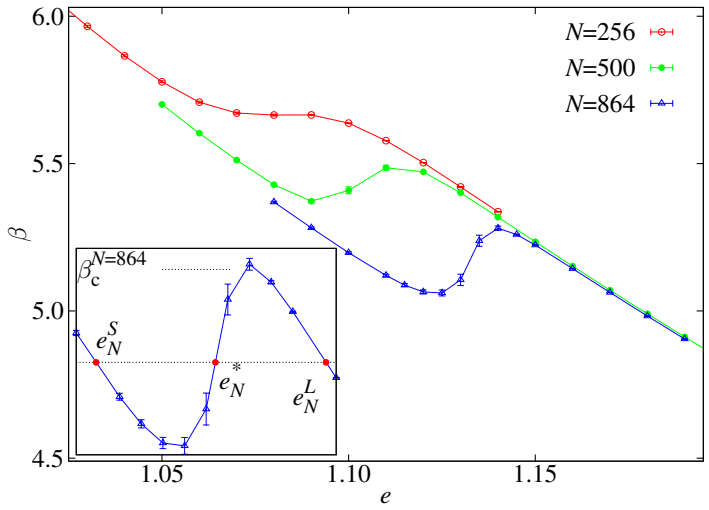

FIGURE 1.14: Efectos de tamaño finito en la construcción de Maxwell. **(Panel principal)** La inversa de la temperatura $\beta(e)$ como función de la densidad de energía e para varios tamaños de la muestra. **(Inset)** Versión agrandada de $\beta(e)$ para $N = 864$, incluyendo $\beta_c^{N=864}$ y las tres soluciones para $\beta(e) = \beta_c^N$: sólida $e_N^S(\beta_c^N)$, punto central $e_L^*(\beta_c^N)$ y fluida $e_N^L(\beta_c^N)$.

regiones de la muestra. Este extraño patrón de fractonización es confirmado por el parámetro de orden cristalino $Q_6(x)$ [Ste83], donde x hace referencia al subconjunto $\mathcal{I}(x)$ de partículas en las que está calculado (formado por las partículas cuyo índice i satisface $|i - xN| < 0.05N$). Mostramos $Q_6(x)$ en la Figura 1.16. Para $x < 0.45$ el parámetro cristalino decae con $1/\sqrt{N}$ (como esperaríamos en una estructura desordenada), mientras que para $x = 0.55$ y $x = 0.95$ obtenemos valores prácticamente independientes de N (como es esperable en una estructura cristalina).

En resumen, a bajas energías el sistema se divide espacialmente entre una parte amorfa y una parte cristalina. Además, las partículas se distribuyen según su tamaño siguiendo un estructura compleja no descrita por ningún patrón de fractonización que conozcamos.

I.2.3.2 Cristalización de esferas duras

La estrategia microcanónica nos ha permitido estudiar la fase de equilibrio pero a base de alargar tremendamente la duración de las simulaciones. Por esta razón, llegado a este punto volvemos al problema inicial: cómo conseguir evitar las metaestabilidades que nos dificultan tan terriblemente la termalización. Hemos visto que la energía no es capaz de forzar una única fase debido a que la fase de baja temperatura es, precisamente, una separación de fases.

Ahora bien, si las metaestabilidades observadas tienen realmente origen en la separación de fases fluido-sólido, debería aparecer exactamente la misma dificultad en cualquier tipo de problema de cristalización/fusión, sin importar el desorden. En particular, debería observarse en el caso más sencillo de todos: la cristalización de esferas duras. Para nuestra sorpresa, cuando nos pusimos a buscar en la lite-

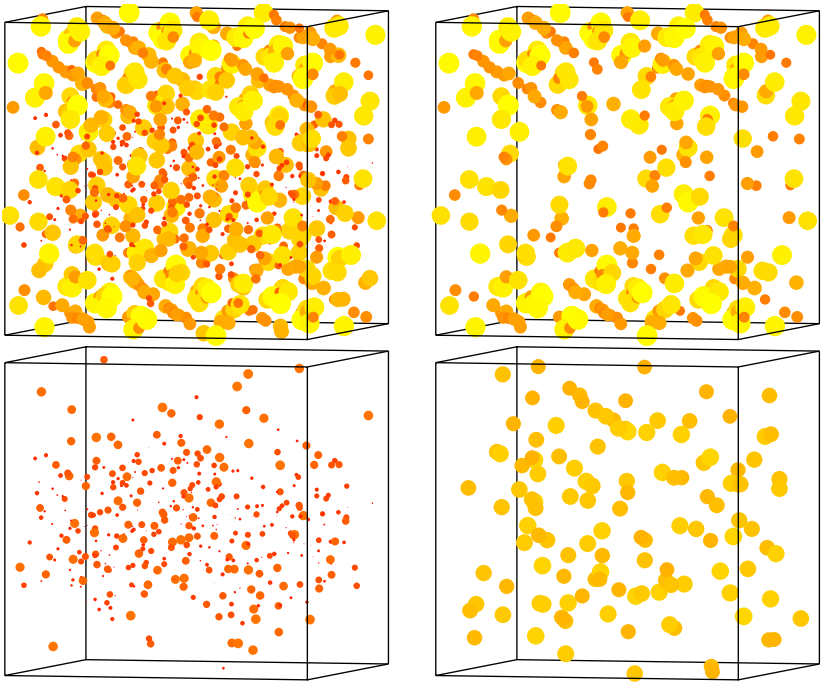

FIGURE I.15: Instantánea de una configuración típica ($N=864$, $e=1.01$). **(Arriba-izquierda)** todo el sistema. **(Arriba-derecha)** partículas con índice $i > 725$ e $i \in [400, 600]$. **(Abajo-izquierda)** partículas con $i < 400$. **(Abajo-derecha)** partículas con $i \in [600, 725]$.

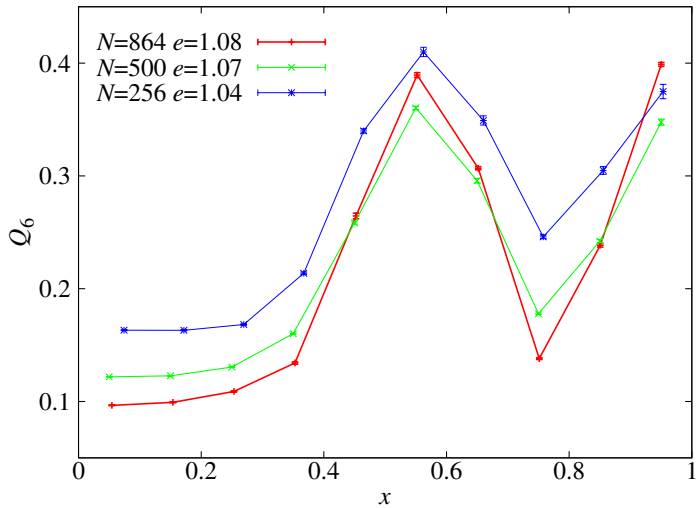

FIGURE I.16: El parámetro de orden cristalino $Q_6(x)$, como función de las partículas de tamaño x, para diferentes valores de N.

ratura un método eficiente para este problema nos encontramos con que aunque la existencia de la transición en esferas duras lleva demostrada desde 1968 [Hoo68], las mejores simulaciones de equilibrio hoy en día no eran capaces de superar las 500 partículas, puesto que sufrían exactamente el mismo problema que hemos descrito antes. Llegado este punto, decidimos dar un paso atrás, y controlar primero el problema en esferas duras, con el objetivo de aplicarlo posteriormente en el problema en el que estábamos trabajando hasta ahora.

Consideramos pues el problema de la cristalización de esferas duras monodispersas. Necesitamos encontrar una o varias coordenadas de reacción que sean capaces de imponer un único estado de equilibrio. Hasta este momento habíamos visto que ni la presión, ni el volumen, ni la energía cumplían esta condición. Necesitamos magnitudes que no puedan, en ningún caso tomar el mismo valor en un fluido y en un cristal. Los parámetros de orden cristalino cumplen esta propiedad.

Tras varios estudios preliminares vimos que necesitábamos fijar simultáneamente dos parámetros cristalinos para combinar tanto simetría rotacional con simetría cúbica para evitar metaestabilidades. Nuestra elección fueron los parámetros Q_6 [Ste83] y C [AU10]. Con ellos, y manteniendo también fijo el número de partículas N y la presión p construimos una nueva colectividad tethered $\hat{Q}_6\hat{C}NpT$.[4] En esta colectividad, los parámetros Q_6 y C pueden fluctuar pero con la restricción de que $\langle Q_6\rangle \approx \hat{Q}_6$ y $\langle C\rangle \approx \hat{C}$. Desde el punto de vista del algoritmo de Montecarlo, los pesos estadísticos son idénticos a los del *umbrella sampling* [Tor74, Wol95, Moro5, Choo6], pero a diferencia de este último método, utilizamos un formalismo de fluctuación disipación para obtener la energía libre de Helmholtz asociada a esta colectividad con mucha precisión a partir de promedios estadísticos obtenidos durante la simulación.

Formalmente, el promedio tethered de cualquier observable $O(\boldsymbol{R}, V, p)$ está definido como

$$\langle O\rangle_{\hat{Q}_6,\hat{C},p} = \frac{\int dV \mathrm{d}\boldsymbol{R}\; O(\boldsymbol{R},V,p)\;\omega_N(\boldsymbol{R},V;\hat{Q}_6,\hat{C},p)}{\int \mathrm{d}V\mathrm{d}\boldsymbol{R}\;\omega_N(\boldsymbol{R},V;\hat{Q}_6,\hat{C},p)}, \tag{I.18}$$

con pesos

$$\omega_N(\boldsymbol{R},V;\hat{Q}_6,\hat{C},p) \;\; = \tfrac{N\alpha}{2\pi} H(\boldsymbol{R}) \mathrm{e}^{-\beta pV} \mathrm{e}^{-\frac{\alpha N}{2}\left[\hat{Q}_6 - Q_6(\boldsymbol{R})\right]^2} \mathrm{e}^{-\frac{\alpha N}{2}\left[\hat{C} - C(\boldsymbol{R})\right]^2}. \tag{I.19}$$

El potencial efectivo está dado por

$$\mathrm{e}^{-N\Omega_N(\hat{Q}_6,\hat{C},p)} = \frac{\beta p}{N!\Lambda^{3N}} \frac{\alpha N}{2\pi} \int \mathrm{d}V \int \mathrm{d}\boldsymbol{R}\, \mathrm{e}^{-\beta pV}\, \mathrm{e}^{-\beta U(\boldsymbol{R})}\, \mathrm{e}^{-\frac{\alpha N}{2}\left[\left\{\hat{Q}_6 - Q_6(\boldsymbol{R})\right\}^2 + \left[\hat{C} - C(\boldsymbol{R})\right]^2\right]}. \tag{I.20}$$

Podemos relacionar este potencial con la densidad de energía libre de Gibbs $g_N(p,T)$ por medio de la expresión

$$\Upsilon_{NpT} = e^{-Ng_N(p,T)} = \int \mathrm{d}\hat{Q}_6\, \mathrm{d}\hat{C}\; e^{-N\Omega_N(\hat{Q}_6,\hat{C},p)}, \tag{I.21}$$

[4] Aunque en esferas duras la temperatura no tiene sentido físico, seguimos el criterio habitual en física química de mantener la temperatura en las expresiones.

que aplicando una aproximación de punto silla conduce a

$$g_N(p,T) = \Omega_N(\hat{Q}_6^*, \hat{C}^*, p) + O(1/N)\,, \tag{I.22}$$

donde $(\hat{Q}_6^*, \hat{C}^*, p)$ es el mínimo absoluto de $\Omega_N(\hat{Q}_6, \hat{C}, p)$, con respecto a $\hat{Q}_6$ y $\hat{C}$. Por lo tanto, las coordenadas $(\hat{Q}_6^*(p), \hat{C}^*(p))$ se obtienen buscando los puntos que cumplen $\boldsymbol{\nabla}\Omega_N = 0$.

Además, puesto que somos capaces de evitar saltos entre fases, y por tanto la función de distribución de probabilidad del volumen V tiene un único pico, podemos extrapolar valores medios a presiones $p + \delta p$ utilizando únicamente datos de una simulación realizada a presión p por medio del método de repesado de histogramas [Fal82, Fer88],

$$\langle O \rangle_{\hat{Q}_6, \hat{C}, p+\delta p} = \frac{\langle O\, \mathrm{e}^{-\beta \delta p V} \rangle_{\hat{Q}_6, \hat{C}, p}}{\langle \mathrm{e}^{-\beta \delta p V} \rangle_{\hat{Q}_6, \hat{C}, p}}. \tag{I.23}$$

Una de las principales ventajas del método tethered, es que los gradientes de $\Omega_N(\hat{Q}_6, \hat{C}, p)$ se pueden medir durante la simulación de la forma

$$\begin{aligned} \boldsymbol{\nabla}\Omega_N(\hat{Q}_6, \hat{C}, p) &= \left(\frac{\partial \Omega_N(\hat{Q}_6, \hat{C})}{\partial \hat{Q}_6}, \frac{\partial \Omega_N(\hat{Q}_6, \hat{C})}{\partial \hat{C}} \right) \\ &= \left(\langle \alpha\, (\hat{Q}_6 - Q_6) \rangle_{\hat{Q}_6, \hat{C}, p}, \langle \alpha\, (\hat{C} - C) \rangle_{\hat{Q}_6, \hat{C}, p} \right). \end{aligned} \tag{I.24}$$

La ecuación (I.22) relaciona (con correcciones que se anulan con $1/N$) el potencial efectivo con el potencial químico $\beta g(p,T)$ en los mínimos de $\Omega_N(\hat{Q}_6, \hat{C}, p)$. Puesto que cerca de la coexistencia de fases, Ω_N tiene dos mínimos, el del fluido y el del cristal FCC, la condición estándar de igualdad de potenciales químicos en la coexistencia de fases, equivale aquí a $\Omega_N^{\text{fluid}} = \Omega_N^{\text{FCC}}$.

Llegados a este punto la estrategia está clara, podemos calcular fácilmente la diferencia de potencial efectivo entre el fluido y el cristal FCC, simplemente integrando $\boldsymbol{\nabla}\Omega_N$ a lo largo de cualquier curva que una los dos mínimos. De esta manera, podemos recuperar $\Delta\Omega(p) = \Omega_N^{\text{FCC}} - \Omega_N^{\text{fluid}}$ y obtener $p_{\text{co}}^{(N)}$ buscando la presión a la cuál $\Delta\Omega(p) = 0$.

Mostramos en la Figura I.17 el mapa de gradientes $\boldsymbol{\nabla}\Omega_N$ en $p = p_{\text{co}}^{(N)}$. Los dos mínimos locales se obtienen donde $\boldsymbol{\nabla}\Omega_N = 0$. Como curva de integración elegimos la línea recta que une los dos mínimos. Parametrizamos la curva por con nuestra coordenada de reacción S ($S = 0$: fluido, $S = 1$: FCC). Aunque para calcular la diferencia de potencial no importa qué curva de integración elijamos, para calcular la tensión superficial necesitamos elegir justamente esta línea recta. En efecto, la coexistencia de fases física es una suma convexa de las dos fases puras [Rue69], así dada la aditividad de Q_6 y C, tenemos que S representa la fracción de partículas en la fase sólida. Presentamos en el panel superior de la Figura I.18 la proyección de $\boldsymbol{\nabla}\Omega_N$ sobre la línea de integración, $\boldsymbol{\nabla}_S\Omega_N$,

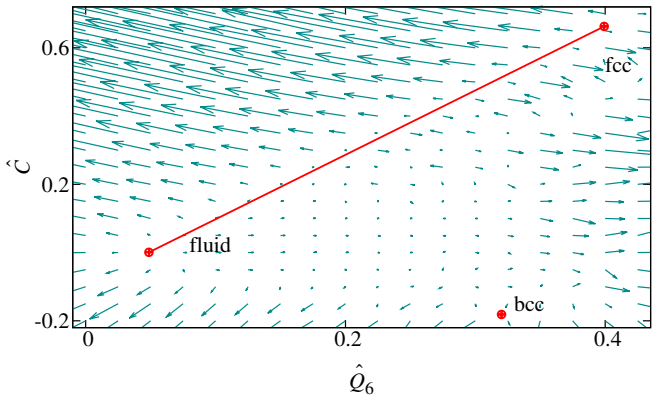

FIGURE I.17: **Top:** mapa de gradientes $\nabla\Omega_{N=256}$, junto con los puntos correspondientes a los mínimos de potencial del fluido y los cristales FCC y BCC. Para mejorar la visibilidad, los gradientes aparecen divididos por un factor $\alpha = 200$.

para la presión de simulación. Podemos extrapolar los gradientes a presiones vecinas utilizando (I.23) y con ellos obtener $\Delta\Omega_N$ como función de la presión. Mostramos estas curvas en el panel inferior de la Figura I.18. Finalmente, podemos calcular la presión de coexistencia, $p = p_{\text{co}}^{(N)}$, buscando la presión que cumple $\Delta\Omega_N\left(p_{\text{co}}^{(N)}\right) = 0$. Una vez calculada esta presión para todos los tamaños, probamos un fit a $p_{\text{co}}^{(N)} = p_{\text{co}}^{\infty} + a_1/N + a_2/N^2$ [Bor92] para $256 \leq N \leq 2916$ con lo que obtenemos

$$p_{\text{co}}^{\infty} = 11.5727(10)\,.$$

Este valor es más preciso (y compatible) con las predicciones de otros autores. La mejor predicción de equilibrio hasta ahora era bastante poco precisa $p_{\text{co}}^{\infty} = 11.50(9)$ [Wiloo]. Para una comparación más justa tendríamos que irnos al método (de no equilibrio) de la coexistencia directa $p_{\text{co}}^{\infty} = 11.576(6)$ [ZT10]. Nos gustaría hacer notar que este último trabajo, para alcanzar un error tan pequeño (pero aún así todavía seis veces mayor que nuestro error) se tuvieron que simular sistemas de hasta $N = 1.6 \times 10^5$ partículas.

Finalmente calculamos la energía libre interfacial, γ: el coste de energía libre por unidad de área de crear un interfaz fluido-cristal. El cálculo de esta magnitud ha sido bastante difícil para esferas duras. De hecho, las predicciones dadas por diferentes autores son mutuamente incompatibles [Dav00, Mu05, Dav10].

La principal dificultad para obtener γ es la necesidad de tener configuraciones mixtas de las dos fases. En cualquier sistema con condiciones de contorno periódicas, tienen que aparecer transiciones geométricas entre configuraciones donde el núcleo de cristal (dentro de una matriz líquida o viceversa) tiene forma de burbuja, cilindro o banda. En efecto, según S crece (la proporción de cristal), la energía libre se minimiza adoptando diferentes geometrías. Presentamos un ejemplo de estas diferentes configuraciones en la Figura I.19. Este fenómeno es el origen de los

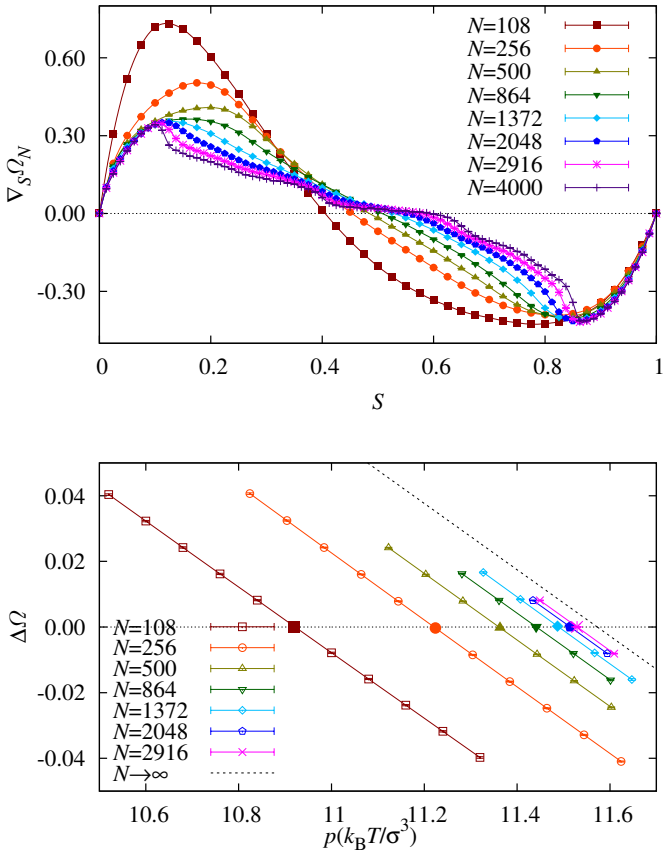

FIGURE 1.18: (**Arriba**) $\boldsymbol{\nabla}\Omega_N$ proyectada sobre la línea fluido-FCC, $\boldsymbol{\nabla}_S\Omega_N$, frente al parámetro de línea S ($S = 0$: fluido, $S = 1$: FCC), para todos los tamaños de sistema en nuestra presión de simulación. (**Abajo**) Diferencia de potencial efectivo $\Delta\Omega(p) = \Omega^{\text{FCC}} - \Omega^{\text{fluid}}$, como función de la presión. En p_{co}^N, $\Delta\Omega_N = 0$. Los valores obtenidos a la presión de simulación se corresponden con los puntos grandes y llenos.

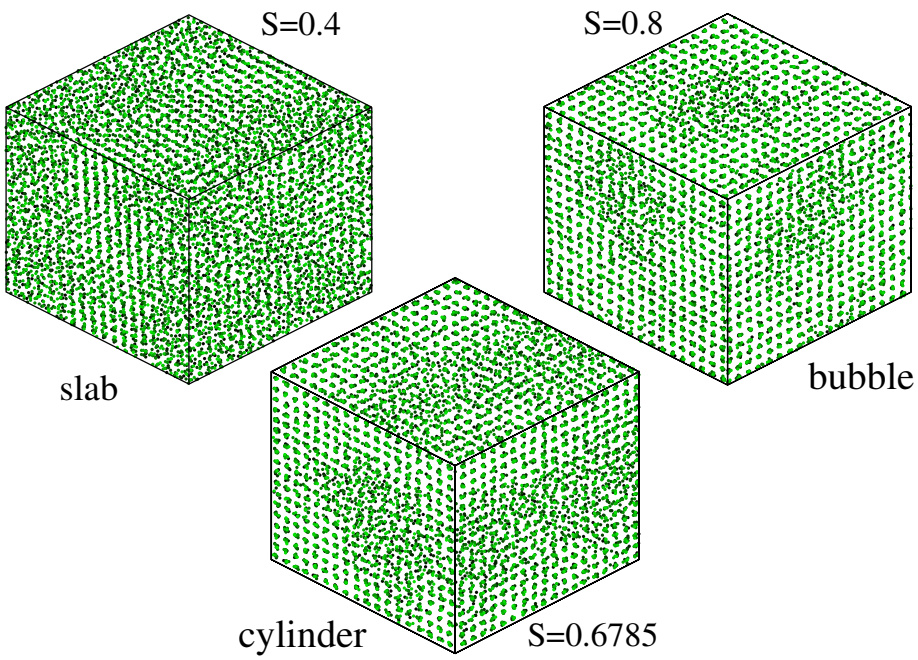

FIGURE 1.19: Instantánea de los tres tipos de configuraciones mixtas para $N = 2916$ partículas. Las partículas se muestran proyectadas en las tres direcciones Cartesianas. Además, para mejorar la visibilidad radios de las partículas son una fracción del real, y la oscuridad es función creciente de la distancia al plano de proyección.

saltos que aparecían para los sistemas mayores en las curvas de $\boldsymbol{\nabla}_S \Omega_N$ del panel superior de la Figura 1.18.

Podemos utilizar estas configuraciones inhomogéneas para calcular γ, en particular, la configuración de banda tiene dos superficies de tamaño L^2 de contacto entre el fluido y el cristal. Podemos así calcular el coste de energía libre de formar esos dos interfaces si comparamos el potencial efectivo de estas configuraciones con las de un cristal perfecto. Así, en $p_{\mathrm{co}}^{(N)}$

$$\gamma_{\{100\}}^{(N)} = k_{\mathrm{B}} T \, N \left(\Omega_{s^*} - \Omega_{\mathrm{FCC}} \right) / \left(2 \left\langle N v \right\rangle_{S^*}^{2/3} \right), \tag{1.25}$$

donde $S^* \approx 0.5$, es la solución central de $\boldsymbol{\nabla}_S \Omega_N = 0$. Finalmente, podemos extrapolar el límite de $N \to \infty$ por medio del ajuste de $\gamma_{\{100\}}^{(N)}$ para $256 \leq N \leq 2916$ a [Bil94]

$$\frac{\gamma_{\{100\}}^{(N)} \sigma^2}{k_{\mathrm{B}} T} = \frac{\gamma_{\{100\}} \sigma^2}{k_{\mathrm{B}} T} + \frac{a_2 - \log N}{6 N^{2/3}} + \frac{a_3}{N} + \frac{a_4}{N^{4/3}} + \ldots, \tag{1.26}$$

obteniendo $\gamma_{\{100\}} = 0.636(11) k_{\mathrm{B}} T / \sigma^2$. Este resultado es compatible con $\gamma_{\{100\}} = 0.64(2)$ [Muo5], $\gamma_{\{100\}} = 0.619(3)$ [Caco3] y $\gamma_{\{100\}} = 0.639(11)$ [Här12], pero no con $\gamma_{\{100\}} = 0.5820(19)$ [Dav10].

I.2.4 Quantum Annealing con interacciones transversales de muchos cuerpos

Siguiendo con nuestra estrategia de búsqueda de nuevos algoritmos para estudiar la transición vítrea, fijamos también nuestra atención en la prometedora computación cuántica, y las nuevas oportunidades que ésta abre.

Dado nuestra experiencia en mecánica estadística y en algoritmos de Montecarlo, la aproximación más cercana a este campo pasa por el método de quantum annealing (también conocido como computación cuántica adiabática). Este algoritmo es la versión cuántica del algoritmo clásico de annealing, en el que se introduce una temperatura ficticia que permite excitaciones térmicas. Estas fluctuaciones ayudan a saltar las barreras presentes en la energía libre, y así a moverse más fácilmente entre todos los mínimos relativos del problema. Posteriormente, esta temperatura se va disminuyendo muy lentamente, de manera que la simulación se mueva lentamente hasta encontrar el mínimo absoluto (el estado de equilibrio en nuestro caso). Este método, pese a ser muy general, falla cuando se trata de aplicar en problemas donde las barreras de energía libre son muy altas, ya que la dinámica de la simulación de Montecarlo se queda estancada en alguno de los valles de la energía libre conduciendo finalmente a un estado que no es el mínimo absoluto. La idea del quantum annealing (QA) [Kad98] es similar, pero esta vez, en vez de introducir fluctuaciones térmicas, se introducen fluctuaciones cuánticas. La mecánica cuántica trae consigo el efecto túnel, por lo que en vez de saltar las barreras, podemos traspasarlas.

Tradicionalmente el QA se ha estudiado con el siguiente formalismo. Se introduce un Hamiltoniano dependiente del tiempo

$$\hat{H}(t) = s(t)\hat{H}_0 + [1 - s(t)]\,\hat{V}, \tag{I.27}$$

donde $\hat{H}_0$ es el Hamiltoniano que queremos minimizar cada caso (o la función de coste, de considerar un problema más general de minimización) y $\hat{V}$ representa las fluctuaciones cuánticas. Este término $\hat{V}$ en principio es arbitrario, mientras no conmute con el Hamiltoniano del problema $\hat{H}_0$, y su estado fundamental sea único y trivial. En los problemas habitualmente considerados (y en el problema que tratamos aquí), $\hat{H}_0$ sólo depende de las componentes z de la matriz de Pauli $\hat{\sigma}_i^z$, donde el índice $i(= 1, \ldots, N)$ recorre todos los espines del sistema. Por esta razón, la elección habitual para $\hat{V}$ es una interacción con un campo transversal de la forma

$$\hat{V}_{\mathrm{TF}} \equiv -\sum_{i=1}^{N} \hat{\sigma}_i^x, \tag{I.28}$$

donde los $\hat{\sigma}_i^x$ $(i = 1, \ldots, N)$ son las componentes x de la matriz de Pauli. Con este término, el algoritmo de QA es muy intuitivo. Así como en el annealing clásico introducíamos una temperatura que íbamos desconectando lentamente, ahora introducimos un campo magnético en la dirección x y lo vamos apagando lentamente por medio del parámetro de control $s(t)$. Así, en $t = 0$, $s(t)$ es $s(0) = 0$, de manera

que $\hat{H}(0) = \hat{V}$, y se va incrementando lentamente con el tiempo hasta que alcanza la unidad en el tiempo τ cuando $\hat{H}(\tau) = \hat{H}_0$, el Hamiltoniano del problema. Por simplicidad, consideramos que el parámetro de control varía linealmente con el tiempo de la forma $s(t) = t/\tau$.

La evolución de un estado cuántico, $|\Phi(t)\rangle$, está dada por la ecuación de Schrödinger,

$$\mathrm{i}\frac{\mathrm{d}}{\mathrm{d}t}|\Phi(t)\rangle = \hat{H}(t)\,|\Phi(t)\rangle\,,\ 0 \leq t \leq \tau. \tag{I.29}$$

De esta forma, el estado inicial $|\Phi(0)\rangle$ es el estado fundamental de $\hat{V}$, que lo conocemos. Si el parámetro $s(t)$ varía muy lentamente (τ muy grande) el estado en cada momento estará muy próximo al estado fundamental de $\hat{H}(t)$. De esta manera, uno puede moverse adiabáticamente desde el estado fundamental inicial (conocido), hasta el estado fundamental del Hamiltoniano problema (desconocido). El teorema adiabático nos asegura que, con este proceso, permaneceremos en el estado fundamental instantáneo en todo momento mientras $\tau \gg \Delta_{\min}^{-2}$, donde $\Delta_{\min}$ es la diferencia de energías entre el estado fundamental y el primer estado excitado. Claramente, para que este algoritmo tenga utilidad práctica en una simulación, $\Delta_{\min}$ no puede disminuir demasiado rápido con el tamaño del sistema, N. En particular, si este *gap* decae exponencialmente con N, como ocurre en la mayoría de las transiciones de primer orden, el tiempo de la simulación crecería exponencialmente con N y el QA no presentaría ninguna ventaja sustancial.

Pese a que los inicios del QA fueron muy prometedores, según se ha ido incrementando la complejidad de los problemas estudiados, han ido apareciendo más y más transiciones cuánticas de primer orden en los parámetros de control [You10, Hen11, Jör08, Jör10a, Jör10b], arruinando así, en la práctica, el rendimiento de este algoritmo. De hecho, se ha llegado a postular que la aparición de estas transiciones cuánticas, es una propiedad de los problemas con paisajes de energía libre más complicados [You10, Hen11, Jör08, Jör10a, Jör10b].

El escenario se hizo aún más pesimista cuando en [Jör10a] se demostró que este problema aparecía incluso en un modelo cuyo estado fundamental era trivial, el modelo ferromagnético p-espín [Jör10a]. Dada la simplicidad de este problema, resulta el mejor banco de pruebas para estudiar las causas del fracaso del QA. De hecho, muy recientemente [Sek12], se ha demostrado en este modelo que la transición de primer orden puede evitarse si además de introducir fluctuaciones vía un campo transverso, se introducen fluctuaciones cuánticas anti-ferromagnéticas. De esta manera, el fracaso del QA no sería tal, sino de la formulación tradicional de éste (I.27).

En esta tesis, hemos profundizado en este problema, estudiando toda una familia de términos de fluctuaciones alternativos. Demostramos que con todos ellos podemos evitar cruzar una transición de primer orden, y sufrir así la divergencia de tiempos asociada. Gracias a considerar dos parámetros de control, somos capaces encontrar trayectorias de annealing que sólo cruzan transiciones de segundo orden, que también ralentizan la dinámica, pero sólo polinómicamente con N.

De esta manera, consideramos el problema de encontrar el estado fundamental

del modelo ferromagnético p-espín (para p impar)

$$\hat{H}_0 = -N \left(\frac{1}{N} \sum_{i=1}^{N} \hat{\sigma}_i^z \right)^p . \tag{I.30}$$

El estado fundamental $|\Phi_0\rangle$ de este modelo es único y está dado por el de todos los espines alineados en la dirección z. Buscamos este estado mediante QA por medio del Hamiltoniano

$$\hat{H}(s,\lambda) = s\left[\lambda \hat{H}_0 + (1-\lambda)\hat{V}_k\right] + (1-s)\hat{V}_{\mathrm{TF}}, \tag{I.31}$$

donde hemos introducido un término extra con respecto a (I.27),

$$\hat{V}_k = +N \left(\frac{1}{N} \sum_{i=1}^{N} \hat{\sigma}_i^x \right)^k , \tag{I.32}$$

inspirado en las fluctuaciones antiferromagnéticas de [Sek12], pero que depende de un parámetro k. El estado fundamental de este término $|\Phi_k\rangle$ depende del valor de k. Si k es impar, los espines estarán alineados según la dirección negativa del eje z. Por el contrario, si es par, se corresponderá con el estado con espín total $\sum_{i=1}^{N} \sigma_i^x = 0$ si N es par, o $\sum_{i=1}^{N} \sigma_i^x = \pm 1$ si N es impar.

El diagrama de fases de $\hat{H}(s,\lambda)$ para cualquier p y k con respecto al espacio de parámetros (s,λ) se puede obtener analíticamente tanto con cálculo semi-clásico, como cuánticamente con la fórmula de Trotter-Suzuki [Suz76]. Los detalles de ambos cálculos están incluidos en el Capítulo 9 y en el Apéndice G, respectivamente. Tras minimizar la energía, obtenemos las siguientes fases clasificadas en términos de su imanación total $\boldsymbol{m} = (m^x, 0, m^z)$:

- Una fase paramagnética cuántica (QP^+) con $m^z = 0$ y $m^x = 1$.
- Sólo para el caso de k impar, una segunda fase paramagnética con $m^z = 0$ y $m^x = -1$.
- Una (o dos) fase(s) ferromagnética(s) (F) con $m^z > 0$.

La fase ferromagnética se obtiene resolviendo la ecuación

$$p\,s\,\lambda \left[1 - (m^z)^2\right]^{p/2-1} m^z + k\,s\,(1-\lambda)(m^z)^{k-1}\theta_0 - 1 + s = 0, \tag{I.33}$$

que para el límite $p \to \infty$ tiene dos soluciones, correspondientes a dos fases ferromagnéticas

- F: $m^z \to 1$ y $m^x \to 0$.
- F': $m^z = \left[\frac{1-s}{k\,s\,(1-\lambda)}\right]^{\frac{1}{k-1}}$ y $m^x = \sqrt{1-(m^z)^2}$.

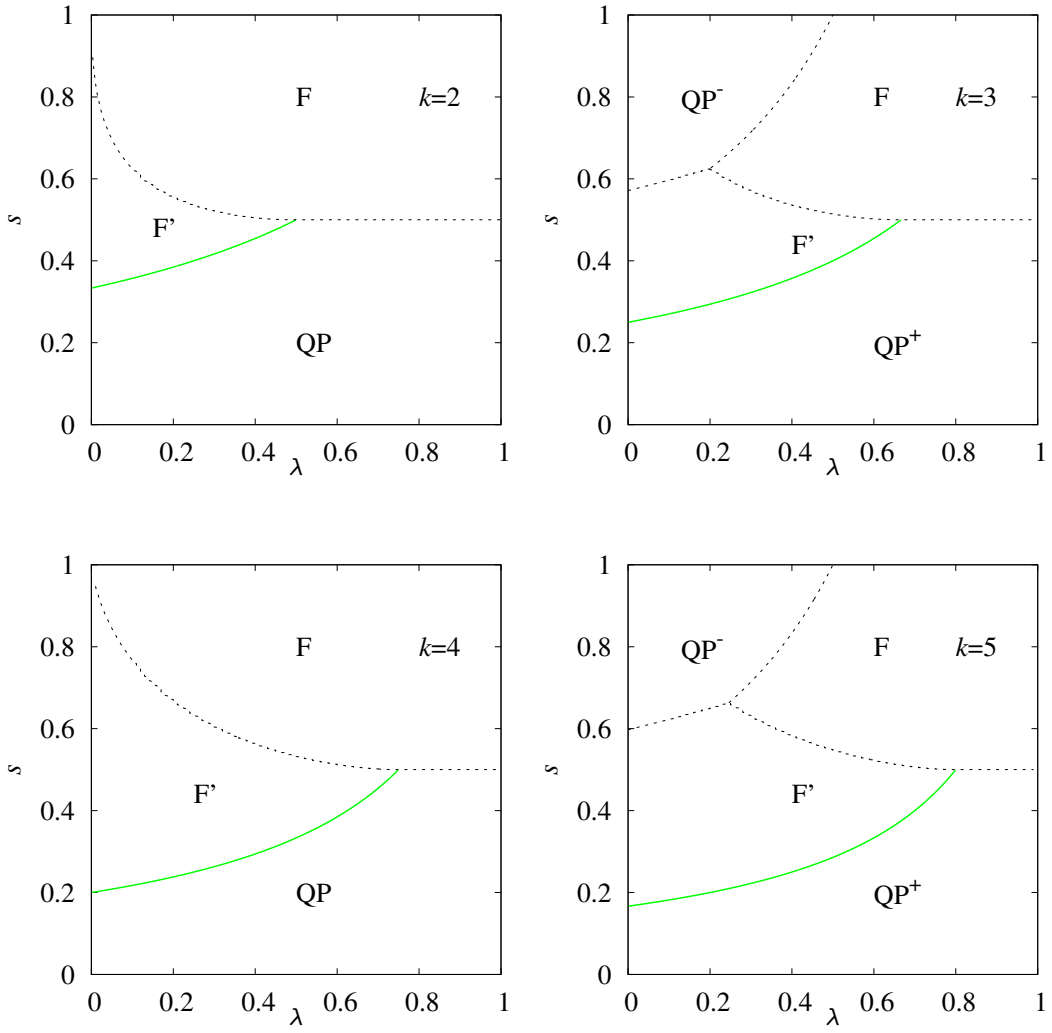

FIGURE 1.20: Diagrama de fases para el límite $p \to \infty$. Las líneas negras se refieren a transiciones de primer orden, mientras que la línea verde es de segundo orden.

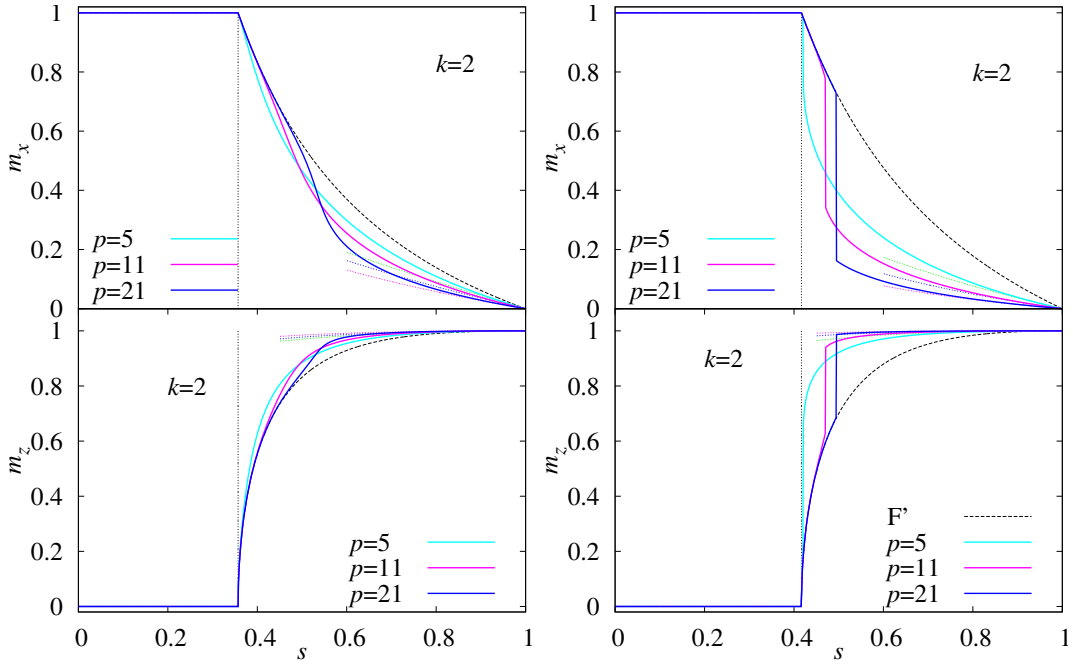

FIGURE I.21: Imanación como función de s para $k = 2$ y para dos valores de λ. **(Izquierda)** La trayectoria sólo detecta una única fase ferromagnética para $\lambda = 0.1$. **(Derecha)** Para todos los valores de p observamos una transición de fase entre dos fases ferromagnéticas cuando $\lambda = 0.3$.

Las transiciones $F - QP^{\pm}$, $F - F'$ serían de primer orden, mientras que la transición $F' - QP^{+}$ es de segundo orden. Mostramos el diagrama de fases en la Figura I.20. De acuerdo con estos diagramas, no es posible encontrar ninguna trayectoria $(s(t), \lambda(t))$ que pueda evitar cruzar una transición de primer orden en el caso de $p \to \infty$.[5]

Sin embargo, cuando consideramos el caso para p finito, la ecuación (I.33) tiene una única solución ferromagnética (que debe ser calculada numéricamente) para un amplio espacio de parámetros como mostramos en la Figura I.21-izquierda. Por otro lado, según p crece, o nos acercamos a la región inferior de la transición $F - F'$ observada en el límite de $p \to \infty$, vuelven a ser posibles dos soluciones ferromagnéticas como las que obteníamos para el caso $p \to \infty$, pero localizadas sólo en una región del espacio. La presencia de dos fases ferromagnéticas origina una transición de fase entre ambas, véase la Figura I.21-derecha.

Esta idea queda más clara en la Figura I.22 donde mostramos el diagrama de fases para $k = 2$, 3, 4 y 5. De acuerdo con este resultado, para k par, siempre es posible encontrar una trayectoria de annealing que sea capaz de evitar sufrir una transición de primer orden, aunque el espacio disponible disminuye a medida que p aumenta. En el caso de k impar, esto sólo es posible hasta cierto valor de p en el que la transición entre fases ferromagnéticas se junta con la fase QP^{-}.

[5] A excepción de la trayectoria trivial sin fluctuaciones cuánticas de $\lambda = 0$ y $s = 1$.

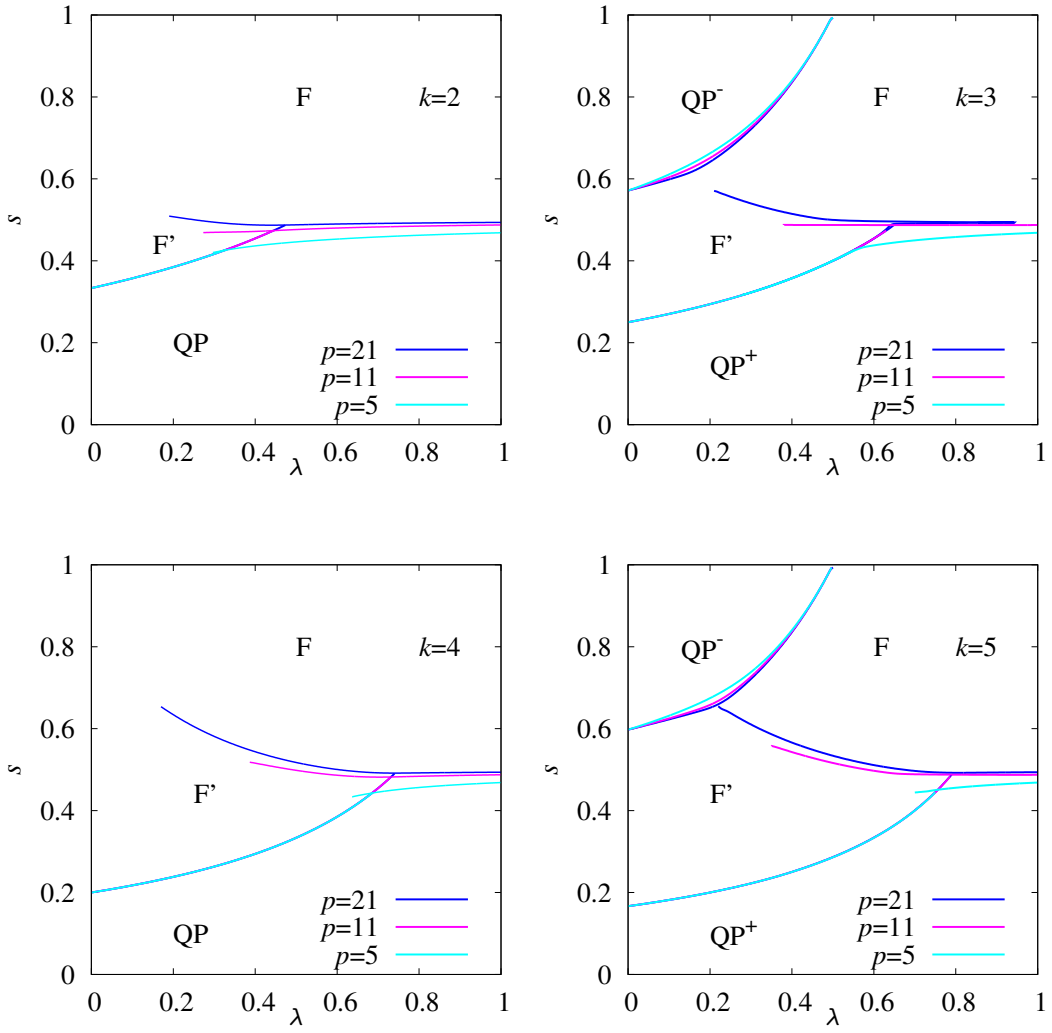

FIGURE 1.22: Diagrama de fases para $k = 2$, 3, 4 y 5. La transición F'-QP^+ es de segundo orden, todas las demás son de primer orden.

Puesto que la solución es válida tanto para k par como para impar, podemos concluir que el éxito o fracaso del sistema no está, al menos únicamente relacionado con la similitud entre los estados fundamentales de los diferentes términos añadidos, como se había postulado en [Bap12], ya que el overlap del estado fundamental de V_k para k impar, con el de H_0 está igual de suprimido en N como el del V_{TF} (el que se utiliza para la formulación tradicional). A raíz de estos resultados, es necesaria la interacción múltiple entre espines.

I.3 Conclusiones

Finalmente, aprovechamos para resumir las conclusiones obtenidas en cada uno de los capítulos de la tesis.

I.3.1 Modelo del Hipercubo

Hemos estudiado un nuevo modelo de campo medio para vidrios de espín sobre un hipercubo unitario en D-dimensiones. La principal ventaja de este modelo es que, dada su distribución espacial, tiene una noción natural de distancia (característica rara en modelos de campo medio).

Hemos probado que, dada la geometría del problema, cualquier mecánica estadística sobre modelos en el hipercubo con conectividad aleatoria sufre efectos de tamaño finito enormes. La solución presentada pasa por restringir el estudio a aquellos grafos sobre donde el número de vecinos está fijo. Generar estos grafos no es trivial, pero hemos resuelto el problema con un algoritmo dinámico de Montecarlo. Aunque no sabemos si el conjunto de grafos accesibles por este método es completo, hemos comprobado que los hipercubos generados son isotrópicos, y que el modelo de Edwards-Anderson definido sobre estos grafos cumple todos los checks de consistencia considerados.

Una vez definido el modelo, hemos estudiado numéricamente la dinámica fuera del equilibrio en la fase vidrio de espín. Las tres características principales son: (i) el envejecimiento consiste en el crecimiento de una longitud de coherencia, como en los sistemas tridimensionales, (ii) el scaling a dos tiempos de la función de correlación implica una infinidad de sectores temporales, y (iii) se ha observado el propagador p^4. Además, hemos estudiado los efectos de volumen finito en nuestro modelo, encontrando que podemos explicar nuestros datos con un ansatz de tamaño finito extremadamente simple.

Siendo este modelo de campo medio, está regido por la teoría RSB. Por lo tanto, combinado con su noción de distancia, se convierte en un patio de pruebas para estudiar la dinámica de no equilibrio en sistemas RSB.

I.3.2 Caos en temperatura

El caos en temperatura es un fenómeno de eventos extremos. Cuando ocurre, sus efectos son muy fuertes y se pueden sentir incluso a distancias muy cortas, como podemos confirmar con las función de correlación espacial a dos temperaturas. Han sido cruciales dos ingredientes para alcanzar esta conclusión. Primero, gracias al superordenador JANUS, hemos tenido acceso a configuraciones mucho más grandes que todo lo estudiado hasta la fecha, y además termalizadas a temperaturas mucho más bajas [ÁB10a, ÁB10b]. En segundo lugar, hemos considerado nuevas herramientas de análisis estadístico basadas en un funcional de grandes desviaciones.

Con este enfoque, somos capaces de cuantificar la dependencia del funcional de grandes desviaciones con el tamaño del sistema, un paso crucial para encontrar un diccionario de tiempo-longitud [Fra98, ÁB10a, ÁB10b, Bar01] para protocolos donde la temperatura varía con el tiempo. La existencia de este diccionario es esencial para poder diseñar experimentos capaces de detectar el caos en temperatura en un vidrio de espín real.

Uno de los resultados más sorprendentes de nuestro análisis ha sido que la longitud de caos escala con el tamaño del sistema como $\xi_C \propto L^a$, con $a \approx 0.4$: es divergente en el límite termodinámico, pero mucho menor que L. Esta dualidad será probablemente muy importante para interpretar los contradictorios experimentos de rejuvenecimiento y memoria [Jon98]. De hecho, aunque el scaling $\xi_C \propto L^a$ proviene de una extrapolación a $L \to \infty$ (extrapolación que es comprometida aún en campo medio), sabemos que la extrapolación relevante en un experimento no corresponde a este límite, sino a $L \sim 100$ espaciados de red [ÁB10a].

I.3.3 Esferas blandas polidispersas

Hemos estudiado un modelo de esferas blandas para líquidos y coloides en la colectividad microcanónica para polidispersidad al 24%. Hemos demostrado gracias a una construcción de Maxwell y extrapolaciones de tamaño finito, que la temperatura crítica para la separación de fase amorfo-cristal cae por debajo de la transición vítrea dinámica, lo que dificulta dinámicamente la observación de esta separación de fases.

A bajas temperaturas, el sistema se divide espacialmente entre una parte amorfa y una cristalina, lo que concuerda con resultados anteriores [Fer07b]. Este estado amorfo es un fluido estable por debajo de la transición vítrea dinámica, lo que lo convierte en un buen candidato para sufrir una transición vítrea termodinámica. Por otro lado, el sólido con separación de fases tiene cierta estructura cristalina. Las diferentes fases que conforman el sólido tienen polidispersidades menores que las del fluido. De hecho, las partículas se distribuyen espacialmente de acuerdo al sus tamaños siguiendo patrones complejos no descritos por ningún escenario de fractonización que conozcamos.

Somos capaces de obtener el sólido de equilibrio pero sólo para tamaños menores

de lo que esperábamos. En efecto, el objetivo de aplicar el algoritmo microcanónico no era otro evitar metaestabilidades, pero la separación de fases frustra nuestro enfoque. Fue este problema precisamente el que nos condujo a investigar la cristalización de esferas duras.

I.3.4 Cristalización de esferas duras

Hemos utilizado el tethered MC [Fero9b, MM11] para estudiar la cristalización de esferas duras. Con este enfoque, podemos movernos suavemente desde el fluido hasta el sólido variando una coordenada de reacción (construida a partir de dos parámetros de orden cristalino). El tethered MC se trata de una simplificación del conocido umbrella sampling, en particular, permite fijar muchos parámetros de orden sin sacrificar precisión ni complicar el formalismo. Al contrario que los trabajos anteriores, somos capaces de equilibrar (encontramos resultados independientes de las condiciones de partida) no sólo a la hora de formar cristales, sino también configuraciones mixtas fluido-cristal con interfaces entre ambos. Nuestra estimación de la presión de coexistencia es, de lejos, la más precisa disponible hasta la fecha. Por otro lado, nuestra estimación de la energía libre interfacial es compatible con la mayoría (aunque no todos) las determinaciones recientes. Si quisiéramos alcanzar sistemas aún mayores, tendríamos que incluir más parámetros de orden, lo que apenas supondría cambios en nuestra estrategia. Este nuevo método se podría generalizar sin mucho problema para estudiar otros líquidos simples, así como investigar la transición vítrea.

I.3.5 Quantum Annealing

Hemos investigado el origen del fracaso de la formulación tradicional del algoritmo de quantum annealing (con un término de campo transversal) en el modelo ferromagnético de alcance infinito p-espín. Hemos demostrado que es posible encontrar trayectorias que eviten encontrarse con ninguna transición de primer orden, si se introduce un segundo término conductor en el problema. Este término adicional favorece la aparición de una transición de segundo orden que no daña el rendimiento del algoritmo.

Estudiamos toda una familia de nuevos términos conductores, concluyendo que la solución al problema presentada por Seki and Nishimori [Sek12] es un caso especial de un término cuántico adicional más general. Estudiamos también las propiedades más importantes de estos nuevos términos, concluyendo que las propiedades del estado fundamental de los diferentes términos que componen el Hamiltoniano no son un factor decisivo para el éxito o el fracaso del quantum annealing.

Bibliography

[ÁB10a] R. Álvarez Baños, A. Cruz, L. A. Fernandez, J. M. Gil-Narvion, A. Gordillo-Guerrero, M. Guidetti, A. Maiorano, F. Mantovani, E. Marinari, V. Martin-Mayor, J. Monforte-Garcia, A. Muñoz Sudupe, D. Navarro, G. Parisi, S. Perez-Gaviro, J. Ruiz-Lorenzo, S. F. Schifano, B. Seoane, A. Tarancon, R. Tripiccione and D. Yllanes (Janus Collaboration): *J. Stat. Mech.* page P06026 (2010). doi:10.1088/1742-5468/2010/06/P06026. arXiv:1003.2569. Cited on pp. 5, 16, 20, 41, 46, 48, 49, 80, 86, 88, 90, 91, 92, 194, 256, and 288.

[ÁB10b] R. Álvarez Baños, A. Cruz, L. A. Fernandez, J. M. Gil-Narvion, A. Gordillo-Guerrero, M. Guidetti, A. Maiorano, F. Mantovani, E. Marinari, V. Martin-Mayor, J. Monforte-Garcia, A. Muñoz Sudupe, D. Navarro, G. Parisi, S. Perez-Gaviro, J. Ruiz-Lorenzo, S. F. Schifano, B. Seoane, A. Tarancon, R. Tripiccione and D. Yllanes (Janus Collaboration): *Phys. Rev. Lett.* **105**, 177202 (2010). doi:10.1103/PhysRevLett.105.177202. arXiv:1003.2943. Cited on pp. 5, 16, 20, 48, 86, 194, 256, and 288.

[Ald57] B. J. Alder and T. E. Wainwright: *J. Chem. Phys.* **27**, 1208 (1957). Cited on p. 116.

[All89] M. P. Allen and D. J. Tildesley: *Computer Simulation of Liquids*. Second edition (Oxford University Press, New York, 1989). Cited on p. 141.

[Alm78] J. R. de Almeida and D. J. Thouless: *J. Phys. A: Math. Gen.* **11**, 983 (1978). Cited on p. 34.

[Ami05] D. J. Amit and V. Martin-Mayor: *Field Theory, the Renormalization Group and Critical Phenomena*. third edition (World Scientific, Singapore, 2005). Cited on pp. 57, 61, 63, and 155.

[And02] V. J. Anderson and H. N. W. Lekkerkerker: *Nature* **416**, 811 (2002). Cited on p. 142.

[Asp02] T. Aspelmeier, A. J. Bray and M. A. Moore: *Phys. Rev. Lett.* **89**, 197202 (2002). doi:10.1103/PhysRevLett.89.197202. Cited on pp. 84, 85, 104, 263, and 267.

[AU10] S. Angioletti-Uberti, M. Ceriotti, P. D. Lee and M. W. Finnis: *Phys. Rev. B* **81**, 125416 (2010). Cited on pp. 142, 148, 244, and 276.

[Aue01] S. Auer and D. Frenkel: *Nature* **413**, 711–713 (2001). doi:10.1038/35099513. Cited on p. 117.

[Ban87] J. R. Banavar and A. J. Bray: *Phys. Rev. B* **35**, 8888 (1987). doi:10.1103/PhysRevB.35.8888. Cited on p. 83.

[Bap12] V. Bapst and G. Semerjian: *J. Stat. Mech.* page P06007 (2012). Cited on pp. 172, 185, 188, and 287.

[Bar98] P. Bartlett: *J. Chem. Phys.* **109**, 10970–10975 (1998). Cited on p. 117.

[Bar00] C. Bartels: *Chem. Phys. Lett.* **331**, 446 (2000). Cited on p. 142.

[Bar01] A. Barrat and L. Berthier: *Phys. Rev. Lett.* **87**, 087204 (2001). doi:10.1103/PhysRevLett.87.087204. Cited on pp. 194 and 288.

[Bar12] F. Barahona: *J. Phys. A: Math Gen.* **15**, 3241 (2012). Cited on p. 170.

[Bel06] F. Belletti, F. Mantovani, G. Poli, S. F. Schifano, R. Tripiccione, I. Campos, A. Cruz, D. Navarro, S. Perez-Gaviro, D. Sciretti, A. Tarancon, J. L. Velasco, P. Tellez, L. A. Fernandez, V. Martin-Mayor, A. Muñoz Sudupe, S. Jimenez, A. Maiorano, E. Marinari and J. J. Ruiz-Lorenzo (Janus Collaboration): *Computing in Science and Engineering* **8**, 41 (2006). Cited on p. 41.

[Bel08a] F. Belletti, M. Cotallo, A. Cruz, L. A. Fernandez, A. Gordillo, A. Maiorano, F. Mantovani, E. Marinari, V. Martin-Mayor, J. Monforte, A. Muñoz Sudupe, D. Navarro, S. Perez-Gaviro, J. J. Ruiz-Lorenzo, S. F. Schifano, D. Sciretti, A. Tarancon, R. Tripiccione and J. L. Velasco (Janus Collaboration): *Comp. Phys. Comm.* **178**, 208–216 (2008). doi:10.1016/j.cpc.2007.09.006. arXiv:0704.3573. Cited on pp. 41, 70, 77, 78, and 80.

[Bel08b] F. Belletti, M. Cotallo, A. Cruz, L. A. Fernandez, A. Gordillo-Guerrero, M. Guidetti, A. Maiorano, F. Mantovani, E. Marinari, V. Martin-Mayor, A. Muñoz Sudupe, D. Navarro, G. Parisi, S. Perez-Gaviro, J. J. Ruiz-Lorenzo, S. F. Schifano, D. Sciretti, A. Tarancon, R. Tripiccione, J. L. Velasco and D. Yllanes (Janus Collaboration): *Phys. Rev. Lett.* **101**, 157201 (2008). arXiv:0804.1471. Cited on pp. 41, 46, 47, and 48.

[Bel09] F. Belletti, M. Guidetti, A. Maiorano, S. F. Mantovani, F. Schifano, R. Tripiccione, M. Cotallo, S. Perez-Gaviro, D. Sciretti, J. L. Velasco, A. Cruz, D. Navarro, A. Tarancon, L. A. Fernandez, V. Martin-Mayor, A. Muñoz-Sudupe, D. Yllanes, A. Gordillo-Guerrero, J. J. Ruiz-Lorenzo, E. Marinari, G. Parisi, M. Rossi and G. Zanier (Janus Collaboration): *Computing in Science and Engineering* **11**, 48 (2009). doi:10.1109/MCSE.2009.11. Cited on pp. 70, 77, and 78.

[Ber92] B. A. Berg and T. Neuhaus: *Phys. Rev. Lett.* **68**, 9 (1992). Cited on p. 142.

[Ber00] L. Berthier, J. L. Barrat and J. Kurchan: *Phys. Rev. E* **63**, 016105 (2000). Cited on p. 75.

[Ber02a] L. Berthier and J.-P. Bouchaud: *Phys. Rev. B* **66**, 054404 (2002). doi:10.1103/PhysRevB.66.054404. Cited on pp. 29, 30, 85, and 111.

[Ber02b] E. Bertin and J. P. Boucheaud: *J. Phys. A* **35**, 3039 (2002). Cited on pp. 75, 223, and 260.

[Ber03a] L. Berthier and J.-P. Bouchaud: *Phys. Rev. Lett.* **90**, 059701 (2003). doi:10.1103/PhysRevLett.90.059701. Cited on pp. 29 and 85.

[Ber03b] L. Berthier, V. Viasnoff, O. White, V. Orlyanchik and F. Krzakala: In *Proceedings of Les Houches 2002*, edited by J.-L. Barrat, J. Dalibard, M. Feigelman and J. Kurchan (Springer, Berlin, 2003). arXiv:cond-mat/0211106v2. Cited on p. 24.

[Ber04] F. Bert, V. Dupuis, E. Vincent, J. Hammann and J.-P. Bouchaud: *Phys. Rev. Lett.* **92**, 167203 (2004). doi:10.1103/PhysRevLett.92.167203. Cited on pp. 85 and 86.

[Bil94] A. Billoire, T. Neuhaus and B. A. Berg: *Nucl. Phys. B* **413**, 795 (1994). Cited on pp. 164 and 280.

[Bil00] A. Billoire and E. Marinari: *J. Phys. A* **33**, L265 (2000). doi:10.1088/0305-4470/33/31/101. Cited on pp. 84, 85, 87, and 263.

[Bil02] A. Billoire and E. Marinari: *Europhys. Lett.* **60**, 775 (2002). doi:10.1209/epl/i2002-00375-2. Cited on pp. 84, 85, 87, 263, 264, and 267.

[Bin03] K. Binder: *Physica A* **319**, 99 (2003). Cited on pp. 143 and 162.

[Bin11] K. Binder, B. Block, S. K. Das, P. Virnau and D. Winter: (2011). arXiv:1103.2241. Cited on pp. 142 and 162.

[Bis02] M. Biskup, L. Chayes and R. Kotecký: *Europhys. Lett.* **60**, 21 (2002). Cited on pp. 143 and 162.

[Bok00] H. Bokil, M. Moore and B. Drossel: *Phys. Rev. B* **62**, 946 (2000). Cited on p. 41.

[Bol97] P. G. Bolhuis, D. Frenkel, S.-C. Mau and D. A. Huse: *Nature* **388**, 235 (1997). Cited on p. 143.

[Bor92] C. Borgs and R. Kotecký: *Phys. Rev. Lett.* **68**, 1734 (1992). Cited on pp. 156 and 278.

[Bou97] J.-P. Bouchaud, L. F. Cugliandolo, J. Kurchan and M. Mèzard: In *Spin Glasses and Random Fields*, edited by A. P. Young (World Scientific, Singapore, 1997). Cited on pp. 27 and 43.

[Bra87] A. J. Bray and M. A. Moore: In *Heidelberg Colloquium on Glassy Dynamics*, edited by J. L. van Hemmen and I. Morgenstern, number 275 in Lecture Notes in Physics (Springer, Berlin, 1987). Cited on pp. 28, 83, 105, 108, and 263.

[Bra94] A. J. Bray: *Adv. Phys.* **43**, 357 (1994). Cited on p. 27.

[Bra09] G. Brambilla, D. E. Masri, M. Pierno, L. Berthier, L. Cipelletti, G. Petekidis and A. B. Schofield: *Physical Review Letters* **102**, 085703 (pages 4) (2009). doi:10.1103/PhysRevLett.102.085703. URL http://link.aps.org/abstract/PRL/v102/e085703. Cited on p. 117.

[Cac03] A. Cacciuto, S. Auer and D. Frenkel: *J. Chem. Phys.* **119**, 7467 (2003). Cited on pp. 142, 165, and 280.

[Cha05] P. Chaudhuri, S. Karmakar, C. Dasgupta, H. R. Krishnamurthy and A. K. Sood: *Phys. Rev. Lett.* **95**, 248301 (pages 4) (2005). Cited on p. 117.

[Cho06] M. Chopra, M. Müller and J. J. de Pablo: *J. Chem. Phys* **124**, 134102 (2006). Cited on pp. 145 and 276.

[Con03] P. Contucci: *J. Phys. A: Math. Gen.* **36**, 10961 (2003). Cited on p. 45.

[Con05] P. Contucci and C. Giardinà: *Ann. Henri Poincare* **6**, 915 (2005). Cited on p. 45.

[Con06] P. Contucci, C. Giardinà, C. Giberti and C. Vernia: *Phys. Rev. Lett.* **96**, 217204 (2006). doi:10.1103/PhysRevLett.96.217204. Cited on pp. 41 and 45.

[Con07] P. Contucci, C. Giardinà, C. Giberti, G. Parisi and C. Vernia: *Phys. Rev. Lett* **99**, 057206 (2007). Cited on p. 41.

[Con09] P. Contucci, C. Giardinà, C. Giberti, G. Parisi and C. Vernia: *Phys. Rev. Lett* **103**, 017201 (2009). Cited on p. 41.

[Cug94] L. F. Cugliandolo, J. Kurchan and G. Parisi: *J. Phys. (France)* **4**, 1641 (1994). Cited on pp. 74, 75, and 259.

[Das08] A. Das and B. K. Chakrabarti: *Rev. Mod. Phys.* **80**, 1061 (2008). Cited on p. 170.

[Dav00] R. L. Davidchack and B. B. Laird: *Phys. Rev. Lett.* **85**, 4751 (2000). Cited on pp. 162, 165, and 278.

[Dav10] R. L. Davidchack: *J. Chem. Phys.* **133**, 234701 (2010). Cited on pp. 142, 162, 165, 278, and 280.

[Dom93] C. de Dominicis, I. Kondor and T. Temesvári: *J. Mod. Phys. B* **7**, 986 (1993). Cited on pp. 80, 82, 262, and 264.

[Dom98] C. de Dominicis, I. Kondor and T. Temesvári: In *Spin Glasses and Random Fields*, edited by A. P. Young (World Scientific, Singapore, 1998). Cited on pp. 80, 82, 262, and 264.

[Dom06] C. de Dominicis and I. Giardina: *Random Fields and Spin Glasses* (Cambridge University Press, Cambridge, England, 2006). Cited on pp. 80, 82, 262, and 264.

[Dot01] V. Dotsenko: *Introduction to the Replica Theory of Disordered Statistical Systems* (Cambridge University Press, Cambridge, 2001). Cited on p. 33.

[Dui92] J. S. van Duijneveldt and D. Frenkel: *J. Chem. Phys* **96**, 4655 (1992). Cited on p. 142.

[Dul04] R. P. A. Dullens and W. K. Kegel: *Phys. Rev. Lett.* **92**, 195702 (pages 4) (2004). Cited on p. 117.

[Dup05] V. Dupuis, F. Bert, J.-P. Bouchaud, J. Hammann, F. Ladieu, D. Parker and E. Vincent: *Pramana J. of Phys.* **64**, 1109 (2005). Cited on p. 24.

[Edw75] S. F. Edwards and P. W. Anderson: *J. Phys. F* **5**, 965 (1975). doi:10.1088/0305-4608/5/5/017. Cited on p. 30.

[Erro4] J. R. Errington: *J. Chem. Phys.* **120**, 3130 (2004). Cited on pp. 142, 157, and 158.

[Evao1] R. M. L. Evans and C. B. Holmes: *Phys. Rev. E* **64**, 011404 (2001). Cited on p. 117.

[Fal82] M. Falcioni, E. Marinari, M. L. Paciello, G. Parisi and B. Taglienti: *Phys. Lett.* **108**, 331 (1982). Cited on pp. 151 and 277.

[Faro1] E. Farhi, J. Goldstone, S. Gutmann, J. Lapan, A. Lundgren and D. Preda: *Science* **292**, 474 (2001). Cited on p. 171.

[Faso4] M. Fasolo and P. Sollich: *Phys. Rev. E* **70**, 041410–1–041410–17 (2004). doi:10.1103/PhysRevE.70.041410. Cited on p. 117.

[Fer88] A. M. Ferrenberg and R. H. Swendsen: *Phys. Rev. Lett.* **61**, 2635 (1988). Cited on pp. 151 and 277.

[Fero6a] L. A. Fernandez, V. Martin-Mayor and P. Verrocchio: *Phys. Rev. E* **73**, 020501 (2006). doi:10.1103/PhysRevE.73.020501. Cited on p. 90.

[Fero6b] L. A. Fernández, V. Martín-Mayor and P. Verrocchio: *Phys. Rev. E* **73**, 020501 (Feb 2006). doi:10.1103/PhysRevE.73.020501. Cited on pp. 118 and 272.

[Fero7a] L. A. Fernández, V. Martín-Mayor and P. Verrocchio: volume 87 of *The Xth international workshop on disordered systems*, pages 581–586 (Taylor and Francis, 2007). doi:10.1080/14786430600919302. Cited on pp. 118, 124, and 272.

[Fero7b] L. A. Fernández, V. Martín-Mayor and P. Verrocchio: *Physical Review Letters* **98**, 085702 (pages 4) (2007). doi:10.1103/PhysRevLett.98.085702. URL `http://link.aps.org/abstract/PRL/v98/e085702`. Cited on pp. 117, 118, 119, 120, 124, 125, 127, 129, 194, 272, 273, and 288.

[Fero8a] L. A. Fernandez, A. Gordillo-Guerrero, V. Martin-Mayor and J. J. Ruiz-Lorenzo: *Phys. Rev. Lett.* **100**, 057201 (2008). doi:10.1103/PhysRevLett.100.057201. Cited on p. 120.

[Fero8b] L. A. Fernández, A. Gordillo-Guerrero, V. Martín-Mayor and J. J. Ruiz-Lorenzo: *Physical Review Letters* **100**, 057201 (pages 4) (2008). doi:10.1103/PhysRevLett.100.057201. URL `http://link.aps.org/abstract/PRL/v100/e057201`. Cited on p. 128.

[Fero9a] L. Fernandez, V. Martin-Mayor, S. Perez-Gaviro, A. Tarancon and A. Young: *Physical Review B* **80**, 024422 (2009). Cited on p. 132.

[Fero9b] L. A. Fernandez, V. Martin-Mayor and D. Yllanes: *Nucl. Phys. B* **807**, 424–454 (2009). Cited on pp. 142, 145, 150, 195, 233, and 289.

[Fer10a] L. A. Fernandez, V. Martin-Mayor, G. Parisi and B. Seoane: *Phys. Rev. B* **81**, 134403 (2010). Cited on pp. 16, 58, and 256.

[Fer10b] L. A. Fernandez, V. Martin-Mayor, B. Seoane and P. Verrocchio: *Phys. Rev. E* **82**, 021501 (2010). Cited on pp. 16, 119, 120, 123, 256, and 272.

[Fer12a] L. A. Fernandez, V. Martin-Mayor, G. Parisi and B. Seoane: *Sent for publication* (2012). Cited on pp. 16 and 256.

[Fer12b] L. A. Fernandez, V. Martin-Mayor, B. Seoane and P. Verrocchio: *Phys. Rev. Lett.* **108**, 165701 (2012). Cited on pp. 16, 119, 120, 141, and 256.

[Fil11] M. Filippone, S. Dusuel and J. Vidal: *Phys. Rev. A* **83**, 022327 (2011). Cited on p. 185.

[Fin94] A. B. Finnila, M. A. Gomez, C. Sebenik, C. Stenson and J. D. Doll: *Chem. Phys. Lett.* **219**, 343 (1994). Cited on p. 170.

[Fis86] D. S. Fisher and D. A. Huse: *Phys. Rev. Lett.* **56**, 1601 (1986). doi:10.1103/PhysRevLett.56.1601. Cited on pp. 38, 105, and 108.

[Fis87] D. Fisher and D. Huse: *J. Phys. A* **20** (1987). Cited on p. 38.

[Fis88a] D. S. Fisher and D. A. Huse: *Phys. Rev. B* **38**, 386 (1988). Cited on p. 38.

[Fis88b] D. S. Fisher and D. A. Huse: *Phys. Rev. B* **38**, 373 (1988). Cited on pp. 39 and 83.

[Fra98] S. Franz, M. Mézard, G. Parisi and L. Peliti: *Phys. Rev. Lett.* **81**, 1758 (1998). doi:10.1103/PhysRevLett.81.1758. Cited on pp. 194 and 288.

[Fre84] D. Frenkel and A. J. C. Ladd: *J. Chem. Phys.* **81**, 3188 (1984). Cited on p. 142.

[Gar79] M. R. Garey and D. S. Johnson: *Computers and Intractability* (Freeman, San Francisco, 1979). Cited on p. 169.

[Glo07] S. C. Glotzer and M. J. Solomon: *Nat. Mater.* **6**, 557 (2007). Cited on p. 116.

[Gra87] P. Granberg, P. Svendlindh, P. Nordblad, L. Lundgren and H. S. Chen: *Phys. Rev. B* **35**, 2075 (1987). Cited on p. 77.

[Gri01a] T. S. Grigera, and G. Parisi: *Phys. Rev. E* **63**, 045102 (2001). Cited on pp. 118 and 272.

[Gri01b] T. S. Grigera and G. Parisi: *Phys. Rev. E* **63**, 045102 (Mar 2001). doi:10.1103/PhysRevE.63.045102. Cited on p. 129.

[Gro96] L. K. Grover: In *Proceedings of the 28th Annual Symposium on the Theory of Computing* (ACM Press, New York, 1996). Cited on p. 172.

[Gro97] L. K. Grover: *Phys. Rev. Lett.* **79**, 325 (1997). Cited on p. 172.

[Han86] J. P. Hansen and I. R. McDonald: *Theory of Simple Liquids* (Academic Press, San Diego, 1986). Cited on p. 124.

[Här12] A. Härtel, M. Oettel, R. E. Rozas, S. U. Egelhaaf, J. Horbach and H. Löwen: *Phys. Rev. Lett.* **108**, 226101 (2012). Cited on pp. 142, 165, and 280.

[Has08a] M. Hasenbusch, A. Pelissetto and E. Vicari: *J. Stat. Mech.* page L02001 (2008). Cited on pp. 67 and 259.

[Haso8b] M. Hasenbusch, A. Pelissetto and E. Vicari: *Phys. Rev. B* **78**, 214205 (2008). doi: 10.1103/PhysRevB.78.214205. Cited on pp. 86 and 96.

[Hen11] I. Hen and A. P. Young: *Phys. Rev. E* **84**, 061152 (2011). Cited on pp. 171 and 282.

[Hér02] D. Hérisson and M. Ocio: *Phys. Rev. Lett.* **88**, 257202 (2002). `arXiv:cond-mat/0112378`. Cited on p. 28.

[Hog03] T. Hogg: *Phys. Rev. A* **67**, 022314 (2003). Cited on p. 171.

[Hoo68] W. G. Hoover and F. H. Ree: *J. Chem. Phys* **49**, 3609 (1968). Cited on pp. 120, 142, and 276.

[Huk96] K. Hukushima and K. Nemoto: *J. Phys. Soc. Japan* **65**, 1604 (1996). doi:10.1143/JPSJ.65.1604. `arXiv:cond-mat/9512035`. Cited on pp. 61, 90, 120, 129, 130, and 170.

[Hus87] D. Huse and D. Fisher: *J. Phys. A* **20** (1987). Cited on p. 38.

[Jim05] S. Jimenez, V. Martin-Mayor and S. Perez-Gaviro: *Phys. Rev. B* **72**, 054417 (2005). Cited on pp. 30 and 85.

[Jon98] K. Jonason, E. Vincent, J. Hammann, J.-P. Bouchaud and P. Nordblad: *Phys. Rev. Lett.* **81**, 3243 (1998). doi:10.1103/PhysRevLett.81.3243. Cited on pp. 27, 29, 85, 194, 257, 263, and 288.

[Jön02] P. E. Jönsson, H. Yoshino and P. Nordblad: *Phys. Rev. Lett.* **89**, 097201 (2002). doi: 10.1103/PhysRevLett.89.097201. Cited on p. 86.

[Jön04] P. E. Jönsson, R. Matheiu, H. Nordblad, P. Yoshino, H. Aruga Katori and A. Ito: *Phys. Rev. B* **70**, 174402 (2004). doi:10.1103/PhysRevB.70.174402. Cited on pp. 83, 86, and 263.

[Jör08] T. Jörg, F. Krzakala, J. Kurchan and A. C. Maggs: *Phys. Rev. Lett.* **101**, 147204 (2008). Cited on pp. 41, 171, and 282.

[Jör10a] T. Jörg, F. Krazakala, J. Kurchan, A. C. Maggs and J. Pujos: *Europhys. Lett.* **89**, 40004 (2010). Cited on pp. 171, 172, 173, 185, 245, and 282.

[Jör10b] T. Jörg, F. Krzakala, G. Semerjian and F. Zamponi: *Phys. Rev. Lett.* **104**, 207206 (2010). Cited on pp. 171 and 282.

[Kad98] T. Kadowaki and H. Nishimori: *Phys. Rev. E* **58**, 5355 (1998). Cited on pp. 170 and 281.

[Kas56] T. Kasuya: *Prog. Theor. Phys.* **16**, 45 (1956). Cited on p. 23.

[Kat07] H. G. Katzgraber and F. Krzakala: *Phys. Rev. Lett.* **98**, 017201 (2007). doi:10.1103/PhysRevLett.98.017201. Cited on pp. 84, 85, 86, 90, 94, 108, 109, 263, 265, 266, 270, 271, and 272.

[Ken06] G. G. Kenning, G. F. Rodriguez and R. Orbach: *Phys. Rev. Lett.* **97**, 057201 (2006). Cited on p. 75.

[Kir83] S. Kirkpatrick, C. D. J. Gelatt and M. P. Vecchi: *Science* **220**, 671 (1983). Cited on p. 170.

[Kof99] D. A. Kofke and P. G. Bolhuis: *Phys. Rev. E* **59**, 618–622 (Jan 1999). doi:10.1103/PhysRevE.59.618. Cited on p. 117.

[Krz00] F. Krzakala and O. C. Martin: *Phys. Rev. Lett.* **85**, 3013 (2000). Cited on pp. 38, 41, and 46.

[Krz04] F. Krzakala: *Europhys. Lett.* **66**, 847 (2004). doi:10.1209/epl/i2003-10261-5. Cited on pp. 84, 85, and 263.

[Lad77] J. C. Ladd and L. V. Woodcock: *J. Chem. Phys.* **51**, 155 (1977). Cited on p. 142.

[Lan00] D. P. Landau and K. Binder: *A guide to Monte Carlo simulations in statistical physics* (Cambridge University, Cambridge, 2000). Cited on p. 133.

[Leu08] L. Leuzzi, G. Parisi, F. Ricci-Tersenghi and J. J. Ruiz-Lorenzo: *Phys. Rev. Lett.* **101**, 107203 (2008). Cited on p. 78.

[Lid11] S. M. Liddle, T. Narayanan and W. C. K. Poon: *J. Phys: Condens. Matter* **23**, 194116 (2011). Cited on p. 116.

[Lus98] R. Lustig: *J. Chem. Phys.* **109**, 8816 (1998). Cited on pp. 120, 126, 128, and 231.

[Mac04] L. G. MacDowell, P. Virnau, M. Müller and K. Binder: *J. Chem. Phys.* **120**, 5293 (2004). Cited on p. 162.

[Mac06] L. G. MacDowell, V. K. Shen and J. R. Errington: *J. Chem. Phys.* **125**, 034705 (2006). Cited on pp. 143 and 162.

[Man03] V. N. Manoharan, M. T. Elsesser and D. J. Pine: *Science* **301**, 483 (2003). Cited on p. 116.

[Mar95] E. Marinari, G. Parisi and F. Ritort: *J. Phys. A* **28**, 327 (1995). Cited on p. 54.

[Mar98] E. Marinari: In *Advances in Computer Simulation*, edited by J. Kerstész and I. Kondor (Springer-Berlag, 1998). Cited on pp. 90, 120, 129, and 130.

[Mar00] E. Marinari, G. Parisi, F. Ricci-Tersenghi, J. J. Ruiz-Lorenzo and F. Zuliani: *J. Stat. Phys.* **98**, 973 (2000). Cited on pp. 38, 41, and 263.

[Méz87] M. Mézard, G. Parisi and M. Virasoro: *Spin-Glass Theory and Beyond* (World Scientific, Singapore, 1987). Cited on pp. 20 and 33.

[Méz01] M. Mézard and G. Parisi: *Eur. Phys. J. B* **20**, 217 (2001). Cited on pp. 52 and 257.

[MM07] V. Martín-Mayor: *Physical Review Letters* **98**, 137207 (pages 4) (2007). doi:10.1103/PhysRevLett.98.137207. URL `http://link.aps.org/abstract/PRL/v98/e137207`. Cited on pp. 120, 126, 128, 135, 136, 142, 145, 150, 162, 165, 192, and 273.

[MM09] V. Martin-Mayor and D. Yllanes: *Phys. Rev. E* **80**, 015701(R) (2009). Cited on p. 233.

[MM11] V. Martin-Mayor, B. Seoane and D. Yllanes: *J. Stat. Phys.* **144**, 554 (2011). doi: 10.1007/s10955-011-0261-4. Cited on pp. 16, 119, 120, 141, 142, 145, 195, 256, and 289.

[Moo98] M. Moore, H. Bokil and B. Drossel: *Phys. Rev. Lett.* **81**, 4252 (1998). Cited on p. 41.

[Moro5] D. Moroni, P. Rein, P. R. ten Wolde and P. G. Bolhuis: *Phys. Rev. Lett.* **94**, 235703 (2005). Cited on pp. 145 and 276.

[Muo5] Y. Mu, A. Houk and X. Song: *J. Phys. Chem. B* **109**, 6500 (2005). Cited on pp. 142, 162, 165, 278, and 280.

[Myd93] J. A. Mydosh: *Spin Glasses: an Experimental Introduction* (Taylor and Francis, London, 1993). Cited on pp. 20, 23, and 26.

[Nag73] S. Nagata, P. H. Keesom and H. R. Harrison: *Phys. Rev. B* **19**, 1633 (1973). Cited on p. 26.

[NN97] M. Ney-Nifle and A. Young: *J. Phys. A* **30**, 5311 (1997). doi:10.1088/0305-4470/30/15/017. Cited on pp. 84, 85, 89, 90, 94, 263, 265, and 266.

[NN98] M. Ney-Nifle: *Phys. Rev. B* **57**, 492 (1998). doi:10.1103/PhysRevB.57.492. Cited on pp. 84, 85, 90, 94, 263, and 266.

[Noyo8] E. G. Noya, C. Vega and E. de Miguel: *J. Chem. Phys.* **128**, 154507 (2008). Cited on p. 142.

[Nuß06] A. Nußbaumer, E. Bittner, T. Neuhaus and W. Janke: *Europhys. Lett.* **75**, 716 (2006). Cited on p. 162.

[Paloo] M. Palassini and A. P. Young: *Phys. Rev. Lett.* **85**, 3017 (2000). Cited on pp. 38, 41, and 46.

[Pap98] C. H. Papadimitriou and K. Steiglitz: *Combinatorial Optimization: Algorithms and Complexity* (Dover, New York, 1998). Cited on p. 169.

[Par79] G. Parisi: *Phys. Rev. Lett.* **43**, 1754 (1979). Cited on p. 34.

[Par80] G. Parisi: *J. Phys. A* **a13**, L115 (1980). Cited on p. 34.

[Par84] G. Parisi: In *Proceedings of Les Houches 1982, Session XXXIX*, edited by J. B. Zuber and R. Stora (North Holland, Amsterdam, 1984). Cited on p. 83.

[Par88] G. Parisi: *Statistical Field Theory* (Addison-Wesley, 1988). Cited on p. 204.

[Par92] G. Parisi: *Field Theory, Disorder and Simulations* (World Scientific, 1992). Cited on p. 115.

[Par97] G. Parisi, P. Ranieri, F. Ricci-Tersenghi and J. J. Ruiz-Lorenzo: *J. Phys A: Math. Gen.* **30**, 7115 (1997). Cited on p. 78.

[Paroo] G. Parisi and F. Ricci-Tersenghi: *J. Phys. A: Math. Gen.* **33**, 113 (2000). Cited on p. 46.

[Paro6] G. Parisi: *Mean field theory of spin glasses: statics and dynamics* (2006). Cited on pp. 52, 71, and 257.

[Par10] G. Parisi and T. Rizzo: *J. Phys. A* **43**, 235003 (2010). doi:10.1088/1751-8113/43/23/235003. Cited on pp. 51, 84, 85, 87, 96, 101, 108, 264, and 267.

[Poloo] J. M. Polson, E. Trizac, S. Pronk and D. Frenkel: *J. Chem. Phys.* **112**, 5339 (2000). Cited on p. 142.

[Pus86a] P. N. Pusey and van Megen: *Nature* **320**, 340 (1986). Cited on p. 116.

[Pus86b] P. N. Pusey and W. van Megen: *Nature* **320**, 340–342 (1986). doi:10.1038/320340a0. Cited on p. 116.

[Pus89] P. N. Pusey, W. van Megen, P. Bartlett, B. J. Ackerson, J. G. Rarity and S. M. Underwood: *Phys. Rev. Lett.* **63**, 2753 (1989). Cited on pp. 116 and 142.

[Ram86] R. Rammal, G. Toulouse and M. A. Virasoro: *Rev. Mod. Phys.* **58**, 765 (1986). Cited on p. 35.

[Riz03] T. Rizzo and A. Crisanti: *Phys. Rev. Lett.* **90**, 137201 (2003). doi:10.1103/PhysRevLett.90.137201. Cited on pp. 84, 85, 87, 88, 96, 108, 263, 264, and 267.

[Rodo3] G. F. Rodriguez, G. G. Kenning and R. Orbach: *Phys. Rev. Lett.* **91**, 037203 (2003). Cited on pp. 24 and 259.

[Rolo3] J. Roland and N. J. Cerf: *Phys. Rev. A* **68**, 062312 (2003). Cited on p. 172.

[Rom11] F. Romano and F. Sciortino: (2011). `arXiv:1101.3877`. Cited on p. 116.

[Rud54] M. A. Ruderman and C. Kittel: *Phys. Rev.* **96**, 99 (1954). Cited on p. 23.

[Rue69] D. Ruelle: *Statistical Mechanics* (Benjamin, 1969). Cited on pp. 155, 156, and 277.

[Sano1] L. Santen and W. Krauth: condmat/0107459 (2001). Cited on p. 124.

[Sano6] G. E. Santoro and E. Tosatti: *J. Phys. A* **39**, R393 (2006). Cited on p. 170.

[Saso5] M. Sasaki, K. Hukushima, H. Yoshino and H. Takayama: *Phys. Rev. Lett.* **95**, 267203 (2005). doi:10.1103/PhysRevLett.95.267203. Cited on pp. 84, 85, 108, 263, and 270.

[Scho7] L. S. Schulman: *Phys. Rev. Lett.* **98**, 257202 (2007). doi:10.1103/PhysRevLett.98.257202. Cited on p. 90.

[Scho9] M. Schrader, P. Virnau and K. Binder: *Phys. Rev. E* **79**, 061104 (2009). Cited on p. 142.

[Scio9] F. Sciortino, A. Giacometti and G. Pastore: *Phys. Rev. Lett.* **103**, 237801 (2009). Cited on p. 116.

[Sek12] Y. Seki and H. Nishimori: *Phys. Rev. E* **85**, 051112 (2012). Cited on pp. 171, 172, 173, 179, 185, 188, 195, 245, 282, 283, and 289.

[Seo12] B. Seoane and H. Nishimori: *J. Phys. A* **45**, 435301 (2012). Cited on pp. 16 and 256.

[She75] D. Sherrington and S. Kirkpatrick: *Phys. Rev. Lett.* **35**, 1792 (1975). Cited on pp. 33 and 257.

[Sim04] N. B. Simeonova and W. K. Kegel: *Phys. Rev. Lett.* **93**, 035701 (2004). Cited on p. 125.

[Sok97] A. D. Sokal: In *Functional Integration: Basics and Applications (1996 Cargèse School)*, edited by C. DeWitt-Morette, P. Cartier and A. Folacci (Plenum, N.Y., 1997). Cited on pp. 91 and 155.

[Sol10] P. Sollich and N. B. Wilding: *Phys. Rev. Lett.* **104**, 118302 (2010). Cited on pp. 116 and 117.

[Ste83] P. J. Steinhardt, D. R. Nelson and M. Ronchetti: *Phys. Rev. B* **28**, 784 (1983). Cited on pp. 121, 142, 274, and 276.

[Suz76] M. Suzuki: *Prog. Theor. Phys.* **56**, 1454 (1976). Cited on pp. 173, 245, and 283.

[Suz07] S. Suzuki, H. Nishimori and M. Suzuki: *Phys. Rev. E* **75**, 051112 (2007). Cited on p. 195.

[Tal06] M. Talagrand: *Ann. Math.* **163**, 221 (2006). Cited on p. 35.

[Tho86] D. J. Thouless: *Phys. Rev. Lett.* **56**, 1082 (1986). Cited on pp. 56 and 258.

[Tor74] G. M. Torrie and J. P. Valleau: *Chem. Phys. Lett.* **28**, 578 (1974). Cited on pp. 142, 145, and 276.

[Tor77] G. M. Torrie and J. P. Valleau: *J. Comp. Physics.* **23**, 187 (1977). Cited on p. 142.

[Veg07] C. Vega and E. G. Noya: *J. Chem. Phys.* **127**, 154113 (2007). Cited on pp. 142, 157, and 158.

[Veg08] C. Vega, E. Sanz, J. L. F. Abascal and E. G. Noya: *J. Phys.: Condens. Matter* **20**, 153101 (2008). Cited on p. 142.

[Vin96] E. Vincent, J. Hammann, M. Ocio, J.-P. Bouchaud and L. F. Cugliandolo: In *Complex Behavior of Glassy Systems*, edited by M. Rubí and C. Pérez-Vicente, number 492 in Lecture Notes in Physics (Springer, 1996). Cited on pp. 20, 24, 25, and 40.

[Wan01] F. Wang and D. P. Landau: *Phys. Rev. Lett.* **86**, 2050 (2001). Cited on p. 142.

[Wil00] N. B. Wilding and A. D. Bruce: *Phys. Rev. Lett.* **85**, 5138 (2000). Cited on pp. 142, 157, 158, 159, and 278.

[Wil10] N. B. Wilding and P. Sollich: *J. Chem. Phys.* **133**, 224102 (2010). Cited on p. 117.

[Wol95] P. ten Wolde, M. J. Ruiz-Montero and D. Frenkel: *Phys. Rev. Lett.* **75**, 2714 (1995). Cited on pp. 142, 145, and 276.

[Woo57] W. W. Wood and J. D. Jacobson: *J. Chem. Phys.* **27**, 1207 (1957). Cited on p. 116.

[Yan04a] Q. Yan, T. S. Jain and J. J. de Pablo: *Phys. Rev. Lett.* **92**, 235701 (pages 4) (2004). Cited on pp. 124 and 130.

[Yano4b] Q. Yan, T. S. Jain and J. J. de Pablo: *Phys. Rev. Lett.* **92**, 235701 (pages 4) (2004). Cited on p. 130.

[Yll11] D. Yllanes: *Rugged Free-Energy Landscapes in Disordered Spin Systems* (Ph.D. thesis, UCM, 2011). arXiv:1111.0266. Cited on pp. 48 and 87.

[Yos57] K. Yosida: *Phys. Rev.* **106**, 893 (1957). Cited on p. 23.

[Yoso3] H. Yoshino: *J. Phys. A: Math. Gen.* **36**, 10819 (2003). Cited on pp. 83 and 263.

[You97] A. P. Young: In *Spin Glasses and Random Fields*, edited by A. P. Young (World Scientific, Singapore, 1997). Cited on pp. 20 and 74.

[You08] A. P. Young, S. Knysh and V. N. Smelyanskiy: *Phys. Rev. Lett.* **101**, 170503 (2008). Cited on p. 171.

[You10] A. P. Young and S. Knysh: *Phys. Rev. Lett.* **104**, 020502 (2010). Cited on pp. 171 and 282.

[Zaco9a] E. Zaccarelli, C. Valeriani, E. Sanz, W. C. K. Poon, M. E. Cates and P. N. Pusey: *Physical Review Letters* **103**, 135704 (pages 4) (2009). doi:10.1103/PhysRevLett.103.135704. URL http://link.aps.org/abstract/PRL/v103/e135704. Cited on pp. 117 and 194.

[Zaco9b] E. Zaccarelli, C. Valeriani, E. Sanz, W. C. K. Poon, M. E. Cates and P. N. Pusey: *Phys. Rev. Lett.* **103**, 135704 (2009). Cited on p. 142.

[ZT10] T. Zykova-Timan, J. Horbach and K. Binder: *J. Chem. Phys* **133**, 014705 (2010). Cited on pp. 142, 144, 157, 159, 165, and 278.